Identify The Gas and Solid Flow Structures Within Bubbling Fluidized Beds by Using The PEPT Technique

LI Yunning

A thesis submitted for the Degree of Doctor of Philosophy

The University of Edinburgh

2016

Declaration

I hereby declare that this thesis has been composed by myself, and is my own work under the supervision of Dr. Fan and Prof. Stefano at the University of Edinburgh and technical supports from the University of Birmingham, except where clearly specified otherwise in the text. The work has not been submitted for any other degree or professional qualification.

LI Yunning

March 2016

List of Publications

Journal Papers:

Y. Li, H. Fan, and X. Fan, "Identify of flow patterns in bubbling fluidization," *Chemical Engineering Science,* vol. 117, pp. 455-464, 9/27/ 2014.

Y. Li, K. Zhang, and X. Fan, " Reconstruction of bubble spatial distribution in a bubbling fluidized bed based on solid motions measured by PEPT technique," *Chemical Engineering Science,* 2016. (submitted)

Y. Li and X. Fan, "Investigation of solid mixing in bubbling fluidized beds by using the PEPT technique," *Chemical Engineering Science,* 2016. (to be submitted)

Conference Papers/ Presentations:

Y. Li, Z. Yang, B. Olafssonand, and X. Fan, "A guide for generating different flow patterns in a bubbling fluidized bed", *PARTEC - International Congress on Particle Technology,* Nuremberg, Germany, 23-25 April 2013.

Y. Li, X. Fan, K. Zhang, and S. Brandani, "Effect of bed height and air distributor on the performance of a bubbling fluidized bed", *PARTEC - International Congress on Particle Technology,* Nuremberg, Germany, 23-25 April 2013.

Y. Li, H. Fan, and X. Fan, "Control of flow patterns in bubbling fluidization", *The 5th International Conference on Applied Energy (ICAE),* Pretoria, South Africa, 1-4 July 2013, ICAE2013-273.

Y. Li and X. Fan, "A study of bubble behaviour and particle dispersion in 3-D bubbling fluidized beds using PEPT technique", *Robert Pfeffer Symposium,* Edinburgh, United Kingdom, 25 June 2014.

Abstract

Fluidized beds have been applied in many industrial processes (e.g. coal combustion, gasification and granulation) as an effective means for providing excellent gas and solids contact and mixing, as well as good heat transfer. Although research on the fluidized bed has been carried out for more than 70 years, uncertainties and difficulties still remain. These challenges exist primarily due to the complex and dynamic flow structure within fluidized beds and the lack of reliable measurement techniques. The positron emission particle tracking (PEPT) technique, developed at the University of Birmingham, enables individual particles to be tracked non-invasively in opaque three-dimensional (3-D) fluidized beds and offers favourable temporal and spatial resolutions. PEPT is considered to be a powerful tool for fluidized bed studies and was utilized in the current study to investigate the dynamic behaviour of solid and gas in fluidized beds. The experiments in this study were conducted in a 150-mm inner diameter (I.D.) column and operated in the bubbling fluidization regime at ambient conditions. The effects of various factors on the solid flow structure were examined: solid properties, superficial gas velocity, bed height-to-diameter aspect ratio (H/D) and pore size of the air distributor. The solid flow structure was classified into four patterns, namely patterns A, B, C and D, in which pattern C was newly observed in this thesis. The solid motion, bubble behaviour (i.e., bubble spatial distribution, bubble size and bubble rise velocity) and solid mixing were assessed for each flow pattern to understand their unique fluidization behaviours. This assessment was achieved by the development of three methods: a method to reconstruct bubble behaviours based on

solid motion, and two methods for estimating the solid mixing profile in this thesis. The results were discussed and compared with the published literature. The bubble rise velocity and bubble size calculated in this research from the PEPT-measured data was in agreement with other research, particularly that of Kunii and Levenspiel, Yasui and Johanson, and Mori and Wen. Finally, a parameter was developed to predict and control flow patterns based on particle kinetic energy and various factors. The outcomes of this study advance the understanding of the complicated dynamics of bubbling fluidized beds and may benefit several industries in the enhancement of fluidized bed design and control to achieve desirable qualities and efficiencies.

Lay Summary

Fluidized beds have been applied in many industrial processes as an effective means for providing excellent gas and solids contact and mixing, as well as good heat transfer. The attractive feature is achieved by solid circulation, where solids are driven by gas and bubbles, and travel around within the bed. A different solid flow pattern will give different mixing efficiency, different gas-solids contact efficiency and different heat transfer rate. Although research on the fluidized bed has been carried out for more than 70 years, uncertainties and difficulties still remain. These challenges exist primarily due to the complex and dynamic flow structure within fluidized beds and the lack of reliable measurement techniques. The positron emission particle tracking (PEPT) technique, developed at the University of Birmingham, enables individual particles to be tracked accurately and non-invasively in opaque three-dimensional (3-D) fluidized beds. PEPT is considered to be a powerful tool for fluidized bed studies and was utilized in the current study to investigate the dynamic behaviour of solid and gas in fluidized beds. The experiments in this study were conducted in a lab-scale bubbling fluidized bed at ambient conditions. The effects of various factors on the solid flow structure were examined: solid properties, superficial gas velocity, bed height-to-diameter aspect ratio (H/D) and pore size of the air distributor. The solid flow structure was classified into four patterns, namely patterns A, B, C and D, in which pattern C was newly observed in this thesis. Key properties of fluidized beds, including solid motion, bubble spatial distribution, bubble size, bubble rise velocity and solid mixing, were assessed for each flow pattern to understand their unique fluidization behaviours.

This assessment was achieved by the development of three methods: a method to reconstruct bubble behaviours based on solid motion, and two methods for estimating the solid mixing profile in this thesis. The results were discussed and compared with the published literature. The bubble rise velocity and bubble size calculated in this research from the PEPT-measured data was in agreement with other research, particularly that of Kunii and Levenspiel, Yasui and Johanson, and Mori and Wen. Finally, a parameter was developed to predict and control flow patterns based on particle kinetic energy and various factors. The outcomes of this study advance the understanding of the complicated dynamics of bubbling fluidized beds and may benefit several industries in the enhancement of fluidized bed design and control to achieve desirable qualities and efficiencies.

Acknowledgments

I would like to express my utmost appreciation and thanks to my supervisor Dr. Xianfeng Fan; you have been a tremendous mentor to me. Thank you for encouraging my research and for allowing me to grow as a young researcher. Your advice on both research as well as my career have been priceless. During my PhD study, Dr. Fan invested significant effort into the project work and thesis writing and revision, and he also helped me in my daily life. The time I spent with Dr. Fan at the University of Edinburgh and in the Positron Imaging Centre at the University of Birmingham will always be a cherished memory. I consider myself fortunate to have been one of his students and will always remain grateful to him.

I would also like to express my gratitude to my second supervisor Prof. Stefano Brandani and examiner Dr. Don Glass for their highly helpful suggestions regarding my project during the first-year interview.

I'm deeply grateful to the University of Edinburgh for giving me the opportunity to study. I have many cherished memories at this amazing school, and my time here has been the most wonderful time of my life thus far.

I'm also grateful to the University of Birmingham and all the lovely people in the Positron Imaging Centre for their technical support of the measurement technique I used during my research.

Furthermore, I would like to express my deep gratitude to Prof. Neil Rowson from the University of Birmingham and Dr. Hyungwoong Ahn from the University of Edinburgh for graciously agreeing to be my viva examiners. Their feedback on my thesis was invaluable.

Finally, I would like to thank my wonderful parents, friends and colleagues at the University of Edinburgh for all the support they have given me during my studies. Without their moral support, my studies would not have been possible.

Contents

List of Figures

List of Tables

Nomenclature

A_0	area of air distributor plate per orifice (m^2)
d_b	bubble diameter (m)
d_{b0}	initial bubble diameter (m)
d_{bm}	maximum bubble diameter (m)
d_o	orifice size of air distributor (μm)
d_p	particle diameter (m)
D	fluidized bed diameter (m)
g	graviational acceleration (m/s^2)
h	height above air distributor (m)
u	superficial gas velocity (m/s)
u_b	bubble rise velocity (m/s)
u_{br}	single bubble rise velocity (m/s)
u_{mf}	minimum fluidization velocity (m/s)
u_{mb}	minimum bubbling velocity (m/s)
ρ_p	particle density (kg/m^3)
ρ_g	gas density (kg/m^3)

Chapter 1: Introduction

1.1 Background and Motivation

Fluidized beds have been widely applied in many industrial sectors due to their excellent mixing behaviour, favourable heat transfer and high efficiency [1]. The first commercial use of large-scale fluidized beds can date back to as early as 1926, when Winkler's coal gasifier went into operation. However, this gasifier was not commercially successful [2]. Later, a fluid catalytic cracking (FCC) unit was built at Exxon's Baton Rouge refinery in 1942, representing the first successful commercial application of fluidized beds [2]. Since then, fluidized beds have spread widely to various industrial processes, such as the chemical, petroleum, power generation, metallurgical, pharmaceutical, food and biochemical industries [3-5].

In a fluidized bed, the fluidizing gas is uniformly injected into the bed through an air distributor at the bed bottom, and particles are suspended by the upward gas and present a fluid-like behaviour. During operation, bubbles or gas voids are the "motor" for solid motion and mixing and induce heterogeneity within the bed. The solid motion and bubble behaviour are therefore very important properties of a fluidized bed and are responsible for the fluidization performance. The efficiency and productivity of fluidized beds vary significantly with the flow structures within a fluidized bed (i.e., solid motion, bubble behaviour, interaction between solid and bubbles, etc.). They are influenced by operational conditions (i.e., superficial gas velocity), solid properties and bed designs (i.e., bed height-to-diameter aspect ratio [H/D] and pore size of the air distributor). Research on the fluidized bed has been carried out both experimentally

and theoretically for many years to understand the dynamic behaviour of fluidized beds and the effect of various factors. However, uncertainties still remain, and results reported in the literature are occasionally conflicting [3, 6]. These inconsistencies are primarily due to the complex dynamic flow structure within the fluidized bed and the lack of reliable measurement techniques. For example, two-dimensional (2-D) planner beds have typically been used to visualize fluidization behaviour [7, 8], but the wall effect on the flow structure can be significant [9]. In addition, invasive measurement techniques (i.e., optical fibre probes and capacitance probes) have been used to investigate the flow behaviour inside three-dimensional (3-D) fluidized beds [4, 8, 10-18]; however, these objects inserted within fluidized beds will alter the flow structure [4, 8, 10, 15, 19-21].

In order to investigate the dynamic and complex flow structure within the fluidized bed, a proper measurement technique is required. The desirable measurement technique should be non-invasive and able to identify 3-D opaque equipment. High spatial and temporal resolutions of the measurement techniques are also necessary, and the measurement area of the technique should be large enough to cover the entire bed material. The positron emission particle tracking (PEPT) technique developed at the University of Birmingham offers these necessary characteristics [22-28]. The PEPT technique enables individual particles to be tracked non-invasively in opaque 3-D vessels. The detectors cover an area of 508 mm × 381 mm and can locate a tracer particle 250 times per second with spatial resolutions of 0.5 mm when the particle velocity is 1 m/s.

In this study, the PEPT technique is used to determine the complex dynamic flow structures within 3-D opaque fluidized beds, and to investigate the effects of various factors on the dynamic behaviour of fluidized beds.

1.2 Research Objectives

The research presented in this thesis focuses on bubbling fluidization. The aim is to find a methodology to predict solid and gas behaviour and solid mixing within bubbling fluidized beds based on bed materials, bed design and operational conditions, and to advance the understanding of the solid and gas dynamic behaviour in bubbling fluidized beds. To achieve this aim, the detailed research includes the following objectives:

1. Track solid motions using the PEPT technique.
2. Calculate and analyse particle vertical and horizontal velocity profiles.
3. Measure and classify different solid flow patterns, including microscopic motions, in bubbling fluidized beds.
4. Investigate the effects of solid properties, superficial gas velocities, pore sizes of air distributors, and H/D on the solid and gas flow patterns.
5. Develop a flow pattern parameter (FPP) to identify and to predict different solid flow patterns based on operational conditions.
6. Reconstruct the bubble spatial distributions for different flow patterns based on solid motion.

7. Develop an activity index (AI) to characterize the solid mixing behaviour and to estimate solid residence time distribution in different solid flow patterns based on PEPT data.

1.3 Thesis Layout

This thesis consists of seven chapters. Chapter 1 briefly discusses the research motivation and objectives of this study and gives the thesis layout.

Chapter 2 reviews the concepts of fluidization, the classification of bed material, the application of fluidized beds, measurement techniques and previous research relevant to this topic, such as research on solid flow patterns, bubble behaviours and solid mixing.

Chapter 3 presents an overview of the PEPT technique, fluidized bed setup, experimental conditions, solid properties and experimental procedures.

In Chapter 4, the effects of various factors on the solid flow pattern, such as solid properties, superficial gas velocities, pore sizes of air distributor and H/D, are examined. A map is presented showing the relative effect of different factors on the solid flow pattern. The solid flow structures are classified into four main groups, namely patterns A to D, based on the overall solid flow pattern, solid microscopic motion and solid vertical and horizontal velocity profiles.

In Chapter 5, a methodology and its feasibility for the reconstruction of bubble spatial distribution based on solid motion are discussed in detail. The bubble spatial distributions for the four flow patterns, and the effect of operational conditions, bed materials and bed designs on the bubble spatial distribution are then presented.

Chapter 6 investigates the solid mixing behaviour for different solid flow patterns, and the effect of solid flow patterns and bubble behaviours on the mixing profile. Solid dispersion coefficients in both vertical and horizontal directions are determined based on tracer particle trajectories. An AI is proposed to characterize the solid mixing behaviour in fluidized beds, and the residence time distribution of particles is calculated based on the AI.

Finally, Chapter 7 provides an overview of the results and conclusions of this study and outlines possible improvements and recommendations for future research.

Chapter 2: Literature Review

In this chapter, published literature on bubbling fluidization is reviewed. This review begins with the basic concepts of fluidized beds, such as fluidization regimes, classification of solid particles, solid motion and bubbling behaviour. The review then focuses on recent research on bubbling fluidized beds—particularly those studies focusing on solid flow patterns, solid mixing, bubble spatial distribution and bubble properties—and major industrial applications of bubbling fluidization techniques. The advantages and disadvantages of different measurement techniques that are frequently used to study gas-solid fluidized beds are also discussed.

2.1 Flow Regimes

Fluidization has been widely used in many industrial processes, such as coal combustion, metallurgy, CO_2 capture, thermal energy storage, renewable energy production, granulation and chemical processing. A typical fluidized bed is a cylindrical column filled with solid particles. The injection of fluids, either gaseous or liquid, fluidizes the particles to facilitate the mixing of solids, the contact of different materials, the contact of solids and fluids and the heat and mass transfer, thereby improving the reaction efficiency and energy efficiency. This study focuses on gas-solid fluidization, in which the gas phase fluidizes solid particles into a fluid-like state. Based on solid flow behaviour, gas-solid fluidization can be classified into different regimes, depending on the specific gas velocity, the size and density of solids and other factors.

2.1.1 Minimum Fluidization

Minimum fluidization is a critical state in gas-solid fluidization. It has been used to characterize the property of bed materials and has also been used as a guide for selecting operational conditions. In a fluidized bed, particles are packed in the column. When an upward-flowing gas imposes a high enough drag force to overcome the particle gravity force and friction force among the particles and between particles and the bed wall, the particles start to fluidize. At the point when particles are just starting to fluidize, the specific gas velocity is called minimum fluidization velocity; the fluidization state is called minimum fluidization. At minimum fluidization, the frictional force between particles and gas just counterbalances the weight of particles, and the vertical component of compressive force between adjacent particles just disappears [2, 5, 29, 30]. Before reaching the minimum fluidization, the drag force exerted on particles by gas per unit area equals the bed pressure drop (as shown schematically in Figure 2.1). Minimum fluidization velocity can be determined experimentally based on the pressure drop profile, as shown in Figure 2.1, or calculated based on empirical correlations. Figure 2.1 is pressure drop profile versus specific gas velocity. At the initial stage, the measured pressure drop linearly increases with specific gas velocity until the maximum point. After the maximum point, solids start to fluidize, and the pressure drop within the bed remains constant and equals the weight of the bed plus the friction with the bed wall. The specific gas velocity corresponding to the maximum pressure drop is taken as minimum fluidization velocity u_{mf}.

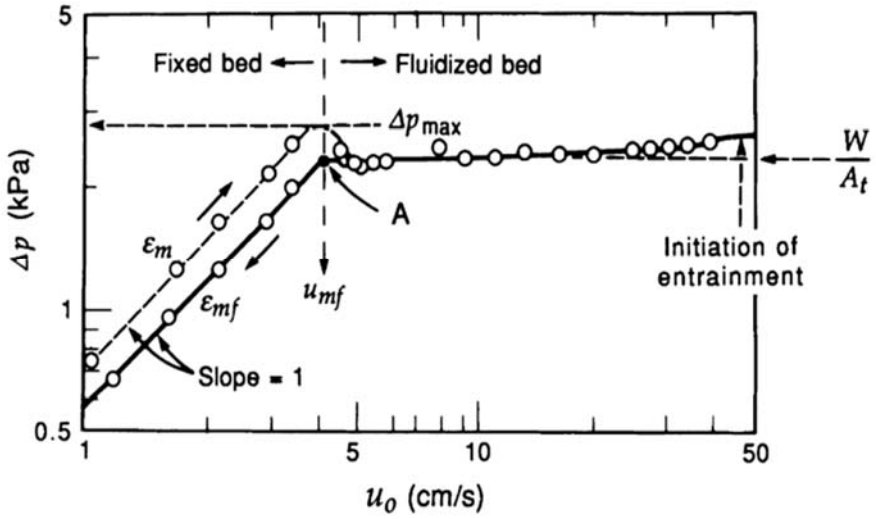

Figure 2.1 Pressure drop profile in a bubbling fluidized bed [2].

Above the minimum fluidization point (i.e., u_{mf}), the bed will expand and the gas will travel up in the form of bubbles. Particles are carried upward with the bubbles and circulated within the bed. A detailed explanation of particle motion induced by bubbles can be found later in section 2.5 of this chapter.

2.1.2 Fluidization Regimes

As indicated by Kunii and Levenspiel [2] and Yang [31], gas-solid fluidization can be described by 5 regimes (Figure 2.2) with drastically different characteristics as a result of particle properties and operating conditions [2, 32]. Below the minimum fluidization velocity, the bed is quiescent and the gas flows along the bed through interstices of particles. Further increases in gas flow rates will then lead to different fluidization regimes, from minimum fluidization regime to bubbling regime, slugging regime, turbulent regime and lean-phase regime with pneumatic transport, as seen in Figure 2.2. In the bubbling regime, gas passes through the bed in the form of bubbles,

as seen in Figure 2.2b. Gas bubbles will form just above the air distributors and coalesce and grow, promoting vigorous motion and mixing of solid particles as the bubbles rise to the bed surface. The slugging regime (Figure 2.2c) occurs only in beds with a high bed aspect ratio (i.e., H/D >~ 2) and the superficial gas velocity in excess of the minimum slugging velocity (i.e., $u_{ms} = u_{mf} + 0.07(gD)^{1/2}$) [2, 31, 33, 34]. Deep beds with large H/D ratios provide enough time for bubbles to coalesce into larger bubbles. When bubbles grow to approximately 2/3 of the bed cross-section, the bed is considered to be entering the slugging regime. In the slugging regime, large bubbles pass periodically through the bed, and the bed surface rises and falls at a regular frequency with large corresponding bed pressure fluctuations [2, 31]. With further increased gas flow rate, the bed in the bubbling regime can transition into either the slugging regime (if the ratio of bed diameter to particle size [D/d_p] is small) or into the turbulent regime (if the D/d_p is large) [31]. In a turbulent regime (Figure 2.2d), bubbles reach the maximum size and start breaking up into smaller-sized gas voids with various shapes [2]. Gas void streams and particle clusters dart to and fro, the bed surface is diffused and difficult to distinguish and entrainment becomes appreciable in this regime [2, 31]. As the gas flow rate increases, the bed will transition into the lean-phase regime with pneumatic transport (Figure 2.2e), where solid particles are carried out of the bed by gas [2]. Due to almost all particles being transported out of the bed in a dilute phase in which the concentration of particles varies along the bed height, continuous operation of the fluidized bed will not be possible without the recycling of entrained solid particles. Furthermore, no bed surface exists in this regime [2]. The research work reported in this thesis focuses on fluidized beds operated in the bubbling fluidization regime.

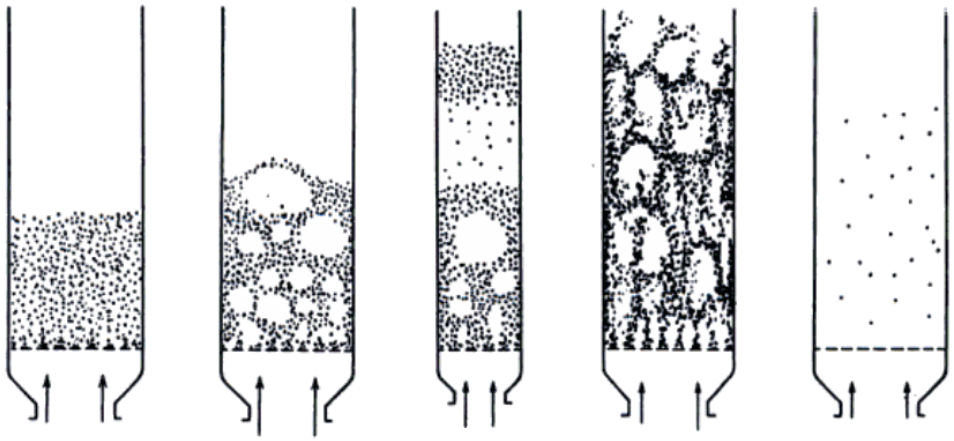

(a) (b) (c) (d) (e)

Figure 2.2 Regimes of fluidization, (a) minimum fluidization regime, (b) bubbling fluidization regime, (c) slugging regime, (d) turbulent fluidization, and (e) lean-phase regime with pneumatic transport [2].

2.2 Geldart Classification of Particles

Fluidization behaviour varies with physical properties of the fluidized particles [35-37]. In 1973, Geldart [38] proposed an empirical classification of particles based on their fluidization properties. That classification has since been widely used by engineers and academics in chemical, civil and pharmaceutical engineering [39]. The particle classification diagram proposed by Geldart (Figure 2.3) summarizes empirical observations on fluidized beds in terms of mean particle size versus the density difference between solid particles and fluidizing gas (ρ_s-ρ_g) [38, 40]. Overall, group C particles have the smallest sizes, group D particles have the largest sizes, group B particles are ranging in size from 40 to 500 microns, and group A particles are in an intermediate state between group B and C particles.

- Geldart group A particles are aeratable solid particles which have small mean particle sizes (20-100 μm) and/or low particle densities (<~1.4 g/cm^3). Beds of these particles exhibit some smooth expansion without bubbles before the beginning of bubbling fluidization, and bubbles will appear at minimum bubbling velocity (u_{mb}). Thus $u_{mb}/u_{mf} > 1$ for group A particles [31]. Fluid catalytic cracking (FCC) catalyst is a representative of group A particles.
- Geldart group B particles are sand-like solid particles and have a mean size of 40-500 microns and a density of 1.4-4 g/cm^3. These particles fluidize well. Vigorous bubbles are formed at the minimum fluidization velocity in beds of these particles, and bubbling fluidization is seen as soon as the superficial gas velocity exceeds u_{mf}. Thus, $u_{mb} \approx u_{mf}$ for group B particles [2]. Glass beads are typical group B particles.
- Geldart group C particles are very fine and cohesive, with a size of 20-30 μm. Fluidization is extremely difficult for these particles due to the interparticle force. These particles tend to rise as a plug of solids or to form gas channels where gas escapes from the air distributor directly to the bed surface without being distributed through the bulk [2, 31]. Face powder, flour, starch, talc, and cement are typical group C particles.
- Geldart group D particles are spoutable solid particles, or those that are large (>~600 μm) and/or dense. Beds of these particles behave irregularly, where large exploding bubbles, severe channelling or spouting behaviour can be observed, especially if the gas is very unevenly distributed. Deep beds of these particles are difficult to fluidize, and the bed is prone to spout rather than

fluidize. Drying grains and peas, roasting coffee beans, gasifying coals and some roasted metal ores are typical group D particles [2, 31].

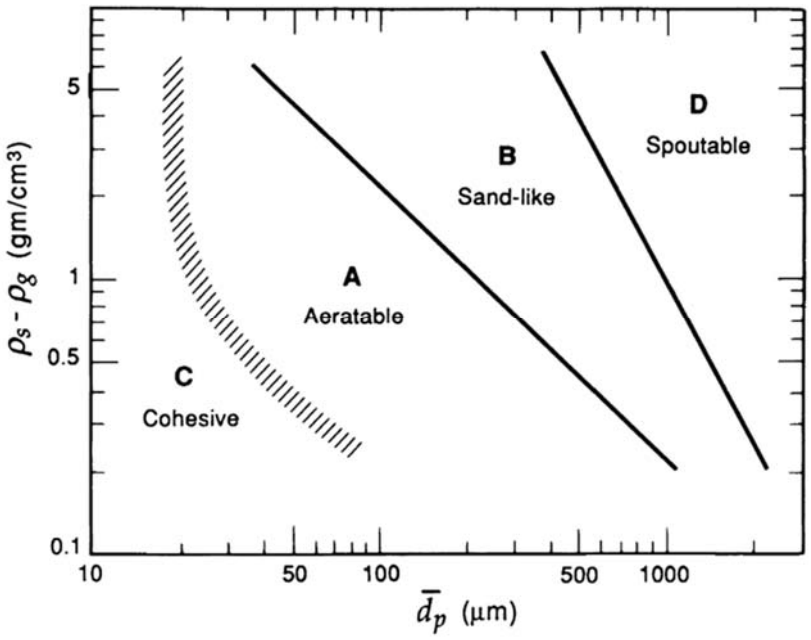

Figure 2.3 Geldart classification of particles [2, 38, 40].

2.3 Industrial Applications

Bubbling fluidization enables intense gas and solids contact and mixing, as well as heat and mass transfer, which are promoted by distributed small bubbles that formed within the bed. As a result, bubbling fluidization has been an ideal solution for many industrial processes and is utilized as a proven technique in various applications [41]. These applications include chemical reactions, cooling and heating processes and drying, coating and granulation in the pharmaceutical industry. For example, the bubbling fluidized bed has been widely applied for combustion processes, and offers high efficiency, good fuel flexibility and low emission conversion, as well as reduced

capital and maintenance costs. José Alberto Pascual Peña [42] investigated over 130 bubbling fluidized bed boilers supplied by Foster Wheeler (FW) from various industries and found the efficiencies of the bubbling fluidized bed boilers were normally over 90%. Bubbling fluidized beds have also been applied for gasification processes. Kaewluan and Pipatmanomai [43] investigated rubber wood chip gasification for yielding synthesis gas in a 100-kW_{th} bubbling fluidized bed gasifier with an I.D. of 300 mm and height of 2500 mm. Air at ambient conditions was fed into the reactor at a fixed flow rate of 72 kg/h, and the feed rate of biomass ranged from 32 to 43 kg/h at 800 °C. The results showed that the carbon conversion efficiency and the gasification efficiency reached as high as 98% and 80%, respectively. Moreover, bubbling fluidized beds have been applied for fast pyrolysis for many years as a result of their reliable feeding system and overall processing capacity over the past several years of operations [41]. The advantages of the bubbling fluidized bed for fast pyrolysis can be summarized as providing high heat transfer rates and uniform temperature distributions; enabling good temperature control; having a short residence time of hot vapour above 200°C, normally below 2 s; and being accessible to be scaled to commercial sizes [41].

Fluidized bed technique was utilized in industries as early as the 1920s when Winkler patented a coal gasifier as the first large-scale, commercially significant use of a fluidized bed [2]. Although this particular commercial application was ultimately unsuccessful, since Winkler's patent the fluidized bed has been applied to various industrial processes, such as physical operations and combustion and gasification. Furthermore, several designs of fluidized bed technology have been proposed, such as

bubbling fluidized beds (BFB) and circulating fluidized beds (CFB) [44]. After decades of study, although the circulating fluidized bed has become more popular, particularly for large-scale operations, the bubbling fluidized bed remains important in energy systems (i.e., combustion or gasification of coal, waste materials or biomass fuels) [45] and is often preferred in small-scale applications [42] due to the following primary advantages [46]:

- flexibility to changes in fuel mix and type
- high heat and mass transfer rates
- favourable gas and solid contact
- uniform and controllable bed temperatures
- accessibility to a range of scales
- economical operation across a range of scales

The lattermost of these advantages is considered especially important since it is usually uneconomic to transport waste or biomass over long distances (i.e., distances >150-300 km), hence small and widely distributed fluidized-bed power plants, fuelled by locally produced biomass, are expected to complement existing large-scale units [46].

Currently, the bubbling fluidized bed is of great interest in chemical looping combustion as an advanced combustion technology that addresses the inherent separation of the greenhouse gas CO_2 [46]. The technology employs two interconnected fluidized beds (i.e., fuel reactor and air reactor), as shown in Figure 2.4, and makes use of a metal oxide as an oxygen carrier to transport oxygen from one

reactor to another, preventing direct contact between combustion air and fuel. In the fuel reactor, the metal oxide is reduced by the fuel, producing CO_2 and H_2O. The latter is then removed by condensation. In the air reactor, the reduced metal oxide is re-oxidized with air producing only N_2 and some unused O_2, after which the oxygen carrier is then reintroduced back to the fuel reactor, restarting the reduction-oxidation loop. Normally, the bubbling fluidization is performed in the fuel reactor, and the fast fluidization is performed in the air reactor. Considerable research has been recently conducted on chemical looping combustion, and over 4,000 hours of operations have been monitored. The findings of this research have established that nearly complete conversion of the fuel and 100% CO_2 capture can be achieved [47]. In addition, bubbling fluidized beds remain a main technique for the fast pyrolysis process, and are the preferred tool for lignin pyrolysis for producing phenols [48]. The bubbling fluidized bed is also preferred in pharmaceutical industries for drying, coating and granulation purposes, and it has long been used for particle cooling and heating processes.

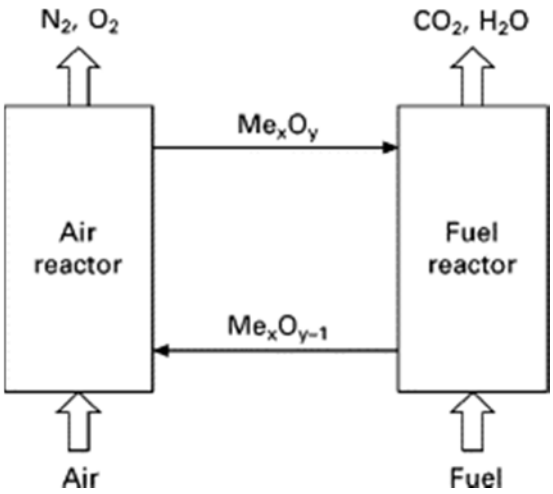

Figure 2.4 Chemical looping combustion [47].

2.4 Measurement Techniques

Measurements of fluidization behaviour in fluidized beds is very important for monitoring and control of chemical reactions, heat and mass transfer, drying and mixing etc., and many direct and indirect measurement techniques have been developed since the 1960s. However, difficulties in measurement have arisen as a result of the opaque nature of fluidized beds, the complex and rapidly changing gas-solid flow structure and nonlinear dynamics in the bed and the chemically aggressive environment [11, 15, 31, 49-51]. This section reviews measurement techniques that have been frequently used for studying fluidized beds, especially for flow patterns and the distribution of gas bubbles and solids. In general, the measurement techniques are categorized into two groups: invasive and non-invasive techniques.

2.4.1 Invasive Techniques

2.4.1.1 2-D Fluidized Bed

Many earlier studies on fluidization were carried out using 2-D transparent fluidized beds to investigate the behaviour of bubbling fluidized beds [8, 9]. The flow of gas and solids within a 3-D fluidized bed is usually not observable due to the high solid concentration in the bed, especially in very dense or opaque systems and large-scale industrial units [3], and only the gas and solids near the vessel wall can be seen. To overcome this challenge, 2-D fluidized beds with two flat transparent plates in parallel and separated by a small distance were used to represent a vertical slice of a true 3-D fluidized bed [8]. The gas-solid flow becomes visible and can be easily seen by the naked eye in a 2-D fluidized bed. High-speed cine photography and video imaging

were then used to record and analyse their behaviours for quantitative information [8]. For example, Goldschmidt et al. [7] visually observed the mixing behaviour of solids in transparent 2-D fluidized beds using digital image analysis. Two sizes of the bed were used: one with dimensions of 15 × 70 × 1.5 cm and the other with dimensions of 57 × 100 × 1.5 cm. Glass beads of two different sizes and colours were used.

Although much useful information can be obtained from the investigation of 2-D fluidized beds, the flow behaviours obtained from a 2-D fluidized bed are often very different from those in 3-D fluidized beds [8]. For instance, Hernandez-Jimenez et al. [9] estimated the wall effect in a 2-D fluidized bed with dimensions of 0.3 × 1 × 0.01 m by using pressure probe measurement and digital image analysis. Glass beads of three different sizes were used as bed materials. The researchers reported that the friction between particles and walls played an important role in the dynamics of 2-D fluidized beds, and the effect of the wall on the gas-solid flow structure within the bed was significant. The wall effect is enhanced in 2-D fluidized beds, while the interaction between particles is reduced [7, 9, 20]. As a result, the fluidization behaviour observed in 2-D fluidized beds cannot directly represent 3-D fluidized beds, and careful consideration is necessary before the extrapolation.

2.4.1.2 Optical Fibre Probe

Optical fibre probes have been popularly used to determine the solid concentration and motion, as well as the bubble properties, in fluidized beds for several decades because of their simple setup and high signal to noise ratio [4, 10-17]. These probes have been developed in various configurations and are mainly based on two working principles:

reflection and transmission [4, 15, 51]. For reflection-type optical fibre probes, the sending and receiving optics (a plastic or quartz glass fibre) are on the same side. Reflection probes have various designs in order to measure local solid velocity and concentration as well as to detect bubbles. Some examples have been shown by Keairns [52], Herbert et al. [53], Zhang et al. [17], Johnsson and Johnsson [54] and Liu et al. [55]. For transmission-type optical fibre probes, the sending and receiving optics are on opposite sides facing toward each other. Transmission probes are very useful for detecting gas voids or bubbles [51]. Examples date back as early as 1958, when Yasui and Johanson [12] were among the first to utilize the transmission probe to measure bubble properties (i.e., bubble rise velocity, bubble vertical thickness, and bubble frequency) in gas-solid fluidized beds. Latter examples include Mainland and Welty [56], Kage et al. [57] and Kim et al. [58].

However, due to its invasive nature, an obvious drawback of the optical fibre probe technique is that inserted probes within fluidized beds may, to some extent, interfere with the flow structure of gas and solids [4, 8, 10, 15, 19-21]. Another main challenge associated with using optical fibre probes is the need for calibration, which becomes even more difficult if the solid concentration is to be measured [11, 21, 31]. In addition, the volume of the area that will be measured by the optical fibre probe lacks definition since this parameter is a function of solid concentrations [4, 11, 15, 17, 51, 59], although development efforts have attempted to overcome this [51, 60]. Moreover, small bubbles are less likely to be detected by optical fibre probes [10, 12, 15, 16, 61].

2.4.1.3 Capacitance Probe

The capacitance probe has been utilized as a simple and accurate measurement technique to study the gas-solid flow behaviour (i.e., solid concentration, particle velocity, bubble spatial distribution, bubble rise velocity) in fluidized beds since 1951 [8, 10, 15, 18]. This technique works based on the change in dielectric constant of the gas and solid mixture in the measuring volume between the two electrodes of the capacitance probe. The dielectric constant is sensitively dependent on the local solid volume concentration and enables the capacitance probes to detect even a slight change in solid concentration [8, 11, 31, 51]. In the original design, two parallel plate electrodes with a separation of several millimetres were used [8, 10, 15, 18, 51, 62, 63]. Werther and Molerus [64] improved the configuration by minimizing the size of the capacitance probe using a central protruding, downward pointing needle to form the sensor electrode and an enclosing metal tube to form the ground electrode. Their design minimized the disturbance to the flow and benefited several researchers who have made subsequent improvements on the design [8, 51]; Almstedt and Olsson [65] added water-cooling to Werther and Molerus [64] design in order to make it feasible in hot and reactive applications. Soong et al. [66] incorporated the guard electrode, which was introduced by Riley and Louge [67] for the plate electrode configuration, in the needle capacitance probe in order to improve the accuracy of measurement.

Nevertheless, the capacitance probe has its disadvantages. One obvious drawback is its invasive behaviour. Although developments have minimized the disturbance, the presence of a probe within fluidized beds may still interfere with the flow [15]. Another difficulty associated with using this measurement technique is that extensive

calibration is required for every gas-solid system and operation condition [10, 15, 68]. Moreover, the capacitance probe detects chord lengths of pierced bubbles instead of actual bubble size, which may indicate a limitation in data interpretation [15, 61, 64]. Furthermore, there has been no considerable improvement on the capacitance probe measurement technique over the last decade [15, 51].

2.4.2 Non-invasive Techniques

Non-invasive measurement techniques are highly desirable in determining flow behaviours in multiphase systems. These measurement techniques are located outside experimental vessels and can provide detailed information of the flow behaviour without interfering with the flow structure. Several non-invasive techniques have been developed, offering various high quality data to interpret the flow characteristics in fluidized beds, such as laser Doppler anemometry, particle image velocimetry, electrical capacitance tomography, X-ray computed tomography and PEPT. Since the current research utilized the PEPT technique to investigate the flow behaviour inside fluidized beds, the development of PEPT technique and its applications will be discussed in greater detail at the end of this section.

2.4.2.1 Laser Doppler Anemometry (LDA)

LDA was developed in 1964 by Yeh and Cummins [69] and has been used to obtain mean velocity, fluctuating velocity and particle size information for multiphase flow systems [8, 10, 16, 21, 70-76]. LDA utilizes the Doppler effect to measure the particle velocity in fluidized beds [76]. In LDA, light beams from a laser source are scattered when a moving particle passes through the measurement volume, and the scattered

lights are then received and collected by a photo-detector. The wavelength or frequency of laser light reflected from a moving source is different from that reflected from a stationary source, which is referred to as the "'Doppler effect'". In the case of LDA measurement for fluidized beds, the moving particles within the bed act as the moving source for the light detector and cause Doppler shifts or interference fringes. The resulting Doppler frequency is proportional to the particle velocity, which makes the measurement possible. The LDA technique offers high spatial and temporal resolutions and can provide detailed and accurate velocity data of particles non-invasively [8, 10, 21, 31, 71, 76-78]. However, LDA has very limited application in dense systems where the solid volume fraction is greater than 5 vol % [21, 31, 74]. When multiple particles co-exist within the measurement volume simultaneously, the Doppler signal of one particle is indistinguishable from the signals of other particles, which yields unreliable LDA measurements. Therefore, the LDA technique is usually used to investigate the flow behaviour in very dilute systems, such as the riser of a circulating fluidized bed [70] or the freeboard region in a fluidized bed [72] as opposed to dense bubbling fluidized beds. Another potential disadvantage of LDA is its time-averaged point information, which is due to the small measurement volume [4, 75].

2.4.2.2 Particle Image Velocimetry (PIV)

PIV was developed as an alternative non-invasive optical measurement technique to obtain instantaneous and full-field qualitative and quantitative information on the flow in fluidized beds during the 1970s [4, 16, 21, 31, 75, 76, 79] as opposed to LDA, which provides point measurement [75, 79, 80]. A typical PIV technique usually consists of a light source (i.e., a pulsed laser) for laser sheeting, a high-resolution charge-coupled

device (CCD) camera for image recording and a computer for image processing [16, 21, 75, 79]. In PIV, a sheet of light illuminates particles in the field, and the particles scatter the light to an image device (i.e., a CCD camera) where particle images are being recorded. The captured images are then transferred to a computer for analysis and determination of the particle velocity. PIV provides detailed, instantaneous, and full-field fast measurement with accurate qualitative and quantitative information, such as the velocity vector profile and spatial distribution of particles in fluidized beds [31, 75, 81]. However, PIV techniques are limited to dilute systems (i.e., 2-D fluidized beds and dilute 3-D fluidized beds) [31] or near wall regions of dense systems, as the laser light will be obstructed after a short distance in systems of high solid volume concentrations [11, 21, 74]. In addition, due to the cross-section (axial plane) slice measurement [82], PIV is usually used to investigate the flow behaviour in 2-D fluidized beds [83], and only the plane in the axial section of a 3-D fluidized bed is measured, which cannot simply represent the entire gas-solid flow structure in 3-D fluidized beds [11, 21].

2.4.2.3 Electrical Capacitance Tomography (ECT)

ECT has been widely applied in fluidization research to measure solid concentration and distribution profile, determine bubble development and distribution (e.g., bubble coalescence) and obtain bubble properties, such as the sizes and rise velocities of bubbles [8, 31, 51, 76, 84-90]. The early development of ECT began in the 1980s at the Morgantown Energy Technology Centre for the investigation of bubbles in gas-solid fluidized beds [8, 76, 84, 91, 92]. At about the same time, Huang et al. [93], Huang et al. [94] and Xie et al. [95] extended ECT applications to multiphase flow

systems, such as oil pipelines and pneumatic conveying, at the University of Manchester Institute of Science and Technology (UMIST) [82, 91]. With the same measurement principle as capacitance probes, the ECT technique makes use of the dielectric constant/relative permittivity or the electrical capacitance of gas and solids. The difference in electrical capacitance between solid and gas is sufficiently large, therefore making the measurement capable of distinguishing bubbles among the solid phase within a fluidized bed [8, 76]. Basically, an ECT system consists of capacitance sensors, a data collection system and an image reconstruction computer [11, 31]. An array of electrodes with equal intervals is mounted around or wrapped around the external surface of the fluidized bed column at a height being measured to compose the capacitance sensor. Capacitances between any pairs of electrodes (i.e., all possible combinations) are measured and collected by the data collection system so that the capacitance data are received in various directions of the system. The captured capacitance values, of which the amplitude varies by the permittivity distribution of the gas-solid mixture, are then fed to a computer, and a cross-sectional image of the gas-solid volume fraction distribution is reconstructed using a proper algorithm [8, 31, 51, 76, 96, 97]. Electrical capacitance tomography is a valuable, low-cost and non-invasive technique that provides fast and detailed measurement of the bubble and distribution of solid volume fraction [15, 51, 76, 98] of the whole cross-section, and the fluidized bed can be imaged at a rate of up to 1000 frames per second [15, 51, 99, 100]. The electrodes of the ECT technique are normally just a few centimetres in height that provide only a 2-D cross-section measurement in radial direction [51]. However, the recent development of ECT by Warsito and Fan [101], called electrical capacitance volume tomography (ECVT), enables the instantaneous 3-D imaging of

the whole field enclosed by the 3-D capacitance sensor around the fluidized bed being captured [15, 51, 91, 102].

The main limitation of the ECT technique is its poor spatial resolution, which is up to several centimetres [8, 15, 51, 76, 90, 103, 104]. This poor spatial resolution is due to the fact that that the image reconstruction of ECT can be very cumbersome, especially for the ECVT technique [91]. The reconstruction resolution is restricted by the soft field nature of ECT measurement. In ECT, the electrical field lines are non-linearly dependent on the electrical property (e.g., permittivity) distribution within the sensor and are distorted by the permittivity field, which is referred to as the solid field effect/problem [15, 51, 97, 104-108]. In addition, applications of ECT in industrial processes with high pressures and/or temperatures carried out in metallic vessels are often troublesome [51].

2.4.2.4 X-ray Computed Tomography (X-ray CT)

X-ray CT is one family of non-invasive measurement techniques that has been extensively used to visualize and characterize gas-solid fluidized beds since the late 1980s. These characterizations include determination of time-averaged voidage distribution, bubble diameter, bubble shape and bubble velocity [16, 103, 109-122]. The technique works by measuring the X-ray attenuations when X-ray beams transmit through an object (i.e., a fluidized bed). The solid phase absorbs or scatters more X-ray photons, while the gas phase essentially lets them pass through. These inherent qualities make the determination of attenuations of X-ray intensity useful for interpreting solid concentrations in the measured region. Basically, X-ray CT consists

of an array of X-ray detectors and a radioactive source that is rotatable around the measured object and emits a beam of X-rays [76, 104, 112]. Each set of source-detector pairs (i.e., in various directions) constitutes an X-ray projection of the transmission-attenuation measurement, which together with all other projections is then digitized and stored on a computer to reconstruct the map of the attenuation coefficient of the measured section by using a mathematical algorithm. Since linear attenuation is a result of mass attenuation and density, the reconstructed map of attenuation coefficient usually gives a straightforward interpretation of the image of density or void fraction distribution [15, 16, 31, 76, 104, 112, 113, 123-125]. The X-ray CT technique has excellent spatial resolution because of the small size of the detectors, enabling detailed information regarding the density distribution or void fraction distribution in fluidized beds to be obtained [15, 51, 76, 104, 114]. The electromagnetic field transmits along a straight-line pattern, and individual field lines are not influenced by the material or medium (i.e., gas-solid distribution) outside of its line; the reconstruction process is therefore much simpler than that of soft-field tomography (i.e., electrical capacitance tomography) [15, 51, 126, 127].

Despite its advantages, X-ray CT also has some limitations. The main drawback is its low temporal resolution. During a measurement, the X-ray CT has to be rotated around the subject (i.e., source-detector direction) to obtain data for all projections, and the process normally takes several minutes to few hours. Hence, it is difficult to capture dynamic information of fast moving objects, such as bubbles in fluidized beds, and the data are always obtained in time-averaged values [51, 76, 104, 114]. Recent developments in ultrafast X-ray CT considerably overcome this limitation [128-133].

However, a number of projections influence the spatial resolution. The increase in the speed of projection acquisition may increase the signal noise and hence reduce the spatial resolution and the opportunity to detect small bubbles (i.e., ≤ 3 cm or 13% of the bed diameter) [104, 117, 120, 130, 134, 135]. In addition, X-ray CT is limited to small vessel sizes (i.e., up to a few tens of cm I.D.) for obtaining good transmission through the fluidized bed [10, 104, 112, 129, 136].

2.4.2.5 Positron Emission Particle Tracking (PEPT)

The PEPT technique was developed in 1987 at the University of Birmingham. It is a variant of the positron emission tomography (PET) technique that has been regularly used in the field of nuclear medicine for diagnostic imaging [11, 21, 76, 137-139]. The PEPT technique non-invasively tracks the real-time motion of a single particle or multiple particles (i.e., ≤ 3) inside 3-D vessels [24, 26, 140, 141]. The motion of tracer particles is then used to calculate solid velocities and to reconstruct solid flow patterns [8, 11, 21, 27, 76, 137, 142, 143]. PEPT makes use of positron emission and labels selected particles with positron emission radioisotopes such as ^{18}F. Such radioisotopes undergo β^+ decay with the emission of positrons. The emitted positron will quickly undergo annihilation with an electron in its surroundings and release the energy by giving off a pair of counter propagating γ-rays. The PEPT then can locate the tracer particle position by triangulating a small number of such γ-ray pairs [8, 11, 76, 137]. The PEPT technique consists of tracer labelling techniques to label the selected particle with a radioisotope that emits 511-keV γ-rays, a PEPT camera to detect the emitted γ-rays, and an algorithm to locate the tracer particle position [8, 23, 25, 76, 137]. The major advantage offered by PEPT is its ability to non-invasively measure

the solid flow quantitatively in 3-D vessels with considerable temporal and spatial resolutions [8, 11, 28, 76, 137, 144]. In addition, since γ-rays are able to penetrate a considerable thickness of material (i.e., steel), particles can be tracked by PEPT in dense or opaque vessels, and PEPT is capable of being applied to actual plants on a pilot scale [137, 145]. Moreover, since various solid materials with sizes down to 60 μm can be labelled and tracked by PEPT (e.g. quartz, coal, polyethylene, oilseeds and metals), PEPT has been deployed in a wide range of science and engineering applications [21, 23, 137], such as the chemical, pharmaceuticals, minerals and food industries [27, 28, 137, 146-151]. For example, PEPT has been used by Stein et al. [142, 152], Wildman et al. [153-155], Wong and Seville [156], Fan et al. [157], Parker et al. [158], Depypere et al. [144] and Laverman et al. [159] in experiments of fluidized beds to follow the particle trajectory and measure the particle velocity, flow pattern and residence time. PEPT has also been used in mixers to investigate the particle motion, velocity and mixing performance, with examples published by Broadbent et al. [160], Parker et al. [158], Laurent et al. [161], Stewart et al. [162] and Ingram et al. [163].

Fluidized beds are typically opaque, which makes the measurement very difficult or sometimes even impossible to investigate the gas-solid flow behaviour inside a 3-D fluidized bed. An ideal measurement technique for fluidized beds is required that is non-invasive to prevent disturbing the flow structure and has high temporal and spatial resolutions to detect rapid changes in the gas-solid flow. The technique should be able to obtain quantitative information of gas and solid movement with snapshots of the history of the flow over different scales of equipment [15, 64, 164, 165]. Although no

single measurement technique currently satisfies all these demands [164], PEPT is one of the available measurement techniques that meets most of these aforementioned requirements; hence PEPT was applied in this research to non-invasively investigate the flow behaviour in 3-D bubbling fluidized beds. The principle of the PEPT technique and the tracer labelling and experimental setups applied in the current research will be discussed in chapter 3.

2.5 Solid Flow Patterns

The pattern of solid circulation, also known as the solid flow pattern, plays an important role in bubbling fluidized beds, and it significantly affects fluidized bed performance in terms of mixing efficiency, heat and mass transfer, chemical reaction, particle transportation and particle attrition, as well as the erosion of the internals [142, 166-169]. These effects can become even more significant in large-scale units [170], such as material processing, catalytic cracking and other large-scale industrial applications. Different solid flow patterns offer differing process productivity and efficiency. For example, Jaiboon et al. [171] investigated the effect of flow patterns on the CO_2 capture capacity from flue gas in fluidized beds by using X-ray diffraction (XRD) analysis. The fluidized bed had an I.D. of 0.025 m and height of 0.80 m, and K_2CO_3/Al_2O_3 solid sorbents were used as the bed material. The researchers found that both CO_2 capture capacity and CO_2 removal efficiency changed dramatically depending on the solid flow patterns in fluidized beds. In addition, a uniform solid flow pattern is of crucial importance for processes that are highly exothermic and where highly active and selective catalysts are employed, such as the UNIPOL™ process that produces polyolefin (e.g., polyethylene and polypropylene). These

requirements are due to the fact that the temperature of a fluidized bed reactor is not allowed to reach the melting temperature of polymers in order to avoid agglomeration problems [172], and the heat transport due to solid flow then becomes a demand for polymerization. In a fluidized bed reactor, the heat removal rate controls the production capacity. Heat removal from a fluidized bed reactor occurs by particle-gas convective heat transfer and the particle-particle and particle-wall conductive heat transfer. Among these means of heat removal, particle convection dominates and accounts for approximately 80%-95% of the heat transfer in fluidized beds [173], being primarily governed by solid flows [167]. Through investigation of the solid circulation pattern, a better understanding of heat distribution and mass transfer, which are required for the efficient design of fluidized beds, can also be achieved [166]. In addition, solids move around due to rising bubbles in bubbling fluidized beds. Particles are picked up by bubbles and carried upwards in the bubble wakes or bubble drifts [174], as shown in Figure 2.5. Investigation of solid flow patterns also enhances the knowledge of bubble motions and gas-solid interactions in fluidized beds. Therefore, understanding the solid flow pattern is essential for quality control, proper design and scale-up of fluidized beds, as well as further development of fundamental fluidization theories [142, 175]. This section reviews observations and findings on solid flow patterns within bubbling fluidized beds.

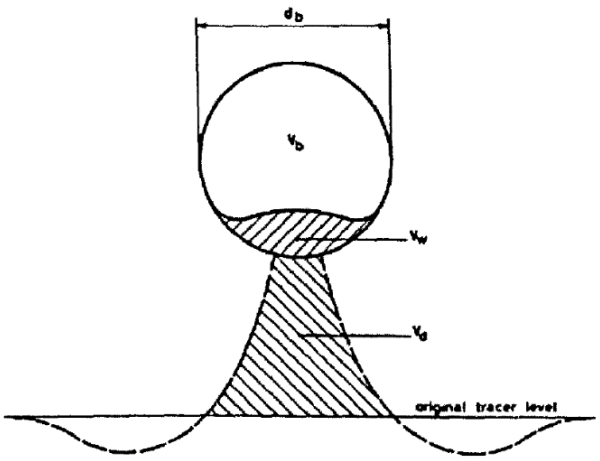

Figure 2.5 Bubble-induced particle upward movement in wake and drift [176].

Since the 1960s, a number of researchers have been working on the identification and control of solid flow patterns. For example, Whitehead et al. [177] investigated the solid flow in a rectangular fluidized bed of silica sand using a rubber stopper tied to a length of string. The bed has a cross-sectional area of 1.22 m × 1.22 m and was packed to an initial fixed bed height of 0.381-1.626 m. The experiment was operated at the superficial gas velocity of 0.046 to 0.427 m/s. The researchers observed decreasing solid flow either around the centre or adjacent to the wall from the bed surface and reported that the downward flowing of solids in the centre predominated and had a much higher velocity than the solid downward flow near the bed wall.

Werther and Molerus [178] investigated the flow behaviour in fluidized beds of Geldart A and B particles by using capacity probes. Porous plates were used as the air distributors and appropriate pressure drops were supplied in each experiment to ensure even distributions of gas across the bed. The researchers measured the bubble distribution and predicted the solid flow based on the relations between gas-solid flows

that particles moved upwards following the rising bubble path and descended to where there was less or no bubble development. Their results showed a strong upward flow of solids existed close to the vessel walls at the bottom section of the bed, and this upward flow of solid shifted towards the centre of the bed as the bed height increased. Werther and Molerus also reported that when the H/D was less than approximately 2, solids from the bed surface descended either in the bed centre or along the bed wall, as shown in Figure 2.6a. Whether the solids would fall in the centre or along the bed wall depended on the distance from the vessel centre and the H/D [178]. For beds with a greater H/D, as shown in Figure 2.6b, the researchers suggested that solids would exhibit a different flow pattern where solids flowed up along the central axis from an intermediate height of the bed and descended near the bed wall from the bed surface.

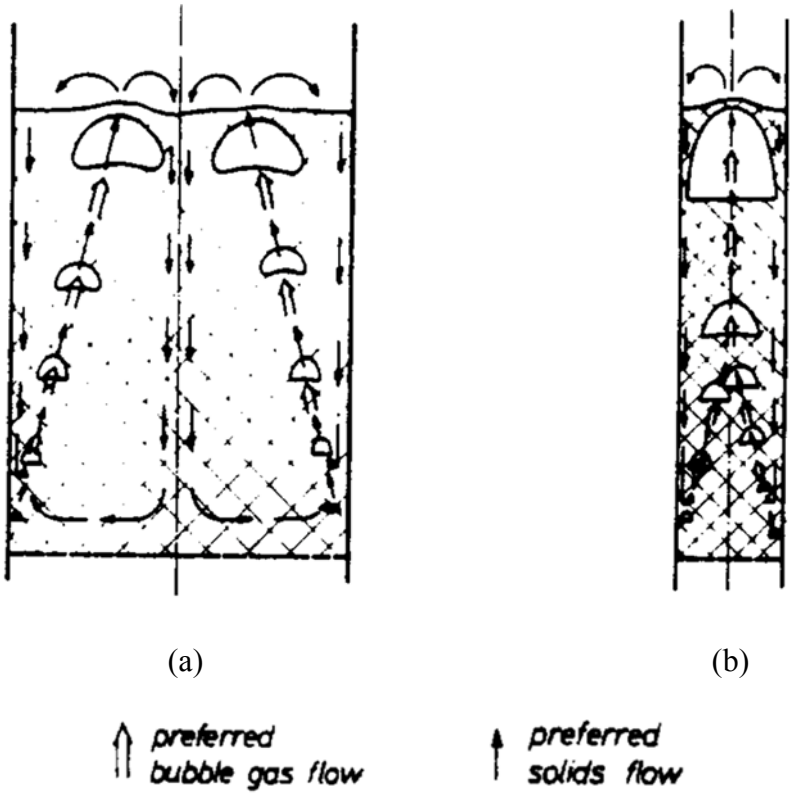

Figure 2.6 Solid flow patterns [178].

Whitehead [179] summarized the observations of Geldart [180], Nguyen et al. [181] and Whitehead et al. [182] on the solid flow pattern in the fluidized bed of Geldart B particles, and indicated that solids moved up at the centre and down along the bed wall in deep fluidized beds. Similar solid flow patterns were also reported in fluidized beds with high superficial gas velocities [31, 179]. Lin et al. [175] applied a computer-aided radioactive particle tracking technique to track a particle with dynamically identical properties to bed bulk materials. The fluidized bed had a bed diameter of 13.8 cm and was packed with glass bead particles to the initial bed height of 11.3-11.5 cm. The bed material had a density of 2500 kg/m^3, and particle sizes ranged from 0.42 to 0.8 mm. The experiments were operated at a superficial gas velocity ranging from 32 to 89 cm/s, which corresponded to a u/u_{mf} of 1.65 to 4.60. The researchers found that the solid flow pattern strongly depended on the superficial gas velocity. At a low fluidization velocity, the solid flow pattern was a toroidal vortex ascending near the bed wall and descending at the centre. As gas velocity increased, a second toroidal vortex in reverse direction, which ascended along the bed centre and descended along the bed wall, was observed in the upper part of the bed when the downward flow of solids still remained at the centre of bed. As the gas flow rate further increased, the extent of the upper toroidal vortex enlarged; in the meantime, the lower toroidal vortex reduced. If the gas flow rate continued increasing, the lower toroidal vortex in which solids ascended along the bed wall and descended near the centre became decreasingly smaller and eventually disappeared, and only the toroidal vortex in which solids ascended along the centre and descended near the bed wall existed within the bed.

In 1991, a comprehensive review of earlier findings on the solid flow pattern in fluidized beds was published by Kunii and Levenspiel [2]. They analysed the observations from Werther and Molerus, Whitehead, Yamazaki et al., Lin et al. and others. Kunii and Levenspiel additionally provided a summary of the solid flow pattern in fluidized beds of Geldart B particles. In this thesis, with consideration of recent literature [175, 179-182], an enhanced version is offered. In shallow fluidized beds where the H/D approaches unity, solids circulate with two vortexes from a side view of the bed. The solids flow upwards along the bed wall and flow down in the bed centre at a low fluidization velocity (u_o/u_{mf}) as seen in Figure 2.7a. As the gas velocity increases, solid motion is close to the pattern in Figure 2.7a, but there are two small vortexes at the top of the bed in which solids also move down along the bed annular region, as seen in Figure 2.7b. A further increase in the gas velocity will enlarge the upper toroidal vortex where solids move up in the bed centre and move down along the bed wall; in the meantime, the lower toroidal vortex where solids move up along the bed wall and down in the centre reduces. This situation becomes severe as the gas flow rate increases; the lower toroidal vortex in Figure 2.7b finally disappears, and the solid flow pattern in Figure 2.7c is approached. Solids have a flow pattern similar to pattern in Figure 2.7a, but solids flow in a reversed direction, where solids are moving up at the bed centre and down along the annular region of the bed. When the H/D is greater than unity, as seen in Figure 2.7d, both the upper and the lower vortex are completely formed, and the upper vortex in which solids move up at the bed centre and move down along the annular dominates the overall performance of the solid bed. For beds with a large diameter ($H/D < 0.5$) and uniform air distributor plates (Figure 2.7e), vortexes are developed at the same height in a reversed circulation direction

between each other, as shown in Figure 2.7e. Figure 2.7f shows the effect of gas channels from the high-pressure-drop tuyeres air distributor on the solid flow patterns in fluidized beds with a large diameter (H/D < 0.5). The gas channels partition the bed into several sections.

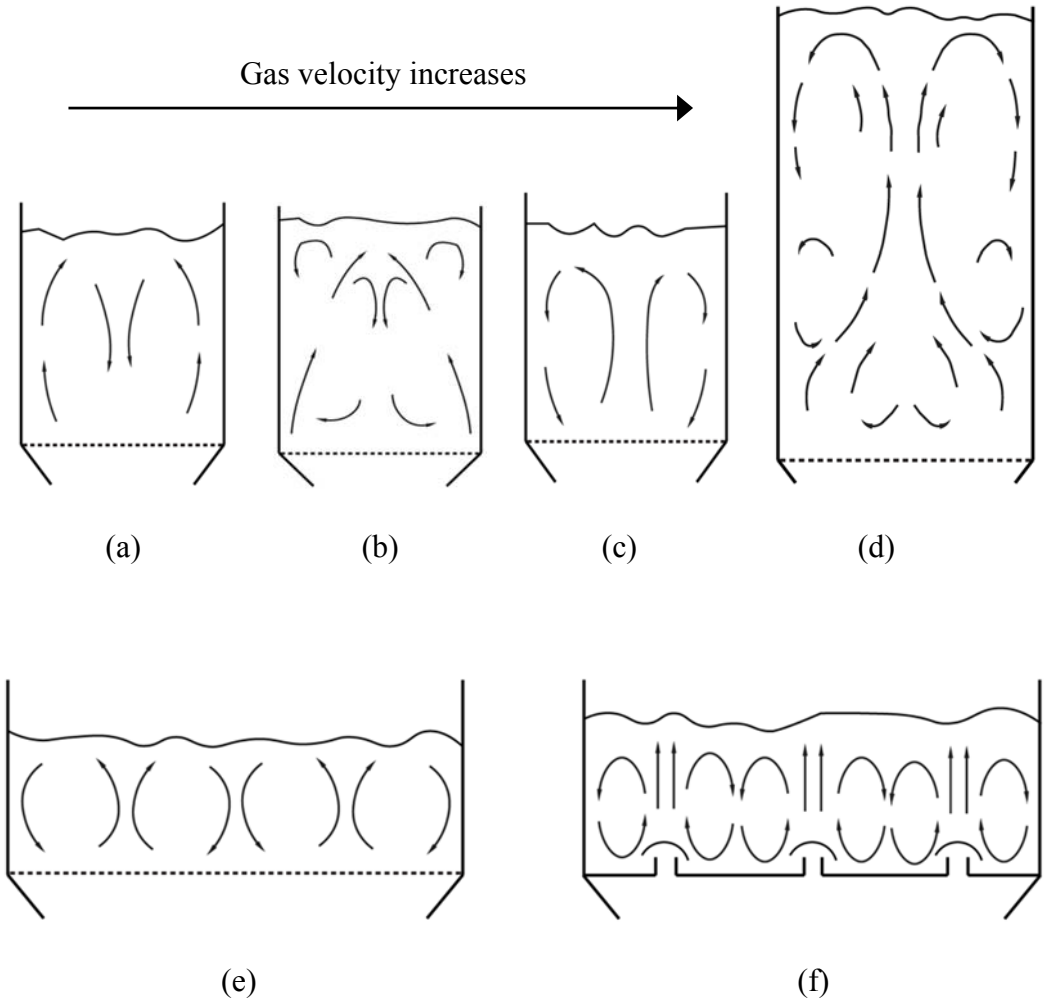

Figure 2.7 Solid flow patterns in bubbling fluidized beds of Geldart B particles, modified from Kunii and Levenspiel [2].

Recently, Stein et al. [142] investigated the solid motion by using the non-invasive PEPT technique in two different bubbling fluidized beds of Geldart B particles. The

small bed was 70 mm in diameter and 430 mm in height, and the large bed was 141 mm in diameter and 600 mm in height. They applied a brass plate with 80 holes of 0.5 mm pore size for the small bed and a steel plate with 130 holes of 1.55 mm pore size for the large bed as the air distributors. The holes in their air distributors were countersunk on the upstream side and arranged in a triangular configuration. Resin beads ranging 0.55-0.75 mm in diameter and having a mean size of 0.66 mm and a density of 1100 kg/m^3 were used as the bed material. The minimum fluidization velocity of the bed material was 0.11 m/s, and the beds were fluidized at the excess gas velocity of 0.15-0.3 m/s. The researchers' results showed that particles moved upwards in the central area of the bed and moved downwards near the vessel wall in the relatively deep fluidized bed, as observed before [179-182], and their results also showed that both upward and downward flow patterns were evident near the air distributor.

Pallares and Johnsson [183] investigated the solid flow behaviour in 2-D fluidized beds by tracking a phosphorescent tracer particle using video records with subsequent digital image analyses. The beds had a cross-section area of 0.02 × 0.4 m and a height of 2.15 m. A perforated plate was used as the air distributor. Bed materials were glass beads with a mean size of 330 μm, a density of 2600 kg/m^3 and a minimum fluidization velocity of 0.12 m/s. The beds were packed with 1.5-7.0 kg materials and operated with the superficial gas velocity of 0.4-1.74 m/s under ambient conditions. Three kinds of cylindrical capsules that were larger than bed material were used as tracer particles. Two of the capsule types were lighter than the bed bulk material and one had a similar density to the bed bulk material. The researchers found similar results for all

experiments, where horizontally aligned vortexes were induced by the bubble flow with alternated rotational direction in shadow beds, while in deep beds the solids flowed upwards in the centre and downwards along the sidewall; this was in agreement with some previous observations [2, 142, 179-182]. Pallares and Johnsson also observed a strong influence of the amount of bed materials or H/D on the solid flow pattern, especially at the bottom of the beds. They reported that the number of solid circulation vortexes depended to a large extent on the amount of bed material or H/D, and no significant influence of the superficial gas velocity could be found; these latter findings were conflicting with previous observations [2, 179-182]. However, these findings were an observation from a 2-D bed where the wall effect was significant and therefore unable to represent 3-D beds.

Fan et al. [184] investigated the solid motion within a 3-D fluidized bed with a 152-mm I.D. using the PEPT technique. Both glass beads and polyethylene particles were used as the bed materials. The glass beads had a mean size of 352 μm, a density of 2700 kg/m^3, and a minimum fluidization velocity of 0.15 m/s. The polyethylene particles had a mean size of 717 μm, a density of 760 kg/m^3, and a minimum fluidization velocity of 0.24 m/s. Beds were packed to a unit height and were operated at superficial gas velocities that ranged from 0.15 to 1 m/s. Fan et al. observed three different solid flow patterns. One pattern was similar to the solid flow pattern in Figure 2.7c, the second pattern was similar to Figures 2.7b and 2.7d, and the third had a large solid circulation vortex over the bed that ascended along one side of the bed wall and descended along the other side. The researchers reported that the solid flow pattern varied greatly with the property of bed materials and the superficial gas velocity.

The research works discussed above has given a better understanding of solid flow behaviour in fluidized beds under different conditions. However, due to the dearth of reliable techniques to directly and non-invasively measure the solid movement within opaque 3-D fluidized beds, experimental investigations were mainly carried out in planner fluidized beds. In many of the experiments, solid flow patterns were determined by using probing techniques, which disturb the solid flow in fluidized beds. Moreover, in a fluidized bed, various factors have effects on the solid flow pattern, such as superficial gas velocity, H/D and air distributor type, among others. In reality, all these factors are interrelated. Understanding their effects and how significant the influence of an individual factor related to other factors on the solid flow pattern is necessary in order to design and control solid/gas flow behaviour in fluidized beds for different processes. The solid flow pattern also has significant impact on bubble behaviour in a fluidized bed [175, 185, 186]. Hence a better understanding of the solid flow structure can help analyse the bubble behaviour and gas-solid flow relations. In the present study, the solid flow structure in a 3-D fluidized bed was mapped, and the effect of various factors on the solid flow behaviour were investigated by using the PEPT technique, such as bed materials, minimum fluidization velocity, superficial gas velocity, H/D and the pore size of the air distributor. The detailed research work of the present study will be discussed in Chapter 4 of this thesis.

2.6 Mixing of Solids

The mixing of solid particles has been recognised as an important factor in fluidized beds, especially for chemical reaction processes [187]. It governs the mixing behaviour

of solid particles as well as the contact between solids and gas, the heat and mass transfer and temperature uniformity, which further influence the overall reaction rate in fluidized bed reactors (e.g., the conversion of fuel in combustion and gasification processes) [31, 170, 188] For instance, an increase in lateral mixing of the bulk bed material will create a more homogeneous temperature field across the cross-sections of the bed [189]. In addition, the mechanical design of fluidized beds, such as the position and number of solid feed and withdrawal points, can be improved through a better understanding of the solid mixing behaviour. Hence, the mixing of solids is of great importance and interest in the research of fluidized beds, particularly for design, operation and control purposes in various processes.

It has been identified that the solid mixing within a fluidized bed mainly occurs by several mechanisms [2, 190, 191]. Solid vertical mixing mainly occurs when bubbles drag solids from their close surroundings into their wake regions [192]. Solids within the wake regions are quite turbulent and the wakes are periodically shed and replenished as the bubbles rise through the bed, which induces the exclusive vertical displacement of solids. Solid horizontal mixing mainly occurs according to four mechanisms: I) when solids are transported into the drifts of bubbles from the dense phase and are drawn up below bubbles as spouts, which implies lateral displacement [193]; II) when bubbles erupt at the bed surface, during which solids are ejected into the splash zone and distributed over the bed surface from the erupting wakes with certain horizontal velocities [194, 195]; III) due to bubble lateral motions, which is a consequence of interaction and coalescence between adjacent bubbles [5, 196, 197]

and IV) due to eddies induced by passing bubbles in the solid main downward flowing stream.

In general, good solid mixing is desirable since it provides uniform temperature throughout a fluidized bed and prevents hot spots. In order to quantitatively evaluate and understand solid mixing in fluidized beds, a range of techniques have been proposed. Kunii and Levenspiel [2] have summarized those techniques as follows [198]:

a) Follow trajectories of individual tagged particles for long periods of time [183].
b) Measure the extent of mixing between two kinds of solids, which are placed in different sections within a bed.
c) Determine the vertical spread of tracer particles that are placed horizontally in a thin layer within a fluidized bed [199, 200], or the horizontal spread of tracer particles that are placed vertically in the front/back or left/right sections of a bed [201].
d) Inject tracer particles into a bed by step injection or pulse injection and measure their residence time distribution or concentration [202].
e) Measure the axial or radial heat flow in a fluidized bed that is divided into two sections, in which one section of solids is heated and the other section contains cooled solids, based on the assumption that the heat transport is caused only by the movement of solids [203].

Many experimental studies on solid mixing have been conducted since the late 1940s using the techniques mentioned above [2, 188, 204-206]. The mixing behaviour of solids was usually characterized by axial or horizontal dispersion coefficients [188], which were typically obtained by fitting a mathematical model to the experimental data [2]. For example, Avidan and Yerushalmi [207] investigated the solid mixing in a 0.15-m I.D. fluidized bed of Geldart A particles in different fluidization regimes (i.e., bubbling, slugging and turbulent). The researchers introduced ferromagnetic tracer particles into the centre of the bed by pulse injection and then used inductance probes to measure the tracer concentration at different heights of the bed. The counter current flow model was fitted to the obtained tracer concentrations in bubbling and slugging fluidized beds and the dispersion model was applied to the turbulent and bubbling fluidized beds in order to estimate the axial dispersion coefficient of solids in these beds. The axial dispersion coefficient of solid was found to increase with the gas velocity as well as with the square root of the bed diameter.

Du et al. [202] used a similar technique to examine both axial and radial solid mixing behaviour in a fluidized bed with a 0.203-m I.D. The bed was operated in bubbling and turbulent regimes at a temperature up to 435°C and a pressure up to 3.5 atm. FCC catalysts with a mean diameter of 60 μm and a density of 1400 kg/m^3 were used as the bed material. Phosphor particles, which had the size and density similar to the bed material, were used as the tracer particles in their experiments. Phosphor particles were excited to emit light by a flash tube that was located at the centre of the bed. Since the flashing time was very short, the whole process of the tracer injection could be treated as a pulse. The tracer concentration was measured by a detector consisting of an optical

fibre and a photomultiplier. The axial and radial solid dispersion coefficients were then determined by fitting a 2-D dispersion model to the experimental data (i.e., tracer concentration). They concluded that the solid dispersion coefficient increased with the gas velocity but was not significantly affected by temperature and pressure.

Bellgardt and Werther [208] estimated the solid mixing in a rectangular fluidized bed with a cross-sectional area of 2.0 m × 0.3 m. Quartz sand was used as the bed material, and carbon dioxide (CO_2) snow pellets were used as the tracer particle. Since the CO_2 snow pellets underwent sublimation, which was an endothermic process and formed a gaseous product (i.e., CO_2), the tracer particles can be detected by measuring the produced gaseous carbon dioxide. They then measured the concentration of the gaseous carbon dioxide and used it to calculate the tracer concentration. The lateral solid dispersion coefficient was thereafter obtained by fitting the one-dimensional dispersion model to the experiential tracer concentration profile. The researchers' results showed that the dispersion coefficient of solids increased with both increasing excess gas velocity ($u-u_{mf}$) and H_{mf} (bed height at minimum fluidization). A similar technique was also used by Chirone et al. [209] to estimate the solid mixing in a bubbling fluidized bed combustor with a 370-mm I.D. Silica sand with a mean size of 725 μm was used as the bed material, and shells of pine-seeds with a size of approximately 30 × 10 mm were used as the biomass fuel particles. The researchers measured the concentration profile of carbon-containing gaseous species with horizontal water-cooled probes and related the fuel particle concentration with the carbon-containing gaseous species concentration. The radial dispersion coefficient of fuel particles was then obtained by fitting a simplified dispersion/pyrolysis model to

the experimental data. Grasa and C. Abanades [210] investigated the solid mixing in two different fluidized beds (i.e., one with a 0.08-m I.D. and another with a 0.15-m I.D.) by following the evolution of coloured tracer particles using image analysis technique [199]. Polyvinyl chloride (PVC) (i.e., white) and coal mixtures (i.e., black) with three different particle sizes were used as the bed materials, and coloured (i.e., red and white) polyethylene beads were used as the tracer particles. The tracer particles occupied the lower 30% of volume of the bed before the bed was suddenly fluidized at a pre-set gas velocity. The mixing process was video recorded, and the tracer concentration at different heights of the bed was determined from the recording. The tracer concentration was then fitted by both the dispersion model and counter current backmixing model of solids in order to yield the axial solid dispersion coefficient. The results indicated that the counter current backmixing model was more reliable for describing the solid mixing behaviour in fluidized beds.

The two most popular models used for obtaining vertical solid dispersion coefficients are the dispersion model and the counter current backmixing model [2, 46, 198].The horizontal solid dispersion coefficient has typically been simply estimated in terms of the Einstein random walk equation [2, 198]. The dispersion model is represented by a differential equation [2] and has been demonstrated to be inadequate for describing the vertical mixing behaviour of solids due to observed oscillation in the concentration responses [46, 197-199, 210], especially in fluidized beds with low gas velocity (i.e., bubbling fluidized beds) [207]. The counter current backmixing model, which was originally proposed by van Deemter [211, 212], considers the convective flow of solids and has gained better acceptance for its favourable representation of the transport

process in bubbling fluidized beds [46, 197-199, 210]. However, the model does not take the lateral solids mixing into account [213] and cannot adequately describe solid mixing in fluidized beds with high gas velocity (i.e., turbulent fluidized beds) [207]. The simultaneous measurement of some parameters for the model can also be difficult [198]. In addition, some of the aforementioned techniques are invasive and can affect the solid flow structure within the bed, therefore the results may be skewed. The use of optical cameras can only monitor the solid mixing close to the wall, and it is difficult to capture the mixing behaviour in the centre or on the other side of the visual point [207, 210]. In the cases where tracer particles are arranged within the bed before the bed has been fluidized, a transition may be observed between the static bed and fluidized bed since it takes time to inject the fluidizing gas and approach a steady state. The existence of this transition can alter the tracer concentration before the bed reaches the steady fluidizing state and the measurement starts and hence affects the result as solids move differently in different stages or regimes. The injection process of additional tracer particles into the bed during the fluidization can also disturb the local flow structure within the bed and subsequently influence the results [198].

Recently, developments of non-invasive measurement techniques have allowed researchers to investigate the solid mixing behaviour in opaque vessels without disturbing the flow structure, such as positron emission particle tracking (PEPT) [1] and radioactive particle tracking [187]. Parker et al. [158] were among the first to use the PEPT technique to quantify the axial solid mixing behaviour in a rotating drum. The PEPT technique was applied to follow the real-time trajectory of the tracer particle that was randomly selected from the bulk material, hence the tracer particle was

identical to the bulk material. In order to estimate the axial solid dispersion coefficient, Parker et al. treated each small compartment within the drum as a starting point. For each starting point, every time the tracer particle fell into this point was recorded as a sample particle, and every axial displacement of these sample particles travelled from this starting point and was followed for a specific duration. The changing rate of the mean squared axial displacement of these particles was then used to characterize the axial solid dispersion coefficient as expressed by the Einstein random walk equation. Since then, several researchers have applied a similar approach, which estimates the solid dispersion coefficient by analysing the trajectory of single tracer particle, to investigate the solid mixing and obtain solid dispersion coefficient in various equipment. For instance, Stein [1] used the same method to characterize the solid mixing behaviour in terms of solid dispersion coefficient in a 2-D fluidized bed, a semi-cylindrical fluidized bed and cylindrical fluidized beds of three different sizes with different bed materials (i.e., resin beads, porous glass and glass ballotini). The tracer trajectories were measured by means of PEPT. Mostoufi and Chaouki [187] quantitatively evaluated the solid mixing in both vertical and horizontal directions in terms of axial and radial solid dispersion coefficients in a 152-mm I.D. fluidized bed of sand and FCC powder by means of the radioactive particle tracking (RPT) technique using the same method as described by Parker et al. [158]. Different air distributor plates (i.e., a stainless steel porous plate and a nozzle-type air distributor plate) were applied in their experiments. Martin et al. [151] applied the approach in a small bladed mixer and proposed a parameter called “mixer effectiveness” (ME), which accounted every element over the entire bed to characterize the solid mixing behaviour of the whole vessel as a single value. In summation, the method suggested by Parker et al.

[158] has been applied in a wide range of equipment and proved to provide a good indication of the solid mixing profile [198].

Due to the use of various measurement techniques and the shortage of verification methods, the value of the solid dispersion coefficient found in the literature has differed by up to 5 orders of magnitude. In the current research, the solid mixing behaviour was studied using the PEPT technique in bubbling fluidized beds. The dispersion coefficient of solids in both vertical and horizontal directions was estimated based on the Einstein random walk theory. A parameter was proposed to evaluate the frequency and opportunity of particles falling into specific regions, and the distribution of solid residence time at each position within the bed was determined. These findings will be discussed in Chapter 6.

2.7 Bubble Behaviours

In bubbling fluidized beds, bubbles have been seen as the primary factor that affects the fluidization quality and the process efficiency, such as gas-solid contact, solid dispersion, mixing and heat and mass transfer [2, 31, 32]. Rising bubbles in a fluidized bed introduce the reaction gas into the bed and, more importantly, perform as "the motor of fluidization" to drive solids circulating and mixing within the bed [8]. Improper bubbling will introduce heterogeneity in the bed, reduce the contact between gas and solids, and thereby reduce the gas residence time, ultimately reducing in turn the mixing and reaction efficiency [50]. Hence, bubble behaviour, such as bubble coalescence, bubble rise velocity, bubble size and their spatial distribution, has been

of great interest in bubbling fluidized bed studies for more than 60 years [181]. This section reviews relevant research on the bubble behaviour in bubbling fluidized beds.

2.7.1 Spatial Distribution of Bubbles

The spatial distribution of bubbles has considerable influence on fluidized bed performance. For instance, large bubbles have small contact area with solids and shorter residence time in the bed, while small bubbles give large solid-gas contact area and longer residence time. If bubbles are developed in a fluidized bed with non-uniform size distribution over the bed cross-sectional area, it will give a wide range of gas residence time and a non-uniform reaction rate within the bed, thereby reducing reaction efficiency. The distribution of gas bubbles within the bed also affects the solid motion, flow patterns and solid mixing. When bubbles plough though solid beds, the rising bubbles carry solids up in their wake and push surrounding solids drifting away from the bubble paths. In a region with frequent bubble development, solids will travel upwards and mix vigorously. Conversely, in a region where with less or no bubble development, solids will move down with much less mixing [178, 191]. An optimally performing bubbling fluidized bed typically requires small bubbles and uniform spatial distribution [2, 214].

Intensive research has been carried out to investigate bubble distribution since 1960s [178, 215, 216]. For instance, Baumgarten and Pigford [215] investigated the bubble behaviour in a transparent rectangular fluidized bed of 7.62 cm × 15.24 cm by means of a γ-ray absorption technique. A sintered bronze plate with a thickness of 2.4 mm was used as the air distributor. The bed materials used were silica-alumina cracking

catalysts and spherical glass beads. Detailed properties of the bed materials are shown in Table 2.1, and the bed was operated at the superficial gas velocity from the minimum fluidization velocity to about 60.96 cm/s. The researchers found that small bubbles were frequently developed near two sides of the rectangular bed, while large bubbles were observed around the centre of the bed. They also determined evident influence of the superficial gas velocity on the bubble size.

Table 2.1 Physical properties of materials [215].

Group	Bed material	Mean particle diameter (μm)	Particle size range (μm)	Particle density (g/cm^3)	Minimum fluidization velocity
1	Glass beads	74	38 - 124	2.44	0.73
2		119	61 - 175	2.45	1.65
3		234	147 - 495	2.60	5.18
4		116	38 - 495	2.52	1.07
5	Silica-alumina cracking catalysts	41	0 - 120	2.17	0.73

Grace and Harrison [217] investigated the bubble behaviour in 2-D bubbling fluidized beds with a width of 45.7 cm and a depth of 1.9 cm by means of cinematographic

technique. Magnetite particles with the minimum fluidization velocity of 8.1 cm/s were used as the fluidized material and were packed to a static bed height of 60 cm. The researchers observed a non-uniform development of bubbles at higher levels above the air distributor and developed a simple coalescence model with an assumption that bubbles were uniformly distributed when they initially developed at the air distributor [178, 218] to interpret the bubble behaviour over the bed. They then reached the conclusion that bubbles were uniformly developed at the air distributor and then rising and increasing gradually to a non-uniform profile due to bubble coalescence, as seen in Figure 2.8.

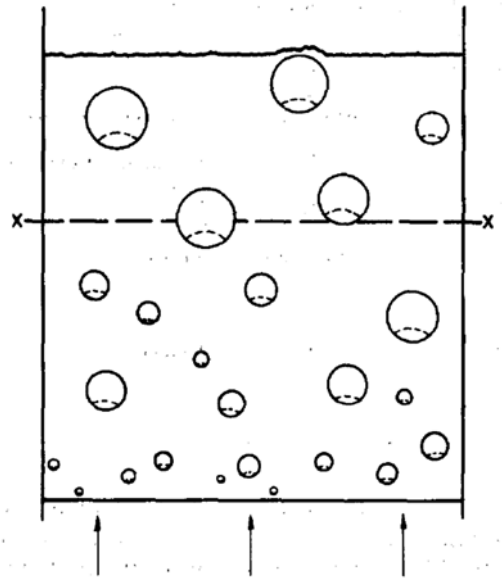

Figure 2.8 Schematic view of bubbles in a fluidized bed [218].

A similar bubble spatial distribution profile was further observed by Geldart [176] in fluidized beds with an H/D of no less than unity. He reported that bubbles near walls tended to rise and coalesce inwards due to the wall effect in the lower bed region,

which induced a downward particle movement near the bed axis, as shown in Figure 2.9. In the upper part of the bed, bubbles developed around the centre and particles mainly moved upwards along the central axis of the bed; meanwhile, particles moved downwards along the bed wall where there was less bubble development.

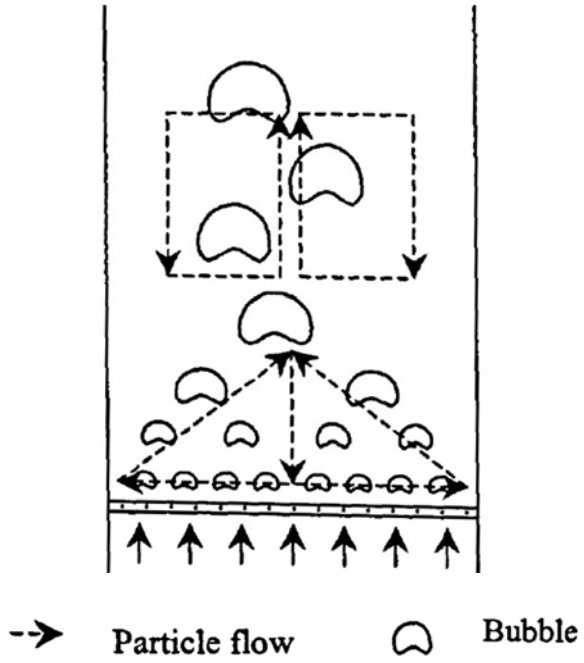

Figure 2.9 Bubble and solid flow patterns in a bubbling fluidized bed [176].

However, Park et al. [216] observed a different profile of bubble development near the air distributor. During their experiments, the fluidization took place in a Lucite tube with a 10-cm I.D. and a 65 cm height with a porous stainless steel air distributor plate. Three groups of electrically conductive petroleum coke particles with nearly spherical shape were used as the bed material. The first group had an average size of 0.0344 cm, a density of 1.846 g/cm^3 and a minimum fluidization velocity of 6.8 cm/s. The second group had an average size of 0.0154 cm, a density of 1.777 g/cm^3 and a minimum

fluidization velocity of 1.83 cm/s. The third group had an average size of 0.0086 cm, a density of 1.784 g/cm^3 and a minimum fluidization velocity of 0.63 cm/s. The settled bed height was approximately 30 cm. Air was used as the fluidization gas and operated from 3.66 cm/s to 27.2 cm/s. The researchers' results showed that, within the bubbling fluidization regime, bubbles were frequently developed near the bed wall when close to the air distributor, and bubbles were more frequently observed around the centre at higher levels of the bed.

This type of bubble spatial distribution profile was further measured by Werther and Molerus [178]. They investigated the bubble behaviour in 3-D fluidized beds with bed diameters of 0.10, 0.20, 0.45 and 1.0 m using a capacitance probe measuring technique [64]. Sintered metal plates with a mean pore size of 5 μm were used as the air distributor and applied to the beds with I.D. of 0.10, 0.20 and 1.0 m. A porous plastic plate with a mean pore size of 40 μm was applied to the bed with a 0.45-m I.D. The bed materials were quartz sand, spherical copper powder and spherical glass beads. The quartz sand had a diameter that ranged from 25 to 125 microns, a density of 2640 kg/m^3, and a minimum fluidization velocity of 0.018 m/s. The copper powder had a diameter that ranged from 25 to 160 microns, a density of 8660 kg/m^3, and a minimum fluidization velocity of 0.014 m/s. The glass beads had a diameter that ranged from 125 to 200 microns, a density of 2950 kg/m^3, and a minimum fluidization velocity of 0.039 m/s. After observation of the bubble development over the bed cross-sectional area at different heights, they found a similar result for all the fluidized beds investigated, in which the bubbles were dominantly developed in an annular zone near the wall when close to the air distributor and then grew and moved up towards the bed

centre as the bed height increased. The researchers also reported that bubbles in the annular zone would merge at a height approximately double the bed diameter (h=2D) and rose along the central axis thereafter, as shown in the sketch in Figure 2.10.

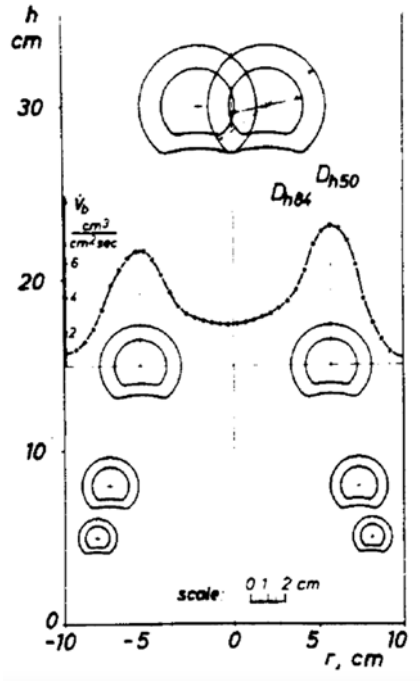

Figure 2.10 Sketch of the bubble flow profile [178].

Lim [214] observed a similar bubble spatial distribution profile in a 2-D fluidized bed by means of a real-time visual system. The bed was 50 cm wide, 100 cm high and 1.3 cm thick and filled with glass beads to a fixed bed height of 70 cm. The bulk density of the bed materials was 1500 kg/m^3. The glass beads had a size of 106-212 μm, classified as Geldart B particles, and the minimum fluidization velocity was 10.3 cm/s. Their results showed that the main bubble path formed near the two end walls of the 2-D fluidized bed from the air distributor and gradually tapered inwards. This bubble flow profile was consistent throughout a range of superficial gas velocities. A similar

spatial distribution of bubbles was also observed by Weber and Mei [219] using electrical capacitance volume tomography (ECVT) in a 10-cm diameter fluidized bed filled with 185-μm glass beads. The minimum fluidization velocity of the glass beads was measured as 3.17 cm/s. Recently, Verma et al. [220] further confirmed this bubble spatial distribution in a fluidized bed with an I.D. of 0.1 m and a height of 1.4 m utilizing the ultrafast electron beam and X-ray scanner. Spherical low linear density polyethylene (LLDPE) particles, alumina particles and glass particles with approximate 1 mm diameters were used as the bed material and were packed to the H/D of 0.5, 1.0 and 2.0. The superficial gas velocity was operated at 1.25 u_{mf}, 1.50 u_{mf}, 2.0 u_{mf} and 3.0 u_{mf}.

However, these investigations of bubble behaviour in 3-D fluidized beds were mostly carried out in a section at a high level of the bed rather than the entire bed or the region close to the air distributors. This experimental process may be due to the limitation of measurement techniques, or the importance of bubble development around the air distributor has been overlooked. For example, bubbles are frequently developed in small sizes at the air distributor, but it is very difficult to properly detect large amount of small bubbles simultaneously, especially when in the vicinity of relevant large bubbles [220]. Furthermore, some techniques have restricted small measurable areas [110, 220-222]. Olowson and Almstedt [222] applied the capacitance probe technique to investigate the bubble behaviour in a layer at 0.55 m above the air distributor in a rectangular fluidized bed with a cross-sectional area of 0.2 m × 0.3 m and concluded that bubbles tended to rise along in the centre of the bed. However, this conclusion was correct only for the bed section observed and when the bed was filled with silica

sands with a mean size of 0.7 mm and operated at an excess gas velocity from 0.1 to 0.6 m/s.

Mudde [110] presented another bubble flow pattern using a three-source X-ray tomographic scanner to study the bubble motion at a layer which was also 0.5 m above the air distributor in a 3-D fluidized bed with 23-cm I.D. Polystyrene particles with a size of 0.56 mm, which were Geldart B particles, were filled as the bed material. The bulk density of the bed material was 625 kg/m^3, and the minimum fluidization velocity was determined to be 0.12 m/s, which was virtually identical to the minimum bubbling velocity. Air at room temperature was supplied to the bed through a porous plate, which was sintered bronze with a pore size ranging from 30 to 70 μm. Their observation was very interesting: large bubbles rose near the centre of the bed, but small bubbles rose along the bed wall, rather than all of the bubbles ring either through the bed centre or along the annular region. This observation was supported by Baumgarten and Pigford [215].

More recently, Saayman et al. [221] investigated the bubble flow structure at a lower bed height, which was from 0.20 to 0.50 m above the air distributor, in a 3-D fluidized bed using fast X-ray tomography (XRT). They observed that the time-averaged solid concentration decreased towards the centre in the radial profile of the bed. This suggested that more bubbles were distributed near the bed centre.

Overall, the bubble spatial distribution reported in the literature was mainly in three patterns in which most of the observations were from a section of the bed and not

including the region close to the air distributor. In the first bubble spatial distribution pattern, bubbles mainly developed along the central region of the bed. In the second bubble spatial distribution pattern, bubbles distributed in an annular structure. In the third pattern, large bubbles were observed around the bed centre, while small bubbles were observed near the bed annular region [178, 216-218]. These bubble distribution patterns were observed under various operation condition and most were obtained from a 2-D fluidized bed due to the lack of proper measurement techniques. However, the wall effect on the bubble flow structure in a 2-D fluidized bed is significant [9], and the bubble spatial distribution observed from a 2-D bed cannot be used to interpret the complex bubble behaviours in 3-D fluidized beds [223, 224]. In addition, overlapped bubbles are difficult to properly detect using X-ray tomography [220]. Furthermore, small bubbles in the centre of the bed cannot be satisfactorily reconstructed from the soft field tomography (i.e., electrical capacitance tomography) [134]. Moreover, the bubble distributions at a higher bed level all have a similar profile [178, 220], while the spatial distribution of bubbles near the air distributor varies significant under different conditions and should be given more attention. The bubble flow structure near the air distributor also greatly influences the bubble development at a higher bed level; therefore, the solid flow patterns in entire beds should be examined. In the present study, the PEPT technique was used to reconstruct the bubble spatial distribution over the bed based on solid motions. A detailed discussion of this aspect of the present study will be presented in Chapter 5.

2.7.2 Bubble Size and Bubble Rise Velocity

Bubble sizes and bubble rise velocities are very important parameters in the design and simulation of fluidized beds [225]. They have been intensively studied since late 1950s, and various empirical correlations have been proposed in order to predict them [28, 226, 227]. Yasui and Johanson [12] were among the first groups to quantitatively study the bubble properties in a fluidized bed and proposed an empirical correlation to predict bubble sizes based on their experimental data. Their experiments were carried in atmosphere conditions in fluidized beds with a 10-cm I.D. and a 15-cm I.D. Various porous plates and a 200-mesh screen were used as the air distributor. Different bed materials with the particles sizes ranging from 41 to 450 μm, such as glass beads, olivine rock, coal, hollow phenolic resin, magnetite catalyst, commercial microspheroidal catalyst and regenerated FCC catalysts, were used. Bubble development was determined by using a transmission optical probe. They observed that the bubble size increased with the increase in the particle size of bed materials, the distance above the air distributor and the superficial gas velocity. The bubble size growth was mainly due to the bubble coalescence. Their results showed that the bubble rise velocity ranged from 0.3 to 0.61 m/s and was not significantly affected by operating conditions, and a relatively constant bubble rise velocity was observed across the column when the bed-depth varied from 0.30 to 0.76 m. Based on these findings, the researchers developed a simple empirical correlation to predict the bubble size based on the particle size, particle density and the fluidization number (u_o/u_{mf}) which was the ratio of superficial gas velocity to minimum fluidization velocity, as shown in Equation 2.1.

Geldart [228] noticed that bubble properties in a 3-D fluidized bed (30.8-cm I.D.) were different from that in a 2-D fluidized bed (68 × 1.27 cm^2) due to the interactions between bubbles, particularly bubble coalescence. He established several equations to relate the two- and 3-D fluidized beds and convert the results obtained from 2-D measurement into 3-D. In his later work, Geldart [180] focused on the investigation of bubble properties in the 3-D fluidized bed by means of direct visual observation. Sand with different sizes and size distributions [228] was used as the bed material, and a perforated metal plate having a total of 3100 holes with 0.32 cm diameter was used as the air distributor. He measured the bubble sizes via observation of bubble bursting at the bed surfaces [229] by taking cine film using a camera located just above the bed. The camera could not observe the bubbles inside in a fluidized bed. However, he measured the bubble bursting at the surfaces of beds with various heights to determine the effect of bed depths on the bubble size. After analysing the experimental results of his studies [180, 229] together with the experimental data from previous researchers [12, 216, 230], Geldart concluded that for many powders, the fluidization behaviour was independent of the mean particle size and the particle size distribution, and the mean bubble size was dependant only upon the air distributor, the height above the air distributor and the excess gas velocity (u_o-u_{mf}). Empirical correlations were then proposed to predict the bubble size, in which the differences between porous and perforated air distributor plates were considered. The correlation of bubble size for porous plate distributors is shown in Equation 2.2.

Mori and Wen [225] analysed the experimentally measured bubble sizes reported in literature [12, 215, 216, 228, 230, 231] and developed a semi-empirical correlation to

predict bubble sizes as a function of bed heights in fluidized beds with various diameters, including pilot scales. They recognised the importance of the initial bubble diameter (i.e., the size of a bubble just formed from the air distributor) and bed diameter in determining the bubble diameter within fluidized beds and took these into consideration. The researchers incorporated these considerations into their correlations by firstly determining the maximum attainable bubble diameter from bubble coalescence within the bed, as shown in Equations 2.3-2.5. Their correlations were applicable to fluidized beds of Geldart B and D solid particles [2].

In 1977, Darton et al. [232] suggested a correlation to predict bubble sizes based on a bubble coalescence model, as shown in Equation 2.6, which later became one of the most popular bubble size correlations from literature [227]. They assumed that bubble coalescence occurred in stages. Between the stages each bubble rose in a path at a separation just sufficient to avoid continuous coalescence with the trailing/following bubble. In this way, bubble sizes increased stage by stage along the bed height towards the bed surface. Their equation agreed quite well with many bubble size data reported in literature [12, 52, 230-233]. However, since they did not consider the bubble splitting and breakage, their model predicted a constantly increasing trend of bubble size. Hence, their correlation is not appropriate for the cases where strong bubble splitting presents, which may due to the fact that a maximum stable bubble size can be easily reached [227], such as fluidized beds of Geldart A particles.

Werther [234] investigated the effect of bed diameter on the bubble development in fluidized beds, and found that the bubble size at a given distance from the air

distributor increased as the bed diameter decreased due to faster development of bubble activities [227]. He initially proposed a bubble size correlation for large columns equipped with porous plate air distributors based on the bubble coalescence and soon extended the correlation to fluidized beds with different air distributors by introducing a specific height above the air distributor for each type of air distributor, which was the height where initial completely developed bubbles should appear [2, 235]. He suggested that this height was zero for the porous plates. In 1981, Bauer et al. [236] further modified this correlation to predict the bubble size at any bed level for fluidized beds filled with Geldart B particles, as shown in Equation 2.7. The operational conditions suitable for their correlation are as follows: the bed diameter is greater than 20 cm, the particle sizes are within 100 to 350 μm and the superficial gas velocity ranges from 1 to 8 cm/s which corresponds to an excess gas velocity (u-u_{mf}) of 5-30 cm/s.

Compared with the bubble size, much less research work on the bubble rise velocity has been reported in literature [227], and insufficient experimental data of bubble rise velocity were available in order to propose a correlation to predict the bubble rise velocity. The correlations for calculating the bubble rise velocity were mainly modified from the correlation originally proposed by Davies and Taylor [237] for predicting the gas bubble properties in liquids. For instance, based on the two-phase theory, Davidson and Harrison [238] proposed a simple correlation to predict the bubble rise velocity, as seen in Equations 2.8-2.9. Their correlation have shown to give the best result for Geldart B particles [227]. Later, Kunii and Levenspiel [2] proposed a separate correlation of bubble rise velocity for Geldart A and B particles by analysing

the experimental data reported by Hilligardt and Werther [239]. Equations 2.9-2.10 presents the bubble rise velocity correlation for Geldart B particles.

Yasui and Johanson [12]:

$$d_b = \rho_p \cdot d_p \cdot \left(\frac{u-u_{mf}}{u_{mf}}\right)^{0.63} \cdot h \tag{2.1}$$

Geldart [180]:

$$d_b = 0.915\left(u-u_{mf}\right)^{0.4} + 0.027h\left(u-u_{mf}\right)^{0.94} \text{ [cm]} \tag{2.2}$$

Mori and Wen [225]:

$$\frac{d_{bm}-d_b}{d_{bm}-d_{b0}} = e^{-0.3h/D} \tag{2.3}$$

$$d_{bm} = 0.65\left[\frac{\pi}{4}D^2\left(u-u_{mf}\right)\right]^{0.4} \text{ [cm]} \tag{2.4}$$

$$d_{b0} = \frac{2.78}{g}\left(u-u_{mf}\right)^2 \text{ [cm]} \tag{2.5}$$

Darton et al. [232]:

$$d_b = 0.54\left(u-u_{mf}\right)^{0.4}\left(h+4\sqrt{A_0}\right)^{0.8} g^{-0.2} \tag{2.6}$$

Werther [2, 234-236]:

$$d_b = 0.835\left[1+0.272\left(u-u_{mf}\right)\right]^{1/3}(1+0.0684h)^{1.21} \text{ [cm]} \tag{2.7}$$

Davidson and Harrison [238]:

$$u_b = u - u_{mf} + u_{br} \tag{2.8}$$

$$u_{br} = 0.711(gd_b)^{1/2} \tag{2.9}$$

Kunii and Levenspiel [2]:

$$u_b = 1.6\{(u - u_{mf}) + 1.13d_b^{0.5}\}D^{1.35} + u_{br} \text{ [m/s]} \tag{2.10}$$

Bubble behaviour has been extensively studied for the last 60 years due to its importance in the gas and solid flow and mixing of fluidized beds. A uniform distribution of bubbles in relatively small sizes can enhance the performance of fluidized beds (e.g., chemical reaction) by achieving uniform and efficient gas and solid contact and mixing as well as heat transfer. However, due to the lack of proper measurement techniques, the bubble behaviour within bubbling fluidized bed has not yet been fully understood and contradictions can still be found in literature. In order to monitor, predict and optimize the performance of industrial processes, a proper measurement technique and a full understanding of bubble behaviour within bubbling fluidized beds is imperative. In this thesis, the spatial distribution of bubbles and the bubble size and rise velocity were investigated in a 3-D bubbling fluidized bed by using the PEPT technique. The detailed results and discussions of this component of the current research will be presented in Chapter 5.

2.8 Summary

Despite the fact that the bubbling fluidized bed has been extensively investigated for over 60 years, it is still not fully understood, and contradictions are still present in the literature. The prediction of solid and gas flow patterns in a 3-D bubbling fluidized

bed remains a significant challenge. One of the primary reasons for this challenge is the limited measurement techniques available to properly monitor solid and gas motions. The unsteady, fast and complex flow structure within bubbling fluidized beds and the opaque nature of the bed in most cases also represent significant challenges for both fluidization research and measurement technique development. In addition, the operational conditions, bed materials and bed design are interrelated and make it more difficult to characterize, understand and predict fluidization behaviour, such as the bubble size, bubble rise velocity, bubble spatial distribution, solid flow pattern and solid mixing. In order to overcome these and fully understand fluidization behaviour, experimental measurements should ideally be conducted in 3-D fluidized beds, using non-invasive measurement techniques with high temporal and spatial resolution and being able to monitor the entire bed rather than a small section. Furthermore, the influence of various parameters on fluidization behaviour should be investigated. These components represent the objectives of this thesis, and details of this research will be reported in following chapters.

Chapter 3: Methods and Materials

This chapter summarizes the materials and methods applied in this study. The chapter begins with an introduction of the PEPT technique, in which the tracer particle labelling methods, PEPT camera for γ-ray detection and algorithms for locating the particle position over time are discussed. A detailed description of the experimental set-up, including particle properties, fluidized bed configuration (i.e., the column and air distributor plates) and operational conditions follows.

3.1 Positron Emission Particle Tracking (PEPT)

PEPT is a non-invasive measurement technique developed at the University of Birmingham [240]. It enables the trajectory of a radioactive tracer particle to be accurately followed three-dimensionally in opaque systems and has been used to study multiphase flows, such as granular materials and viscous fluid flows in engineering processes [137, 241]. The PEPT technique consists of three components: the radioactively labelled tracer particles, γ-ray camera, and algorithms for locating the particle position along with time information. The γ-ray camera has two heads of sensitive detectors that are set opposite to each other to collect the γ-rays emitted from the tracer particles, as seen in Figure 3.1. The tracking procedure can be briefly described in the subsequent steps.

1) Preparation of tracer particle: the particle is radioactively labelled using a radioisotope that purely undergoes β^+ decay.

2) Positron emission/β^+ decay: the radioactive tracer particle undergoes β^+ decay and emits positrons, which quickly annihilate with close electrons and give off pairs of counter-propagating 511-keV γ-rays.
3) Detection of γ-rays: the PEPT camera detects the γ-rays, and a line of response (LOR) is defined each time when two γ-rays of a pair are detected coincidently.
4) Locating the tracer particle: events (i.e., LORs) are processed using an algorithm based on the minimum distance approach, during which erroneous events are discarded and positions of the tracer particle are determined through triangulation.

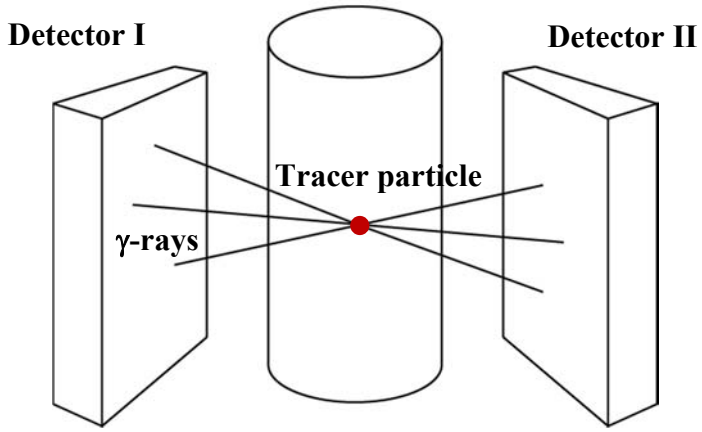

Figure 3.1 PEPT technique.

3.1.1 Positron Emission, Electron-positron Annihilation and γ-rays

A positron, which is the antiparticle of an electron, is released during a β^+ decay when a proton inside the nucleus of a radioisotope (which contains more protons than its necessary for stability) is converted into a neutron [76, 137]. The released positron will collide with an electron in the local surroundings and cause electron-positron

annihilation. As a result, their mass energy will be released in the form of a pair of counter-propagating 511-keV γ-rays. Figure 3.2 illustrates these processes. The PEPT camera will then collect these γ-rays and use them to determine the position where the annihilation takes place by triangulation [137]. Normally, the positron emitted from the radioisotope through β^+ decay will meet an electron within 20 ps [1] and can only travel away from the radioisotope position for up to 2 mm. The slight displacement means that the position where the annihilation takes place is very close to the radioisotope, hence the position determined by the PEPT is in close proximity with where the tracer particle (labelled with a positron-emitting radioisotope) is located. Therefore, the resolution of a positron-based tracking technique, such as PEPT, is considerably high [1].

In most cases, the γ-rays emitted in pairs from the β^+ decay are exactly back-to-back (i.e., 180 degrees) and have an energy of 511 keV, which provides an advantage in PEPT detection of the γ-rays in order to locate the tracer particle. However, minor deviation from collinearity of up to 0.3° can occur [1, 137, 240]. This deviation arises due to the residual momentum of the positron just prior to the annihilation. The released positron should lose all of its energy before annihilation with an electron, and the initial momentum of the positron-electron annihilation system should be 0 in order to have exactly back-to-back 511-keV γ-rays. While in some cases, the positron maintains some residual momentum when it meets with an electron and undergoes annihilation, which gives the positron-electron annihilation system an initial momentum, resulting in a slight acolinearity for the conservation of momentum [1, 242].

The γ-rays are a deeply penetrating radiation, and can go through a considerable thickness of solid material with little attenuation, such as 36.7%-50% attenuation through an 11-15-mm thickness of steel or a 30-45-mm thickness of aluminium [1, 137, 198, 240]. In addition, the deflection of γ-rays by magnetic fields is minimal to none, making the PEPT technique applicable for most engineering equipment [1, 3].

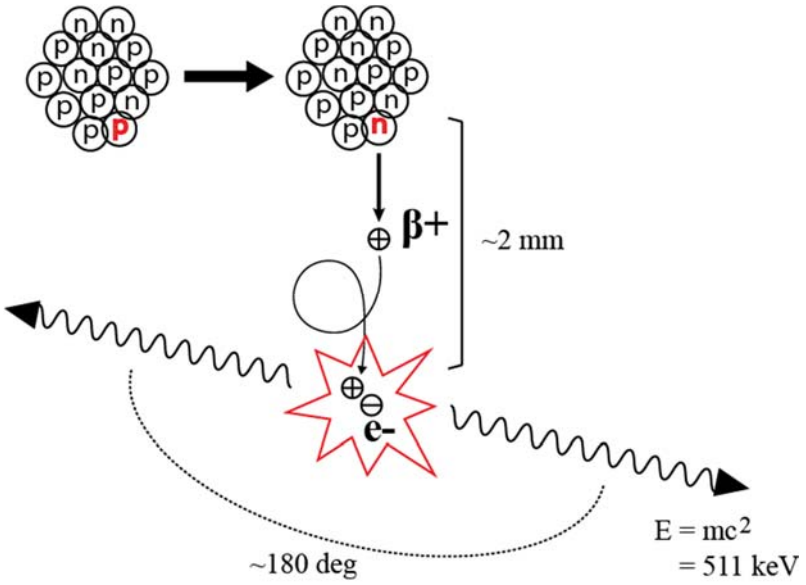

Figure 3.2 Positron emission and electron-positron annihilation.

3.1.2 Labelling Methods for Tracer Particles

The PEPT technique uses a positron-emitting radioisotope and detects pairs of 511-keV counter-propagating γ-rays arising from annihilation of the emitted positrons in order to track the tracer particle locations accurately and non-invasively in opaque 3-D vessels. Many radioisotopes can be potentially used for the PEPT, such as ^{15}O, ^{13}N,

^{11}C and ^{18}F among others. [1]. However, in order to choose the appropriate radioisotope for the PEPT technique, the half-life of the radioisotope, fraction of β^+ decay and the possibility to be labelled onto the experimental materials have to be considered. The half-life is defined as the time taken for half of the radioisotope to undergo decay, and it characterizes the rate of radioisotope exponential decay. Each radioisotope has its own exponential decay pattern, and the timescale of decay for different radioisotopes varies from extremely short (i.e., within a picosecond) to extremely long (i.e., several billion years). The radioisotope used for the PEPT technique should have a sufficient long half-life to cover the full timescale of an experiment but should also be necessarily short to avoid radioactive contamination after the experiment since it is not realistic to separate and recover the radioactive materials from the bed bulk for each test [1, 25]. In addition, the ideal radioisotope used for the PEPT technique should undergo purely β^+ decay) and release only 511-keV counter-propagating γ-rays, as other extra γ-ray emissions can cause erroneous detection of coincident events and reduce the accuracy for locating the tracer particle position [1, 25]. Typical radioisotopes used at the University of Birmingham Positron Image Centre are ^{18}F, ^{22}Na ^{61}Cu and ^{66}Ga [3, 28, 139]. Among them, ^{18}F is the most frequently applied radioisotope, because ^{18}F undergoes purely β^+ decay (i.e., β^+ decay fraction =1) and does not emit any γ-rays other than the 511-keV counter-propagating γ-rays from annihilation [23, 25, 198]; this provides a high level of accuracy in the detected locations. Its half-life is 110 min, which is sufficient for most experimental timescales (i.e., 2 hours) and is also necessarily short to be left inside the equipment after the experiments; the radioactivity of the tracer particle will decay to a negligible level overnight [25, 198]. In this study, ^{18}F has been used to radioactively label the

tracer particle and has been produced from either purified water or solid materials by direct bombardment using a 33-MeV ^{3}He beam generated from the Scanditronix MC40 Cyclotron, after which some oxygen element present in the purified water or solid materials will be converted to ^{18}F via the reactions ^{16}O(^{3}He, p)^{18}F and ^{16}O(^{3}He, n)^{18}Ne $\rightarrow$ ^{18}F [3, 198].

Three methods can be applied to radioactively label particles. The first technique is the direct activation, where the particle is directly bombarded using a 33-MeV ^{3}He beam for 60-minute irritation at a currency of 10 μA. After the bombardment, some oxygen components in the particles are converted into ^{18}F radioisotopes via the reactions ^{16}O(^{3}He, p)^{18}F or ^{16}O(^{3}He, n)^{18}Ne $\rightarrow$ ^{18}F. In the meantime, some short-living radioisotopes can also be produced from other structural elements of the solid material, such as ^{10}C (19.3 s half-life), ^{12}N (11 ms half-life), ^{27}Si (1.16 s half-life), ^{29}P (4.1 s half-life) and ^{26}Al (6.4 s half-life) [3, 28]. The production of these radioisotopes can be purified by waiting for a "cooling" time of 20 minutes, after which the majority of radioactivity (i.e., > 90%) serving for the PEPT experiments will be from ^{18}F [25]. The ^{18}F produced in this manner exists in the tracer particle as a structural element, within a layer of approximately 0.3 mm in depth. Hence, it is hardly replaced by ions in experimental systems nor worn by experimental environments [3]. Direct activation is a fast and easy technique for radioactively labelling a particle [198]: the tracer particle can be produced from materials with identical properties to the bed bulk material [3, 28], and the radioisotope (i.e., ^{18}F) hardly leaks out as it has been chemically bonded inside the tracer particle [198]. However, this method has some limitations. For example, the particle being labelled has to be at least 1 mm in size [1, 25, 28, 198].

Since the radioactivity achieved in a single particle is proportional to the square of particle diameter under fixed irradiation time and electrical current, if the size of tracer particle is very small its radioactivity will be not enough to cover the experimental timescale [3, 198]; for most cases the radioactivity of tracer particle should be within 300-1000 μCi [23, 198]. Another limitation of this method is that the particle being labelled has to contain oxygen components [1, 198]. In addition, the particle being labelled must be able to resist high temperatures since the temperature produced during the bombardment can destroy organic material [1, 3, 25, 28, 198].

The second method is the ion-exchange technique, which is used to radioactively label smaller particles (i.e., <1 mm) and organic materials. Instead of directly bombarding the solid particle being labelled to produce ^{18}F, the ^{18}F is produced from purified water by bombarding the water with a ^{3}He beam generated from a cyclone [1, 198]. The water is then radioactive with F^- ions. Theoretically, two types of anion exchange resins can be potentially used to adsorb ^{18}F ions from radioactive water via an ion-exchange process: the weak base anion exchange resin and the strong base anion exchange resin [1, 3, 25, 28, 198]. However, the uptake of ^{18}F in a weak base anion exchange resin is strongly controlled by water pH. The free base amines in weak base anion exchange resin, i.e., $RCH_2N(CH_3)_2$, interact with water and form $RCH_2NH(CH_3)_2^+OH^-$, in which the OH^- performs as a counter ion and can be exchanged by ^{18}F. However, the dissociation of the "hydroxide" form is very weak, and any significant concentration of hydroxide ions in water can convert the resin back to the undissociated free base form, i.e., $RCH_2N(CH_3)2$, immediately, resulting in the loss of the anion exchange capacity [3, 25, 28]. Moreover, the affinity of ^{18}F ion to a

weak base anion exchange resin is much weaker than that of hydroxide ions. Hence, the ^{18}F adsorption in weak base anion exchange resins can only be performed at a considerably low pH. Strong base anion exchange resins are less influenced by water pH or hydroxide ions than weak base anion resins since the affinity of an ^{18}F ion to a strong base anion exchange resin is stronger than that of hydroxide ions and are hence more suitable to uptake ^{18}F [3, 25, 28]. The strong base anion exchange resins used are quaternary ammonium derivatives and are provided in chloride forms, i.e., R-$CH_2N(CH_3)_3^+Cl^-$ or R-$CH_2N(CH_3)_2(CH_2CH_2OH)^+Cl^-$. Where R is the organic backbone, -$CH_2N(CH_3)_3^+$ and -$CH_2N(CH_3)_2(CH_2CH_2OH)^+$ are functional groups and Cl^- is the counter ion. Since the affinity of ^{18}F ion to the functional groups is much weaker than that of the Cl^- ion, the resin particles in chloride forms cannot be directly used to uptake ^{18}F from the radioactive water and hence have to be converted into fluorine forms or hydroxide forms before the labelling. To convert a strong base anion exchange resin from a chloride form to a fluoride form, the resin slurry is poured into a glass column with a glass frit of porosity of 50-80 μm and eluted with 8-10 bed-volumes of 1 M KF solution, followed by rinsing with 10 bed-volumes of distilled and deionized water. After the conversion, F^- ions act as counter ions rather than Cl^- and can then be exchanged with ^{18}F ions in the radioactive water under certain conditions. Particles with small sizes (i.e., > 60 μm) can be radioactively labelled via this ion-exchange technique, and high radioactivity (i.e., 350-1500 μCi) can be achieved using this method. However, only particles having a high affinity for ^{18}F ions can be labelled via this technique [3, 198]. In addition, the ion-exchange resins are amine polymers, and their density, size and other properties may not be identical to the bed bulk material used in PEPT experiments.

The third method is surface modification, which is an important technique to improve the selective adsorption of chemicals onto particular surfaces for various areas [3, 23, 28]. With growing interests in the PEPT technique by users from various engineering areas, experimental materials have extended from mainly large glass beads and resins to a wide range of organic and inorganic particles, such as apatite, fine sand, fine glass beads, coal, crystallised cellulose, polyethylene and oil seeds [23, 198]; most of these particles are smaller than 1000 μm and have a poor capacity to adsorb ^{18}F ions naturally. Thus these materials are difficult to be radioactively labelled either through direct activation or ion exchange. In this study, surface modification has been carried out via chemical activation using metallic ions, in order to solve this issue. Fe^{3+} ions are used in this study rather than other metallic ions (i.e., Pb^{2+} and Cu^{2+}) since Fe^{3+} is most chemically active and can adsorb onto most solid surfaces. During the process, Fe^{3+} ions are first introduced to the solid surface as active sites and act as a bridge, which encourages $^{18}F^{-}$ anions to bind onto on the solid surface through ion-exchange. Modifying the surface chemistry of solids significantly enhances the ^{18}F adsorption onto particles. The adsorbed metallic ions on the solid surface first enhances the adsorption of hydroxides in water, and the adsorbed hydroxides are then replaced by ^{18}F, therefore the radioactivity labelling in a single particle increases significantly. For example, under optimized experimental conditions, the radioactivity achieved on a single particle increased from 67 to 600 μCi for hydroxyapatite, from 2 to 400 μCi for quartz, and from 2 to 152 μCi for polyethylene [3, 23, 28]. The surface modification technique leads to a considerable extension of tracer materials for PEPT study, and it was also the method used to radioactively label tracer particles in this research.

3.1.3 PEPT Camera

The positron camera used for the PEPT technique in this study was the ADAC Forte dual-headed camera, which has two gamma detection heads, as shown in Figure 3.3. The two heads can be rotated around a horizontal axis and adjust to a separation distance between 250 mm and 800 mm, with the system of interest to be measured being placed in the middle of them. Each head is a sensitive scintillation detector that contains a single sodium iodide crystal with a 16-mm thickness, which is lightly doped with thallium NaI(Tl) [243, 244]. The heads have an area of 590 × 470 mm^2 with truncated comers, and it has a field of view (FOV) of 508 mm × 381 mm for useful detection. Each head is optically coupled to an array of 55 photomultiplier tubes (PMTs) where 49 of them are 76-mm tubes and 6 of them are 50-mm tubes. Each of these photomultipliers is connected to a separate analogue-to-digital converter (ADC), and these 55 ADC channels are controlled by a single-board computer (SBC) within the head. Every time a γ-ray collides with the crystal, a scintillation occurs in the crystal and the scintillation centroid is determined via software. The software compares the relative light intensity in each PMT with a spatial resolution of around 6 mm to determine the scintillation centroid [243, 244] (digital electronics), which is more flexible than an analogue circuit (i.e., multiwire proportional chamber [MWPC] camera), and the results feature less distortion near the edge of the crystal [198, 243]. A sample of raw data from the PEPT camera system that has been written representing the LORs is illustrated in Figure 3.4. These LORs will be used in determining the tracer particle locations and are discussed in the next section.

Figure 3.3 ADAC Forte camera.

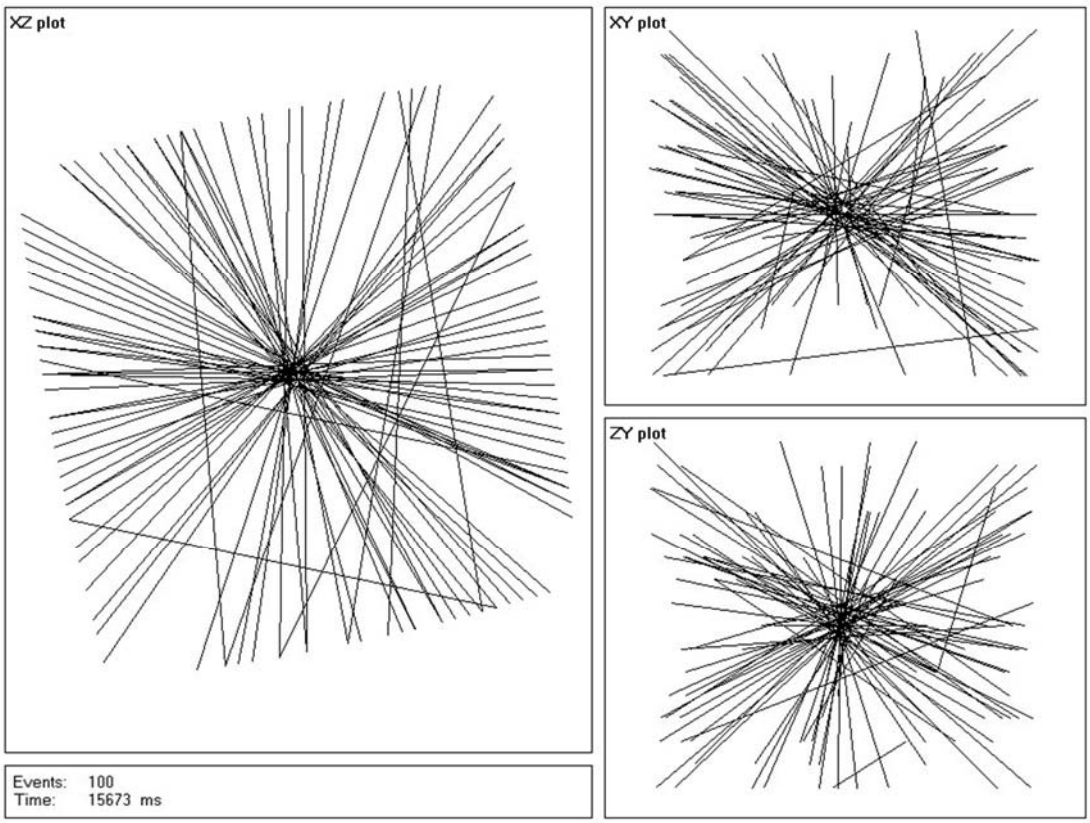

Figure 3.4 Snapshot of raw LOR data from the PEPT camera system [244].

The main advantage of the ADAC Forte camera is its high-speed data acquisition. This high-speed data acquisition is benefited by the use of very fast pulses and separate digital channels that allow signals from different regions of the crystal, to some extent, to be processed in parallel. Specifically, the dead time per pulse is approximately 170 nanoseconds (ns), and each head can operate at a singles rate of over 2 mega (M) counts per second (cps). The two detectors are operated in coincidence with a resolution time of 7.5 ns [243], and the intrinsic total efficiency or quantum efficiency (i.e., the ratio of the total number of events which are detected to the total number of γ-ray photons' incidence on the detector) of each head for detecting γ-rays is approximately 23% at 511 keV. As a result, the useful coincidence rate of 100 k/s can be achieved at a dead time of around 15% [244]. The energy resolution of the detectors, expressed by $\frac{\text{full width at half maximum (FWHM)}}{energy\ of\ \gamma-ray}$, of the ADAC Forte camera is also impressive and is better than 15% (i.e., in the case of PEPT technique, the photopeak of the γ-rays is 511 keV), which is sufficient to discriminate against photons that are scattered (low energy) by more than 30°. The intrinsic photopeak efficiency (i.e., the ratio of the number of full energy events to the total number of γ-ray incidents on the detector) is 16%. As a result, a useful photopeak logging rate of 100k /s can be achieved with the dead time of 30% [243]. In addition, the intrinsic spatial resolution of the camera (i.e., FWHM of the back projected image of a point source) is approximately 6 mm (i.e., 4-8 mm) [243, 244]. Overall, the ADAC Forte camera has favourable detecting efficiency and imaging resolution, high logging rates and a short dead time, which is desirable for efficiently detecting accurate tracer particle positions.

For example, a tracer particle that moves at a rate of 1 m/s will be located by the PEPT camera to within 0.5 mm in three-dimensions 250 times per second, and a slow moving tracer particle can be located to within 100 μm in three-dimensions 50 times per second by the PEPT camera [198, 243, 244].

3.1.4 Algorithms for Locating the Tracer Particle Position

Each positron-electron annihilation emits a pair of 511-keV counter-propagating γ-rays. When a pair of γ-rays simultaneously collides the two γ-ray detection heads, the coincident detection of the pair of γ-rays is considered as an event, and the straight line connecting the centroids of scintillations on the two detector is defined as a LOR. Theoretically, for each event, the tracer particle should lie on the LOR, as seen in Figure 3.5a. However, in practice, not all LORs actually pass through the exact location of the tracer particle. Possible erroneous reconstructions include random events where γ-rays of two different events are incorrectly recorded as a coincidence detection (Figure 3.5b) because their incidences on the two detectors occurred within a coincidence timing window and scatters (i.e., Compton scattering) where the γ-ray is deflected from its original path by interaction with matter in the field of measurement (Figure 3.5c). In order to eliminate the erroneous events and enhance the accuracy for locating tracer particle positions, a location algorithm has been developed. Based on the algorithm, LORs that pass further away from the true location of the tracer particle are regarded as corrupted events, and the LORs that pass close to the tracer particle locations are regarded as uncorrupted events. The points, which minimize the sum of perpendicular distances to the uncorrupted LORs, are considered

close to the tracer particle locations. The algorithm locates the tracer particle positions by first discarding most (if not all) of the corrupt events and then calculating the tracer particle location using only the uncorrupted events [28, 139].

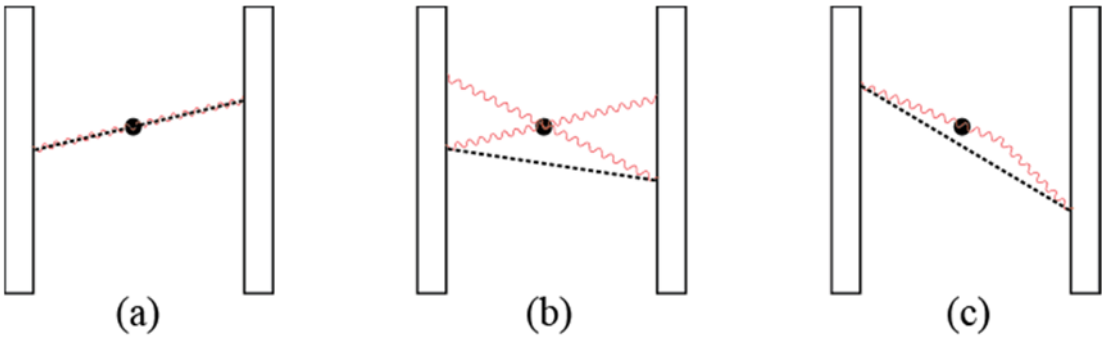

Figure 3.5 (a) True reconstruction, (b) erroneous reconstruction due to random events, and (c) erroneous reconstruction due to (Compton) scattering [1, 198].

The location algorithm starts from dividing the sequential LORs within a second into many sets containing a specific amount (n) of LORs, and each set is used for calculating one tracer particle location. For example, a set SX contains N sequential LORs, named L1 … LN, and the sum of perpendicular distances from the point (x,y,z) to all LORs of set SX is given by:

$$D_{SX}(x,y,z) = \sum_{SX} d_i(x,y,z) \tag{3.1}$$

Where $d_i(x,y,z)$ is the perpendicular distance from the point (x,y,z) to the i^{th} LOR. The minimum solution for $D_{SX}(x,y,z)$ can be obtained when:

$$\begin{cases} \frac{\partial D_{SX}(x,y,z)}{\partial x} = 0 \\ \frac{\partial D_{SX}(x,y,z)}{\partial y} = 0 \\ \frac{\partial D_{SX}(x,y,z)}{\partial z} = 0 \end{cases} \tag{3.2}$$

Which gives the first approximation (x_0,y_0,z_0) for the tracer particle location, and the mean deviation of all LORs of set SX from the point (x_0,y_0,z_0) is then:

$$\overline{d(x_0, y_0, z_0)} = \frac{D_{SX}(x_0,y_0,z_0)}{N} \tag{3.3}$$

Where $D_{SX}(x_0,y_0,z_0)$ is the sum of perpendicular distances between point (x_0,y_0,z_0) and all LORs of set SX and N is the amount of LORs in set SX.

The perpendicular distance between the point (x_0,y_0,z_0) and each LOR of the set SX is calculated. If any $d_i(x_0,y_0,z_0)$, which is the perpendicular distance from the i^{th} LOR in the set SX to the point (x_0,y_0,z_0), is larger than $k \cdot \overline{d(x_0, y_0, z_0)}$, this LOR is discarded leaving a new set SX1, which is a subset of the original set SX. The k here is a fixed parameter that defines the extent to which the LORs should be discarded, and optimum value of k normally lies in between 1 and 1.5 [245]. The new set SX1 will contain less LORs, where the amount of LORs left in set SX1 is N1 (< N). The remaining sequential LORs are then renamed in order as L1, L2 … LN1. Here, an improved approximate tracer particle position (x_1,y_1,z_1) will be found as the same way using Equations 3.1 and 3.2. The improved approximate position gives the minimum value of D_{SX1}, which is the sum of perpendicular distances between a point and all LORs in set SX1. As a consequence, another new set SX2 will be generated, which is a subset

of set SX1 and contains a smaller amount of LORs than that of SX1. The location algorithm proceeds by iteration in this way, selecting subsets based on the minimum distance principle and improving approximations of the tracer particle location until only a specified fraction (f) of the LORs of the original set SX remains, where the iteration should end. The final set SXF contains f·N of LORs, and the final approximation of the tracer particle location (x_F,y_F,z_F) is obtained from the final set SXF based on the minimum distance principle. Hence, the position (x_F,y_F,z_F) has been determined as the tracer particle location at a time that lies somewhere within the time interval covered by the set SXF. Every single event or LOR has its time of measurement t_i recorded, and the exact corresponding time for the tracer particle position (x_F,y_F,z_F) is calculated by taking the average from all the t_is of set SXF, as shown in Equation 3.4:

$$t = \frac{\sum_{SXF} t_i}{NF} \tag{3.4}$$

Where NF is the amount of LORs in the final set SXF.

Having located the tracer particle position once, a new original set, which contains a specific amount (n) of sequential LORs, starts immediately from the last LOR of the previous final set for calculating the next tracer particle position. Although some LORs are discarded as corrupt events for the previous tracer particle locations, they may be associated with later particle locations and hence are involved in the subsequent original sets. Typically, a radioactively labelled tracer particle can be located 100-200 times per second, and extensive time-position data can be obtained in which the

position of the tracer particle is located every 5-10 ms. The instantaneous velocity (v_i) of tracer particle at time t_i then can be calculated by using three sequential tracer particle positrons (x_{i-1},y_{i-1},z_{i-1}), (x_i,y_i,z_i) and (x_{i+1},y_{i+1},z_{i+1}):

$$v_i(v_{xi}, v_{yi}, v_{zi}) = \begin{cases} v_{xi} = \frac{\frac{x_i - x_{i-1}}{t_i - t_{i-1}} + \frac{x_{i+1} - x_i}{t_{i+1} - t_i}}{2} \\ v_{yi} = \frac{\frac{y_i - y_{i-1}}{t_i - t_{i-1}} + \frac{y_{i+1} - y_i}{t_{i+1} - t_i}}{2} \\ v_{zi} = \frac{\frac{z_i - z_{i-1}}{t_i - t_{i-1}} + \frac{z_{i+1} - z_i}{t_{i+1} - t_i}}{2} \end{cases} \quad (3.5)$$

$$|v_i| = \sqrt[2]{{v_{xi}}^2 + {v_{yi}}^2 + {v_{zi}}^2} \quad (3.6)$$

Where v_{xi} is the instantaneous velocity at time t_i in the x direction, v_{yi} is the instantaneous velocity at time t_i in the y direction, v_{zi} is the instantaneous velocity at time t_i in the z direction and $|v_i|$ is the tracer particle speed at time t_i.

3.2 Experimental Set-up

The experimental set-up in this study consisted of a fluidized bed and the PEPT technique. The fluidized bed was placed in between the two γ-ray detectors of the PEPT camera as seen in Figure 3.6, and the PEPT technique was applied in this study to directly measure the particle motion within the fluidized bed. The two detectors of the PEPT camera were placed closely to the fluidized bed in order to collect as much as γ-rays in its field of view (FOV) and reduce deviations to locate the tracer particle more accurately. The fluidization system consisted of a bed of particles and a gas

supply system, as shown in Figure 3.7. In this section, the properties of bed material, bed configurations and operational conditions of the experiment are discussed.

Figure 3.6 Experimental setup.

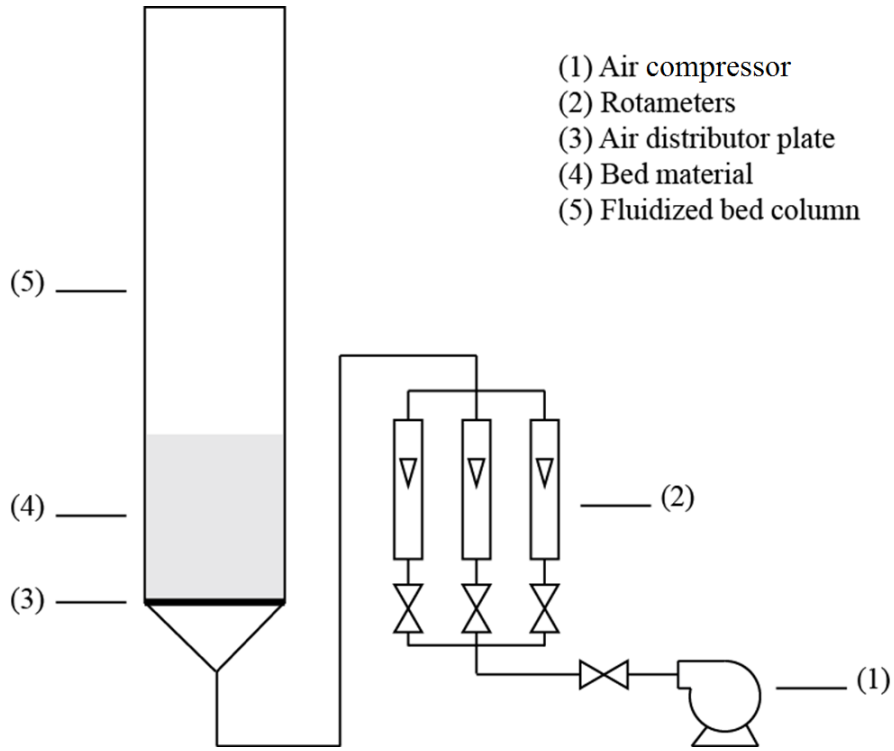

Figure 3.7 Schematic diagram of the fluidized bed.

3.2.1 Particle Properties

Research work in this project mainly focused on the bubbling fluidization of Geldart B particles [38]. Four types of particles were used as the bed material to investigate the effect of material density and particle size on the bubbling fluidization and to further advance the understanding of bed materials, fluidized bed configurations and operational conditions on gas and solid flow patterns. The four bed materials were silica sand, small glass beads, large glass beads and polyethylene, and all were spherical in shape. Research showed that the effect of particle shape on the solid flow structure was minor except where particles were large and flat [31, 246]. Hence, effects of particle shape were not considered in this study. Details of particle properties applied in this study are shown in Table 3.1: both silica sand and glass beads had a

similar density of 2700 kg/m^3, and polyethylene had a density of 760 kg/m^3. The silica sand had a mean size of 117 μm, and the mean sizes of small glass bead, large glass bead and polyethylene were 352 μm, 880 μm and 717 μm, respectively. The particle size distribution of each bed material was measured by sieving, and the results are shown in Figure 3.8. The minimum fluidization velocities of the bed materials were experimentally measured to be 0.046 m/s for the silica sand, 0.15 m/s for the small glass beads, 0.57m/s for the large glass beads and 0.24 m/s for the polyethylene.

Since particle properties significantly affect their flow behaviours in a fluidized bed, the tracer particles were therefore randomly selected from the bed bulk materials for each experiment in order to ensure that the particle tracked by the PEPT technique had identical properties with the bed material and could efficiently represent the solid flow behaviour of the bed bulk material in a fluidized bed.

Table 3.1 Properties of bed materials.

Material	Size range (μm)	Mean size (μm)	Density (kg/m^3)	u_{mf} (m/s)
Silica sand	60-210	117	2700	0.046
Small glass bead	220-470	352	2700	0.15
Large glass bead	700-1100	880	2700	0.57
Polyethylene	400-1050	717	760	0.24

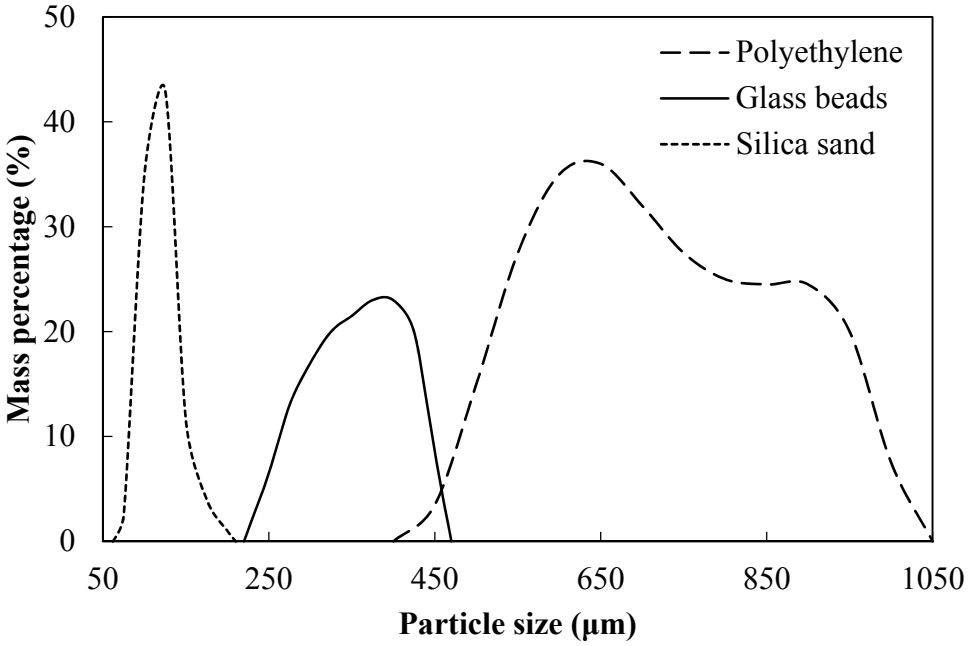

Figure 3.8 Size distribution of bed materials.

3.2.2 Fluidized Bed Configuration

The fluidization was performed in a Plexiglas cylindrical column. It had an I.D. of 152 mm and a height of 1000 mm. The air distributor plate was placed between the bottom of the column and a conical section from which the gas was injected into the bed. The conical section was filled with objects to enhance the uniformity of gas distribution before entering the bed of particles [247]. In order to further make sure the gas distribution enters the bed was uniform and ensure a stable fluidization of the bed during experiments, the air distributors were carefully chosen. Five types of air distributor plates, as shown in Table 3.2, were applied to investigate the effect of distributor pore sizes on the fluidization behaviour. The sintered metal filter plates

applied had three different pore sizes: 1 μm, 10 μm, and 15 μm. The stainless steel wire meshes used had two different sizes: 60 μm and 230 μm.

Table 3.2 Porous air distributor plates.

Material	Type	Mean pore size (μm)	Wire diameter (μm)	Opening ratio
Sintered metal filter	Porous	1	N/A	24%-28%
Sintered metal filter	Porous	10	N/A	24%-28%
Sintered metal filter	Porous	15	N/A	24%-28%
Stainless steel mesh	Porous	60	40.6	36%
Stainless steel mesh	Porous	230	190.5	30%

3.2.3 Operational Conditions

Experiments were conducted under various conditions and were designed to investigate the effect of particle size, particle density, bed aspect ratio (H/D), the pore size of the air distributor and superficial gas velocity on solid and gas flow patterns. The fluidized beds of silica sand and small glass beads were packed with different amounts of particles, corresponding to the H/D of 1 unit, 1.5 units and 2 units.

Experiments for fluidized beds of large glass beads and polyethylene were carried out for unit beds (i.e., H/D=1). The fluidization gas used was air at ambient temperature that was supplied by a GA11CFF air compressor. The gas flow rate was measured and controlled by means of calibrated rotameters. The superficial gas velocity ranged from 0.17 to 0.40 m/s for the silica sand bed, 0.18 to 0.64 m/s for the small glass bead bed, 0.83 to 1.12 m/s for the large glass bead bed and 0.30 to 0.63 m/s for the polyethylene bed. The pressure drops across the beds and air distributors were measured with a FC0510 micro-manometer interfaced to a PC through an RS232 interface. To avoid disturbing the flow structure within the fluidized beds, the pressure drop was measured each time after a PEPT experiment was completed. The pressure drop across the air distributor was 12 mbar at a gas velocity of 0.2 m/s for the stainless steel wire mesh porous plate with mean pore size of 230 μm, and the pressure loss from the air distributor for all experiments was less than 8%. The pressure under the air distributor ranged from 3.3 to 4 bars, and the pressure drop across the air distributor measured for all operating gas velocities largely exceeded the pressure drop across the fluidized bed (i.e., > 30%), which ensured the bed fluidized uniformly even at high H/D ratios [31, 247].

All experiments were carried out within the bubbling fluidization regime, which was characterized by both measured pressure drops across the bed and visual observations. Each experiment lasted for a sufficiently long time (i.e., 2 hours) for the PEPT measurement to make sure that the tracer particle had travelled throughout the bed, and to obtain reliable information for interpreting the gas-solid flow structures within

bubbling fluidized beds. Table 3.3 summarizes the experimental conditions applied in this study.

Table 3.3 Experimental conditions.

Bed material	Silica sand	Small glass bead	Large glass bead	Polyethylene
Particle density (kg/m^3)	2700	2700	2700	760
Particle size (μm)	60-210	220-470	700-1100	400-1050
Mean size (μm)	117	352	880	717
u_{mf} (m/s)	0.046	0.15	0.57	0.24
Pore size of the air distributor (μm)	1	1, 10, 15, 60, 230	230	230
H/D	1, 1.5, 2	1, 1.5, 2	1	1
Superficial gas velocity (m/s)	0.17, 0.22, 0.34, 0.40	0.17, 0.21, 0.31, 0.40, 0.49, 0.57, 0.64	0.83, 0.98, 1.12	0.30, 0.48, 0.63

Chapter 4: Classification and Prediction of Solid Flow Patterns in Bubbling Fluidized Beds

4.1 Introduction

The solid flow pattern is of utmost importance in bubbling fluidized beds. It dominates solid mixing, gas-solid contact, heat and mass transfer and the process efficiency and energy consumption in fluidized beds [142, 166-169, 248]. Furthermore, the importance of the solid flow pattern in bubbling fluidized beds is particularly significant in large-scale industrial processes [170], such as catalytic cracking, coal combustion and gasification, metallurgical processes, granulation and drying [248]. Both numerical and experimental studies have been carried out to investigate solid flow structure within fluidized beds by identifying the effects of operational conditions, particle properties and bed geometry on fluidization behaviours. For example, Li and Kwauk [249] proposed an energy minimization multi-scale model (EMMS) to characterize the meso-scale flow structure in a bubbling fluidized bed [250]. Xiong et al. [251] proposed a smoothed particle hydrodynamic method to model dense particle-fluid flows in bubbling fluidization. Herzog et al. [252] predicted the solid flows, pressure drop and bed expansion ratio in a gas-solid fluidized bed using their developed computational fluid dynamics (CFD)-codes with the considerations of solid-phase properties and momentum exchange coefficients. Ku et al. [253] followed the Eulerian-Lagrangian approach to simulate solid flow patterns, bed expansion, pressure drop and fluctuation in a bubbling fluidized bed by considering drag force correlations and particle-particle and particle-wall collisions. Wang et al. [254]

developed a drag model to simulate the meso-scale flow structure in solid-gas bubbling fluidized beds and achieved good agreements between their simulated and experimental data. Yang et al. [169] utilized a directional force probe located with different penetrations into the bed to experimentally investigate the solid flow pattern. Trisakti et al. [255] used a disk-shaped plastic pellet with different properties of the bed material to measure the particle flow behaviour within a 2-D fluidized bed of glass beads by means of video camera recording. Kai et al. [256] applied photochromic dye as a new method to visualize the particle movement within a 2-D fluidized bed. The pores of all their particles were impregnated with an aqueous solution of a photochromic dye for making light yellow tracer particles that turned to dark blue immediately after irradiation by an ultraviolet light beam and enabled the movement of the tracer particles to be monitored by a high-speed video camera.

However, many factors can affect solid/gas flow pattern in a fluidized bed and make fundamental analysis, modelling and prediction of fluidization behaviour very difficult. In a fluidized bed, gas is introduced into a bed through an air distributor and forms many bubbles or voids. The bubbles or voids will drive solid particles circulating around within the bed [159, 257, 258]. The solid flow pattern is dominated by the bubble size, bubble rise velocity and bubble distribution within the bed, which further depend on the superficial gas velocity, pore size of the air distributor, density and size of solid particles and column diameter, among other factors. In practice, all factors are interrelated and the impact of a parameter on the solid flow pattern could vary under different conditions [259]. For example, bubbles drive particles; the moving particles interact with the bed wall and packed particles and in turn have effects on the bubble

behaviours. The interaction between particles and bubbles will affect the macroscopic and microscopic behaviour of the bed, bubble size, bubble rise velocity and bubble distribution [260-262]. Hence, though solid flow patterns have been investigated for years, the need remains for additional more elaborate studies.

There have been several measurement techniques developed to measure and analyse the fluidization behaviour and the effects of various factors, such as PEPT [22, 139, 159], X-ray densitometry/tomography [221], electrical capacitance volume tomography [219], ultra-fast magnetic resonance imaging [263], the measurement of pressure fluctuations [264], LDV measurement and analysis of gas and particulate phase velocity profiles [265], LDA [72] and cross-sectional wire mesh sensors [266]. In this chapter, the solid flow in a bubbling fluidized bed was measured using the PEPT technique. The impacts of operational parameters and bed geometries, such as bed aspect ratio (H/D), particle properties, the pore size of the air distributor and superficial gas velocity, on the solid flow behaviour were investigated, and their relative significances and potential interrelations were estimated. A flow pattern parameter (FPP) was developed to identify the flow structure in bubbling fluidized beds based on the bed design and operational conditions. The results will be beneficial for quality control, proper design and scale-up of fluidized beds, as well as further development of fundamental fluidization theories [142, 175].

4.2 Solid Flow Patterns

Solid flow patterns in bubbling fluidized beds were investigated by the PEPT technique under different operational conditions. Four distinct flow patterns were

observed, and classified as patterns A-D, as shown in Figure 4.1. In pattern A (Figure 4.1a), solids move up along one side of the bed from the bottom to the splash zone, and then all the way down to the air distributor along the other side, generating a large circulation vortex. In pattern B (Figure 4.1b), solids move inwards and upwards to the centre of the bed from the bed bottom, then flow up along the central axis, resulting in a descending solid flow along the bed wall. A toroidal vortex of solids that travels upwards along the centre and downwards by the bed wall is observed in this flow pattern. In pattern C (Figure 4.1c), solids move upwards near one side of the bed wall from the bottom of the bed; as a result, there is a descending solid flow along the other side of bed wall. This generates a solid circulating vortex in the bottom section of the bed near the air distributor. In the top section of the bed, solids move upwards around the central axis to the bed surface and flow downwards along the bed wall, resulting in a similar toroidal vortex of pattern B. In the intermediate section of the bed, solids from the top circulation vortexes encounter with particles from the bottom circulation vortex, and mix and are redirected to top and bottom sections. In pattern D, the fluidized bed can be seen as three sections as shown in Figure 4.1d. A toroidal vortex of solids that moves upwards along the bed wall and downwards at the centre is observed in the bottom section of the bed, and a reversed toroidal vortex of solids that travels upwards along the central axis and downwards by the bed wall is observed in the top section of the bed. In the intermediate section of the bed, particles from the bottom section encounter the particles from the top section of the bed, and solids mix and are redirected. In this solid flow pattern, four small solid circulation vortexes can be observed.

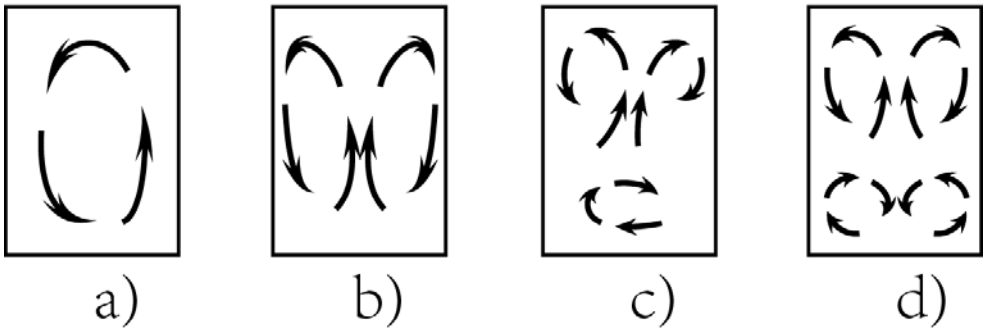

Figure 4.1 Solid flow patterns in bubbling fluidized beds observed by the PEPT technique.

Figure 4.2 shows the PEPT particle velocity vector maps from the view of the x-y plane and z-y plane for the pattern A. It can be seen that particles travel at high speeds in the circulation vortex. However, velocities of particles in the corners at the bed bottom are very slow. In order to have the detailed information of the solid motion within the entire fluidized bed, the particle velocity in both vertical and horizontal directions at different bed heights were analysed using a MATLAB programme. In this programme, the bed was divided into many small cubes with the dimension of 5 mm, and the calculation step was 3 mm. The particle velocity was calculated for each time when the tracer particle passed a cube, and the velocity data were then used for obtaining the average vertical and horizontal velocities of the particles in each cube. Figure 4.3 provides the vertical and horizontal velocity maps of particles at a height of 35 mm above the air distributor for the pattern A. It can be seen that, at the bottom of the bed, particles mainly travel up along the left-hand side of the bed wall and descend along the right-hand side (Figure 4.3a). There is a thin annulus close to the bed wall where particles move slowly in the vertical direction, and this could be due to the particle to wall friction and uneven bubble development. The particle horizontal

motion in the bottom section is quite different from that observed in the vertical map, as seen in Figure 4.3b. Particles are more active around the centre of the cross-section but have little horizontal movement near the bed wall. The solid velocity profile of this pattern does not change much at a higher bed level. At the bed height between 60 and 100 mm, particles move slowly in the centre of the vortex. Above this height (Figure 4.4a), the up-flow stream of particles moves slightly inwards from the bed wall to the centre with higher velocities. When the bed height is above 110 mm, particles are close to the splash zone, and the horizontal motion of particles becomes dominant, as seen in Figure 4.4b. Since particles are mainly carried up due to rising bubbles, this pattern indicates that bubbles are unevenly distributed in the pattern A. Bubbles mainly rise along one side of bed and move gradually inwards to the centre with increasing rise velocities and bubble sizes.

Pattern A has been considered to a poor solid flow structure where particles undergo a large circulation vortex within the bed, and there is a large dead zone at the bottom corner of the bed. In addition, the particle motion is not uniform in either a vertical direction or a horizontal direction within the entire bed, which offers poor gas and solid contact and mixing behaviour in pattern A.

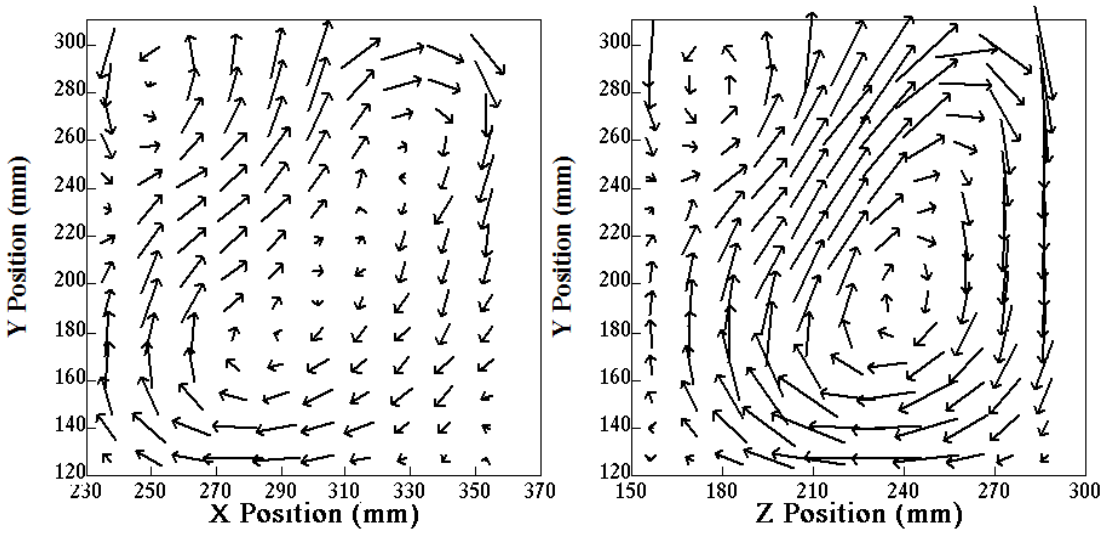

Figure 4.2 Solid flow pattern A.

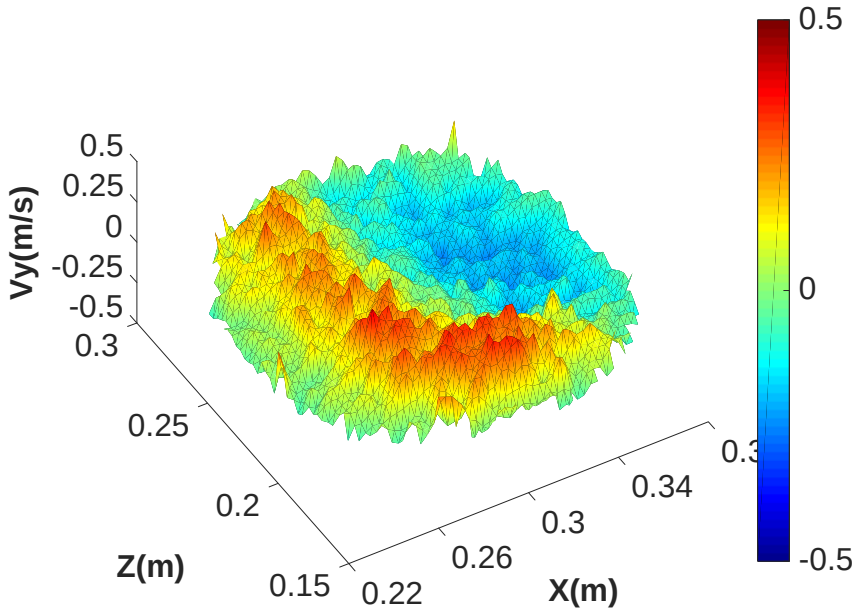

(a)

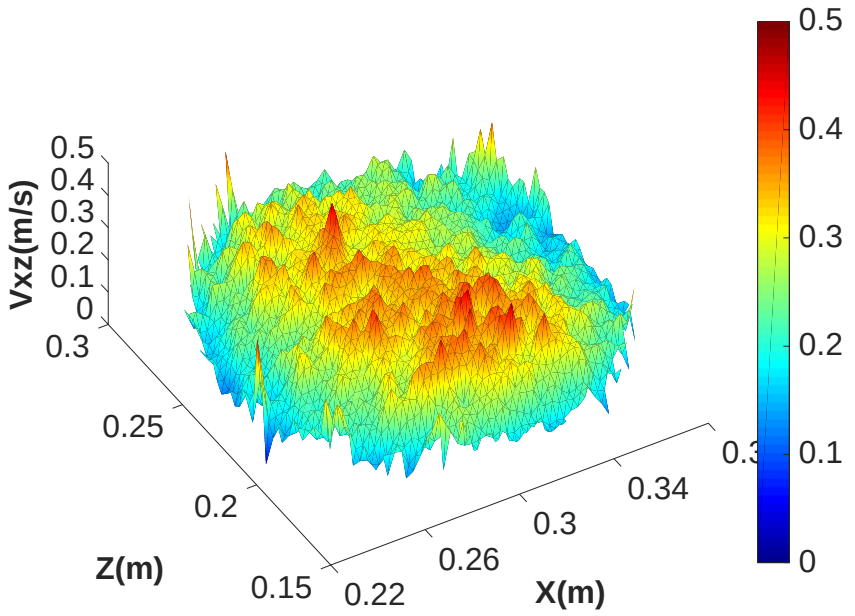

(b)

Figure 4.3 Particle velocity map of pattern A in a layer 35 mm above the air distributor: a) vertical direction; b) horizontal direction.

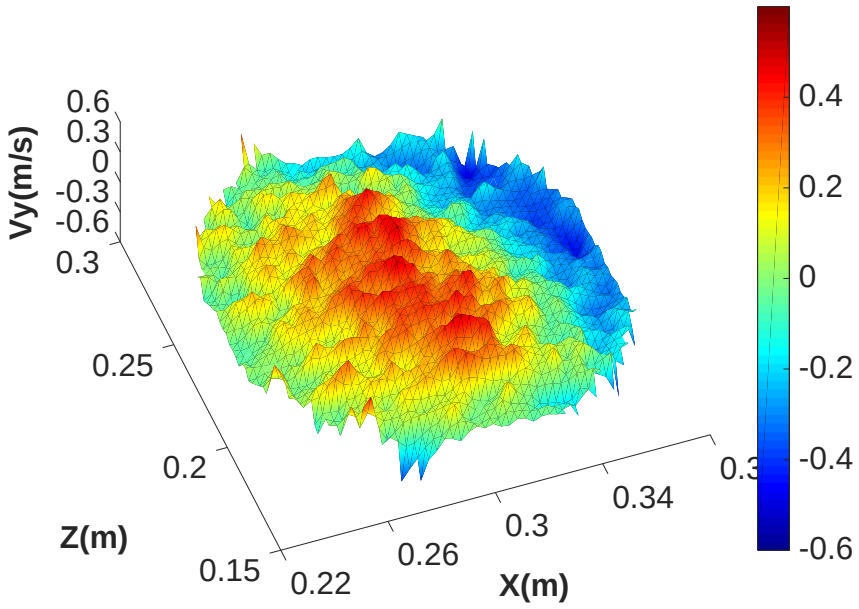

(a)

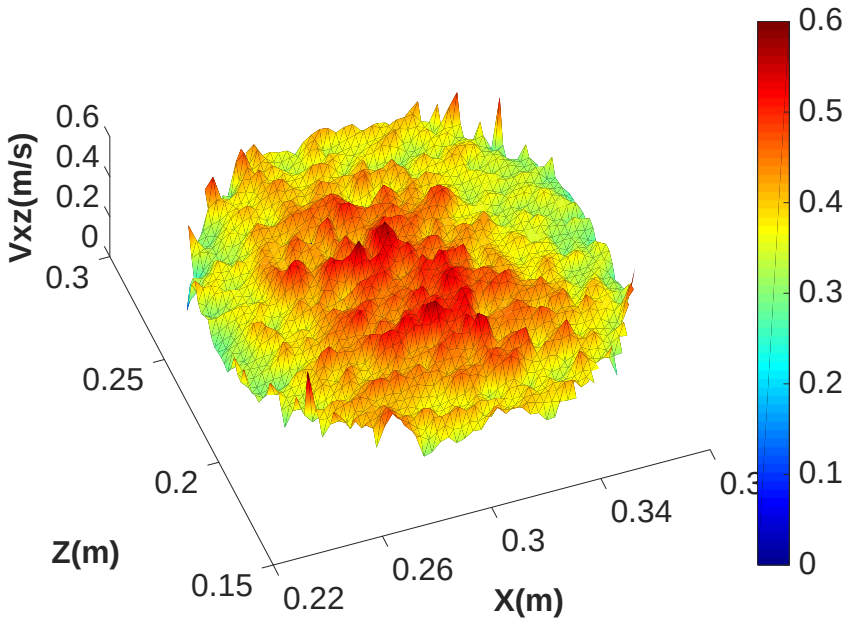

(b)

Figure 4.4 Particle velocity map of pattern A in a layer 110 mm above the air distributor: a) vertical direction; b) horizontal direction.

Figure 4.5 shows the PEPT particle velocity map from the view of the x-y plane and z-y plane for pattern B. It can be seen that at the bottom of the bed, particles move at a slow but uniform velocity. This indicates a uniform gas distribution at the bottom of the bed. At a higher level of the bed, particles moved upwards along the centre axis with increasing velocities, and descend along the bed wall forming two vortexes in the top section of the bed. Figure 4.6 shows the particle vertical and horizontal velocity maps in the layer 35 mm above the air distributor for pattern B. A uniform vertical velocity profile can be seen in Figure 4.6a, which indicates that upward moving particles and downward moving particles are uniformly distributed over the whole cross-section near the air distributor. While in the horizontal direction (Figure 4.6b),

particles move more vigorously around the centre of the cross-section but slowly near the bed wall. The particle horizontal movement is dominant near the air distributor. When the bed height increases to 110 mm, particles mainly move upwards along the centre of the bed with increased vertical velocities and move downwards near the bed wall (Figure 4.7a), and particles are travelling with quite uniform velocities in the horizontal direction over the whole cross-section (Figure 4.7b). Particles in the circulation vortex travel very slowly and mainly move in the horizontal direction, as seen in Figures 4.5 and 4.7.

Pattern B has been frequently reported and used to validate the modelling and simulation work in the literature [184, 248]. The uniform particle vertical velocity near the air distributor indicates a uniform distribution of gas voids over the cross-section. This generates a large contact area for solid and gas near the air distributor. At a higher level, the upward solid stream moves inwards with increasing velocities, and indicates the bubble coalesces towards the centre. The bubble size and rise velocity increase, and the bubble residence time should decrease. The efficiency for gas-solid contact and mixing is very high near the air distributor but declines at a higher bed level in pattern B.

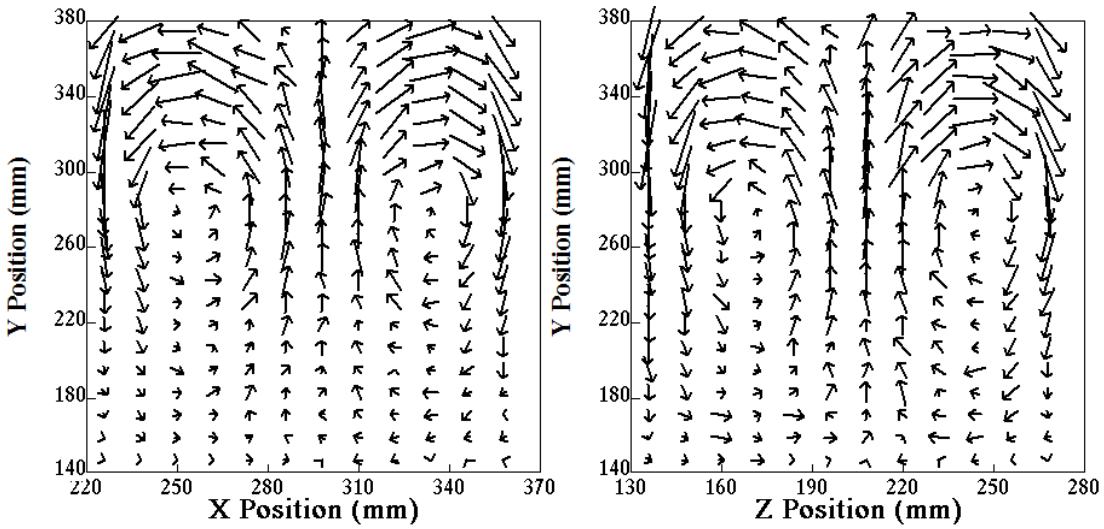

Figure 4.5 Solid flow pattern B.

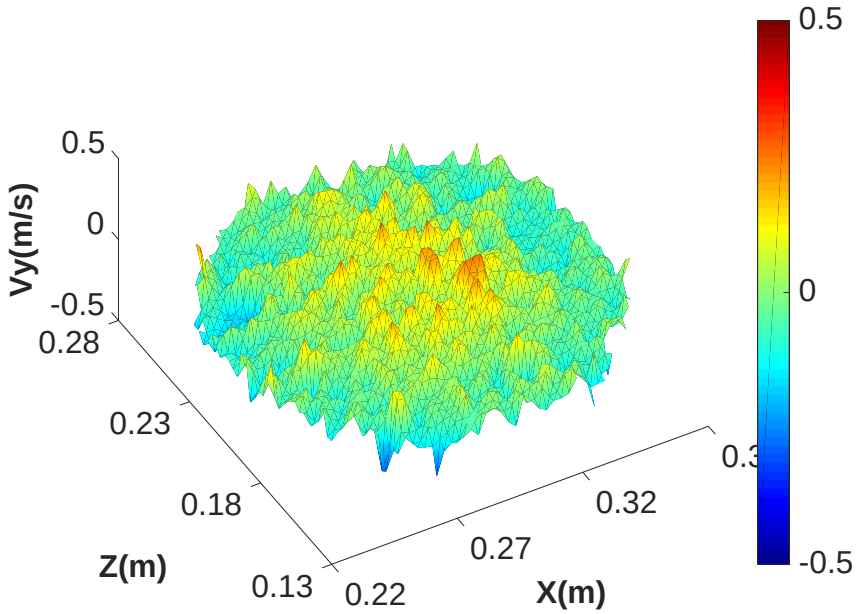

(a)

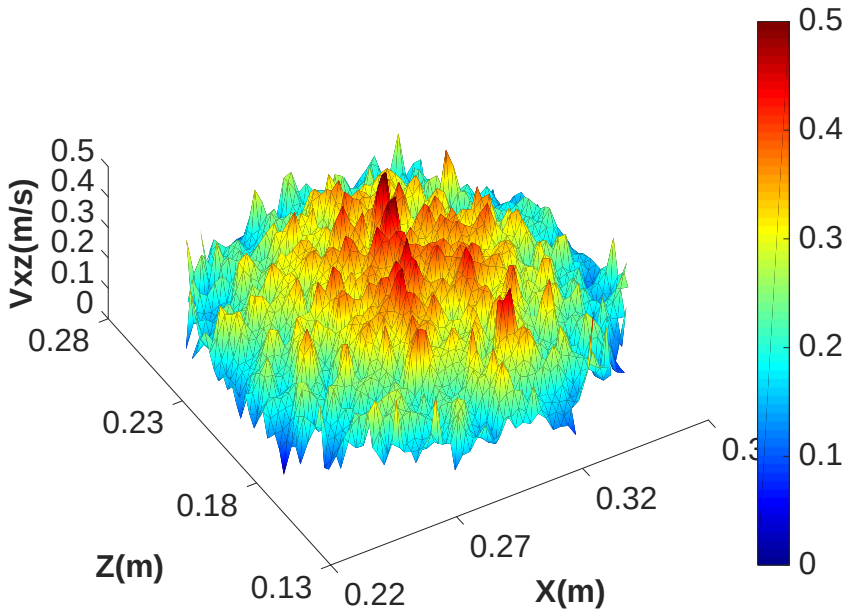

(b)

Figure 4.6 Particle velocity map of pattern B in a height of 35 mm above the air distributor: a) vertical direction; b) horizontal direction.

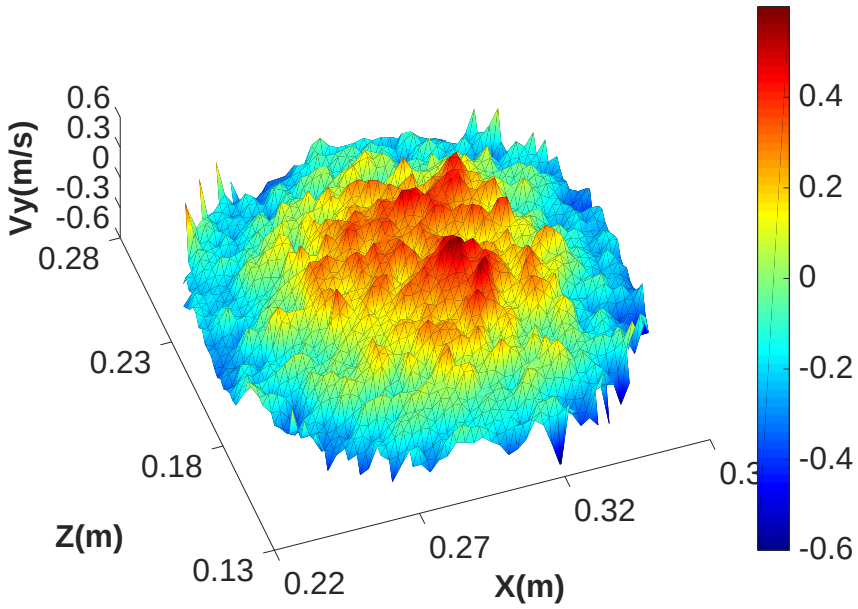

(a)

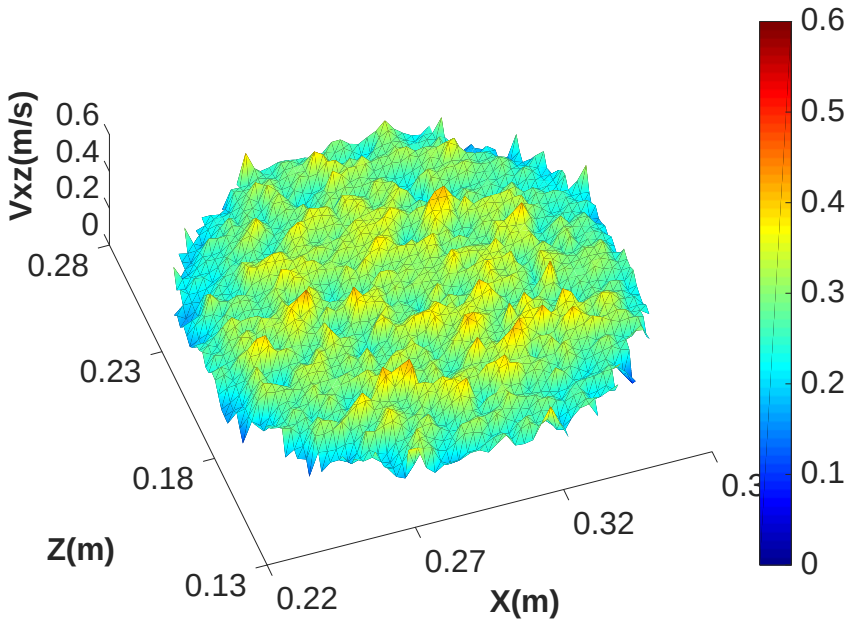

(b)

Figure 4.7 Particle velocity map of pattern B in a layer 110 mm above the air distributor: a) vertical direction; b) horizontal direction.

Figure 4.8 shows the PEPT particle velocity vector diagrams from the view of the x-y plane and z-y plane for pattern C. It can be seen that particles travel with high speeds at the bottom of the bed and in the splash zone. In the intermediate section, particles from the circulation vortexes in the top section encounter particles from the circulation vortex in the bottom section, and particles mix and move with slower but uniform velocities. A slowly descending solid stream is also seen along one side of the bed wall. Figure 4.9 gives the particle velocity maps in both vertical and horizontal directions at a layer 35 mm above the air distributor for pattern C. It can be seen from Figure 4.9a that particles have relatively uniform and small vertical velocities near the air distributor, and there is only a small area near the bed wall where particles mainly

move upwards with a slightly higher velocity. A uniform particle horizontal velocity map is also seen in Figure 4.9b, which indicates a uniform convective movement of solids in the horizontal direction, and the particle horizontal movement dominates the area near the air distributor. When the layer height increases to 110 mm above the air distributor, the area where particles mainly move upwards increases and the particles rise with higher velocities as shown in Figure 4.10a. The particle horizontal velocity maintains a uniform distribution over the cross-sectional area and dominates this layer, as shown in Figure 4.10b. When the layer height increases to 170 mm above the air distributor, the ascending flow of particles move slightly inwards to the centre (Figure 4.11a). When the bed height is above 260 mm, the ascending stream of particles moves further inwards to the centre, leaving particles near the bed wall moving downwards (Figure 4.12a), while particle horizontal velocities continue being uniformly distributed and dominate the whole cross-section (Figure 4.12b).

Overall, the fluidization performance of pattern C is better than that of pattern B and pattern A. Solid velocity in the bed majority of flow pattern C is relatively uniform and increases slowly with the bed height. There is no obvious dead zone within the bed. These indicate that air bubbles have a very uniform distribution and remain in small sizes within the bed majority of pattern C. Around the intermediate level of the bed, the solid flow structure is fairly complex. Bubbles experience splitting during their rising and rise slowly, offering a longer bubble residence time for good gas-solid contact and mixing. This is a desired solid flow pattern for good gas-solid contact and mixing as well as reaction efficiency in a fluidized bed.

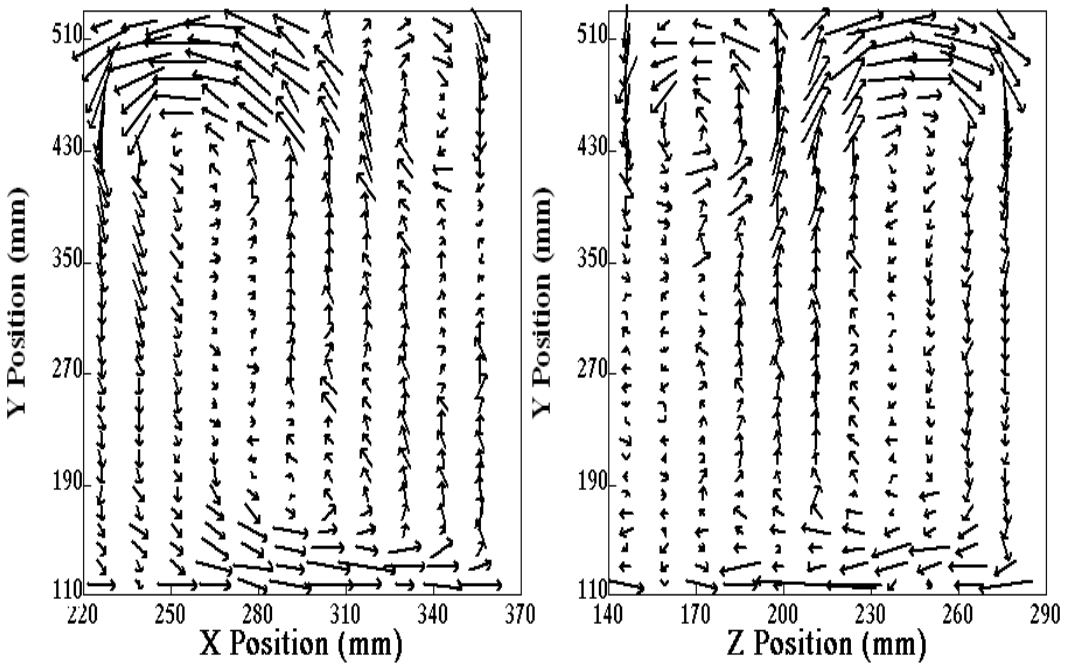

Figure 4.8 Solid flow pattern C.

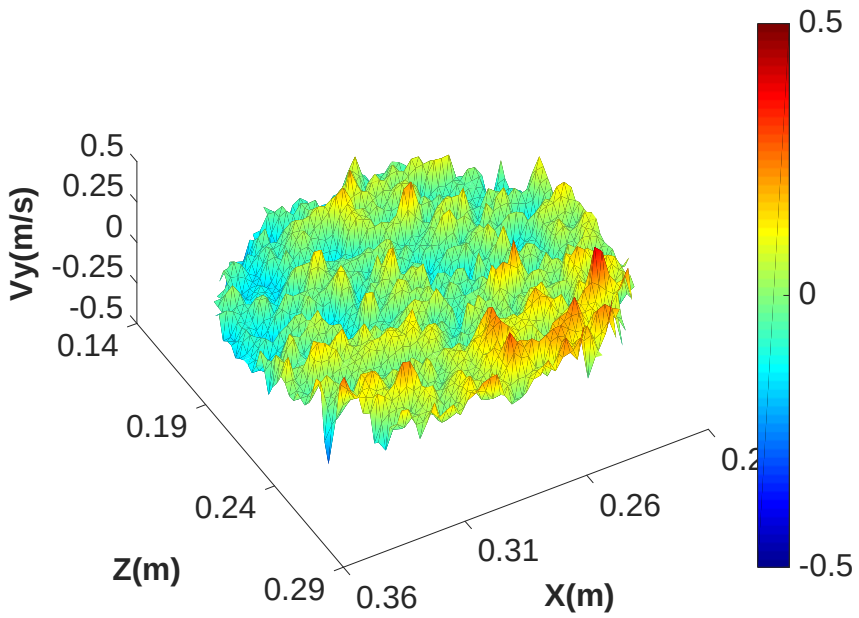

(a)

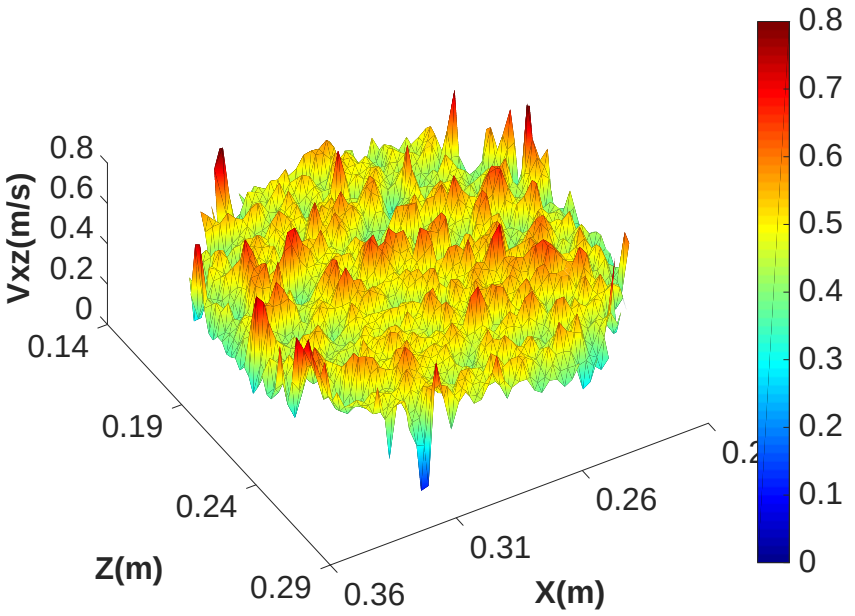

(b)

Figure 4.9 Particle velocity map of pattern C in a layer 35 mm above the air distributor: a) vertical direction; b) horizontal direction.

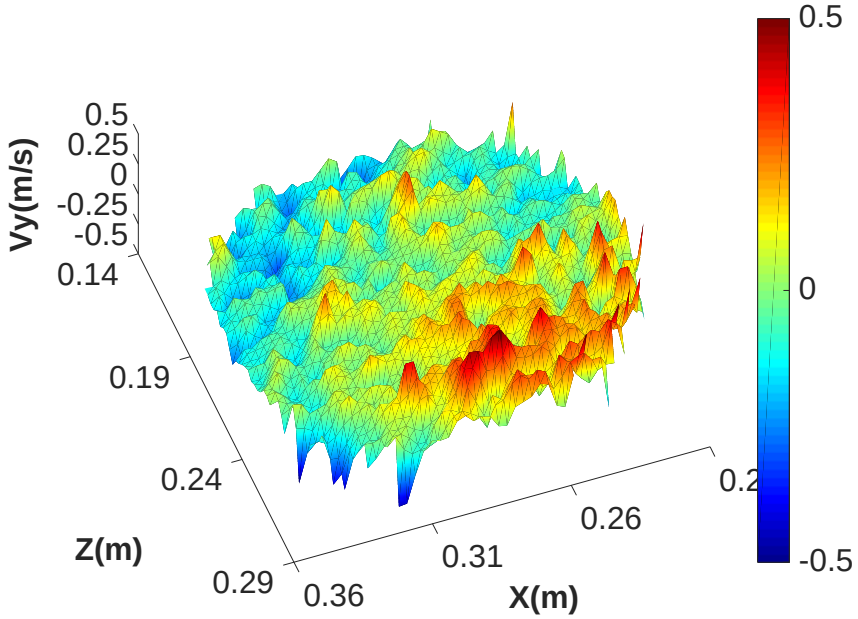

(a)

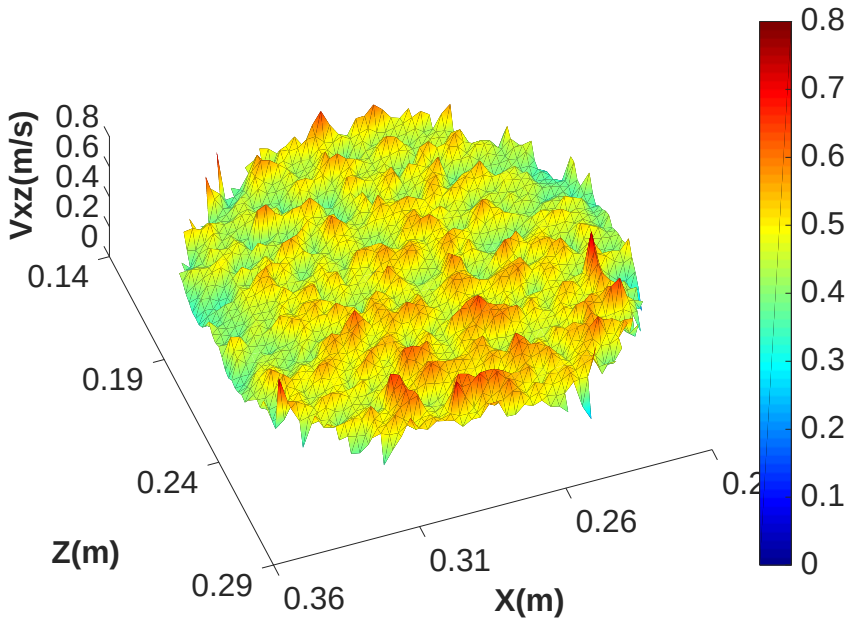

(b)

Figure 4.10 Particle velocity map of pattern C in a layer 110 mm above the air distributor: a) vertical direction; b) horizontal direction.

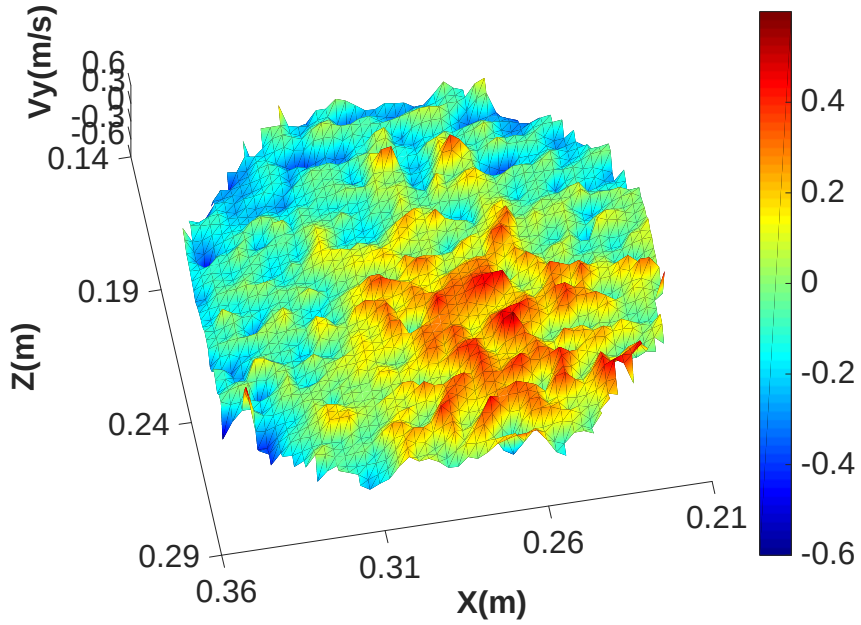

(a)

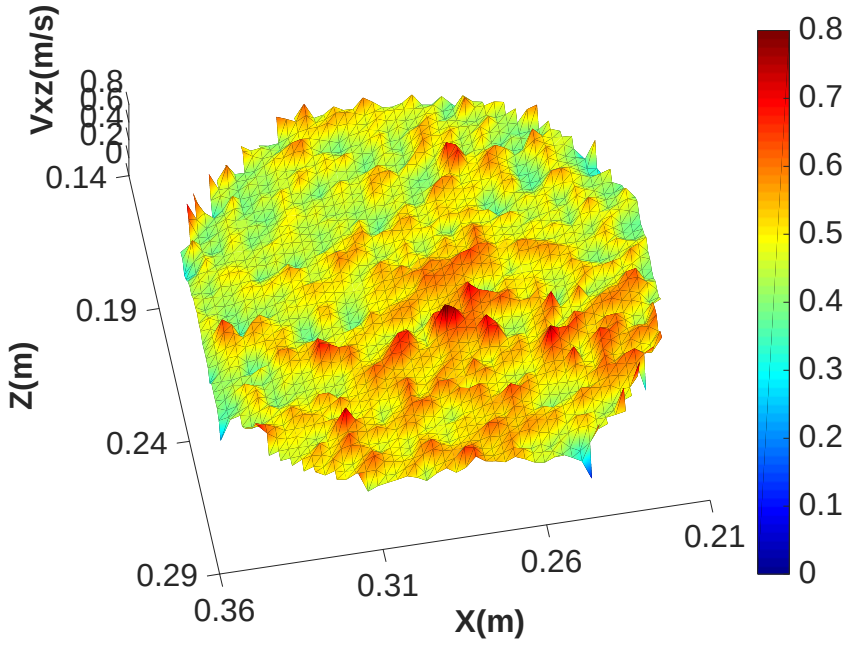

(b)

Figure 4.11 Particle velocity map of pattern C in a layer 170 mm above the air distributor: a) vertical direction; b) horizontal direction.

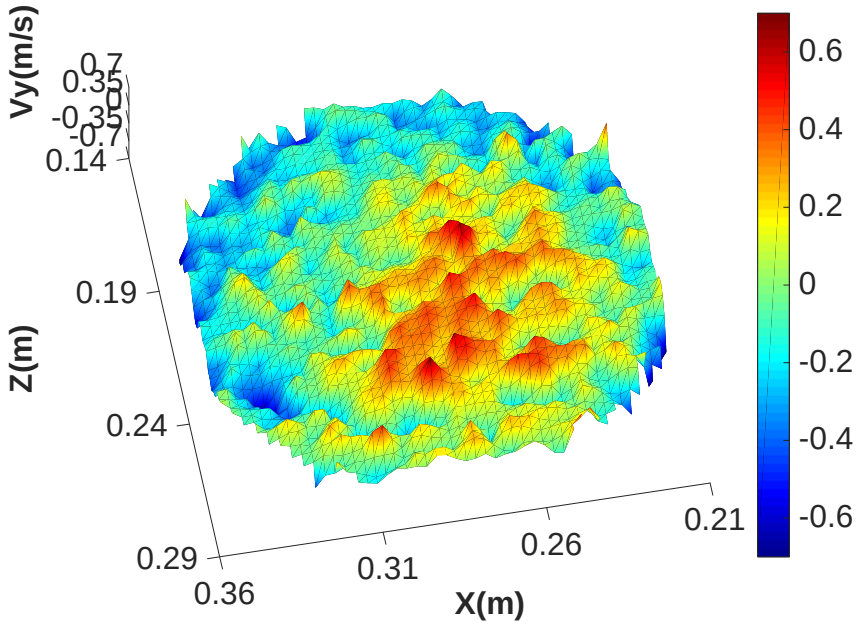

(a)

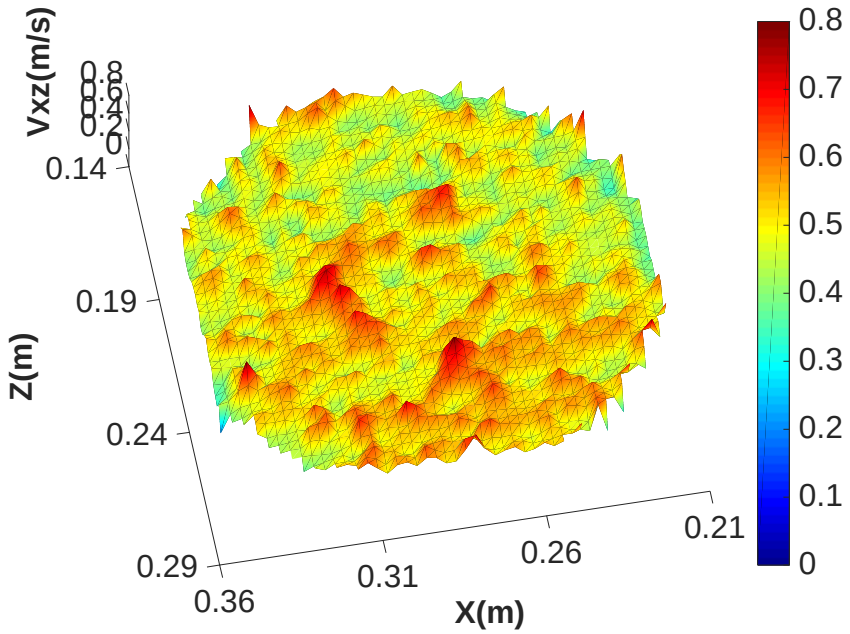

(b)

Figure 4.12 Particle velocity map of pattern C in a layer 260 mm above the air distributor: a) vertical direction; b) horizontal direction.

Figure 4.13 shows the PEPT particle velocity vector diagrams from the view of the x-y plane and z-y plane for pattern D. It can be seen that in the bottom section, particles ascend along the annulus from the air distributor. In the top section of the fluidized bed, particles from bed surface and splash zone return back to the intermediate section along the bed wall but rarely travel downwards in the centre. In the intermediate section of the bed, particles from the circulation vortexes in the bottom section encounter particles from the circulation vortexes in the top section, and particles mix and are redirected to the top and bottom sections. Figures 4.14-4.17 show the particle vertical and horizontal velocity maps in different layers (i.e., 35, 90, 140 and 170 mm above the air distributor). It can be seen that the horizontal velocity of solids is uniform

throughout the entire bed and progressively increases with the bed height (Figures 4.14b, 4.15b, 4.16b and 4.17b). The annulus structure of up-flowing particles moves gradually inwards to the centre of the cross-section with increasing bed height in the bottom section of the bed (Figures 4.14a and 4.15a). In the intermediate section, the particle vertical velocity becomes slightly slower and with uniform distribution over the cross-sectional area (Figure 4.16b), which can indicate a change in bubble properties. In the bed top section, particles mainly move upwards around the centre and downwards near the bed wall with slightly increased velocities (Figure 4.17b).

Pattern D has been considered as the most desirable flow structure among the four different flow patterns. The uniform and dominant particle horizontal velocity indicates an efficient convective mixing behaviour of solids. The solid particles participate in more different circulations within pattern D than in pattern C, B and A. The collision of the descending flow of particles from the top section with the ascending flow of particles from the bottom section push particles inwards to the bed centre and enhance the solid mixing. In addition, the collisions split bubbles into smaller sizes at the intermediate height of the bed, resulting in longer bubble residence times as well as better gas and solid contact. Although the particle collision and the downward particle flows in the main gas stream may cause some gas backmixing that reduces the process efficiency, pattern D has an overall better fluidization performance than pattern C, B and A.

The deviations between upward and downward solid fluxes within the fluidized bed were evaluated at different bed heights for the four flow patterns in order to assess the

reliability of the method. It was calculated by first finding the number of upward particles as well as the number of downward particles within the same layer and then obtaining the deviation of these two. A smaller deviation should indicate that the tracking time is long enough and provides a higher reliability of the measurement and vice versa. The results show that the maximum and minimum deviations of the up- and down-flows in different layers are 17.6% and 0.1%, respectively, with an average error of 6.35%. This confirms that the technique is relatively reliable and the results can suitably represent the general solid flows in fluidized beds.

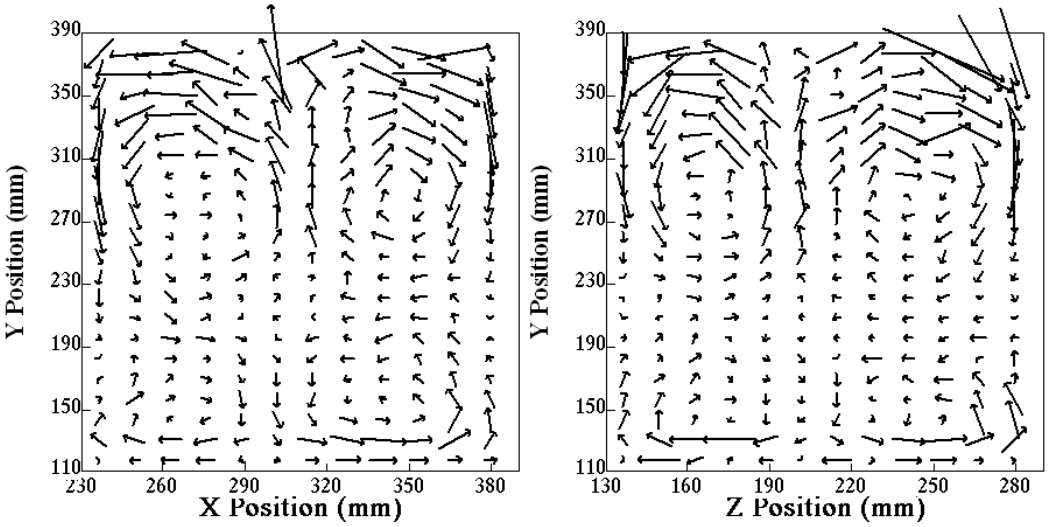

Figure 4.13 Solid flow pattern D.

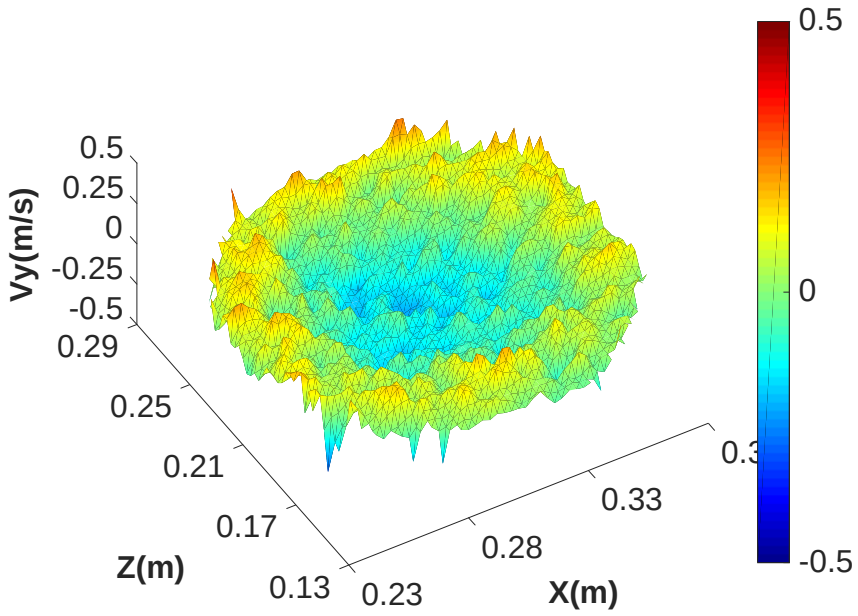

(a)

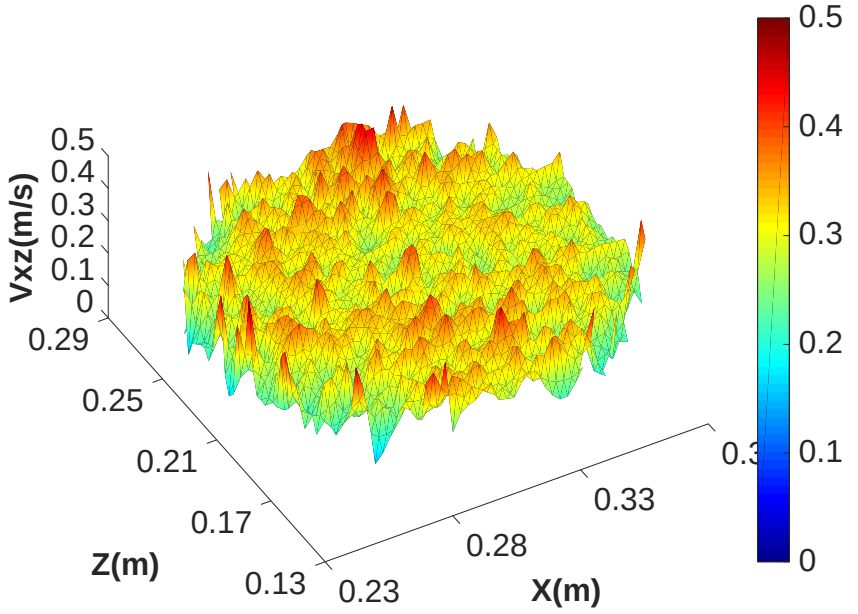

(b)

Figure 4.14 Particle velocity map of pattern D in a layer 35 mm above the air distributor: a) vertical direction; b) horizontal direction.

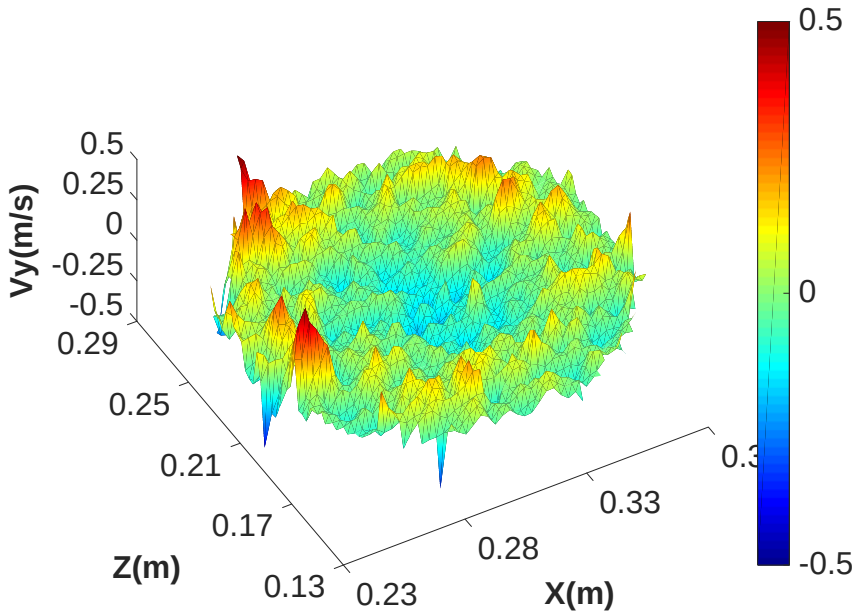

(a)

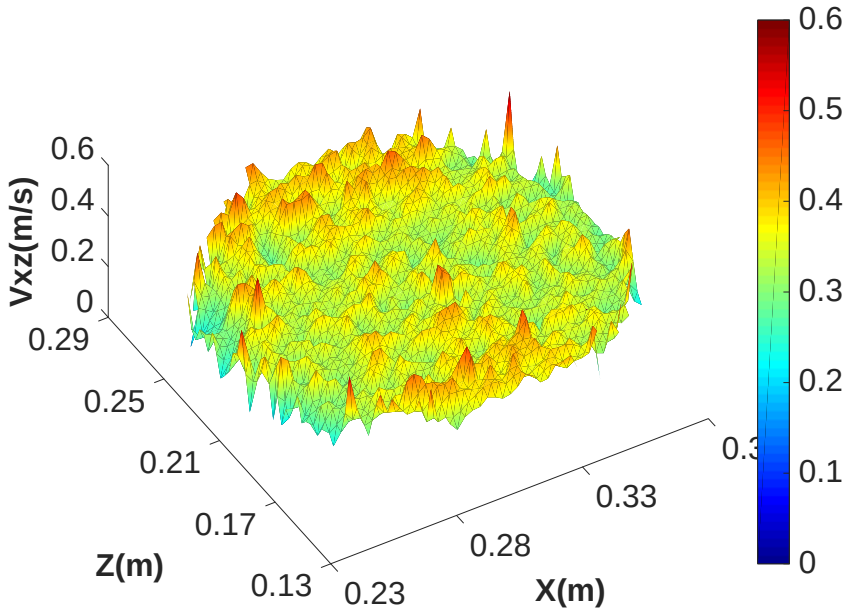

(b)

Figure 4.15 Particle velocity map of pattern D in a layer 90 mm above the air distributor: a) vertical direction; b) horizontal direction.

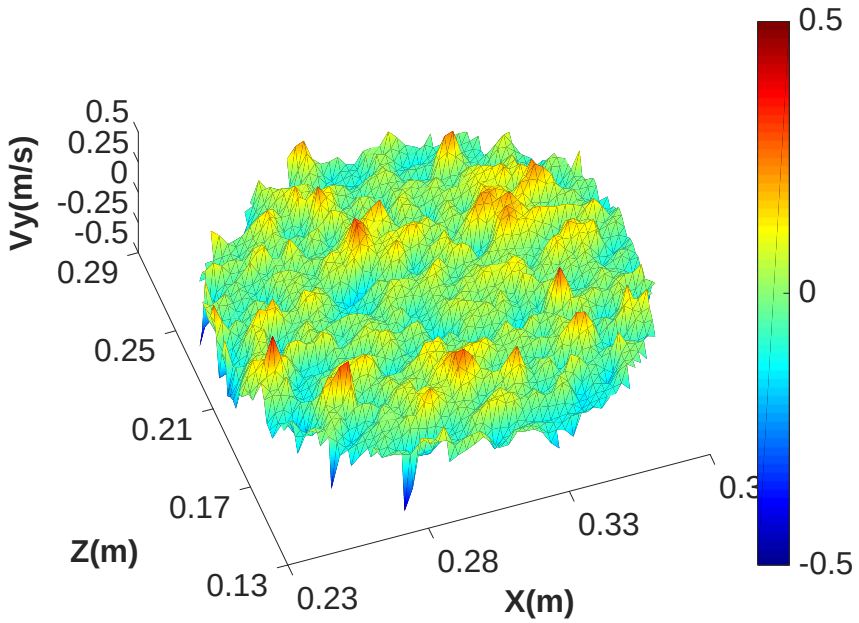

(a)

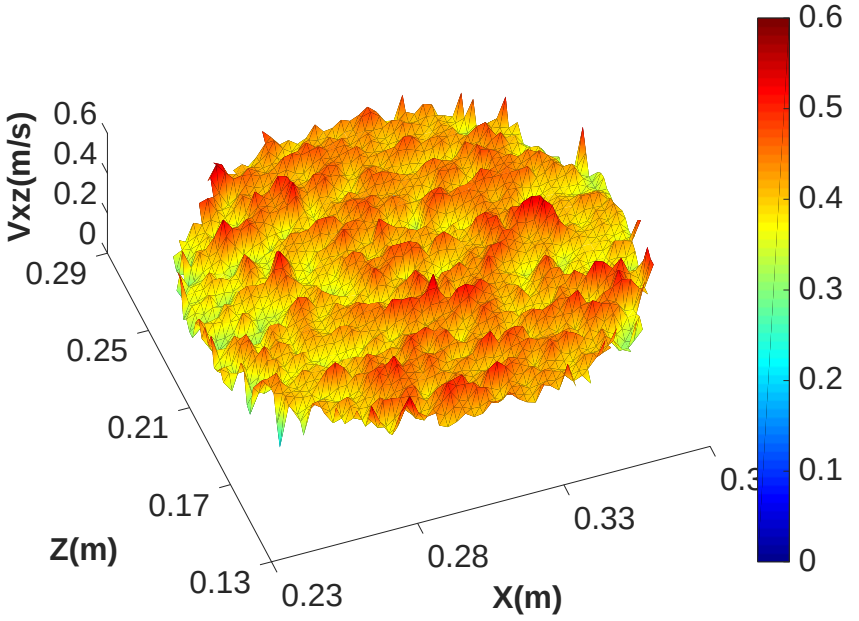

(b)

Figure 4.16 Particle velocity map of Pattern D in a layer 140 mm above the air distributor: a) vertical direction; b) horizontal direction.

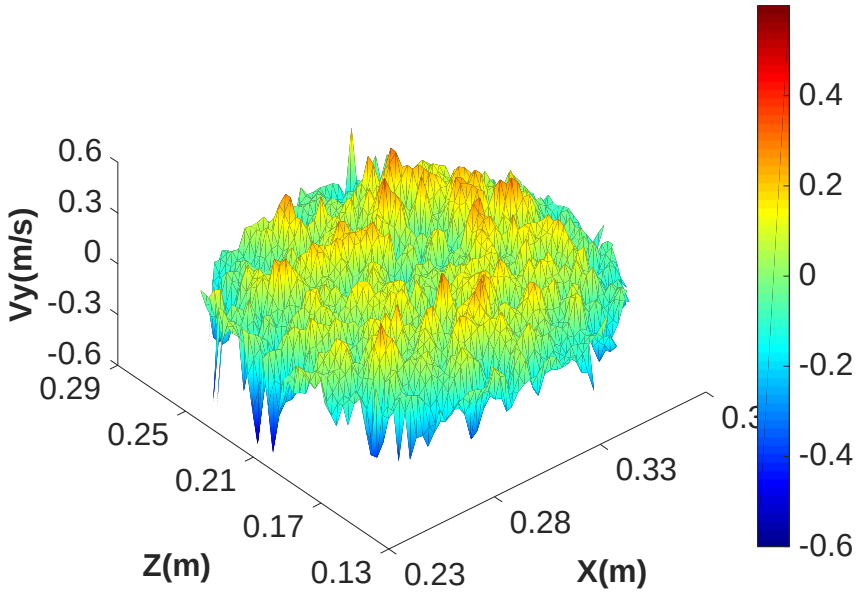

(a)

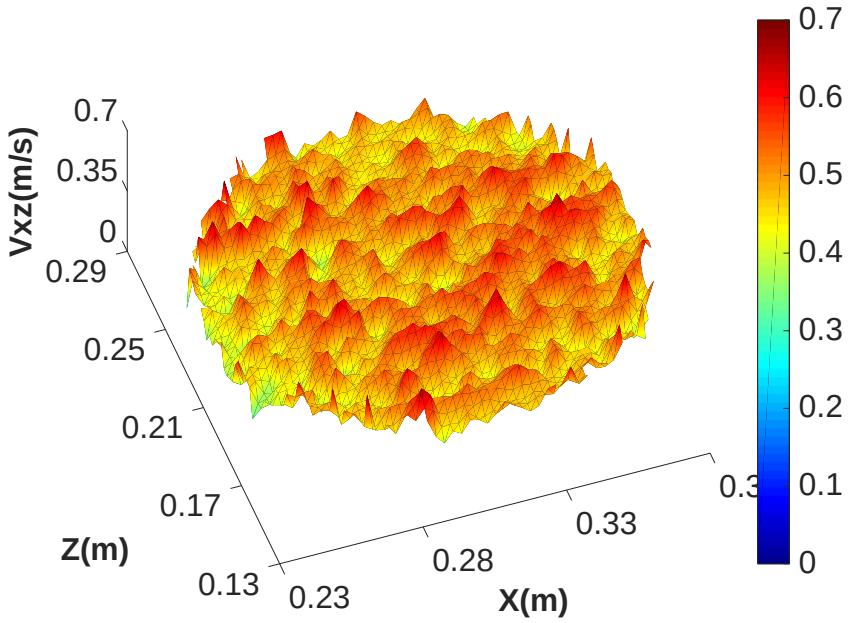

(b)

Figure 4.17 Particle velocity map of pattern D in a layer 170 mm above the air distributor: a) vertical direction; b) horizontal direction.

4.3 Microscopic Behaviour of Solids within Fluidized Beds

The trajectories of tracer particles were followed in bubbling fluidized beds using the PEPT technique under different operational conditions and bed designs. Figure 4.18 presents typical solid trajectories over a circulations cycle for pattern A-D in three planes of view as well as showing the speed of tracer particle. Figure 4.18a presents a record of tracer motion for 2 seconds in pattern A. The observation starts from point A, where the tracer particle travels up with rising bubbles all the way up to point B in the splash zone, with a speed of 400-1200 mm/s. Then the particle descends back to the bed bottom (point C), completing a large circulation vortex, and moves to point D with a speed of 100-1000 mm/s due to the solid concentration difference. At point D, the particle is picked up again by rising bubbles and flows up to point E at the bed surface with a speed of 100-1200 mm/s to start a new circulation. This large solid circulation vortex in vertical planes (i.e., x-y and y-z) has been observed many times over the full tracking of data in pattern A, indicates that the solid microscopic behaviour agrees well with the solid overall flow of pattern A (Figure 4.2). When the tracer particle circulates along the large vortex, it not only travels in the vertical planes but also migrates in the lateral plane as seen in the x-z plane of view in Figure 4.18a. It can be seen that the displacement in the lateral plane is large in the solid ascending path but much smaller in the solid descending path. This is due to the fact that solid lateral displacement occurs in the following circumstances: I) when particles that near a bubble are transported into the drift of the bubble as if spouts; II) when particles are ejected into the splash zone by bubble eruptions and III) due to bubble lateral motions (i.e., a consequence of interaction and coalescence between adjacent bubbles) [2, 190,

191, 193-195]. While in the solid descending path, the lateral displacement of solids only happens due to solid eddies induced by passing bubbles [5, 196, 197].

Figure 4.18b presents a record of tracer motion over 3 seconds in pattern B. The solid circulation is different from that in Figure 4.18a (pattern A). In the observation, the particle travels up by rising bubbles from point A to point B at the bed surface along the central axis with a speed of 400-1000 mm/s. The particle then moves downwards to point C due to solid concentration difference and generates a circulation vortex at the centre left of the bed in the x-y plane of view. Subsequently, the particle further descends to the bed bottom and moves around point D within a small area due to solid concentration differences until it is picked up by bubbles and moves upward with bubbles along the centre all the way up to the bed splash zone (point E). At point E, the particle starts descending to the bed bottom (point F) near the bed wall with a speed of 100-1200 mm/s, completing a large circulation vortex in right part of the bed in the x-y plane. The solid microscopic behaviour in pattern B agrees well with the overall solid flow pattern in pattern B (Figure 4.5).

Figure 4.18c presents a record of tracer motion over 6 seconds in pattern C. Three solid circulation vortexes can be seen over the 6-second record from the x-y vertical plane, where two vortexes appear in the top section of the bed, along with one in the bed bottom. The observation starts from point A where the particle starts to descend in a rather tortuous manner to the bed bottom (point B) with a speed of up to 1200 mm/s. At point B, the particle is picked up by rising bubbles and flows to point C in the splash zone with a speed up to 1600 mm/s. This completes a solid circulation in the top left

vortex within the bed and starts the solid circulation in the top right vortex. The particle then descends from point C to an intermediate height of the bed at point D and completes a circulation in top right vortex. At point D, the particle is redistributed and moves around before it flows downwards to the bed bottom (point E) and subsequently moves to point F. From point F, the particle starts an ascending flow with rising bubbles to the bed centre (point G), generating a small solid circulation vortex in the bottom section. The particle undergoes three main circulations. In pattern C, particles from the top section and bottom section of the bed encounter each other at around the centre of the bed and are redirected into different circulation vortexes.

The solid dynamic behaviour in pattern D changes significantly. Figure 4.18d shows a record of tracer motion over 4 seconds in pattern D. It can be seen that there are four solid circulation vortexes in the x-y vertical plane (i.e., vortex A-B-C-D, D-E-F, F-G-H, and H-I-J-K). These four solid circulation vortexes have been observed many times over the full particle trajectory data, and the only difference among every observation is that the particle flows into any of these four circulation vortexes randomly after it has been redirected at the intermediate height of the bed. The observation starts from point A at the intermediate level of the bed, where the particle flows downwards to point B near the bed wall and is picked upwards by rising bubbles to point C with a speed of up to 400 mm/s. The particle then moves to the bed centre (point D) and generates the bottom left solid circulation vortex. At point D, the particle ascends with bubbles towards the splash zone (point E), followed by a descending flow along the centre to an intermediate height at point F with a speed of up to 900 mm/s. This generates the top left solid circulation vortex. The particle at point F moves up,

following the rising bubbles around the central axis to the splash zone (point G). From point G, the particle starts moving downwards near the bed wall and traveling inwards to the bed centre at point H due to solid concentration difference. The particle travels with a speed up to 1000 mm/s during this journey and generates the top right solid circulation vortex. Subsequently, the particle at point H starts to moves outwards to point I near the bed wall due to solid concentration difference and returns back to the bed bottom (point J) before it is picked up again by rising bubbles to the bed centre (point K). This generates the bottom right solid circulation vortex in pattern D. The particle at point K is mixed and moves around until the particle travels downwards to the bed bottom and moves towards the left bed wall in the x-y plane, beginning a new circulation. In this flow pattern, solids undergo many circulations at the top and bottom regions, and the mixing efficiency is very high at the intermediate level of the bed due to the collision of different vortexes. This would suggest that the efficiency of the mass and heat transfer should be much better in fluidized beds of pattern D.

Overall, the motion of particles in fluidized beds is not random and follows specific patterns. The solid microscopic behaviour of each flow pattern agrees very well with overall solid flow patterns.

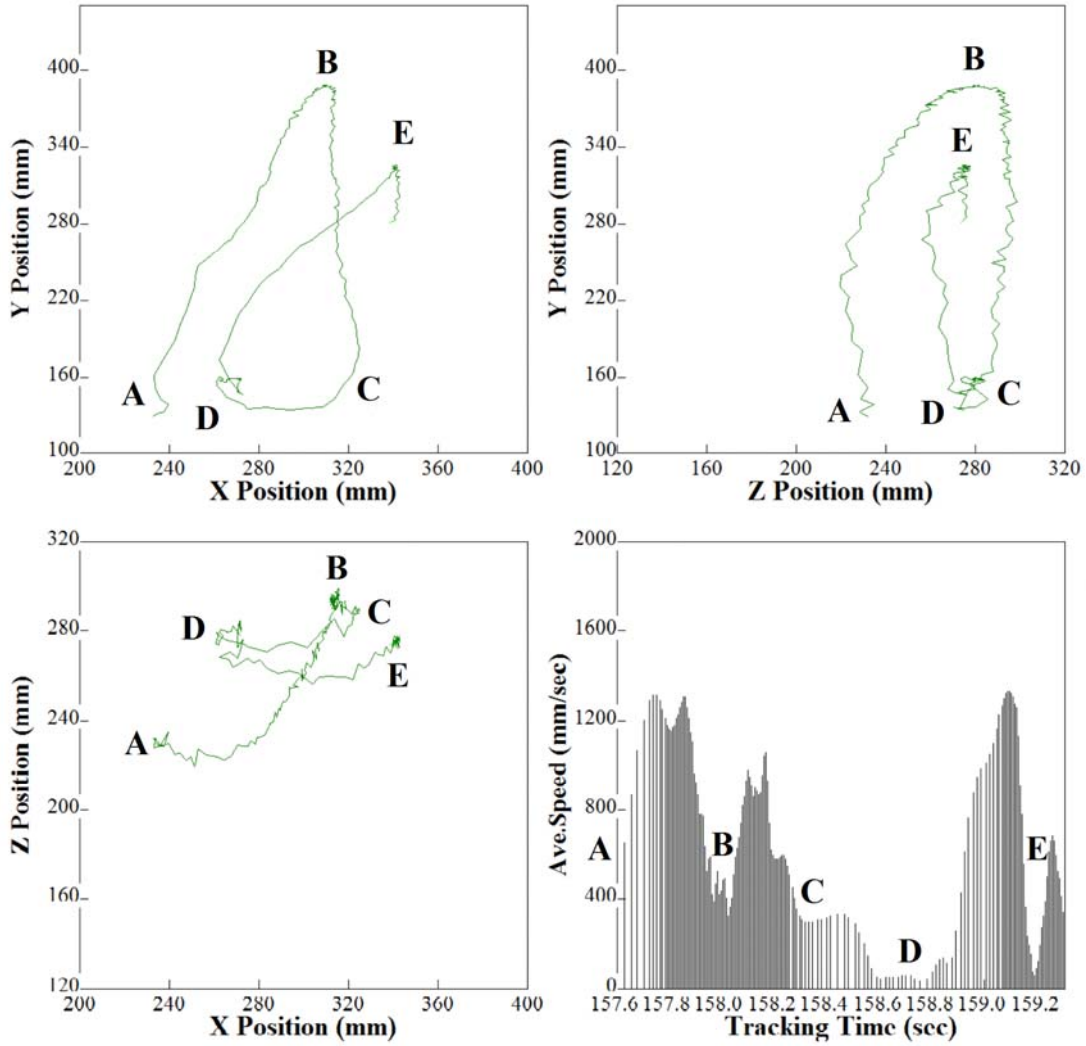
Y Position (mm)
X Position (mm)
Z Position (mm)
Ave.Speed (mm/sec)
Tracking Time (sec)
A
B
C
D
E

(a)

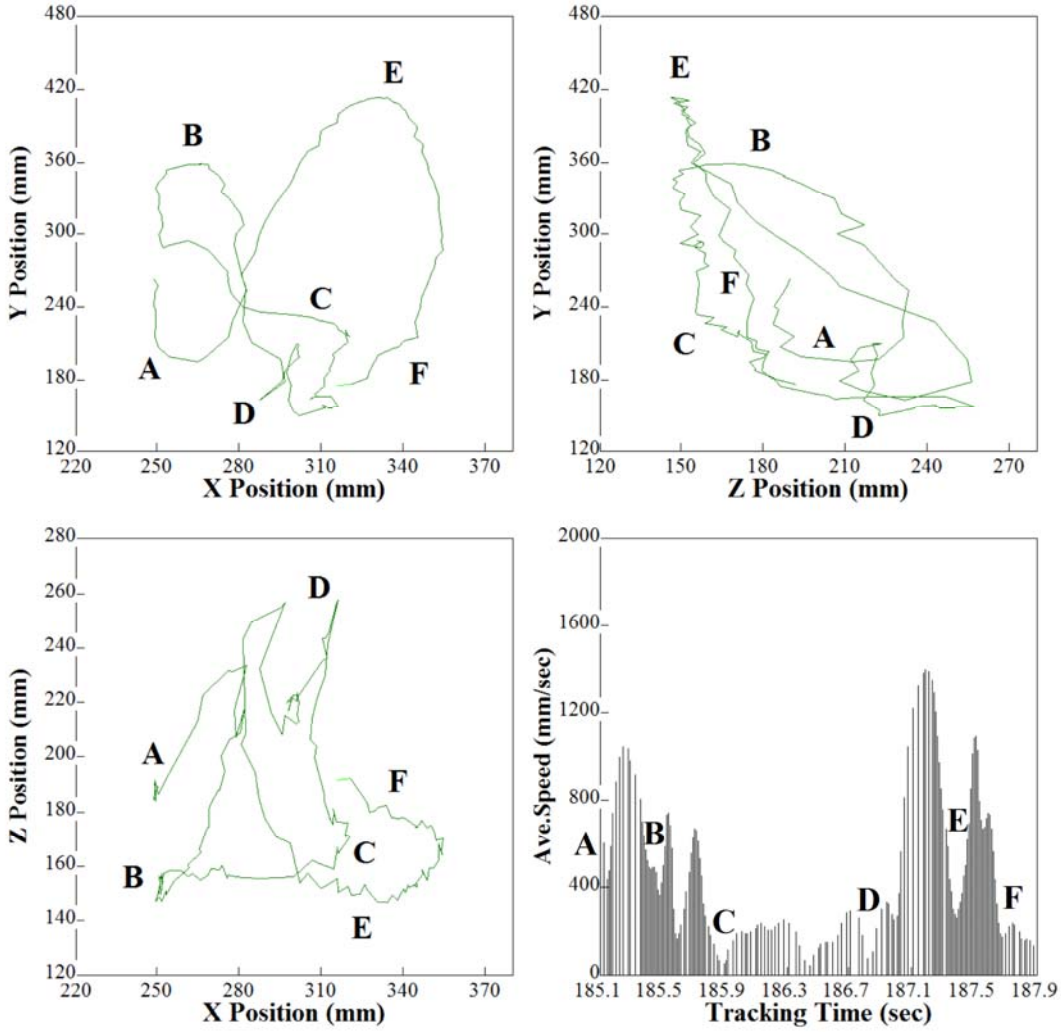
Y Position (mm)
X Position (mm)
Y Position (mm)
Z Position (mm)
Z Position (mm)
X Position (mm)
Ave.Speed (mm/sec)
Tracking Time (sec)
A
B
C
D
E
F

(b)

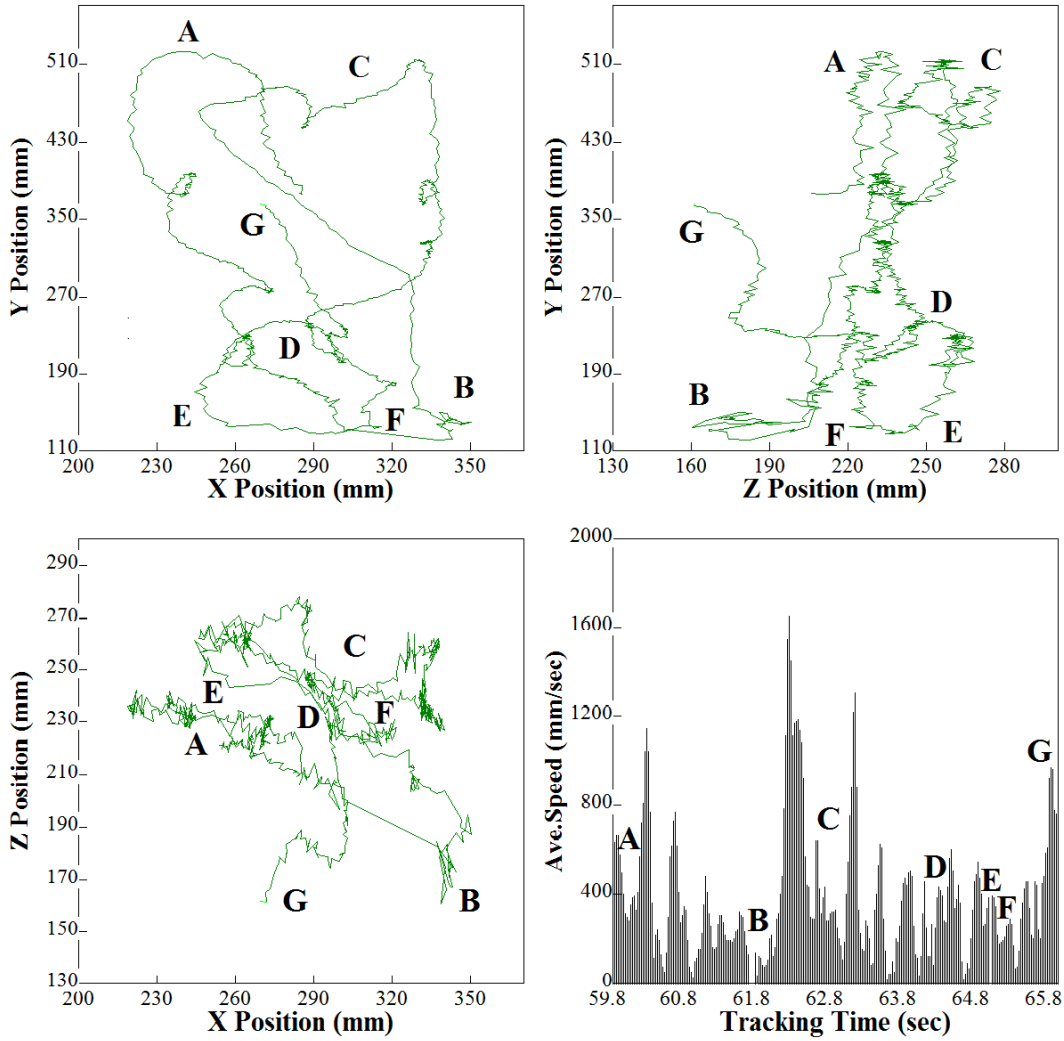
Y Position (mm)
X Position (mm)
Z Position (mm)
Ave.Speed (mm/sec)
Tracking Time (sec)
A
B
C
D
E
F
G

(c)

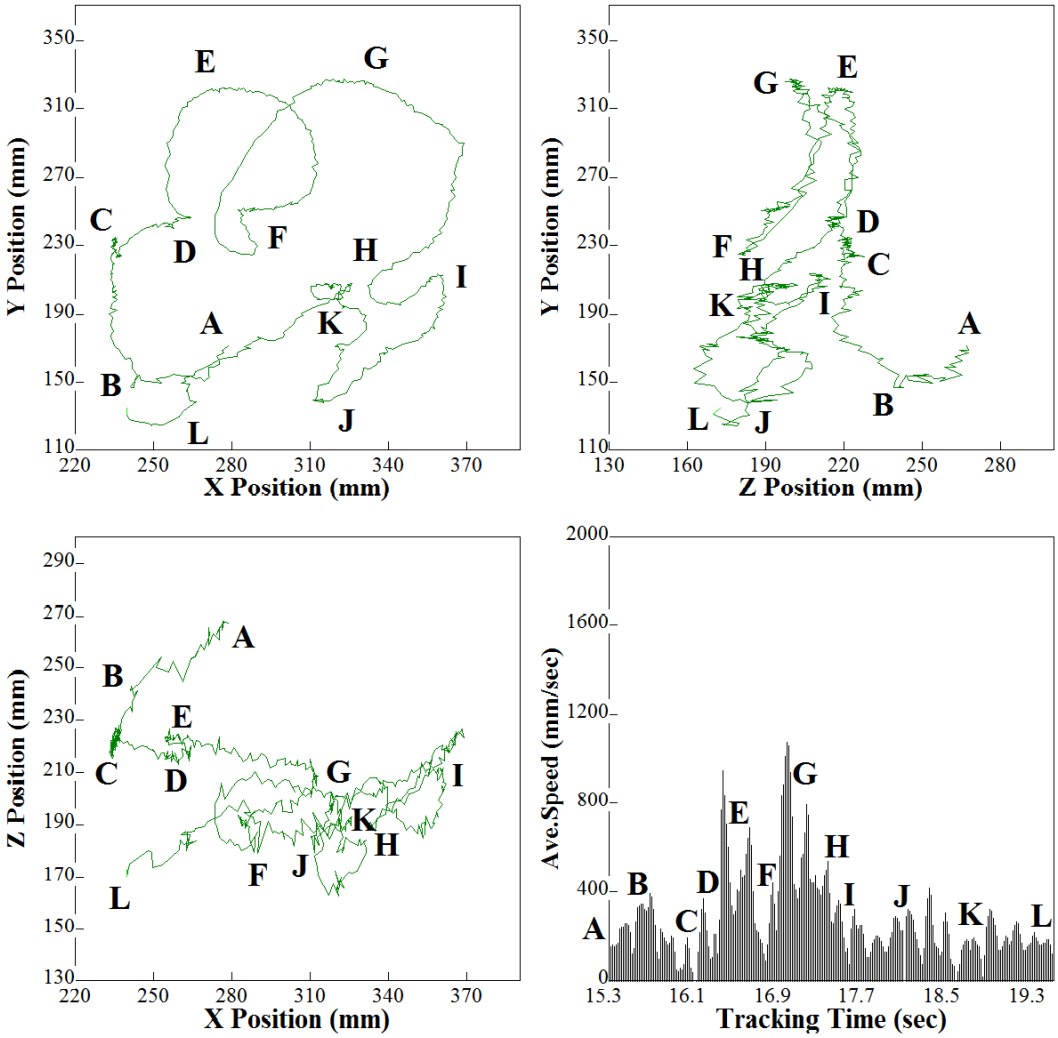

(d)

Figure 4.18 Trajectory of a tracer particle measured by the PEPT technique: a) pattern A; b) pattern B; c) pattern C; d) pattern D.

4.4 Effects of Solid Properties, Operational Conditions and Bed Aspect Ratios on Solid Flow Patterns

Solid flow patterns are dominated by various factors, such as solid properties, superficial gas velocities, the pore size of the air distributor and H/D. Different operational conditions and bed designs will generate different flow patterns, and each flow pattern (i.e., pattern A-D) is a result of a combination of these factors. Generally, pattern A was observed in fluidized beds of 200-450 μm glass beads when the pore size of the air distributor was larger than 60 μm and the superficial gas velocity was lower than 0.49 m/s. Pattern B was observed in both 200-450 μm glass beads beds and 50-200 μm silica sand beds. In the glass beads bed, pattern B was observed when the pore size of the air distributor was larger than 60 μm and the superficial gas velocity was higher than 0.49 m/s; meanwhile, in the silica sand bed, the pattern was observed when the superficial gas velocity was equal or lower than 0.22 m/s. Pattern C was observed when the pore size of the air distributor was between 15 and 60 μm in glass bead fluidized beds and when the H/D was more than 1.5 units and the superficial gas velocity was between 0.22 m/s and 0.4 m/s in silica sand fluidized beds. Pattern D was observed when the pore size of the air distributor was smaller than 15 μm in glass bead beds and when the H/D was low or the superficial gas velocity was high in silica sand beds.

In order to understand the effects of various factors on the solid flow structure, the influences of bed geometry and operational conditions have been investigated. Figures 4.19-4.20 present the flow pattern maps in terms of the pore size of the air distributor,

bed material properties, H/D and superficial gas velocity. It can be seen from Figure 4.19 that, in fluidized beds of glass beads with a mean size of 352 μm, the pore size of the air distributor and superficial gas velocity have significant effects on the solid flow structure. A decreased pore size of the air distributor gives a more uniform solid flow structure and vice versa. An increase in the superficial gas velocity within a certain range will generate a better solid flow pattern. In addition, an increase in the H/D may result in a large intermediate section of the bed where bubbles split and have a relatively uniform size and solids move in a relatively uniform velocity. The intensification of particle to particle and particle to bubble interaction increases, thereby providing better solid-gas contact and mixing [71, 76]. However, the effects are different for silica-sand fluidized beds. Figure 4.20 presents the effects of H/D and superficial gas velocities on the solid flow pattern in silica-sand beds. It can be seen that an increase in the superficial gas velocity will generate a more uniform flow structure and vice versa, while an increase in the H/D within a certain range will results in a poorer solid flow pattern.

It is also worth clarifying that, besides the four main flow patterns (i.e., patterns A-D), some transitional solid flow patterns have also been observed during the experiments. In a transitional flow pattern, solid circulation patterns are very different in the x-y plane and y-z plane. For example, an A-B transition pattern is a solid flow structure that behaves like a pattern B in the x-y plane but like a pattern A in the z-y plane, as seen in Figure 4.21a. An A-C transitional pattern presents as a pattern A in the x-y plane but as a pattern C in the z-y plane (Figure 4.21b). A C-D transitional pattern shows a pattern D in the x-y plane but a pattern C in the z-y plane (Figure 4.21c). After

investigating solid velocities in both vertical and horizontal directions and the solid microscopic behaviour of these transitional flow patterns, it has been considered that A-B transition patterns can be classified as pattern B, A-C transition patterns can be classified as pattern C, and C-D transition patterns can be classified as pattern D.

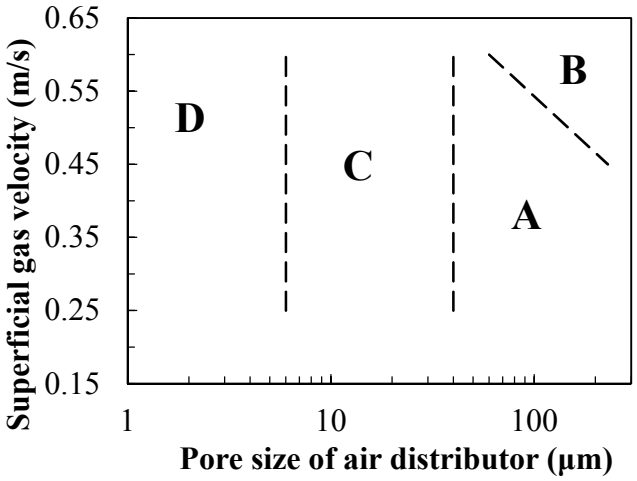

Figure 4.19 Effects of air distributors and superficial gas velocities on the solid flow pattern in small glass bead beds.

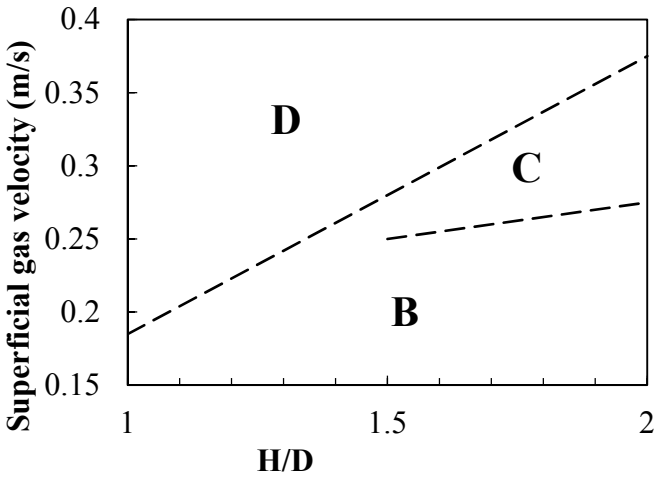

Figure 4.20 Effect of bed aspect ratios and superficial gas velocities on the solid flow pattern in silica-sand beds.

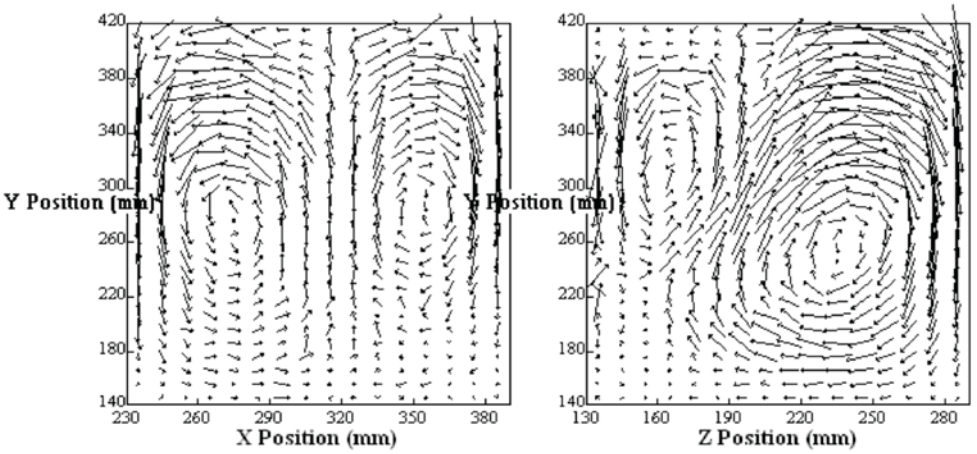

a) A-B transitional pattern

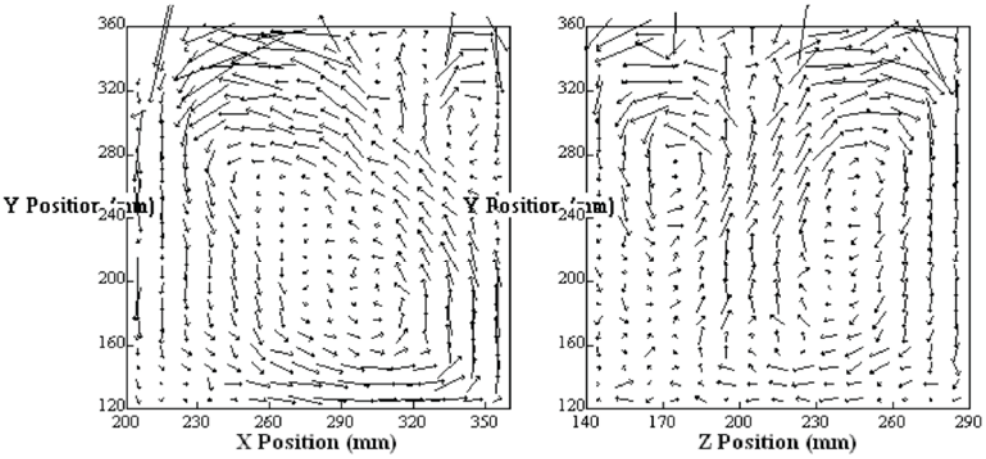

b) A-C transitional pattern

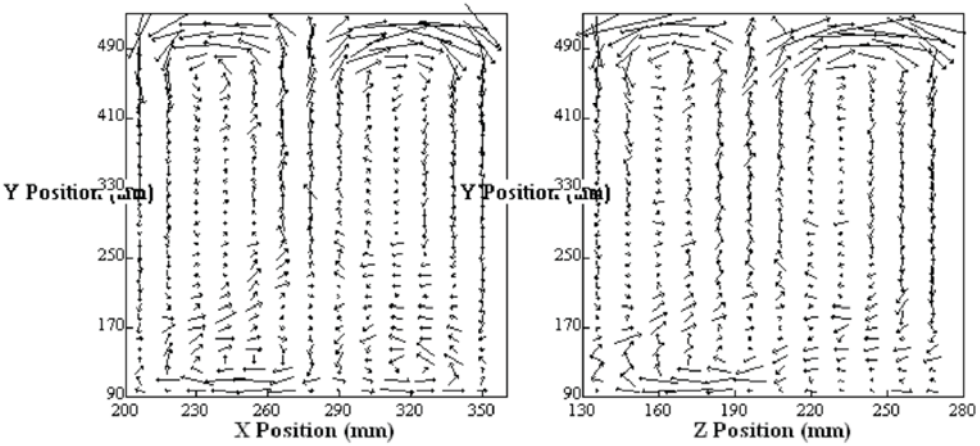

c) C-D transitional pattern

Figure 4.21 Transitional flow patterns: a) A-B; b) A-C; c) C-D.

4.5 Identifying Solid Flow Patterns

The results measured by the PEPT technique have shown that the solid flow structure in a bubbling fluidized bed is controlled by the superficial gas velocity, the H/D, the pore size of the air distributor and the particle properties. Each flow structure is the result of a combination of various factors. In this section, attempts are made to identify the solid flow patterns in 3-D bubbling fluidized beds based on operational conditions, bed design and particle velocities.

In order to determine the conditions under which different flow patterns will be generated, a number of PEPT experiments have been conducted to analyse the effects of superficial gas velocity, H/D and the pore size of the air distributors on flow patterns. The experimental results are then classified into 4 groups based on their flow pattern. Investigations start from calculating the kinetic energy of particles within the fluidized bed, because the particle kinetic energy has been considered to be an important parameter that relates to the solid flow structures, particularly at the bottom section of the fluidized bed. Figure 4.22 shows how the kinetic energy per unit mass (v^2) of glass bead fluidized bed varies with the height above the air distributor. Different solid flow patterns are illustrated using different colours; however, it is difficult to separate different patterns, which indicates that the particle kinetic energy is not the only parameter that affects the solid flow structures. The solid flow patterns cannot be classified based only on the differences in the particle kinetic energy. In order to identify certain solid flow patterns for the fluidized beds of Geldart B particles, an 'Flow Pattern Parameter (FPP)' has been proposed based on the PEPT measurement.

The FPP takes the particle kinetic energy, minimum fluidization velocity, superficial gas velocity, the pore size of the air distributor and the H/D into account. The form of the FPP is given below as,

$$FPP = \frac{H}{D} \cdot \sqrt{\frac{v^2}{d_o^4 \times \left(u - u_{mf}\right)^2}} = \frac{H}{D} \cdot \frac{|v|}{d_o^2 \times \left(u - u_{mf}\right)} \ (1/\text{mm}^2) \qquad (4.1)$$

Where H is the height of fixed bed (mm), D is the bed diameter (mm), v is the particle speed (mm/s), d_o is the pore diameter of air distributor (mm), u is the superficial gas velocity (mm/s) and u_{mf} is the minimum fluidization velocity (mm/s).

The FPP has been calculated based on all experimental data carried out in fluidized beds of glass beads. Figure 4.23 shows the relationship between the FPP value and the solid flow patterns for the fluidized bed of glass beads, and it shows that the solid flow patterns can be clearly separated via the FPP, where each flow pattern falls into a specific FPP range. Pattern B can be found when the FPP is greater than 10 but less than 50 ($1/\text{mm}^2$). Pattern A can be found when the FPP is between 20 ($1/\text{mm}^2$) and 2×10^3 ($1/\text{mm}^2$). Pattern C can be found when the FPP is between 3×10^3 ($1/\text{mm}^2$) and 6×10^4 ($1/\text{mm}^2$), in which A-C transition pattern can be found when the FPP is between 3×10^3 ($1/\text{mm}^2$) and 2×10^4 ($1/\text{mm}^2$). Pattern D can be found when the FPP is larger than 5×10^5 but less than 6×10^6 ($1/\text{mm}^2$). It is also interesting to note that the FPP value for the A-C transitional pattern falls between the FPP value of pattern A and pattern C and is much closer to pattern C, which further verifies that the A-C transitional pattern

shows similar properties to pattern C and can be considered as pattern C as mentioned previously.

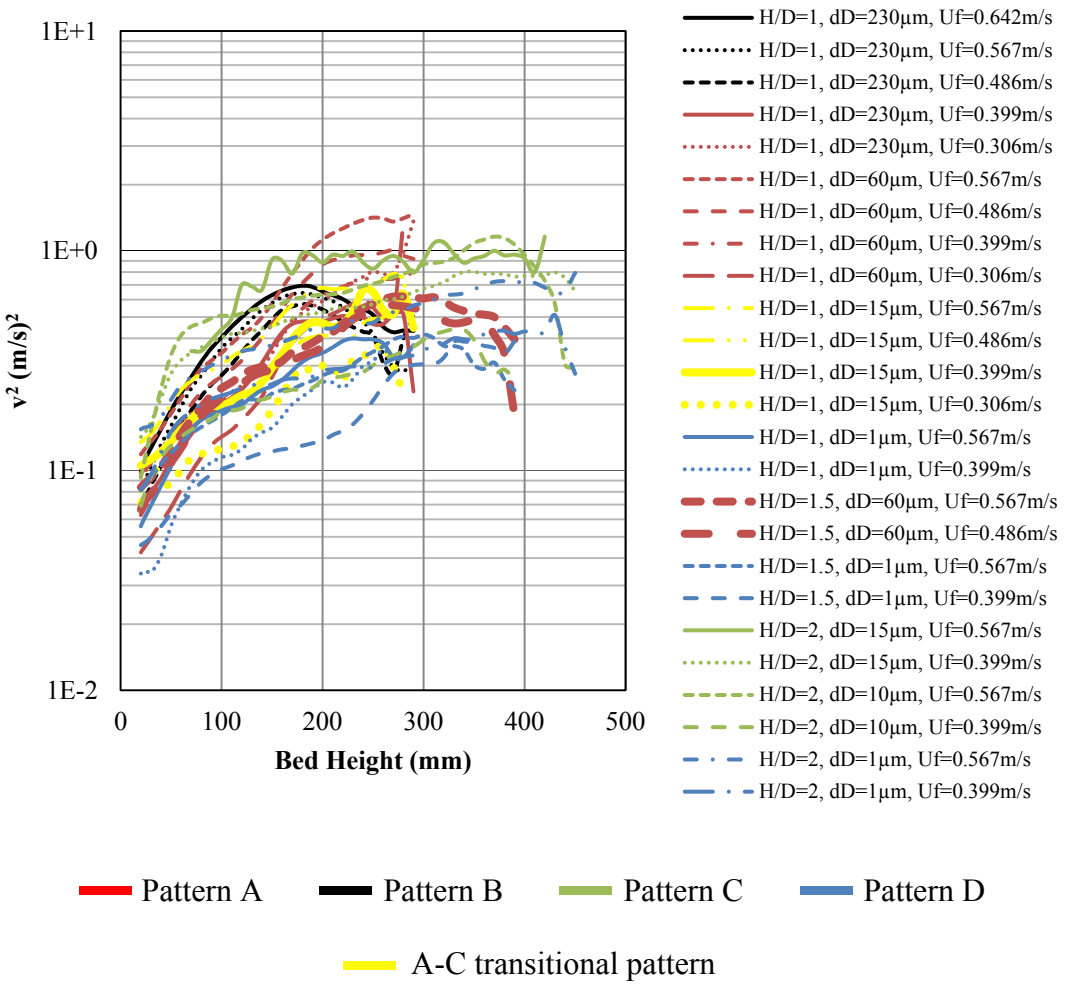

Figure 4.22 Average kinetic energy of particles for the 4 solid flow patterns (bed materials: 352-micron glass beads).

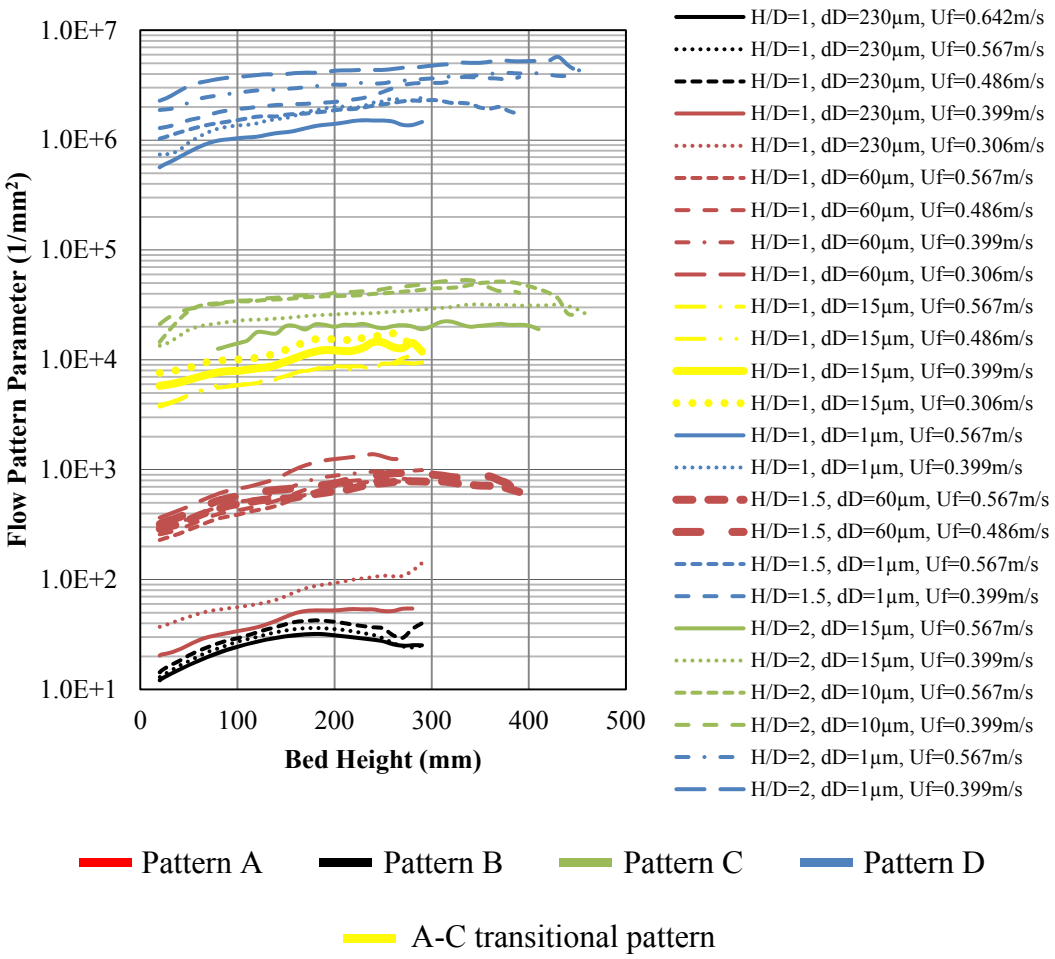

Figure 4.23 Identifying solid follow patterns based on the FPP (bed materials: 352-micron glass beads).

Benefiting from the FPP expression (Equation 4.1), it is possible to identify a solid flow pattern in a fluidized bed as long as the FPP value is in the range covered by the prospected pattern. The FPP is a result of the H/D times the absolute speed of particle and then divided by the squared pore size of the air distributor and the excess gas velocity. From Equation 4.1, it can be seen that the pore size of the air distributor has a greater effect on FPP than the H/D or the excess gas velocity due to the fact that its effects are squared, hence a slight modification of the pore size of the air distributor

will significantly change the FPP value, thereby altering the solid flow pattern. It also can be seen that, for a fixed particle velocity, increasing the pore size of the air distributor or the excess gas velocity will reduce the value of the FPP, and an increased H/D will give a high value for the FPP. Figure 4.24 shows an example for how to identify a solid flow pattern based on the excess gas velocity ($u-u_{mf}$), the pore size of the air distributor, the H/D and the average kinetic energy of particles (v^2) in fluidized beds of glass beads. In general, the pore size of the air distributors has a dominant effect on the FPP. A small change in the pore size will result in a significant change in FPP, hence generating different solid flow patterns even though the measured particle kinetic energy and other parameters are the same. For example, the FPP is in an order of 10^6 to 10^7 when the pore size is 1 μm, the particle squared velocity is between 0.2 and 0.5 $(m/s)^2$, the H/D is between 1 and 2 units and the excess gas velocity is between 150 and 300 mm/s, while the value of FPP will be reduced to the order of 10^4 to 10^5 when the pore size changes to 10 μm with the other conditions remaining the same. When the pore size of the air distributors is fixed, an increasing excess gas velocity ($u-u_{mf}$) will result in a decreased FPP value and sometimes a change in the solid flow pattern as well. For example, when the pore size of the air distributor is 0.23 mm, the H/D is 1 and the particle squared velocity is between 0.2 and 0.5 $(m/s)^2$, the increase in the excess gas velocity within the range of 150-300 m/s will reduce the FPP value and change the solid flow from pattern A to pattern B. Similarly, when the pore size of the air distributor is 60 μm, the H/D is 2 units and the squared particle velocity is 0.5 $(m/s)^2$, increasing the excess gas velocity within the range of 150-300 mm/s will result in a decrease of the FPP as well as a change of the solid flow pattern from C to A. However, when the pore size of the air distributor is 1 μm, an increase in the excess

gas velocity will slightly decrease the FPP value but does not change the solid flow pattern within the experimental conditions presented in the present study. Figure 4.24 also clearly shows that the measured particle kinetic energy has an effect on the solid flow pattern. For example, under the same excess gas velocities ($u-u_{mf}$) and the same pore size of the air distributor, a higher v^2 will result in a slightly higher FPP value.

The borderlines for different solid flow pattern zones have been determined from PEPT experiments. There is a blank zone between the pattern D zone and the pattern C zone, which is due to a sizeable difference between the smallest FPP value of pattern D and the largest FPP value of pattern C. An FPP located within the blank zone should either generate a solid flow pattern D or C. C-D transitional flow patterns may also be generated when the FPP value is located within the blank zone. There are not enough experimental data to cover this blank zone within the conditions of the current study, thus the results presented here cannot provide an accurate borderline between pattern C and D. Overall, the FPP can be potentially used as a useful means to identify the fluidization behaviour for Geldart B particles within the bubbling regime when the H/D is from 1 to 2 units. Further experimental work must be designed to generate a more universally applicable, dimensionless FPP number for a wider range of operational conditions, bed materials and bed geometries. The measured parameter of particle velocity will also be removed from the FPP number. Sufficient experimental data will help to determine a more accurate classification, including the borderline between the solid flow pattern C and D zones.

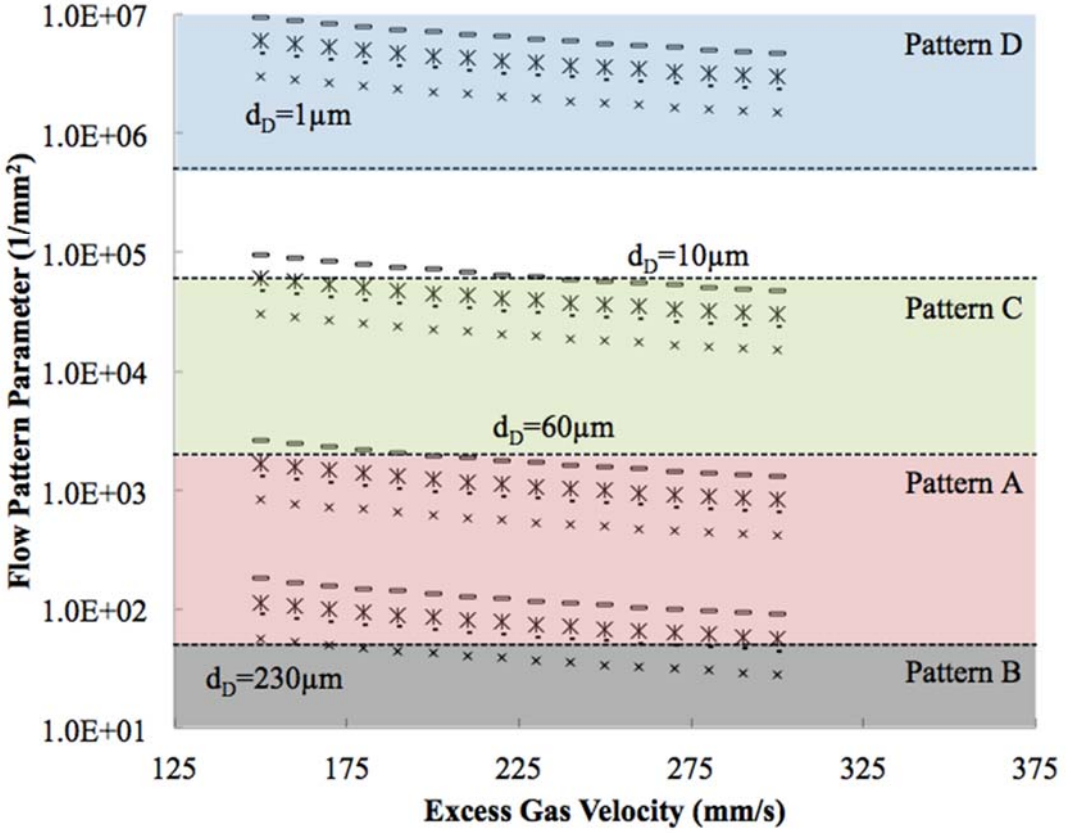

Figure 4.24 The FPP versus excess gas velocity ($u-u_{mf}$) for a known average kinetic energy of particles, where the particle kinetic energy (v^2) for ××××× (H/D=1) and * * * * * (H/D=2) are 0.2 $(m/s)^2$ and for ····· (H/D=1) and ----- (H/D=2) are 0.5 $(m/s)^2$.

4.6 Conclusion

Four solid flow patterns have been found within the fluidized bed of Geldart B particles operated in the bubbling fluidization regime using the PEPT technique. Pattern A gives poor gas and solid contact and mixing behaviour and should be avoided for industrial applications. Pattern B and pattern C can be considered as acceptable flow structures where the fluidization performance and the process

efficiency improved. However, pattern D has been determined to be the most desirable flow structure that provides favourable and uniform gas and solid contact and mixing as well as better heat and mass transfer behaviour. Pattern D will benefit industrial processes with high efficiency and product quality.

The aforementioned flow patterns are the result of a combination of operational conditions, properties of bed materials and bed designs. A FPP has been proposed to identify the flow pattern in a bubbling fluidized bed based on PEPT experimental data rather than computational simulation. The FPP combines the effect of particle kinetic energy, minimum fluidization velocity, superficial gas velocity, the pore size of the air distributor and the H/D. The FPP gives a clear classification of different solid flow patterns. Each pattern falls into a specific range of FPP values. Different solid flow patterns can be identified through the FPP value. The FPP can provide some useful information for the operational control of fluidized beds and benefit academic research and industrial sectors by optimizing their production. However, the FPP presented here is still in its initial stages. Further development is required to generate a more universally applicable, dimensionless FPP number for a wider range of operational conditions and materials. The new FPP number will only contain a combination of operational conditions, bed design and particle properties without any measured parameters from the experiments.

Chapter 5: Reconstruction of Bubble Spatial Distribution

5.1 Introduction

Bubbles are one of the major components of bubbling fluidization. They are responsible for how much gas flows through the bed in addition to serving as the "motor of fluidization" to drive solids circulating and mixing within the bed and to enable the process uniformly performed throughout the bed [8]. However, improper bubbling will introduce heterogeneity of bubble distribution, bubble size and their residence time in the bed, thereby reducing the reaction and process efficiency [50]. Bubble properties, including bubble size, bubble rise velocity and bubble spatial distribution, are believed to be the primary factors associated with gas residence time, gas-solid contact, solid dispersion, mixing and heat and mass transfer [2, 31, 32, 178]. For instance, non-uniform bubble size developed over the bed cross-sectional area gives a broad gas residence-time distribution and therefore a non-uniform reaction, because large bubbles reduce solid and gas contact in addition to having a short residence time. Large bubbles have rising velocities higher than small bubbles and therefore shorter residence times. In addition, rising bubbles carry solids up in their wake and enhance the solid mixing in the regions close to the bubble paths. Conversely, in the regions having less bubble activity, solids move downwards and feature less mixing and low reaction efficiency [178, 191]. For an optimally performing bubbling fluidized bed, bubbles should be small and the spatial distribution of bubbles should be uniform across the entire bed [2, 214].

Intensive investigations have been carried out since the 1960s to characterize and predict bubble properties using various techniques, such as bubble size, bubble rise velocity and bubble spatial distribution [178, 181, 215, 216]. However, most research either focuses on 2-D fluidized beds or a section of 3-D fluidized beds. For instance, Baumgarten and Pigford [215], Grace and Harrison [217] and Lim et al. [214] investigated the bubble behaviour in 2-D bubbling fluidized beds by using a γ-ray absorption technique, cine photograph or a real-time visual system [178, 214]. Mudde [110] studied the bubble motion at a height of 0.5 m above the air distributor in a 3-D fluidized bed with a 23-cm I.D. using a three-source X-ray tomographic scanner. Saayman et al. [221] investigated the bubble flow structure from a height of 0.20 to 0.50 m above the air distributor in a 3-D fluidized bed using the fast X-ray tomography. The spatial distribution of bubbles near the air distributor has not been given adequate attention, and contradictory descriptions of bubble spatial distribution have been frequently reported in literature since the 1960s [178, 216-218]. This inadequacy in research is due to the fact that the bubble spatial distribution obtained from 2-D fluidized beds [223, 224] cannot explain the complex bubble behaviour in 3-D beds since the wall effect would significantly alter the flow structure [9] and X-ray tomography cannot distinguish multiple bubbles on the same path of X-rays.

In this chapter, the development of an approach to reconstruct bubbles and their spatial distribution in a 3-D bed based on the solid motion measured by the PEPT technique is discussed. The bubble size and rise velocity were first calculated based on solid motion. The spatial distribution of bubbles was then reconstructed in 3-D bubbling

fluidized beds. The interaction between solid flow patterns and bubble behaviour and the specific surface area of bubbles were also investigated. The results garnered from this investigation have been verified with well-known correlations and published literature.

5.2 Reconstruction of Bubble Spatial Distribution

In order to reconstruct the bubble spatial distribution from the particle time-position data that has been obtained by the PEPT technique, it is necessary to know the positions and sizes of all bubbles in a fluidized bed. These can be determined based on the observations presented by Davidson and Harrison [238], Rowe and Partridge [192], Davidson et al. [267] and Kunii and Levenspiel [2]. In a bubbling fluidized bed, particles in bubble wakes or in bubbles travel upwards at an average velocity as high as that of the bubbles. As illustrated in Figure 5.1, when a single bubble travels upward through a bed of particles, the particles tend to flow around the bubble in a manner somewhat similar to the encounter when a body moves through a fluid stream [184]. Typical bubbles have a nearly spherical cap and a flattish base, which is called bubble wake. Rowe and Partridge [192] and Kunii and Levenspiel [2] have demonstrated that particles in the bubble wake and in a bubble are carried along with the bubble as if attached to it for a certain distance. Within the bubbles and the bubble wakes, particles may move around within a limited space. However, the average upward velocity of the particles in the bubble wake or the bubble should be equal to the bubble rise velocity. Kunii and Levenspiel [2] and Yang [31] further demonstrated that the wake fraction, which has been defined as the ratio of wake to bubble by volume ($f_w = V_w/V_b$), averages approximately 0.35 for most Geldart B particles. There are also

0.2%-1.0% solids by volume in the bubbles. In consideration of the total volume of bubbles in a fluidized bed, the amount of solids in the bubble wakes and bubbles is significant and large enough for the calculation of the bubble rise velocity. In addition, bubbles and their wakes rise with a velocity faster than the surrounding particles [2, 268]. Therefore, the upward velocities of particles in bubble wakes or bubbles can be regarded as the bubble rise velocities, and they are large enough to be recognised apart from the rest of the upward velocities of particles.

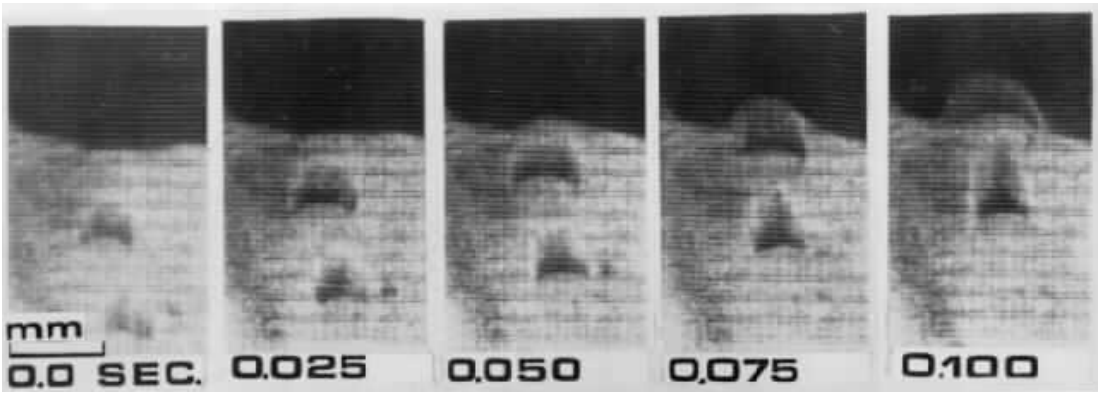

(a)

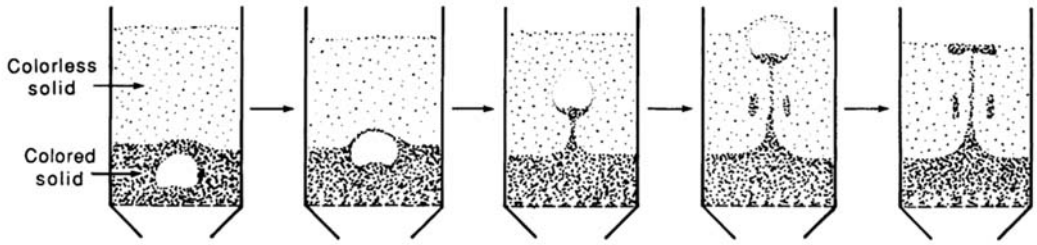

(b)

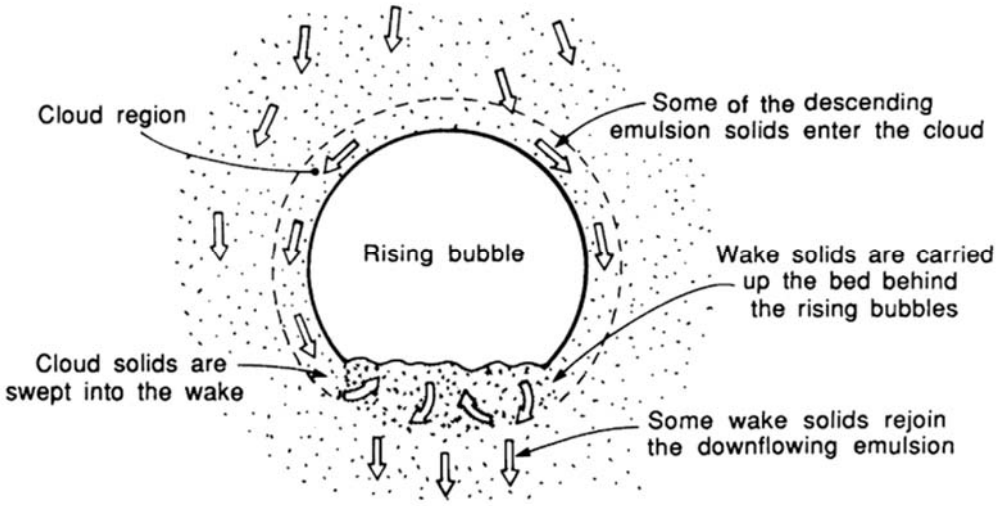

(c)

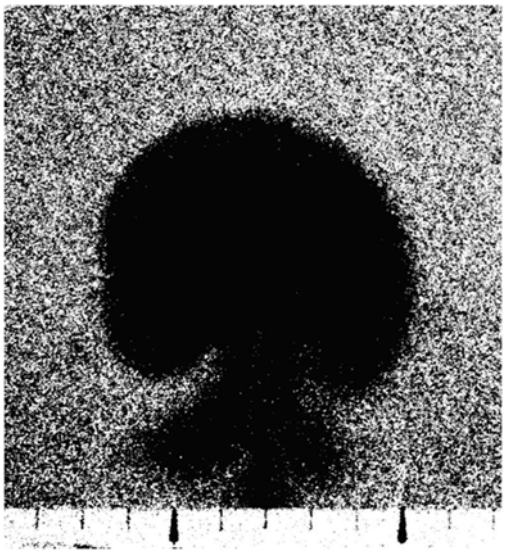

(d)

Figure 5.1 Bubbles in a fluidized bed: (a) photographs of rising bubbles captured by Levy et al. [269]; (b) sketches of photographs by Rowe and Partridge showing the entrainment of solids by a rising bubble [2, 174, 192]; (c) sketch of a single rising bubble [2]; (d) photograph of a single rising bubble [2, 174, 192].

Based on the above discussions, the bubble spatial distribution can be determined via upward particle velocity maps. To this end, the bed was divided into many layers with a thickness of 5 mm. Each layer was then divided into many cubes with a dimension of 5 mm. The upward velocity v_y of the tracer at each position was calculated using 3 points on its trajectory as shown in Figure 5.2. The upward particle velocity map of each layer was then constructed based on the particle velocity data from individual cubes as shown in Figure 5.3. According to Davidson and Harrison [238], Rowe and Partridge [192], Davidson et al. [267] and Kunii and Levenspiel [2], the bubble rise velocity is equal to the upward velocity of particles in the bubble wake or bubble. The upward particle velocities in the bubble wakes or bubbles are higher than particles in other regions and should correspond to the peaks in the upward particle velocity map. The peaks in the v_y map therefore correspond to the bubble positions in each layer. As shown in Figure 5.3, there are a number of peaks in the layer and the peaks in each layer have different rise velocities. Several of them have been numbered as an example to illustrate the method. In order to define the bubble rise velocities and bubble positions from the v_y maps, it has been found that the top 20% of the v_y in each layer account for almost all of the peaks within the layer. To find the bubble positions, the upward velocity of particles in each cube was compared with the value that is 80% of the highest velocity in the layer. If the particle upward velocity was greater than 80% of the highest velocity in the layer, the particle was seen within one of the peaks on the rise velocity map, and the position of the particle was considered to be the same as a bubble position. The velocity of this particle was then considered to be a bubble rise velocity. This approach will be further discussed in the following sections.

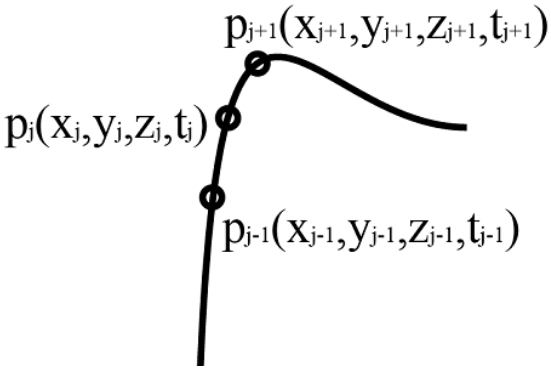

Figure 5.2 Calculation of particle velocity based on PEPT data.

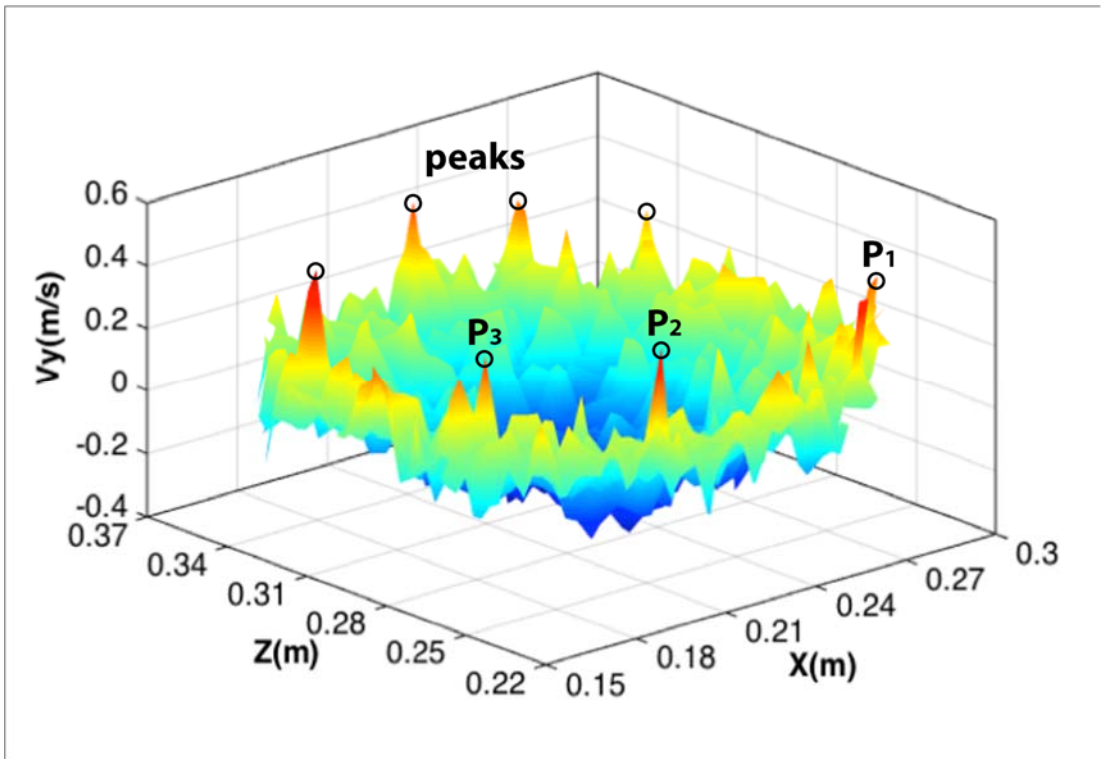

Figure 5.3 Identification of bubble rise velocities from an upward particle velocity map.

Once the bubble positions in each layer of bed and their rise velocities have been calculated, the bubble size can be estimated using empirical correlations from the

literature. Several correlations for bubble rise velocity have been proposed as a function of the bubble size in literature [28, 226, 227]. Fan et al. [184] compared the bubble rise velocities calculated from PEPT results with the velocities calculated from different empirical correlations and confirmed that the correlation proposed by Kunii and Levenspiel [2] was in particularly suitable agreement with the PEPT results. Therefore, Kunii's correlation (Equations 5.1-5.2) was used to calculate the bubble size from the bubble rise velocity data obtained by PEPT.

$$u_{br} = 0.711(g d_b)^{1/2} \tag{5.1}$$

$$u_b = 1.6\left\{\left(u - u_{mf}\right) + 1.13 d_b^{0.5}\right\} D^{1.35} + u_{br} \tag{5.2}$$

Where u_{br} is the rise velocity of a bubble with respect to the emulsion phase (m/s), g is the gravitational acceleration (m/s^2), d_b is the bubble diameter (m), u_b is the velocity of a rising bubble through a bed (m/s), u is the superficial gas velocity (m/s), u_{mf} is the minimum fluidization velocity (m/s) and D is the fluidized bed diameter (m).

After determining the bubble positions and sizes for each layer of the bed, the bubble spatial distribution in the entire bed can then be reconstructed. Typical results are presented in Figures 5.5, 5.8, 5.11 and 5.14, in which the bubbles are illustrated in a reduced scale for a better view; the actual bubble sizes are indicated by the colour bar.

5.3 Spatial Distribution of Bubbles

Four solid flow patterns (patterns A-D) have been classified in the previous chapter as shown in Figure 4.1 [28, 157, 167, 248]. In this section, the bubble spatial distribution has been reconstructed and the bubble sizes and rise velocities have been calculated for each flow pattern to investigate the bubble behaviour in the bubbling fluidized bed under different experimental conditions and understand their relationship to the solid flow patterns.

5.3.1 Flow Pattern A

The bubble spatial distribution for pattern A has been reconstructed based on solid motion measured by the PEPT technique and is presented in Figure 5.4. The bubbles in pattern A form a narrow channel structure, from one side of the bed wall moving gradually inwards to the bed centre as the bed height increases. The bubble path unevenly covers less than one-third of the cross-sectional area of the bed and the bubble sizes increase significantly along with the bed height. At the layer just above the air distributor (Figure 5.4b), bubbles are formed near one side of the bed wall, and the bubble spatial distribution is not uniform over the layer. At a higher layer of 140-170 mm above the air distributor, bubbles move inwards to the centre of the bed, and bubble sizes increase significantly from around 1 cm to 4.5 cm as shown in Figure 5.4c. The significant increase in bubble size indicates bubble coalescence during the bubble rising. Large bubbles have short residence times within the bed and thereby reduce their interaction time with solids. In addition, for a fixed flow rate, large bubbles have smaller total surface areas for making contact with the solids. Hence, the

bubble behaviour in pattern A is not ideal for industrial processes. The reconstructed bubble spatial distribution of pattern A is in agreement with the solid flow pattern observed using the PEPT technique (Figure 5.5).

To further verify the reconstructed bubble spatial distribution, the rise velocity and the diameter of the reconstructed bubble at any height above the air distributor are calculated from the experimental data. The results are then compared with the predictions by the well-known empirical correlations proposed by Yasui and Johanson [12], Davidson and Harrison [238], Mori and Wen [225], Darton et al. [232] and Kunii and Levenspiel [2]. The correlations proposed by Yasui (Equation 5.3), Mori (Equations 5.4-5.6) and Darton (Equation 5.7) are used to calculate the predicted bubble size, and the correlations proposed by Davidson (Equations 5.1, 5.8) and Kunii (Equations 5.1-5.2) are used to calculate the predicted bubble rise velocity.

Yasui and Johanson [12]:

$$d_b = \rho_p \cdot d_p \cdot \left(\frac{u-u_{mf}}{u_{mf}}\right)^{0.63} \cdot h \tag{5.3}$$

Mori and Wen [225]:

$$\frac{d_{bm}-d_b}{d_{bm}-d_{b0}} = e^{-0.3h/D} \tag{5.4}$$

$$d_{bm} = 0.65\left[\frac{\pi}{4}D^2\left(u-u_{mf}\right)\right]^{0.4} \text{ [cm]} \tag{5.5}$$

$$d_{b0} = \frac{2.78}{g}\left(u-u_{mf}\right)^2 \text{ [cm]} \tag{5.6}$$

Darton et al. [232]:

$$d_b = 0.54\left(u - u_{mf}\right)^{0.4}\left(h + 4\sqrt{A_0}\right)^{0.8} g^{-0.2} \tag{5.7}$$

Davidson and Harrison [238]:

$$u_b = u - u_{mf} + u_{br} \tag{5.8}$$

Where d_b is the bubble diameter (m), ρ_p is the particle density (kg/m^3), d_p is the particle diameter (m), u is the superficial gas velocity (m/s), u_{mf} is the minimum fluidization velocity (m/s), h is the height above the air distributor (m), d_{bm} is the maximum bubble diameter (m), d_{b0} is the initial bubble diameter (m), D is the fluidized bed diameter (m), g is the gravitational acceleration (m/s^2) and A_0 is the area of air distributor plate per orifice (m^2).

The comparisons between bubble size and rising velocity calculated from PEPT results and the predictions from empirical correlations for pattern A are presented in Figures 5.6-5.7. It can be seen from Figure 5.6 that the bubble sizes calculated from PEPT results highly agree with those calculated from the well-known empirical correlations proposed by Yasui and Johanson [12] (Equation 5.3) and Mori and Wen (1975) (Equations 5.4-5.6), especially when the bed height is below 0.12 m. For heights above 0.15 m, bubble sizes increase significantly because the bubbles are close to splash zone and frequent bubble coalescences and bursts present near the bed surface [2]. Figure 5.7 presents the comparison for bubble rising velocity. It can be seen that the velocity correlation proposed by Kunii, particularly based on Mori's or Yasui's bubble size

correlation, is in greater agreement with the bubble rise velocity calculated using the current study's reconstruction method as opposed to Davidson's correlation under the same conditions of this flow pattern. This can be explained by the fact that that the bubble rise velocity correlation proposed by Davidson and Harrison was originally developed for estimating the rise velocity of large spherical cap bubbles in liquids [270], whereas the correlation proposed by Kunii and Levenspiel was developed from a gas-solid fluidized bed of Geldart B sand particles and under similar operational conditions and bed geometries to the present study, where the bed diameter was 0.2-1.0 m and the superficial gas velocity was 0.09-0.3 m/s [2].

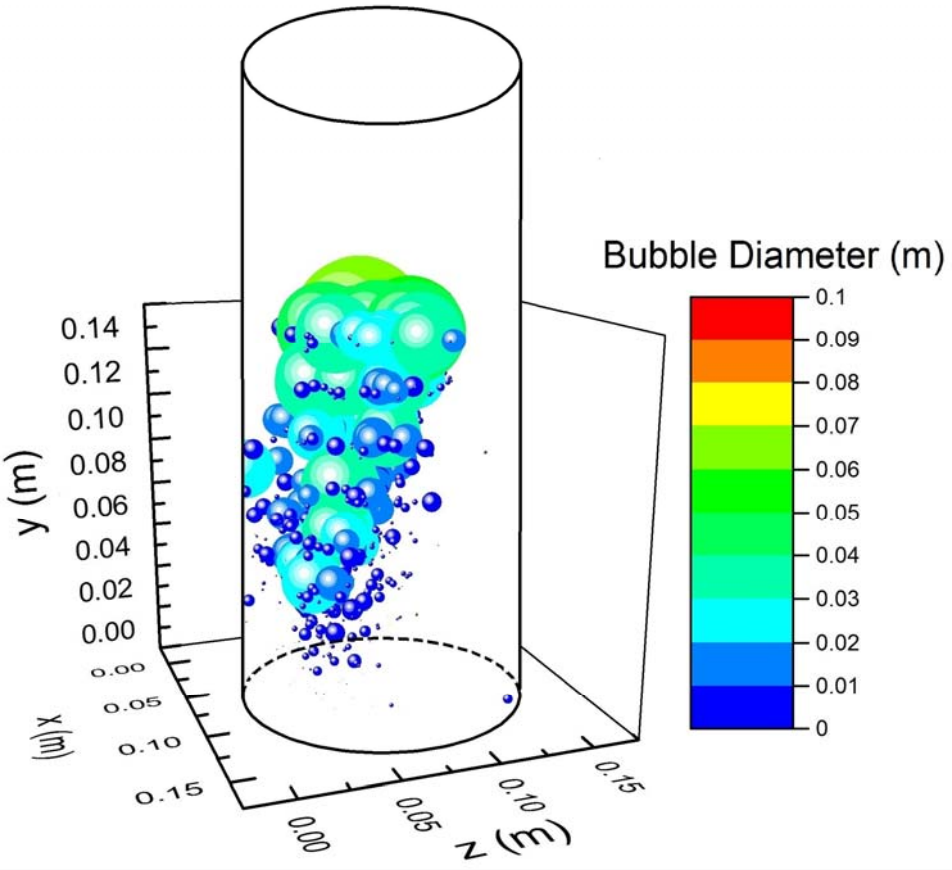

(a)

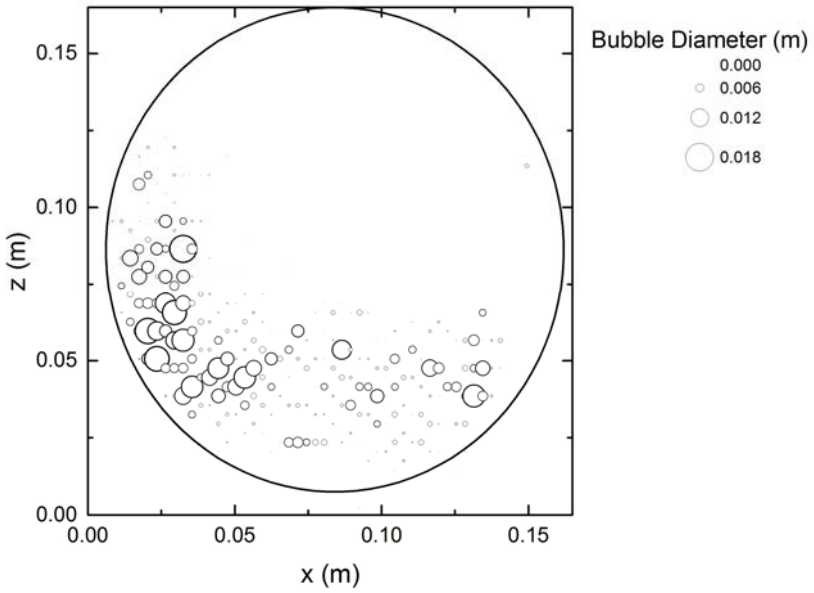

(b)

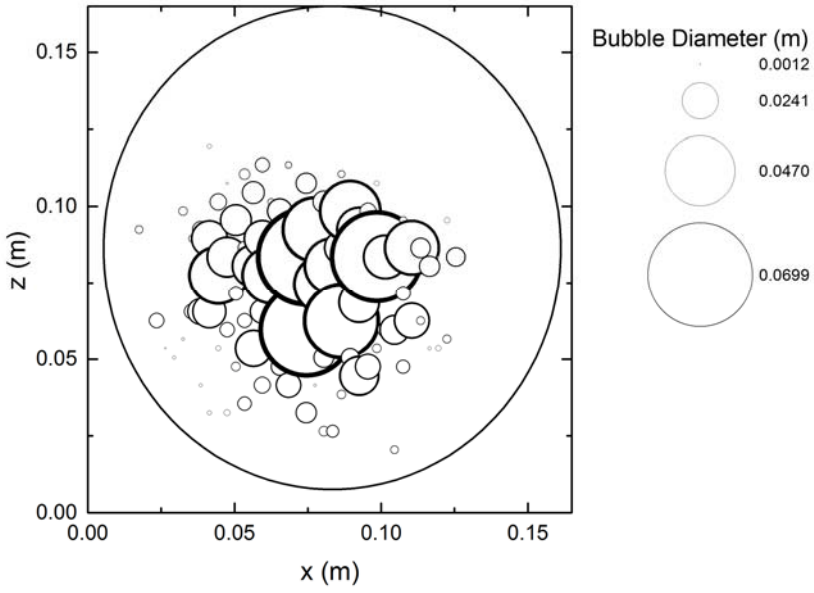

(c)

Figure 5.4 Bubble spatial distribution of flow pattern A: (a) overall view; (b) a layer at a bed height of 20-50 mm; (c) 140-170 mm layer.

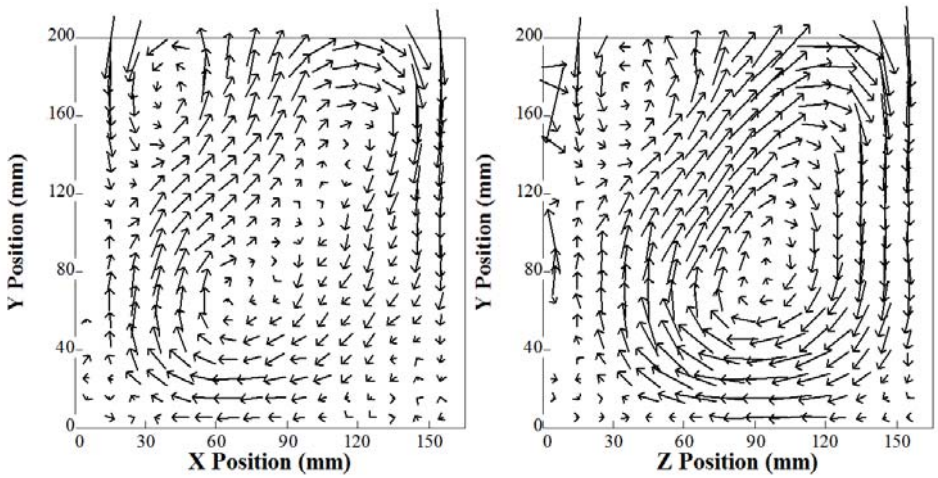

Figure 5.5 Flow pattern A.

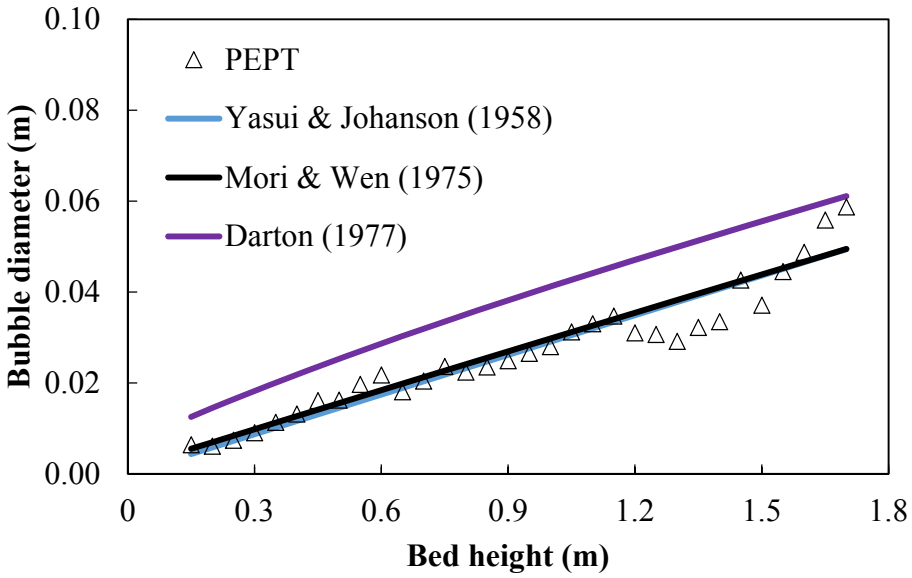

Figure 5.6 Bubbles size versus bed height for flow pattern A.

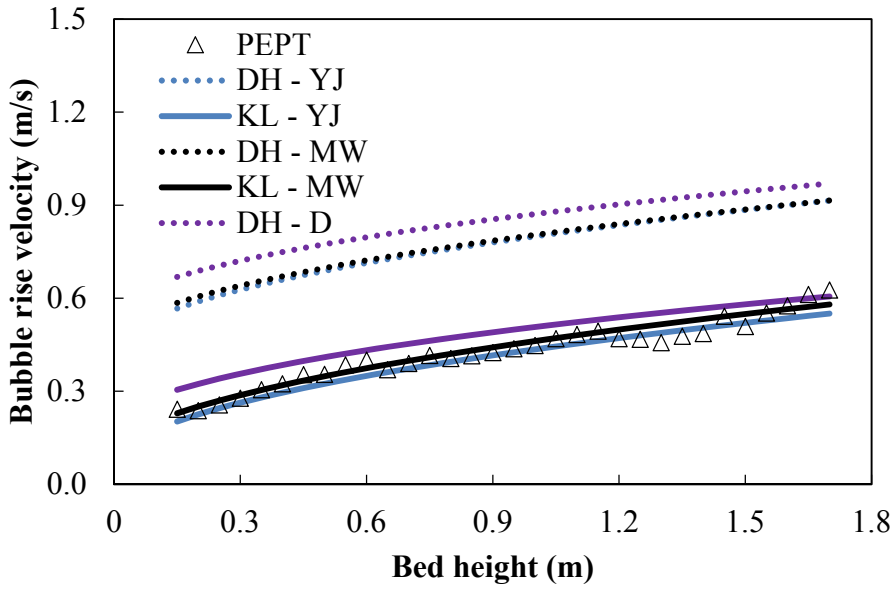

Figure 5.7 Bubble rise velocity versus bed height for flow pattern A.

DH-YJ is the bubble rise velocity predicted from Davidson & Harrison's (bubble size to rise velocity) correlation based on Yasui & Johanson's bubble size empirical correlation and KL refers to Kunii & Levenspiel's correlation, MW refers to Mori & Wen and D refers to Darton.

5.3.2 Flow Pattern B

The bubble spatial distribution for pattern B is presented in Figure 5.8. In comparison with pattern A, bubbles in pattern B are much more uniformly distributed within the bed, especially in the lower section of the bed, and bubble sizes increase slowly in the lower section. At a layer of 0-30 mm above the air distributor, bubbles are distributed relatively uniformly over the entire cross-section as shown in Figure 5.8b. The bubble sizes are small, and the bubble rising velocities should be slow. The uniform distribution of bubbles and small bubble sizes provide a large contact area for bubbles

and solids and a longer residence time for the gas-solid contact in this layer. As bubbles rise to a higher level of 70 mm above the air distributor, the bubbles move inwards slightly to the centre but still occupy the majority of the cross-section area. Bubble sizes grow slowly from 7.5 mm to 15 mm at a rate of 0.25-0.35 m/s, as shown in Figures 5.8a-c. Meanwhile, in flow pattern A, the bubble sizes increase from 6.5 mm to 22 mm, and bubbles are distributed in a small area near the bed wall, particularly at the bottom section. When the bed height is greater than 80 mm, the bubbles are distributed mainly in the centre region of the bed and grow significantly, as shown in Figures 5.8d-e. At this height of the bed, the bubbles are close to the splash zone, the contact area of bubbles and solids decreases and the bubble residence time decrease significantly. The reconstructed spatial bubble distribution for pattern B agrees well with the solid flow pattern measured by PEPT (Figure 5.9) and agrees with the observation presented by Grace and Harrison [217].

The bubble diameters and bubble rise velocities of pattern B are calculated using the same method as described for the flow pattern A. To verify the calculated results, they are compared with the bubble size and bubble rising velocities predicted from the empirical correlations proposed by Yasui, Mori, Darton, Davidson and Kunii, as shown in Figures 5.10-5.11. The results indicate that bubble sizes calculated from PEPT experimental results highly agree with the results calculated from the correlations proposed by Mori and Wen and Yasui and Johanson, and bubble rise velocities calculated from PEPT experimental results agree well with the correlation proposed by Kunni and Levenspiel, combined with Mori's or Yasui's bubble size correlations, especially when the bed height is below 0.12 m. Above this height, the

bubble rise velocity and the bubble size increased significantly with the bed height according to our experiments, and the calculated bubble sizes are similar to Darton's predictions. The increases in the bubble size and bubble rise velocity in the higher levels of the bed are due to the decrease of the solid concentration in the region close to splash zone.

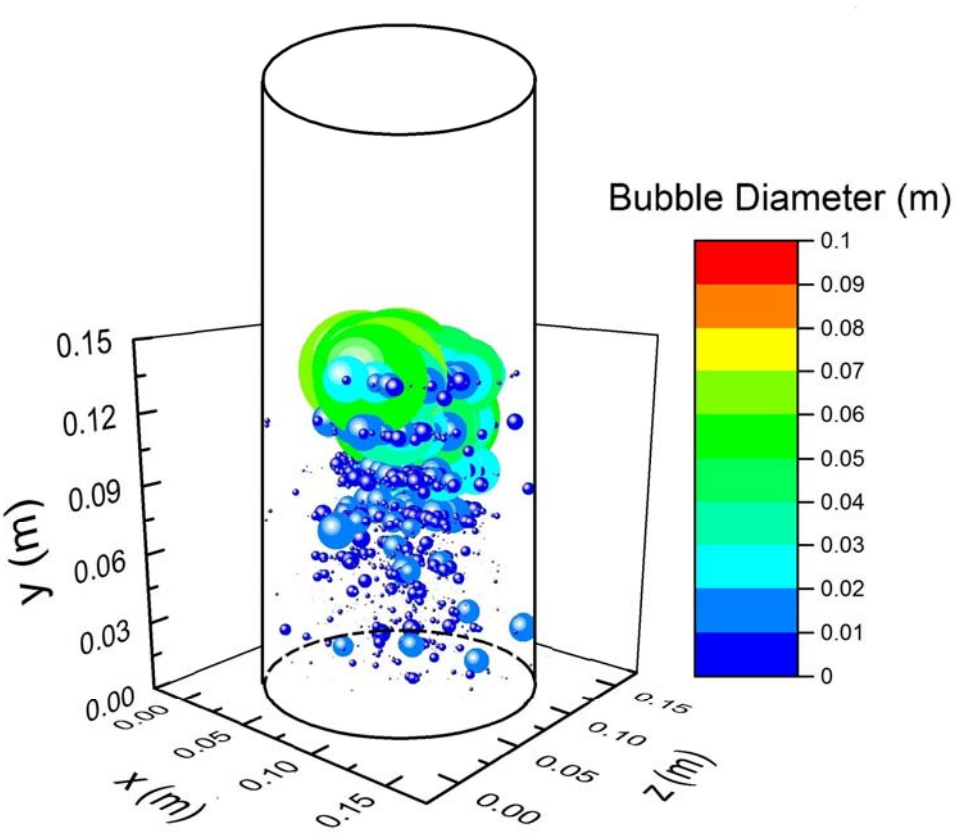

(a)

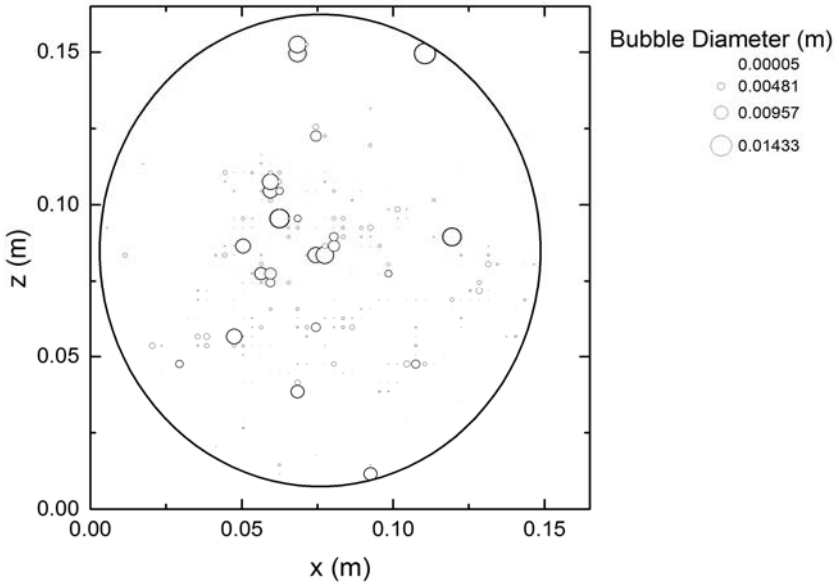
Bubble Diameter (m)
0.00005
0.00481
0.00957
0.01433
z (m)
x (m)
0.00
0.05
0.10
0.15

(b)

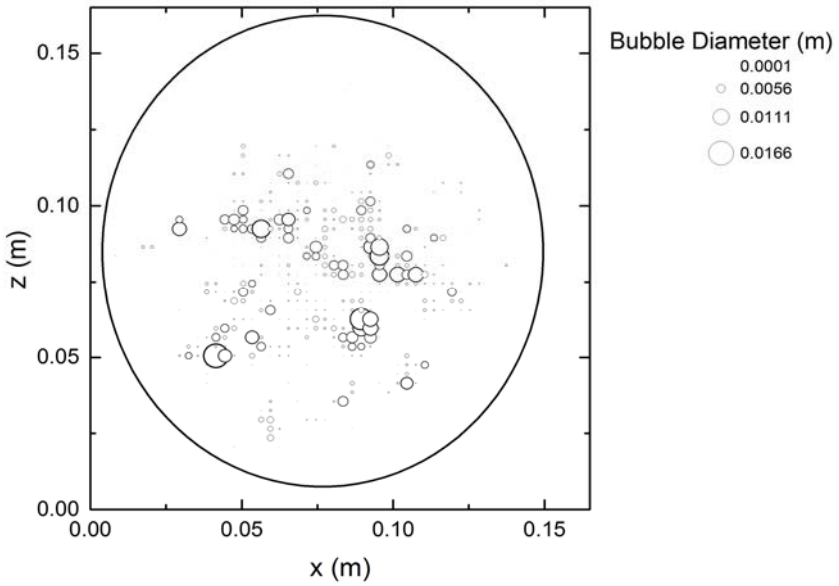
Bubble Diameter (m)
0.0001
0.0056
0.0111
0.0166
z (m)
x (m)
0.00
0.05
0.10
0.15

(c)

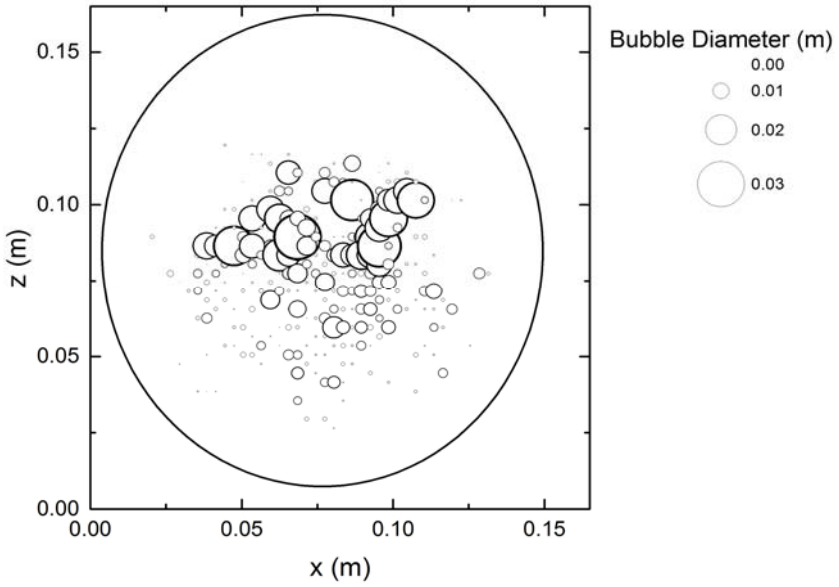

(d)

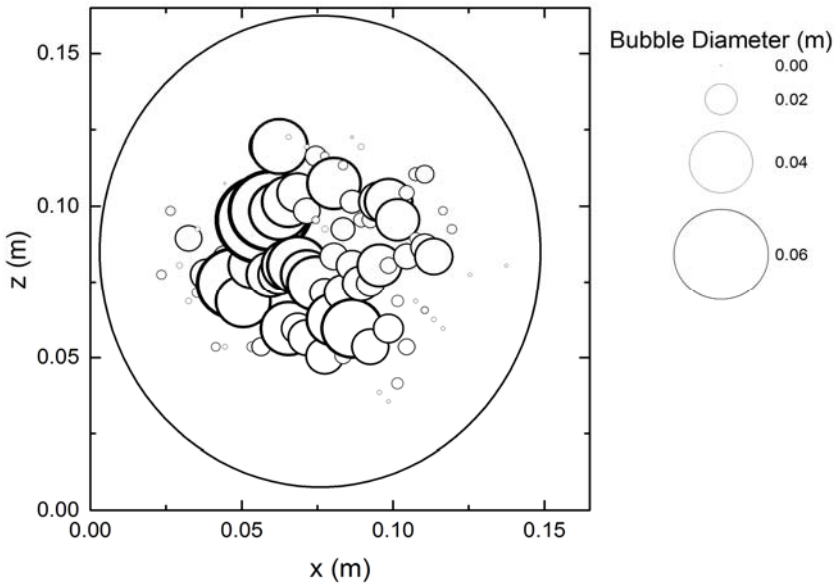

(e)

Figure 5.8 Bubble spatial distribution of flow pattern B: (a) overall view; (b) a layer at a bed height of 0-30 mm; (c) 40-70 mm layer; (d) 80-110 mm layer; (e) 120-150 mm layer.

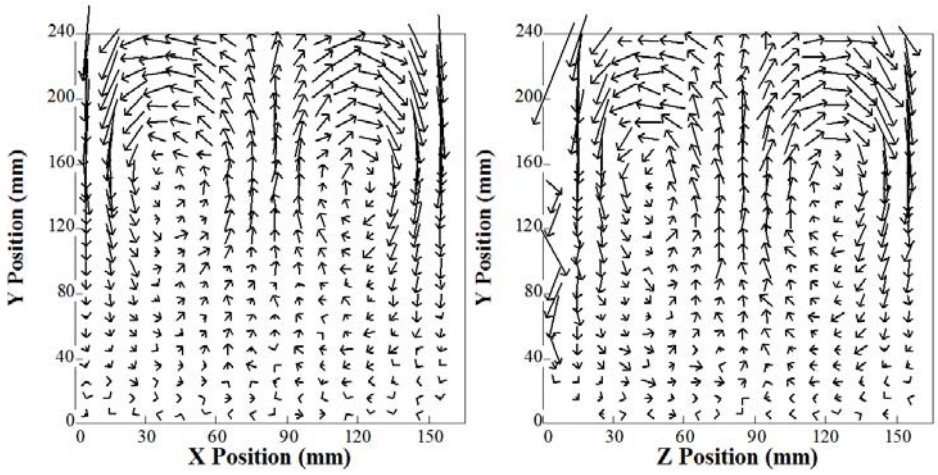

Figure 5.9 Flow pattern B.

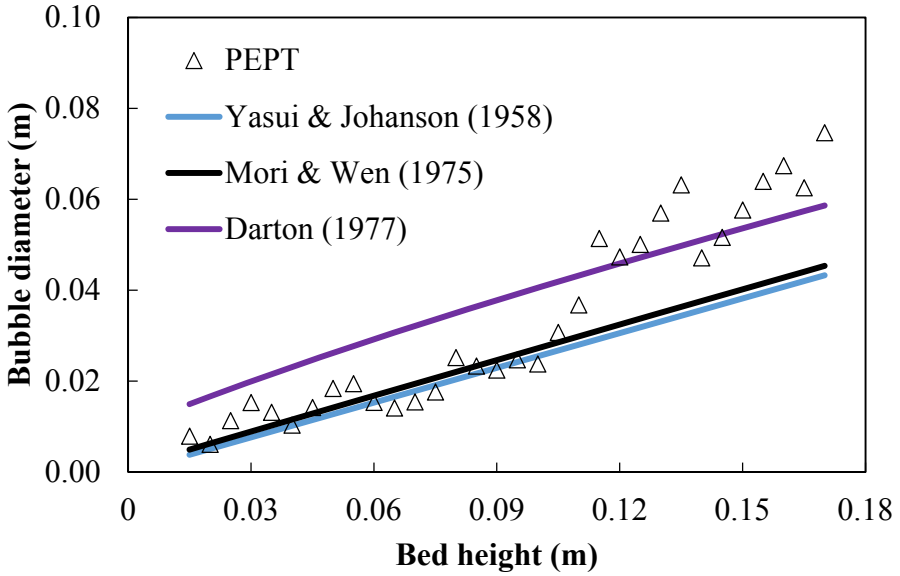

Figure 5.10 Bubbles size versus bed height for flow pattern B.

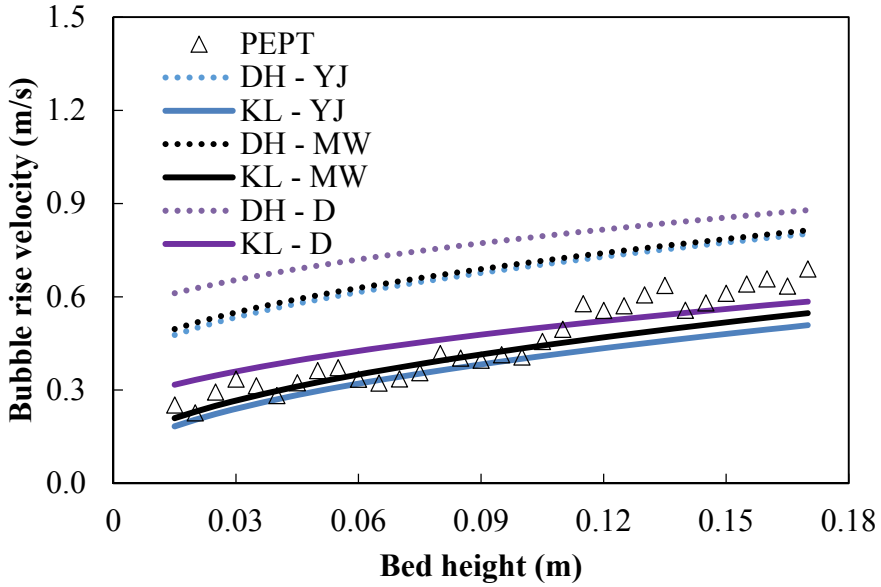

Figure 5.11 Bubble rise velocity versus bed height for flow pattern B.

DH-YJ is the bubble rise velocity predicted from Davidson & Harrison's (bubble size to rise velocity) correlation based on Yasui & Johanson's bubble size empirical correlation and KL refers to Kunii & Levenspiel's correlation, MW refers to Mori & Wen and D refers to Darton.

5.3.3 Flow Pattern C

Pattern C is mainly observed in a fluidized bed where the ratio of bed height to bed diameter is equal or greater than 1.5 units. The overall bubble spatial distribution for pattern C is presented in Figure 5.12, in which Figure 5.12b shows the bubble spatial distribution in a layer just above the air distributor. The bubbles uniformly spread over the cross-sectional area, and the bubble sizes are small. This gives a large contact area between bubbles and solids and a longer bubble residence time. As the bed height increases from 30 mm to 130 mm (Figures 5.12c-d), bubbles gradually concentrate

toward one side of the bed, and several relatively large bubbles can be observed in this layer. When the bed height increases from 160 to 230 mm, bubbles move towards the bed centre and bubble size increases gradually, as shown in Figures 5.12e-f. In these layers, gas-solid contact and bubble residence time decrease due to the increase in bubble size and rising velocity. At a bed height of 220-250 mm (Figure 5.12g), the bubble size decreases significantly rather than increasing with the bed height. This indicates that bubbles have split within this layer. The decreased bubble sizes should give a larger solid-gas contact area and longer bubble residence time. Above the bed height of 260 mm, bubble sizes increase again considerably due to the low solid concentration in the splash zone (Figure 5.12h). The bubble spatial distribution in pattern C agrees well with solid flow pattern observed using the PEPT technique as shown in Figure 5.13.

To validate the reconstructed spatial bubble distribution, the bubble sizes and bubble rise velocity calculated from the PEPT results for pattern C are compared with the predictions from the empirical correlations of Yasui, Mori, Darton, Davidson and Kunii, as seen in Figures 5.14-5.15. The results indicate that the bubble sizes and rise velocities of pattern C calculated from PEPT data agree very well with the results predicted from the well-known empirical correlations proposed by Mori and Wen, Darton and Yasui and Johanson, especially when the bed height is less than 0.2 m. The sudden decrease in both bubble size and bubble rise velocity for pattern C at the bed height from approximately 0.21 m to approximately 0.28 m is due to bubble splitting. This decrease cannot be reflected by empirical correlations. The bubble splitting and the decrease of the bubble size can also be reflected from the reconstructed bubble

spatial distribution in Figure 5.12, and the re-increase in the bubble size and rise velocity is due to the bubble coalescence and burst in the top section of the bed.

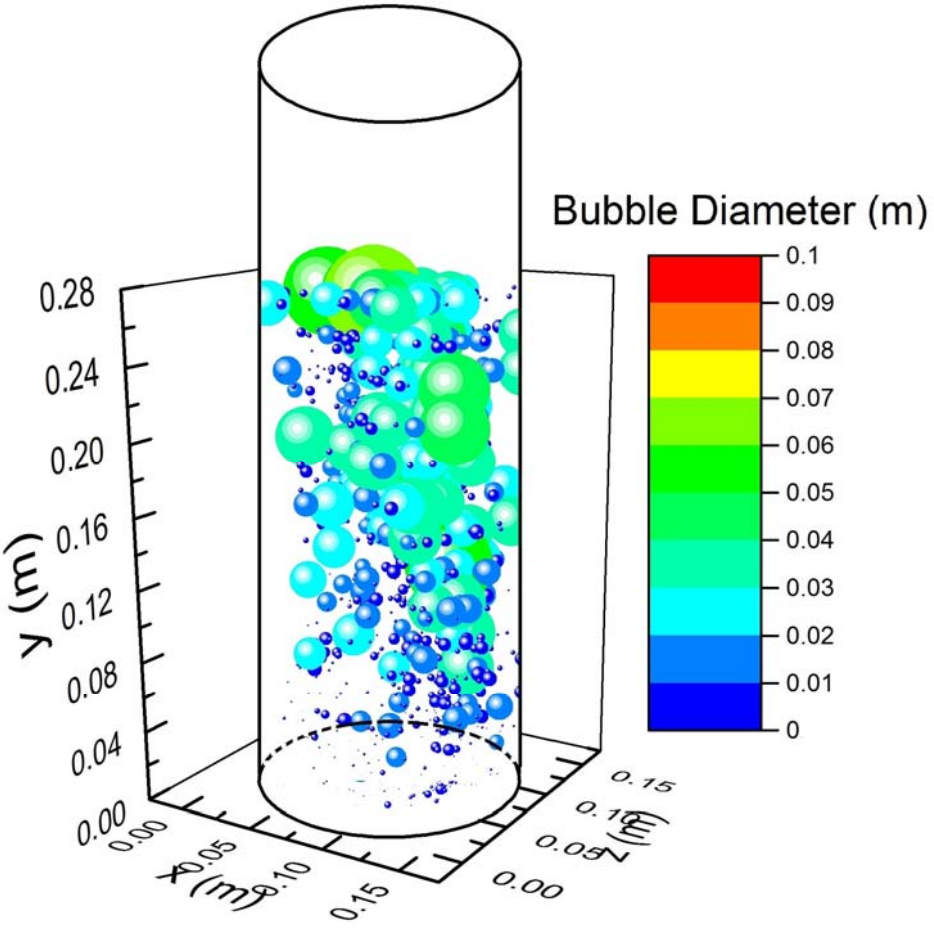

(a)

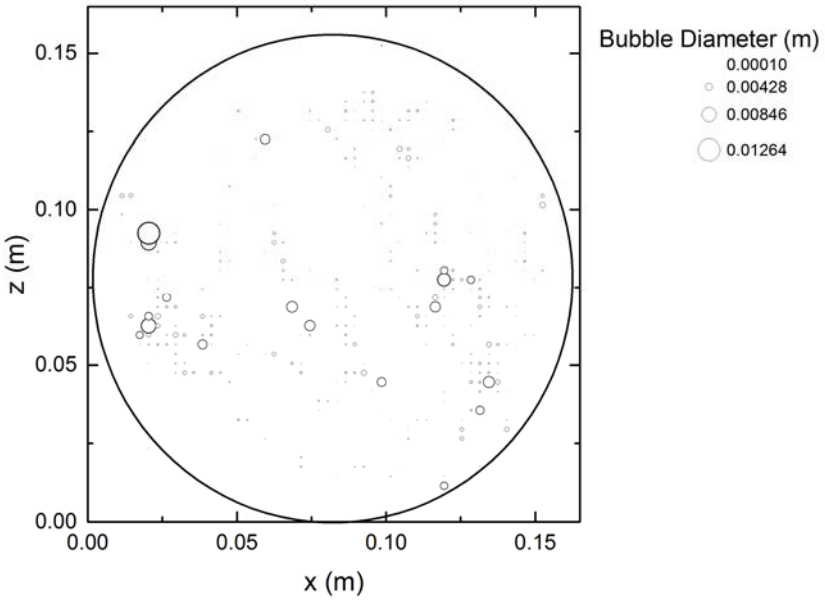
Bubble Diameter (m)
0.00010
0.00428
0.00846
0.01264
z (m)
x (m)
0.00
0.05
0.10
0.15

(b)

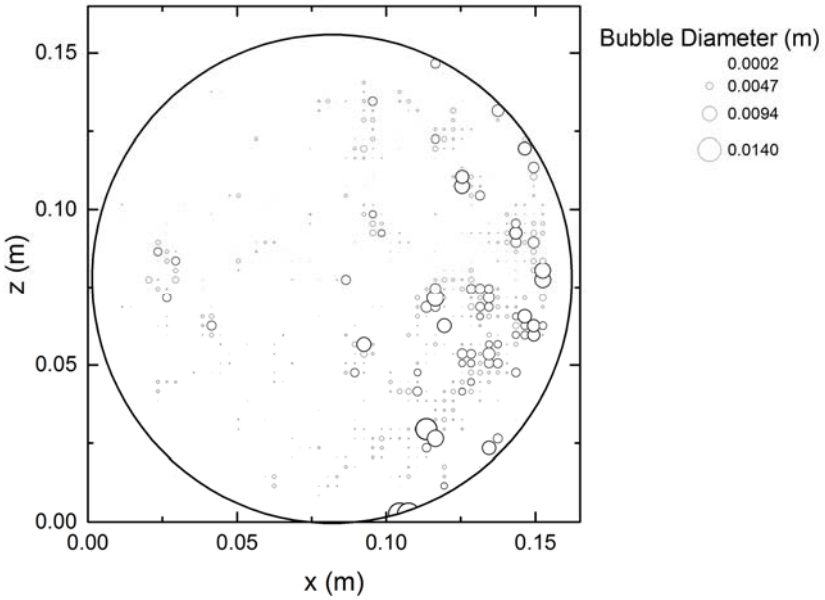
Bubble Diameter (m)
0.0002
0.0047
0.0094
0.0140
z (m)
x (m)
0.00
0.05
0.10
0.15

(c)

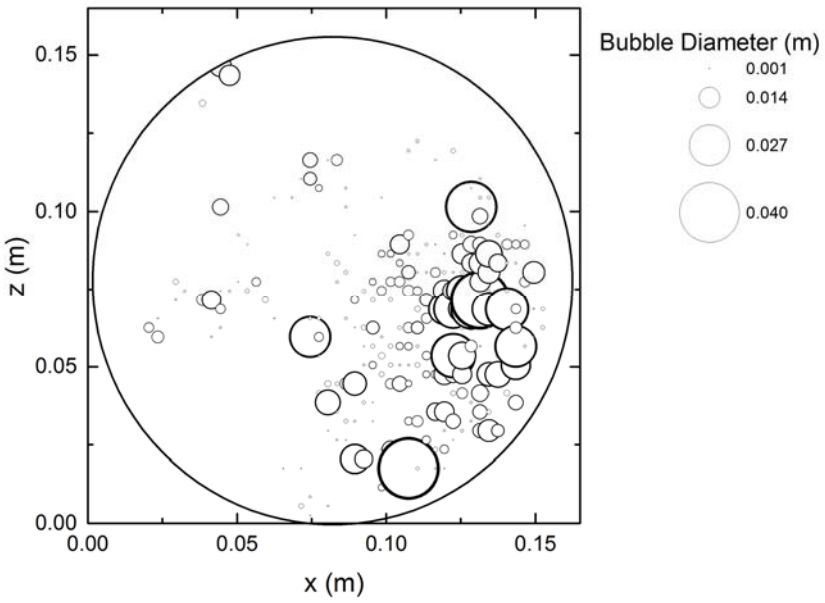
Bubble Diameter (m)
0.001
0.014
0.027
0.040
z (m)
x (m)
0.00
0.05
0.10
0.15

(d)

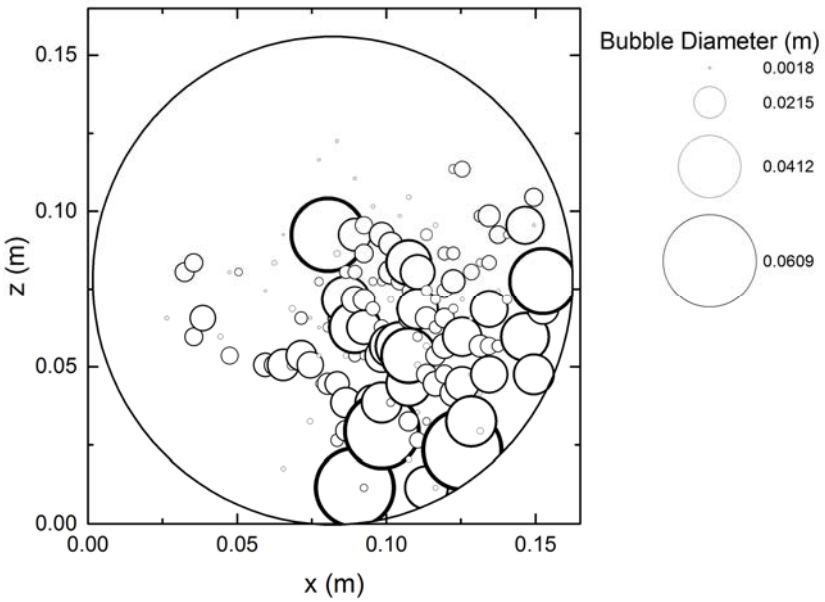
Bubble Diameter (m)
0.0018
0.0215
0.0412
0.0609
z (m)
x (m)
0.00
0.05
0.10
0.15

(e)

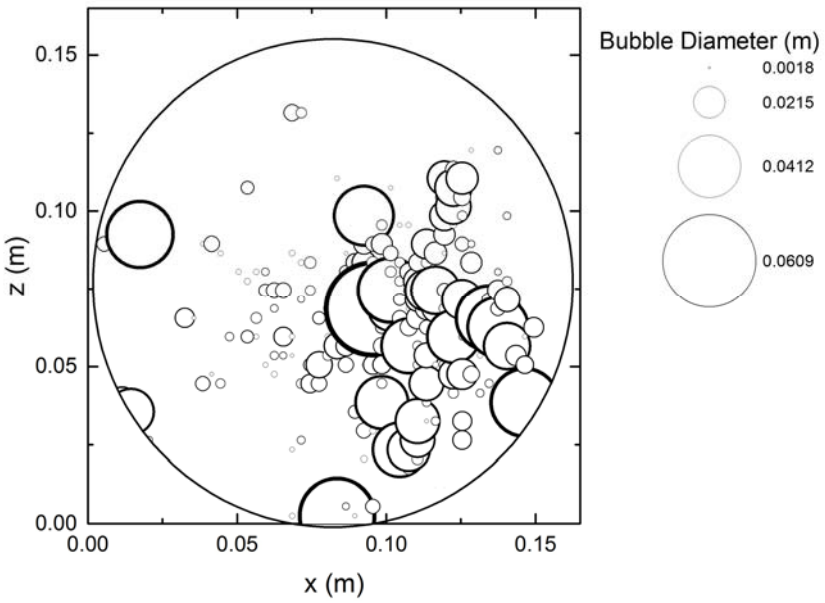
Bubble Diameter (m)
0.0018
0.0215
0.0412
0.0609
z (m)
x (m)
0.00
0.05
0.10
0.15

(f)

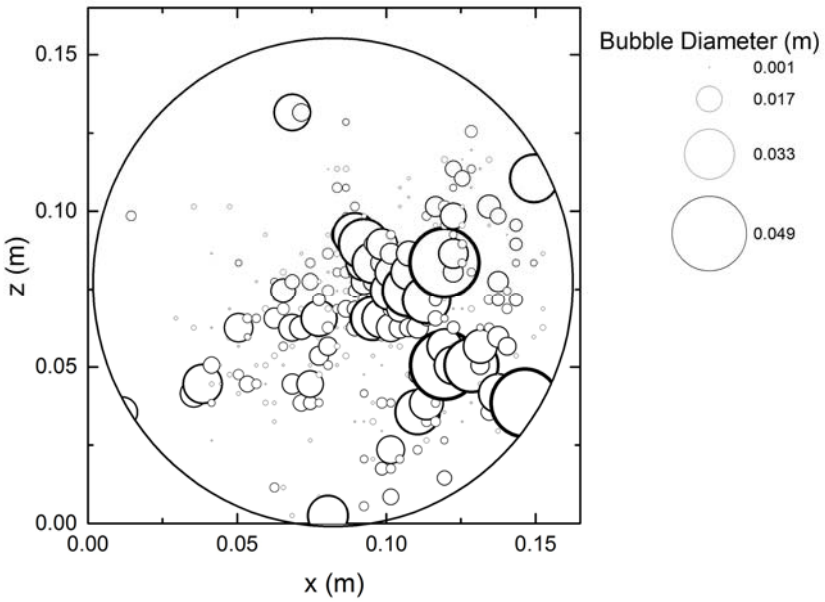
Bubble Diameter (m)
0.001
0.017
0.033
0.049
z (m)
x (m)
0.00
0.05
0.10
0.15

(g)

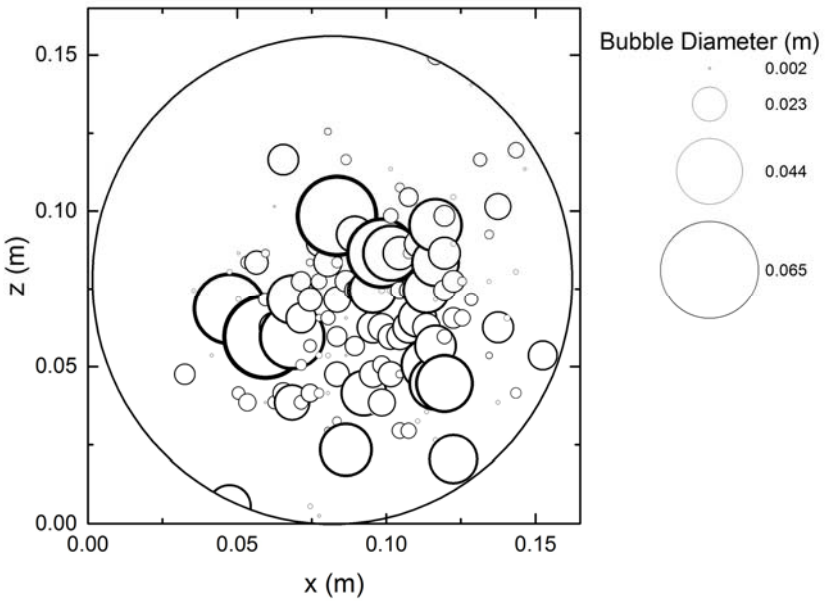

(h)

Figure 5.12 Bubble spatial distribution of flow pattern C: (a) overall view; (b) a layer at a bed height of 0-30 mm; (c) 30-50 mm layer; (d) 100-130 mm layer; (e) 160-190 mm layer; (f) 200-230 mm layer; (g) 220-250 mm layer; (h) 260-290 mm layer.

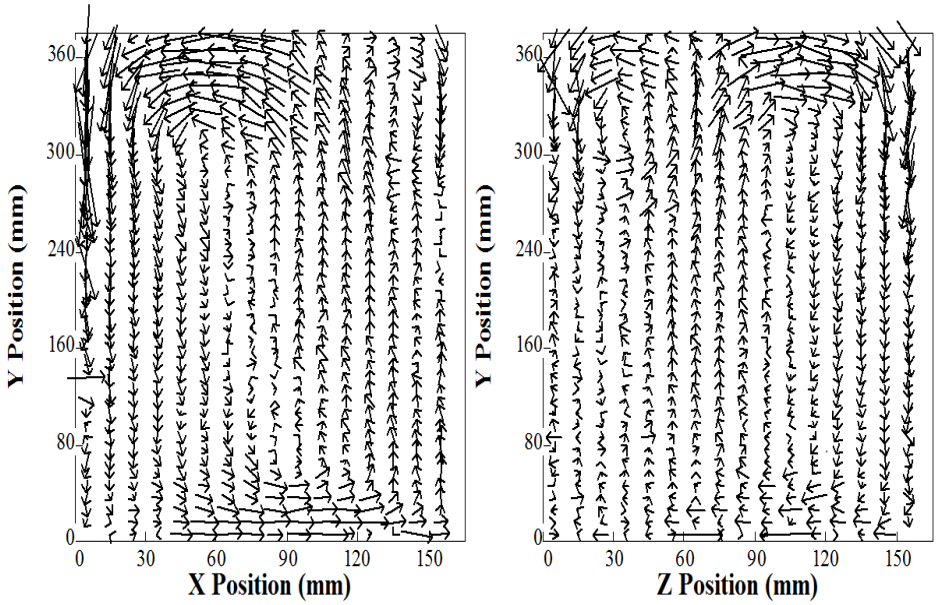

Figure 5.13 Flow pattern C.

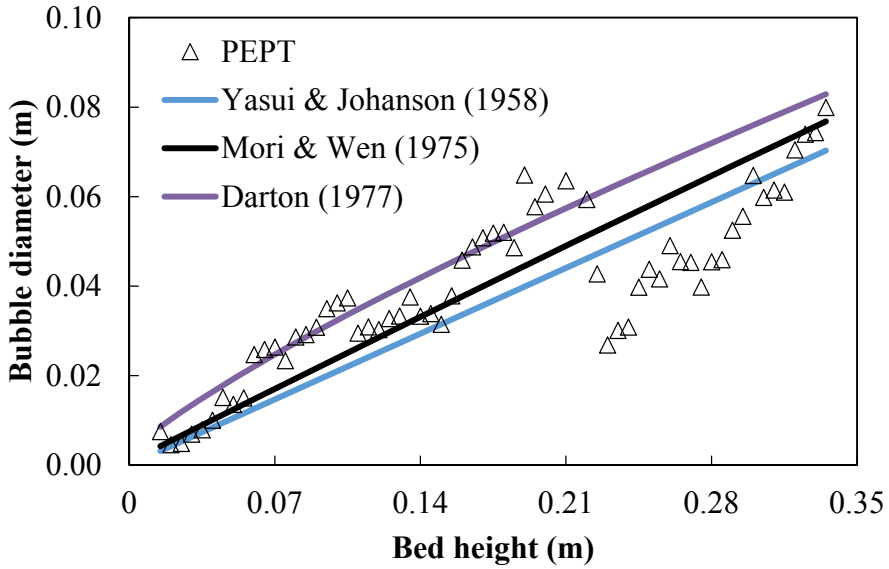

Figure 5.14 Bubbles size versus bed height for flow pattern C.

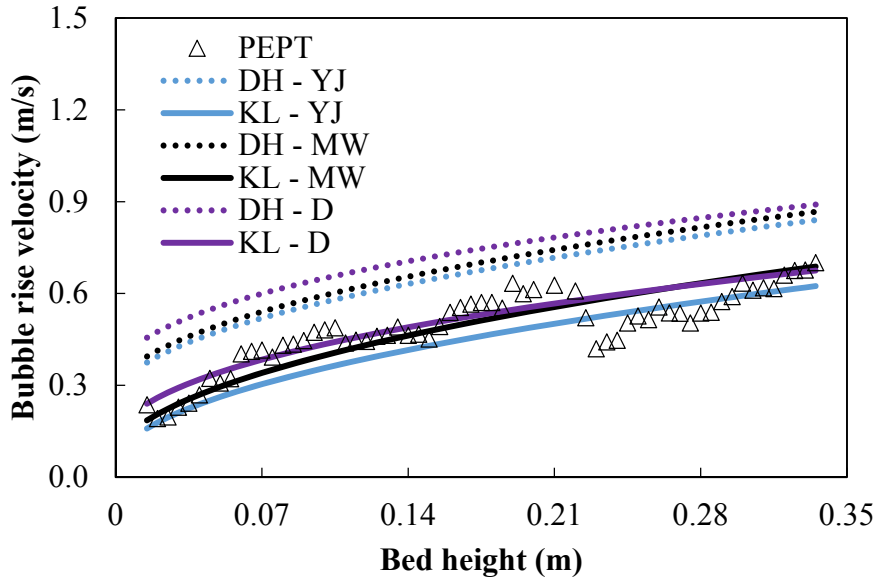

Figure 5.15 Bubble rise velocity versus bed height for flow pattern C.

DH-YJ is the bubble rise velocity predicted from Davidson & Harrison's (bubble size to rise velocity) correlation based on Yasui & Johanson's bubble size empirical correlation and KL refers to Kunii & Levenspiel's correlation, MW refers to Mori & Wen and D refers to Darton.

5.3.4 Flow Pattern D

Figure 5.16 shows the bubble spatial distribution for pattern D. It can be seen from Figure 5.16b that bubbles in pattern D are distributed uniformly in the annular region of the bed at the layer near the air distributor, and bubble sizes are small. At a bed level of 80-110 mm (Figure 5.16c), bubbles gradually move inwards to the bed centre. Bubble sizes increase, and several relatively large bubbles can be observed. At a bed height of 120-150 mm (Figure 5.16d), the large bubbles disappear, while bubbles with small and middle sizes remain until they reach a bed height of 180 mm, which indicates that large bubbles split into smaller bubbles in this layer of the bed. The bubble spatial distribution in pattern D agrees well with solid flow pattern observed using the PEPT technique (Figure 5.17), and the results also agree well with the observations presented by Werther and Molerus [178], Lim et al. [214], Weber and Mei [219] and Verma et al. [220].

Recently, Maurer et al. [271] measured the bubble distribution within a 14-cm I.D. fluidized bed of Geldart A/B particles by means of an ultra-fast X-ray tomographic scanner under ambient conditions. The researchers applied alumina particles with a mean size of 289 μm and a density of approximately 1350 kg/m^3 as the bed material. The minimum fluidization velocity (u_{mf}) was measured to be 3 cm/s, and the packed bed height was 51 cm. Maurer et al. measured the bubble distribution at different heights of the bed from 12.9 cm to 48.1 cm under the fluidization number (u/u_{mf}) of 1.5-4.0. Their results are shown in Figure 5.18, where the bubble centroids are plotted using an "x". At a 12.9-cm bed height, they observed a ring structure of bubble

distribution. The bubble distribution became more uniform and more bubbles formed over the ring structure with increasing gas velocity at this height. As the bed height increased, they observed a decrease in bubble numbers, and centroids of bubbles moved inwards to the bed centre. The researchers also reported that the inward movement of bubbles became faster as the gas velocity increased due to a higher coalescence rate. Their results are similar to the bubble spatial distribution of pattern D obtained from the PEPT results.

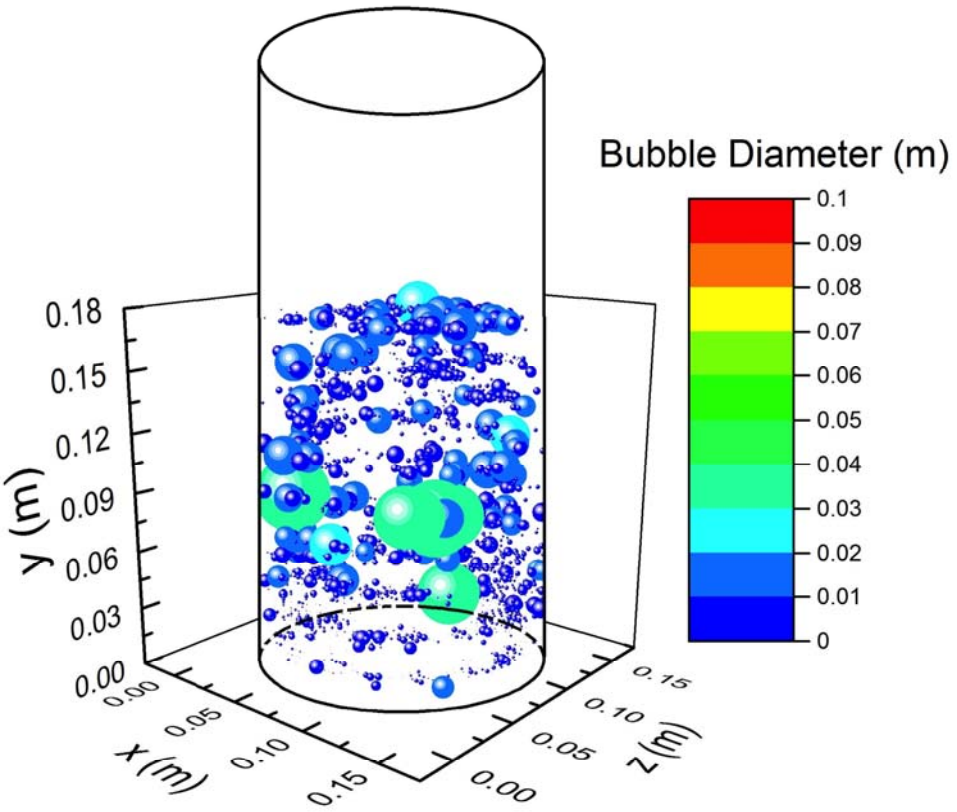

(a)

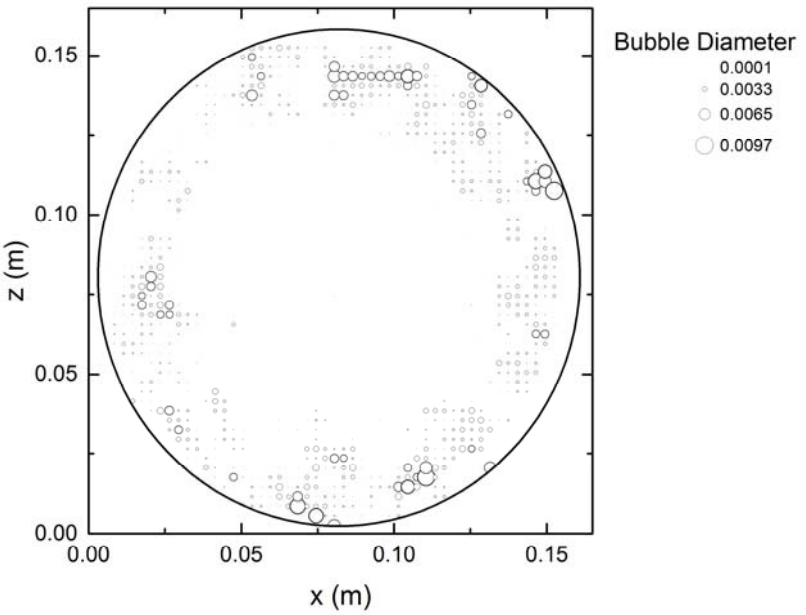
Bubble Diameter
0.0001
0.0033
0.0065
0.0097
z (m)
x (m)
0.00
0.05
0.10
0.15

(b)

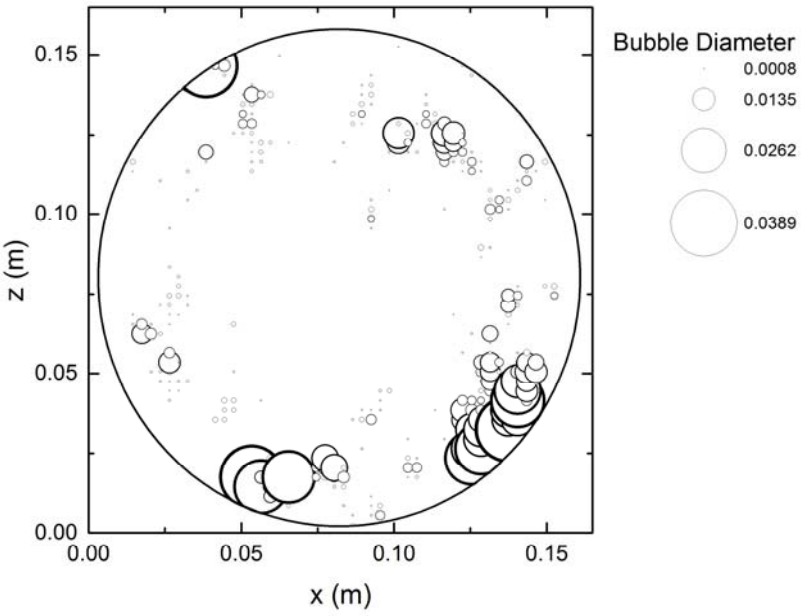
Bubble Diameter
0.0008
0.0135
0.0262
0.0389
z (m)
x (m)
0.00
0.05
0.10
0.15

(c)

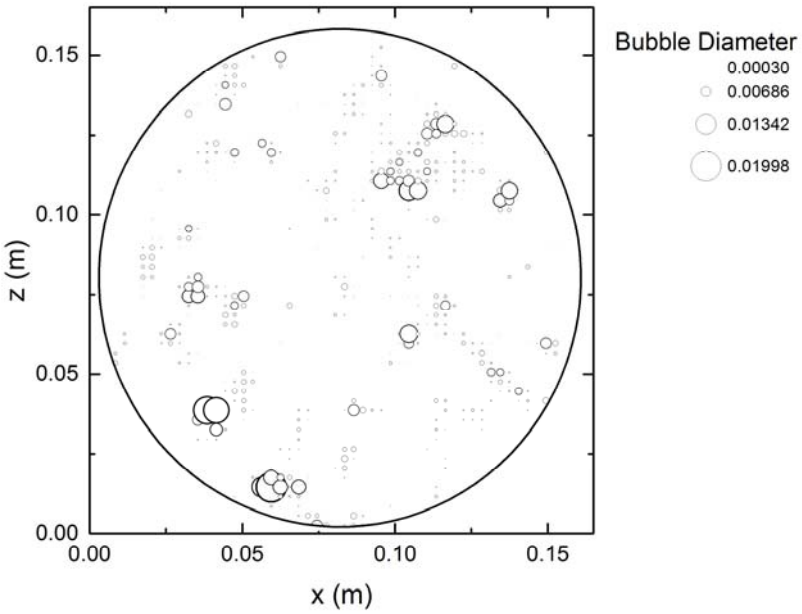

(d)

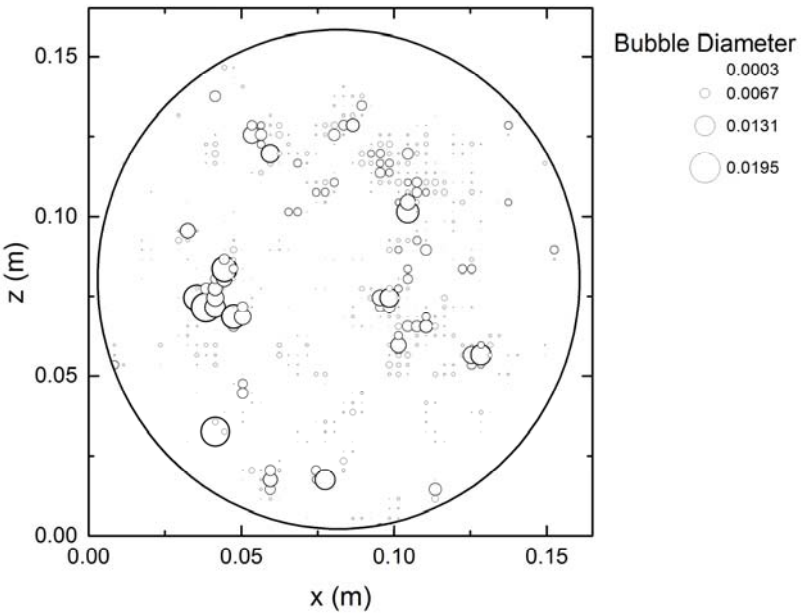

(e)

Figure 5.16 Bubble spatial distribution of flow pattern D: (a) overall view; (b) a layer at a bed height of 20-50 mm; (c) 80-110 mm layer; (d) 120-150 mm layer; (e) 140-170 mm layer.

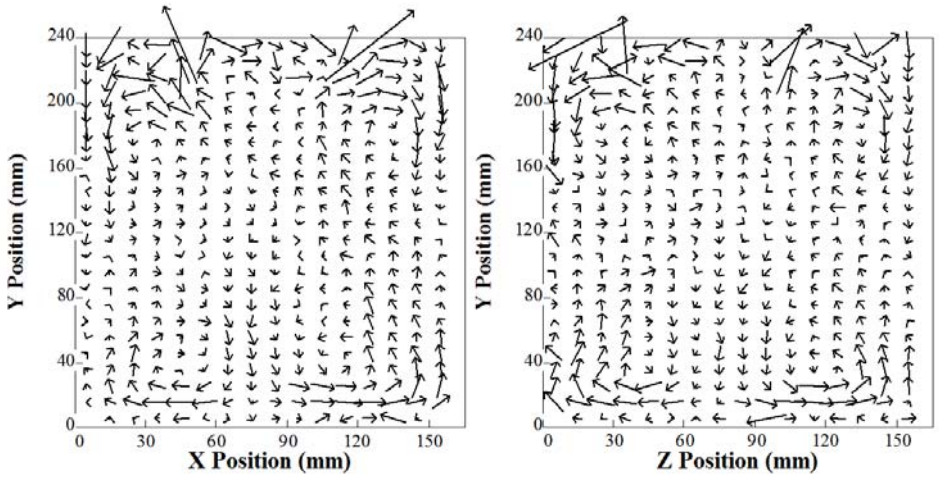

Figure 5.17 Flow pattern D.

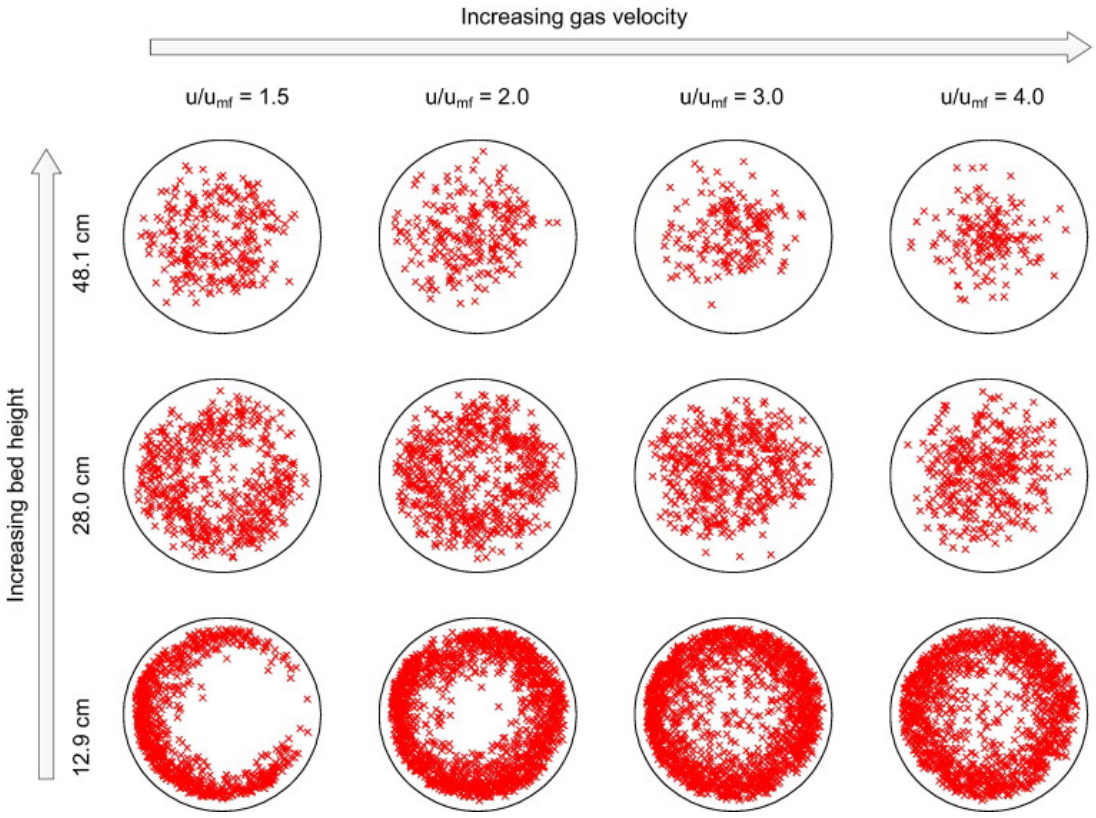

Figure 5.18 Distribution of bubble centroids at different heights and under different gas velocities measured by Maurer et al. [271].

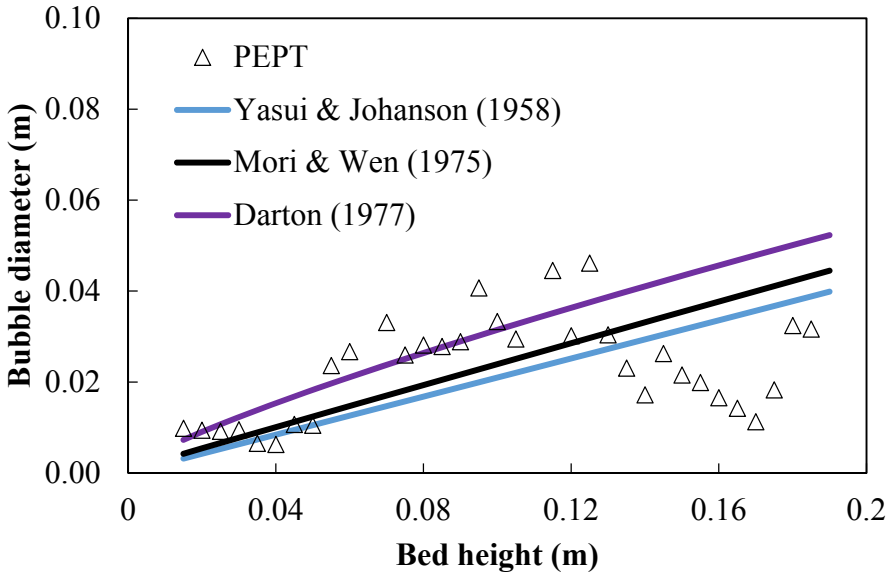

Figure 5.19 Bubbles size versus bed height for flow pattern D.

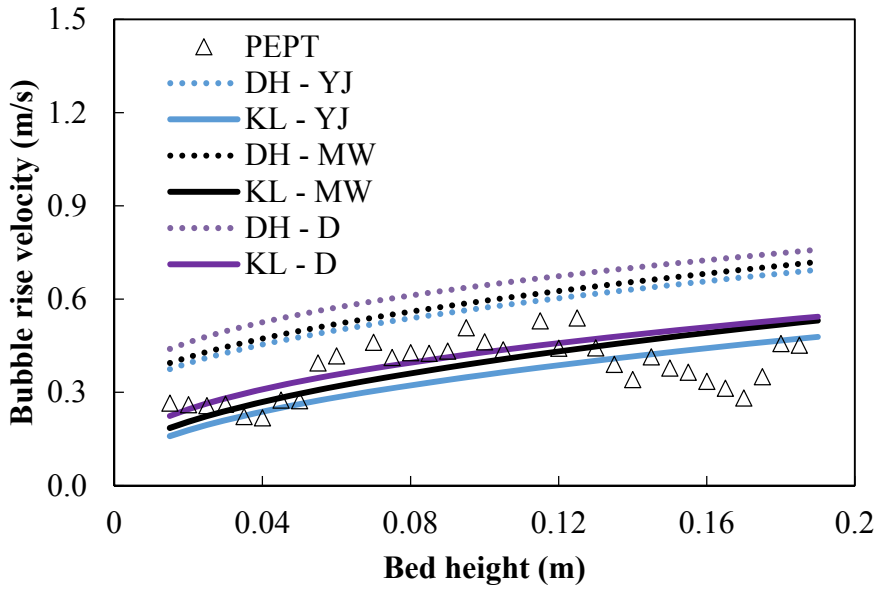

Figure 5.20 Bubble rise velocity versus bed height for flow pattern D.

DH-YJ is the bubble rise velocity predicted from Davidson & Harrison's (bubble size to rise velocity) correlation based on Yasui & Johanson's bubble size empirical correlation and KL refers to Kunii & Levenspiel's correlation, MW refers to Mori & Wen and D refers to Darton.

The interesting phenomenon observed in the bubble spatial distribution of this pattern is that the bubble size is quite uniform within the entire bed, except several large bubbles observed in the intermediate section. The bubble behaviour in pattern D is very different from bubbles in patterns A and B, in which bubble size and bubble rise velocity increase significantly with bed height. This unique bubble behaviour provides a large contact area and long bubble residence time for gas-solid interaction.

The bubble rise velocity and the bubble size of flow pattern D are calculated and compared with the predictions from the empirical correlations proposed by Yasui, Mori, Darton, Davidson and Kunii for verification of the reconstruction methods. The results are shown in Figures 5.19-5.20. It can be seen that the bubble sizes and rise velocities calculated from PEPT data are very similar to the values calculated from empirical correlations, especially when the bed height is below 0.11 m. The increases of bubble size and bubble rise velocity between the height of 0.06 and 0.11 m are due to the bubble coalescence, which can also be reflected from the reconstructed bubble spatial distribution in Figure 5.17. The following decreases in bubble sizes and rise velocities at the bed height from 0.11 m to 0.17 m are due to bubble splitting, which is only observed by the PEPT measurement, whereas the empirical correlations have not considered bubble splitting. Overall, the bubble sizes and rise velocities in the reconstructed bubble spatial distribution agree very well with the predictions from well-known empirical correlations and observations from recently published literature [271]. This further confirms that the reconstruction method proposed in the present study should be acceptable.

From Figures 5.7, 5.11, 5.15 and 5.20, it can be seen that the bubble rising velocities calculated using Kunii's correlation based on the predicted bubble size from Yasui, Morri or Darton demonstrate better agreement with the bubble rise velocity obtained using the PEPT technique as opposed to the results predicted through Davidson's correlations. This is because that the correlation of bubble rise velocity proposed by Davidson and Harrison was originally developed for estimating the rise velocity of large spherical cap bubbles in liquids [270], whereas the correlation proposed by Kunii and Levenspiel was developed from a gas-solid fluidized bed of Geldart B sand particles with an I.D. of 0.2-1.0 m and under the superficial gas velocity of 0.09-0.3 m/s [2]. The operational conditions and bed geometries used in Kunii's study were similar to those in the experiments conducted in the present study, where the bed materials are glass beads and silica sand with sizes ranging in the Geldart B classification, the bed I.D. is 0.15 m and the superficial gas velocity ranging from 0.17 to 0.64 m/s. This further confirms that the correlation proposed by Kunii and Levenspiel is more applicable for PEPT-based experiments than Davidson's correlations, as has been suggested by Fan et al. [184].

5.4 Specific Area of Bubbles

In order to further characterize the bubble behaviour and understand the fluidization performance of different flow patterns, the specific surface areas of bubbles for patterns A, B, C and D were calculated. Figure 5.21 presents the distribution of bubble specific surface area for different flow patterns in fluidized beds of 352-μm glass beads. The specific surface area of air bubbles is defined as the bubble surface area per unit

volume of gas in a fluidized bed. It can be calculated by dividing the total bubble surface area in a unit of time by the gas flow rate. The total bubble surface area in the fluidized bed was calculated from the number of bubbles that were generated per unit time at different bed heights.

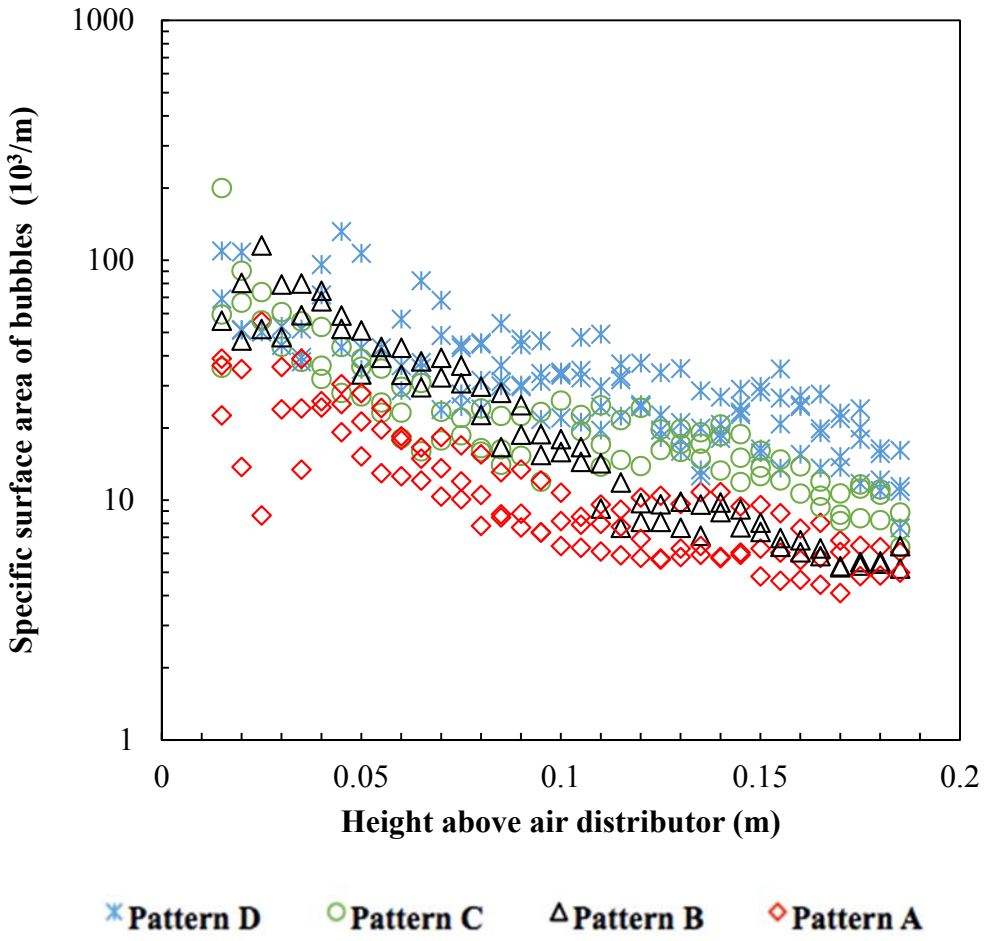

Figure 5.21 Specific surface area of bubbles against the height in fluidized beds.

The results indicate that the distribution of bubble specific surface area varies significantly with different solid flow patterns according to the following hierarchy:

D > C > B > A. Pattern D features the largest bubble specific surface area, while bubbles in pattern A feature the smallest specific surface area. The specific surface areas for pattern B and C can be discussed based on two sections: the lower and upper sections of the bed. Below the intermediate height of the bed, the bubble specific surface area in pattern B is greater than that in pattern C. Conversely, above this height, the specific surface area in pattern B decreases along the bed height more rapidly than that in pattern C, and the bubble specific surface area in pattern C becomes greater than that in pattern B. The bubble specific surface area presented in Figure 5.21 is in robust agreement with solid flow patterns and reconstructed bubble spatial distributions.

5.5 Conclusion

The bubble spatial distribution in a bubbling fluidized bed can be reconstructed based on the solid motion measured using the PEPT technique. The bubble spatial distribution in a fluidized bed varies significantly with solid flow patterns. In pattern A, bubbles move upwards in a narrow channel, and bubbles grow relevantly fast from several millimetres to several centimetres as the bed height increases. In pattern B, bubbles are uniformly distributed near the air distributor and move inwards to the centre as the bed height increases. Bubble sizes are relatively uniform and smaller than 2.5 cm when bed height is below 10 cm, generating a large contact area for gas and particles. Conversely, above this level, the bubble sizes increase significantly along the bed height. In pattern C, the bubbles are distributed over the entire cross-sectional area, but the population of bubbles is higher on one side of the bed. In addition, the variation of bubble size in the same layer is large. In pattern D, bubbles are formed

uniformly in the annular region near the air distributor and then move inwards as the bed height increases. Bubble sizes are small and relatively uniform throughout the entire bed. Optimal solid-gas contact area and sufficient bubble residence time can be expected in pattern D.

The bubble spatial distribution agrees well with recently published results, in which pattern D was observed by means of an X-ray tomographic scanner in the lower section of a 14-cm I.D. fluidized bed (12.9 cm/51 cm) [271]. To further validate the bubble reconstruction method, bubble sizes and rise velocities calculated using the measured PEPT data have been compared with well-known empirical correlations. The results show that the bubble size and rise velocities calculated from the PEPT results for the reconstruction of bubbles agree well with the predictions from well-known empirical correlations proposed by Yasui and Johanson, Mori and Wen and Darton. This indicates that the method proposed in the current study for reconstructing the bubble spatial distribution from the PEPT data is acceptable.

The bubble surface area generated in pattern D is much larger than that in pattern A, B, and C. In combination with the previous findings discussed in this thesis, these data further confirm that pattern D offers the best gas-solid contact and mixing behaviour, where bubbles are generated in small sizes and uniformly distributed throughout the bed.

Chapter 6: Qualifying Mixing of Solids in Bubbling Fluidized Beds

6.1 Introduction

Solid mixing is a key factor of fluidized beds, especially for chemical reaction processes and their large-scale applications [187, 202]. Solid mixing affects the contact between solids and gas, heat and mass transfer and therefore the overall reaction/conversion rate in fluidized bed reactors (e.g., the conversion of fuel in combustion and gasification processes) [31, 170, 188]. An excellent solid mixing profile will create a more homogeneous temperature field across the bed [189], which prevents hot spots from forming [2, 214] and is also ideal for exothermic or endothermic reversible reaction processes. Conversely, poor solid mixing typically reduces the conversion and selectivity of solids [2]. Hence, to fully understand the mixing process of solids in a fluidized bed is of critical importance for the design, operation and control of fluidized beds in various physical and chemical processes.

Various techniques have been proposed to experimentally estimate the solid mixing in fluidized beds since the late 1940s [2, 188, 204-206]. For example, researchers [199, 201, 210] have used a layer of tracer particles placed horizontally inside fluidized beds and measured the tracer concentration in collected samples. Some researchers [2, 198, 200] have placed two types of particles at different layers of the bed and examined the extent of their intermixing. Others [2, 202, 207-209] have introduced tracer particles by step- or pulse-injection into the bed and determined the residence time distribution

and concentration of the tracer particles. Another approach employed [2, 198, 203] has been measurement of the heat flow between different-temperature particles placed in the top or bottom sections of the bed, followed by investigation of the solid mixing behaviour based on the assumption that the heat transport in the fluidized bed was caused only by the motion of solids. Researchers [2, 183, 198] have also followed individual tracer particles for a long period of time and examined the solid mixing profile. Despite this wealth of different approaches, experimental difficulties have always arisen in the determination of solid mixing in fluidized beds. These challenges exist due to the highly dynamic and complicated flow structure within the fluidized bed [183, 188, 272] and the lack of an appropriate measurement technique [198, 207, 210]. The solid mixing behaviour in a fluidized bed has been mainly represented in terms of vertical or horizontal dispersion coefficients, while the results differ significantly in the literature due to the various techniques used [1, 2, 187, 207, 273]. In addition, the dispersion coefficient is usually obtained by fitting one of the two most popular models to the experimental data [2, 46, 198, 274], the dispersion model or the counter current backmixing model [212], while both feature some restrictions and limitations [198, 207, 213].

In this study, the non-invasive PEPT measurement technique [28, 137, 139, 158, 243] was applied in order to investigate the mixing behaviour of solids in opaque 3-D fluidized beds. The dispersion coefficients of particles in vertical and horizontal directions were calculated at different locations within the bed based on particle trajectories. The results were analysed and compared with the bubble spatial distribution and solid flow patterns in order to estimate the relationship between solid

mixing behaviour and bubble spatial distribution/solid flow patterns. An active index (AI) has been developed in this chapter to evaluate the solid mixing behaviour within fluidized beds based on the inflow and outflow of tracer particle through a specific volume. The AI was obtained at different positions in the bed to investigate its relationship with solid flow patterns. The distribution of average residence time of the tracer particle at different positions within the bed was also determined based on the AI. The results will help to understand the solid mixing behaviour within fluidized beds and the effects of solid flow patterns on the solid mixing.

6.2 Dispersion Coefficient of Particles

The dispersion coefficient of solids is defined by analogy with the diffusion coefficient, which describes molecular particle motion in fluids [1, 198] and was first introduced by Einstein [275] who considered the motion to be a “random walk” [1, 276]. The solid dispersion coefficient expresses the vertical and horizontal components of the particle motion [1] and has been commonly used to quantify the solid mixing in fluidized beds [2, 166, 187, 277-279]. An ideal method to determine the solid dispersion coefficient is to follow the dispersion of a number of tagged particles [151], where all the tagged particles are released from the same starting position at the same time, as illustrated in Figure 6.1. These particles would move further apart within the fluidized bed if particles undergo good dispersion and the solid mixing is uniform over the bed. Otherwise, particles can remain localized if they tend to follow a specific circulation pattern within the bed, indicating that the solid mixing is poor. To analyse the dispersion of a number of particles in the bed, the fluidization must be stopped before samples are taken from various locations for analysis. The sampling tube will

disturb the fluidization state. After several samplings, the positions of the particles may shift; therefore, the results may be incapable of representing the actual dispersion within the bed. It is also not possible to directly use this method to simultaneously analyse the dispersion of the particles within a fluidized bed experimentally, since no measurement technique has been developed to track a number of particles simultaneously [151]. This section describes the analysis of solid dispersion in the current research and the determination of the solid dispersion coefficient without stopping the fluidization and disturbing the particle dispersion state based on the PEPT data.

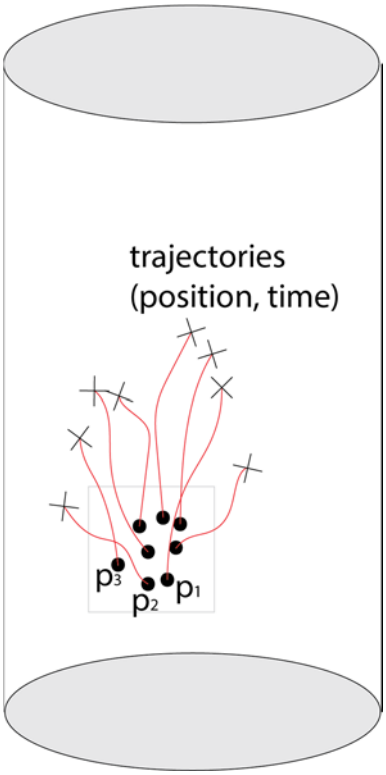

Figure 6.1 A sample of tagged particles and their dispersion.

During the PEPT experiments, a tracer particle was randomly selected from the bed bulk material, and the real time motion of the tracer particle was measured. Based on the ergodic hypothesis [280, 281], if the tracer particle has been tracked for a long enough period, the motion of the tracer particle can effectively represent the general behaviour of particles moving through the vessel. Hence, by examining the trajectories of a tracer particle that has travelled throughout the entire bed, it is possible to obtain a reasonably accurate estimation of the solid mixing and dispersion profile within the equipment. This was done by first dividing the bed into many small compartments and then analysing the dispersion of the particles from different positions. Figure 6.2a gives a schematic of the division in the x-y plane of view. The compartment in the highlighted shadow will be used as an example to describe the method used in this study to evaluate the dispersion coefficient. The compartment is located at (x=295-310, z=210-225, y=160-190) and is designated as the releasing position from which sample tagged particles will be released. During the experiment, the tracer particle fell into this compartment many times, as seen in Figure 6.2b. Imagining that each passage through this compartment is recorded as an individual particle, “n” passages through this compartment can be assumed to be “n” particles releasing from this position, and the subsequent positions of these “n” particles are the result of particle dispersion. However, this assumption will result in an overlap of each sequence of data if these “n” particles are all taken into account, and the successive estimates of solid dispersion will not be independent. In order to avoid dependent estimations, a number of particles (i.e., N=100) were randomly selected from these “n” particles and used as sample tagged particles that release from the compartment position at the same time. The subsequent positions of these N particles were followed as if tracking the dispersion

of a number of tagged particles, and 300 succeeding positions were followed in the present study. In addition, since the tracer particle was followed by the PEPT technique every 3-10 ms during the PEPT experiments, the exact time interval between successive positions of these N particles can be different. Hence, the time intervals for each instantaneous displacement of the N particles were averaged in order to reconstruct the solid dispersion process over time. Figure 6.3 illustrates the reconstructed solid dispersion of 100 sample particles releasing from the compartment. It can be seen that particles are within the compartment at the beginning and progressively disperse as time goes on. The dispersion coefficient can then be obtained from the mean squared displacement of the dispersing particles using the Einstein relation [275], as shown in Equation 6.1 for the vertical direction (1-D) or Equation 6.2 for the horizontal direction (2-D) [1, 158], where S is the mean displacement at time interval t, and D is the solid dispersion coefficient. In the present research, the solid dispersion coefficient was calculated in both vertical and horizontal directions in order to understand the different mechanisms of solid mixing and to evaluate their relevant contributions.

$$S^2(dt) = 2Ddt \qquad \text{(1-D)} \tag{6.1}$$

$$S^2(dt) = 4Ddt \qquad \text{(2-D)} \tag{6.2}$$

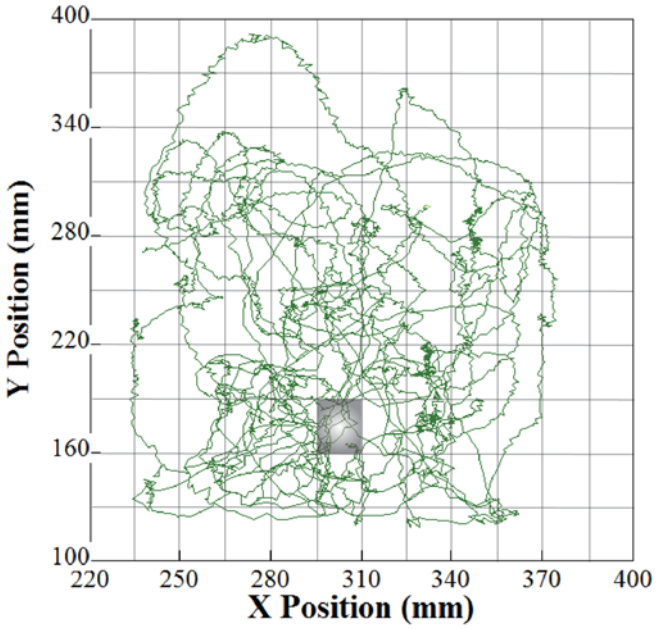

(a)

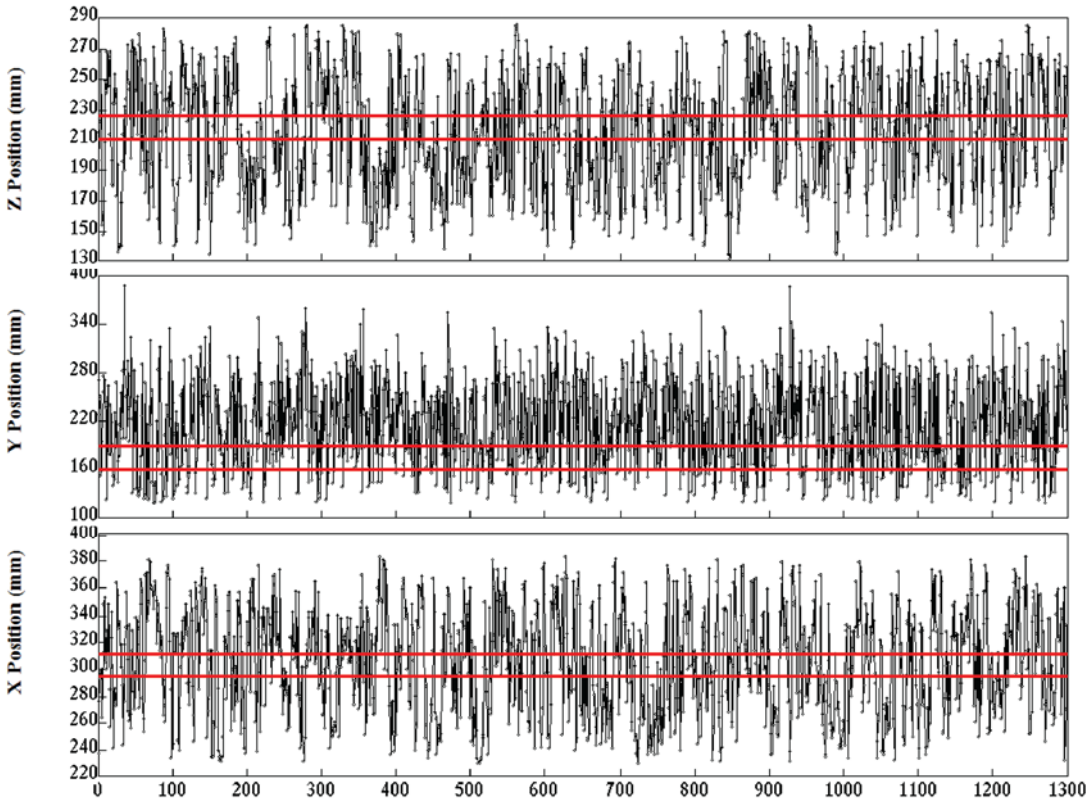

(b)

Figure 6.2 Illustration of the method for calculating solid dispersion coefficients: a) bed division; b) location of the sample compartment.

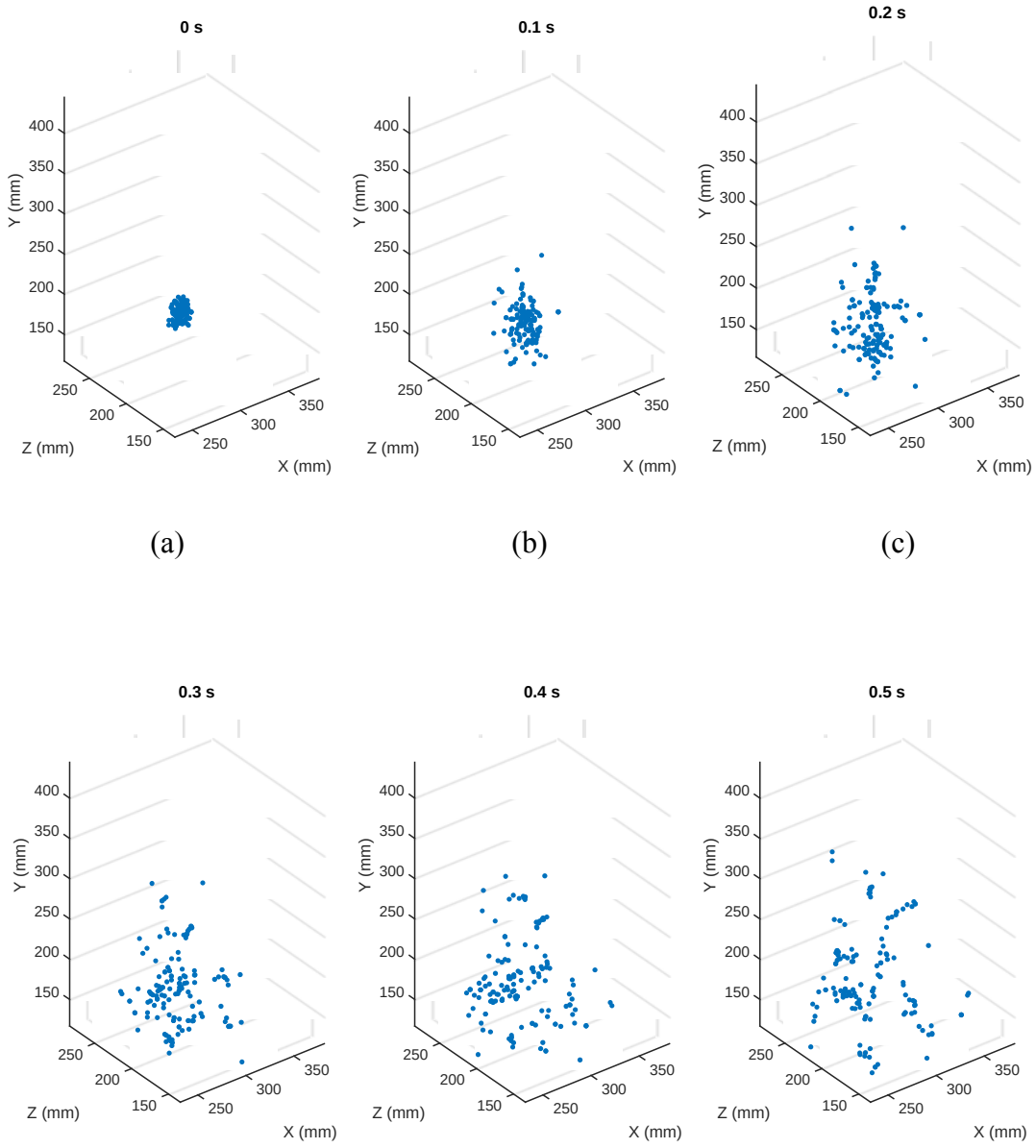

Figure 6.3 Dispersion of particles at different times: (a) 0 s; (b) 0.1 s; (c) 0.2 s; (d) 0.3 s; (e) 0.4 s; (f) 0.5 s.

Parker et al. [158] and Mostoufi and Chaouki [187] used similar methods to estimate the solid vertical dispersion coefficient. However, these two research groups selected

the sample particles at a given interval from the entirety of particles passing through the compartment instead of randomly, which may not efficiently represent the dispersion of solids. In this section, both vertical and horizontal solid dispersion coefficients are obtained using the aforementioned method. This method begins with the calculation of mean squared vertical and horizontal displacements of particles over time. As discussed previously, N particles are released from the starting position (x_0, z_0, y_0) within the fluidized bed at the same time, t = 0, as illustrated in Figure 6.3a. Then the next recorded position of each particle is given by (x_{i1}, z_{i1}, y_{i1}), and the time interval between these two successive positions will be t_{i1}. Where "i" represents the i^{th} particle and "1" represents the first recorded position starting from the releasing point. As mentioned previously, t_{i1} is different for each investigated particle, hence the average will be used as the time when particles disperse to their second recorded positions from the releasing point, and this is given by Equation 6.3.

$$t_1 = \frac{1}{N}\sum_{i=1}^{N} t_{i1} \tag{6.3}$$

The instantaneous vertical displacement of each released particle at t = t_1 can then be defined through Equation 6.4, and the instantaneous horizontal displacement at t = t_1 can be calculated through Equation 6.5.

$$S_{vi}(t_1) = y_{i1} - y_0 \tag{6.4}$$

$$S_{hi}(t_1) = \sqrt{(x_{i1} - x_0)^2 + (z_{i1} - z_0)^2} \tag{6.5}$$

Where $S_{vi}(t_1)$ is the instantaneous vertical displacement of the i^{th} particle at t = t_1,

$S_{hi}(t_1)$ is the instantaneous horizontal displacement of the i^{th} particle at t = t_1 and (x_{i1}, z_{i1}, y_{i1}) is the second position of the i^{th} particle from the starting point.

The instantaneous displacement is obtained for all the released particles in order to get the mean squared displacement of these particles from the starting point, which is calculated through Equation 6.6, and the new mean position of these dispersed particles is given by Equation 6.7.

$$\begin{cases} S_v(t_1)^2 = \frac{1}{N}\sum_{i=1}^{N} S_{vi}(t_1)^2 \\ S_h(t_1)^2 = \frac{1}{N}\sum_{i=1}^{N} S_{hi}(t_1)^2 \end{cases} \tag{6.6}$$

$$\begin{cases} x_{t1} = \frac{1}{N}\sum_{i=1}^{N} x_{i1} \\ y_{t1} = \frac{1}{N}\sum_{i=1}^{N} y_{i1} \\ z_{t1} = \frac{1}{N}\sum_{i=1}^{N} z_{i1} \end{cases} \tag{6.7}$$

Where $S_v(t_1)$ is the mean squared vertical displacement of these N particles from the starting position at t = t_1, $S_h(t_1)$ is the mean squared horizontal displacement of N particles at t = t_1 and (x_{t1}, z_{t1}, y_{t1}) is the mean position of N particles at t = t_1.

The particles will continue dispersing to (x_{i2}, z_{i2}, y_{i2}), having the mean dispersion time and instantaneous displacement of:

$$\begin{cases} t_2 = \frac{1}{N}\sum_{i=1}^{N} t_{i2} \\ S_{vi}(t_2) = y_{i2} - y_{t1} \\ S_{hi}(t_2) = \sqrt{(x_{i2} - x_{t1})^2 + (z_{i2} - z_{t1})^2} \end{cases} \quad (6.8)$$

Where t_{i2} is the time interval for the i^{th} particle between (x_{i2}, z_{i2}, y_{i2}) and the starting position, t_2 is the mean time when particles disperse to (x_{i2}, z_{i2}, y_{i2}), $S_{vi}(t_2)$ is the instantaneous vertical displacement of the i^{th} particle at t = t_2 and $S_{hi}(t_2)$ is the instantaneous horizontal displacement of the i^{th} particle at t = t_2.

The calculation is iterated until the mean squared displacement of the released particles becomes stable against time, which means that particles have sufficiently dispersed; the dispersion coefficient of particles in the vertical direction (D_v) and horizontal direction (D_h) can then be determined by Equation 6.9 from the linear, increasing portion.

$$\begin{cases} D_v = \frac{1}{2} \cdot \frac{d{S_v}^2}{dt} \\ D_h = \frac{1}{4} \cdot \frac{d{S_h}^2}{dt} \end{cases} \quad (6.9)$$

Figure 6.4 gives the plots of the vertical and horizontal mean squared displacements of particles against time, and the slopes of the linear portion are related to the solid dispersion coefficient. It can be seen that the mean squared displacement increases constantly and nearly linearly over time at the beginning. This is because particles are moving apart from each other and dispersing progressively in the bed; this is also evident in Figure 6.3a-c, where particles undergo significant displacements. However,

after a specific time (i.e., 1-2 s), the mean squared displacement becomes roughly stable against time, which indicates that particles have completely dispersed within the bed and have generated a uniform mixture. This is also evident in Figure 6.3d-f where the solid dispersion is less obvious and particles are uniformly distributed throughout the bed. Particles are in dynamic equilibrium at this time and no further dispersion will take place due to the fact that the concentration gradient has vanished [187]. The vertical and horizontal dispersion coefficients of the solids can then be obtained according to Equation 6.9 from the linear slopes in Figure 6.4.

It has been identified that solid mixing occurs by several main mechanisms and is initiated by bubbles [2, 190, 191]. Solid vertical mixing mainly occurs when bubbles drag surrounding solids into their wake regions [192]. Solids within the wake regions are quite turbulent, and the wakes are periodically shed and replenished as the bubbles rise through the bed, thereby inducing sizeable vertical displacement. While the solid horizontal mixing can occur according to four different mechanisms: 1) when solids are transported into the drifts of bubbles from the dense phase and are drawn up below the bubbles as spouts [193]; 2) when bubbles erupt at the bed surface, and solids are ejected from the bubble wakes or top of bubbles and distributed over the bed surface [194, 195]; 3) due to bubble lateral motion, which is the consequence of interaction and coalescence between adjacent bubbles [2, 190, 191, 193-195] and 4) due to eddies induced by passing bubbles during the solid downward movement [5, 196, 197]. Hence uniform dispersion coefficients obtained at different positions of a fluidized bed should demonstrate favourable solid mixing behaviour as well as indicate uniform bubble development. Ideally, the dispersion coefficient of solids should be uniform and large

in both vertical and horizontal directions to indicate that particles are spread homogeneously and rapidly over the entire bed [282]. A non-uniform dispersion coefficient profile, despite some large values may be obtained in limited areas within the bed, may be due to bubble bypass and the heterogeneous distribution of bubbles which induce a strong solid motion in specific regions. This scenario involving a non-uniform dispersion coefficient profile and will widen the gas and solid residence time distributions and reduce gas-solid contact efficiency [31]. Therefore, it is crucial to investigate the dispersion of solids that feed at different positions and evaluate the distribution uniformity as well as the magnitude of the dispersion coefficient over the bed; this is also crucial for minimizing excess air and improving fluidized bed designs [282].

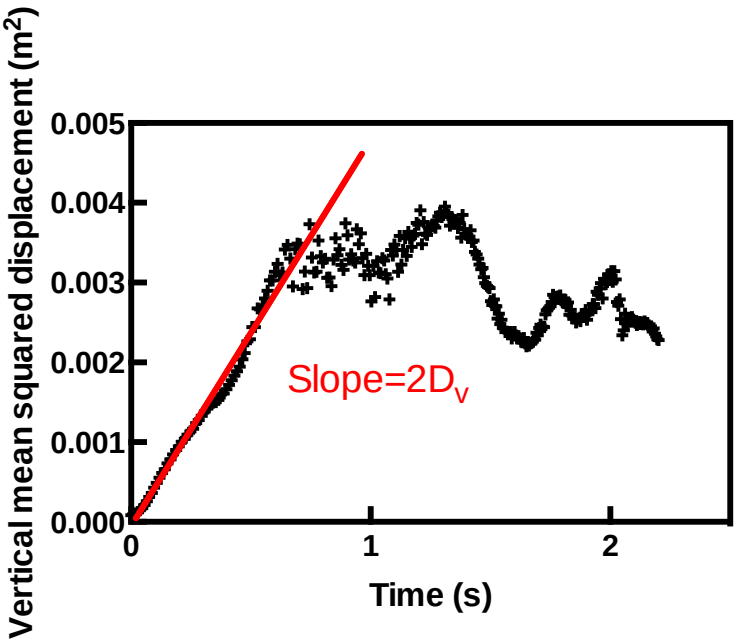

(a)

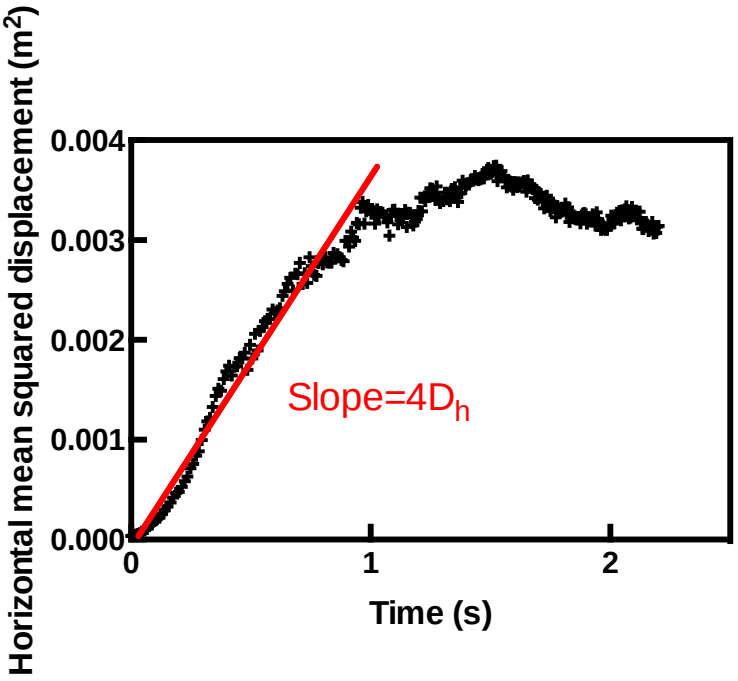

(b)

Figure 6.4 Mean squared displacement of particles: (a) vertical direction; (b) horizontal direction.

The uniformity of solid vertical and horizontal dispersion coefficients has then been evaluated for the four flow patterns in the bottom, intermediate and top sections of the fluidized bed in the present study (Table 6.1). The mean dispersion coefficient at different layers has been also calculated to investigate the solid dispersion as a function of bed heights, and the results are presented in Figure 6.8. The solid dispersion coefficient is within the range of 3.3-7.1×10^{-3} m^2/s and 1.0-1.5×10^{-3} m^2/s in the vertical and horizontal directions, respectively, similar to results reported in the literature [283, 284]. Although pattern A has a relatively large dispersion coefficient in the bottom section, the distribution uniformity of the obtained dispersion coefficient is not

favourable. Dispersion uniformity has been counted among the most important factors in fluidized bed efficiency, and the dispersion coefficients in both the vertical and horizontal directions are of the same order and do not have a sizeable difference. In the bottom section of the bed, the hierarchy of solid mixing behaviour among the four patterns from better to worse, has been identified as B > D > C > A in the vertical direction and C and D > A and B in the horizontal direction.

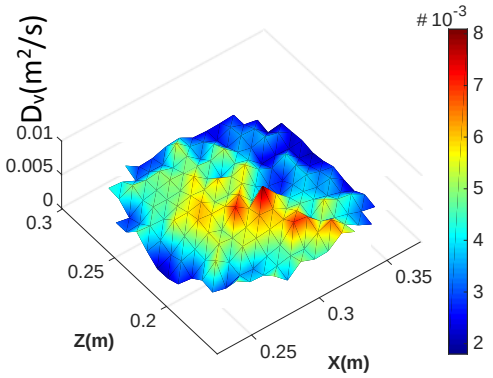

(1-a)

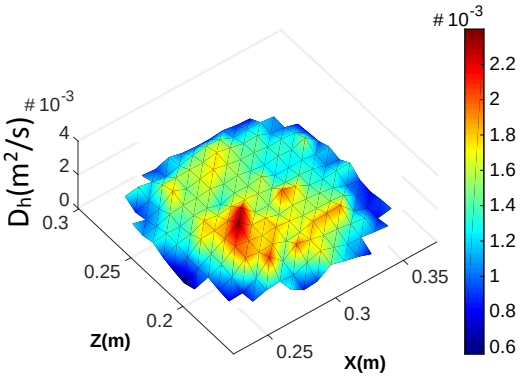

(1-b)

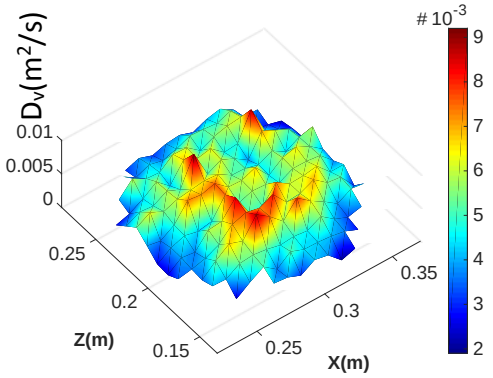

(2-a)

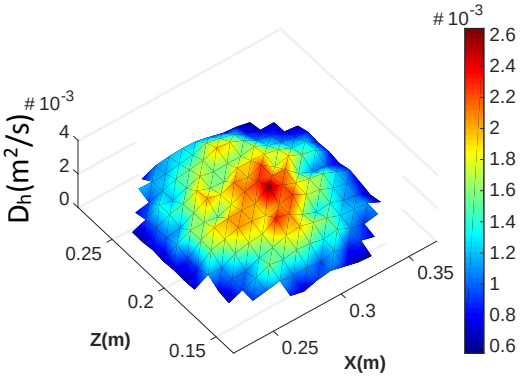

(2-b)

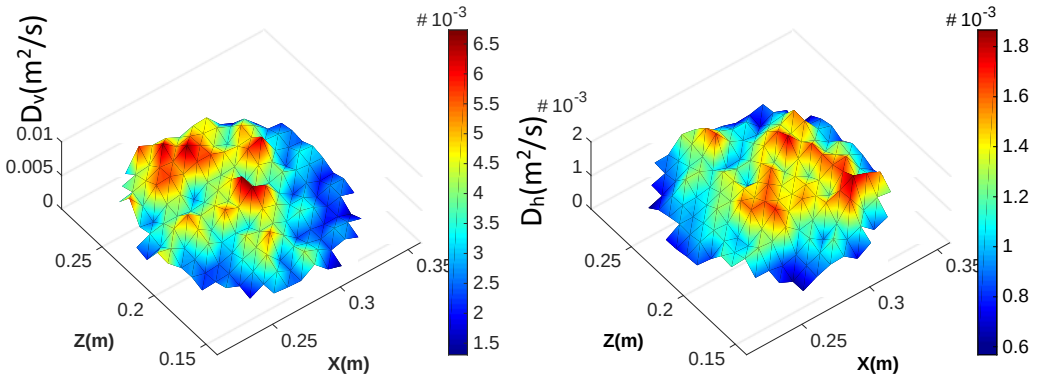

(3-a) (3-b)

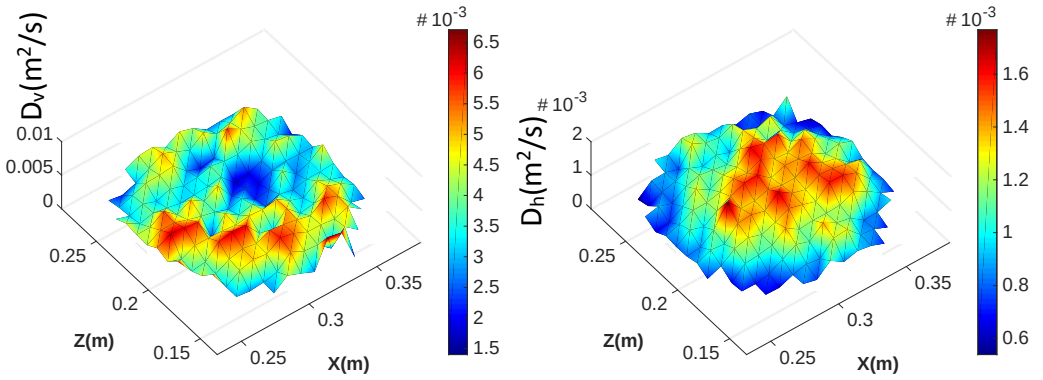

(4-a) (4-b)

Figure 6.5 Dispersion coefficient map for the lower section of the bed (30-80 mm): (1) pattern A; (2) pattern B; (3) pattern C; (4) pattern D; (a) vertical direction; (b) horizontal direction.

When solids are released and disperse from the intermediate section, which is 90-140 mm above the air distributor, the obtained dispersion coefficient is different from that obtained near the air distributor. As shown in Figure 6.6, the dispersion coefficient is large near the centre and small near the bed wall in both vertical and horizontal directions in pattern A; the vertical dispersion coefficient is uniform over the layer in

patterns B, C and D, while the distribution in the horizontal direction in patterns C and D are more uniform than in pattern B. The solid horizontal dispersion coefficient in pattern B is large in the centre of the layer and small near the bed wall. Comparing the dispersion uniformity (Figure 6.6 and Table 6.1) and coefficient magnitude (Figures 6.6 and 6.8) for the four flow patterns in the intermediate section of the bed, the hierarchy of solid mixing has been identified as D > B > C > A in the vertical direction and D > C > A and B in the horizontal direction.

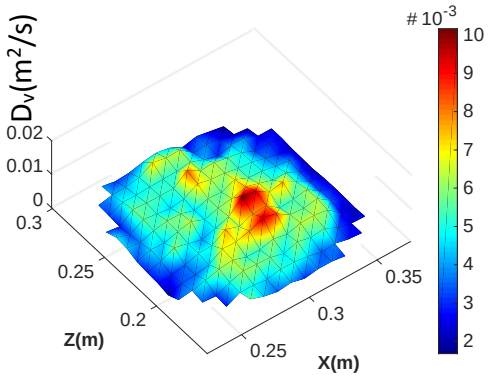

(1-a)

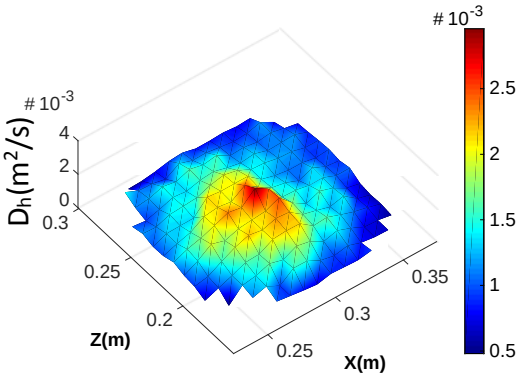

(1-b)

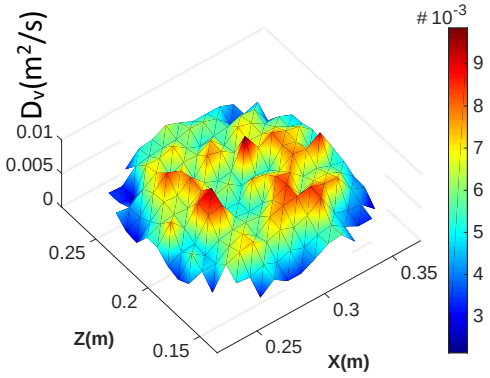

(2-a)

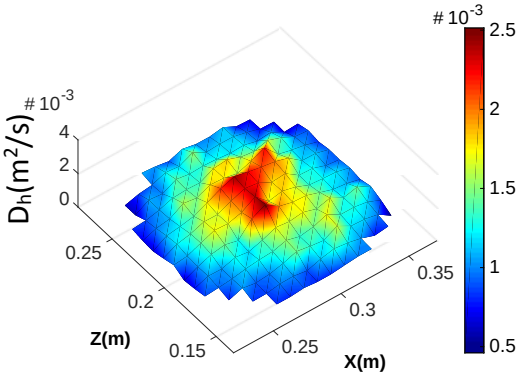

(2-b)

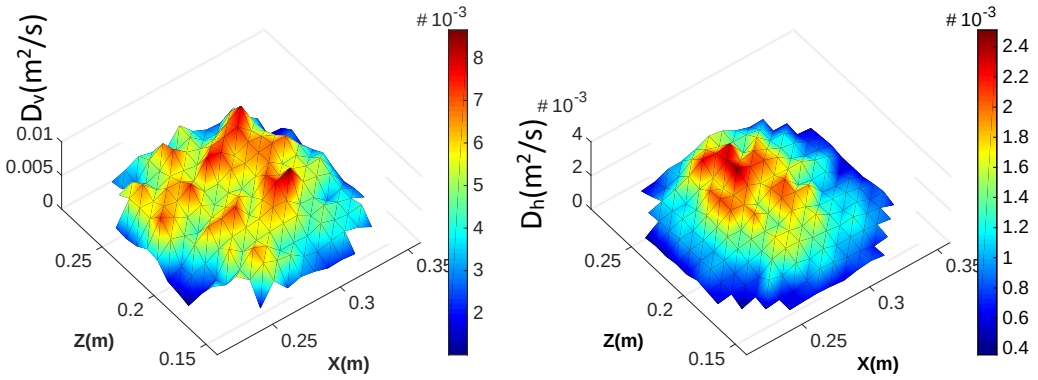

(3-a) (3-b)

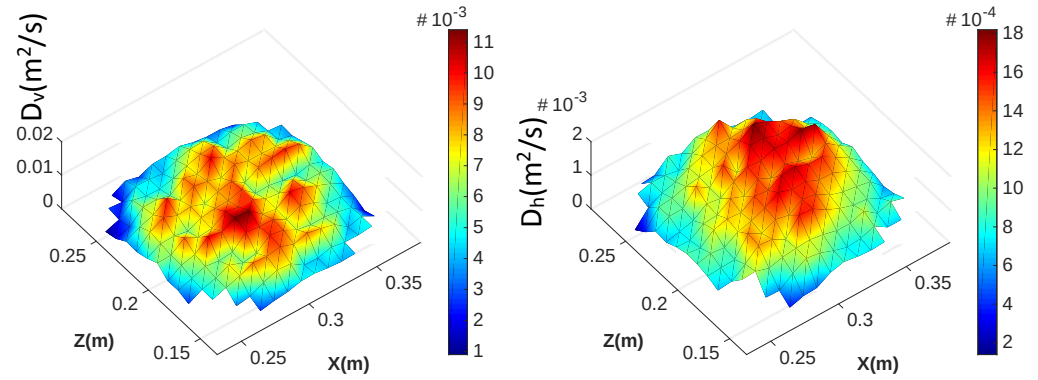

(4-a) (4-b)

Figure 6.6 Dispersion coefficient map for the intermediate section of the bed (90-140 mm): (1) pattern A; (2) pattern B; (3) pattern C; (4) pattern D; (a) vertical direction; (b) horizontal direction.

The particle dispersion in the top section of the bed can be seen from the coefficient map shown in Figure 6.7. In pattern A, the vertical dispersion coefficient is not uniform and is large only within a narrow area near one side of the bed wall. Meanwhile, the horizontal dispersion coefficient is large around the centre of the layer and small near the bed wall. In pattern B, the vertical dispersion coefficient is large near the bed wall

and small in the centre. The horizontal dispersion coefficient is similar to pattern A, being large in centre and small close to bed wall. The vertical dispersion coefficients in patterns C and D are very uniform in the top layer. Similarly, the horizontal dispersion coefficients of pattern C and D are more uniform than those of patterns A and B. Compared with the bubble spatial distribution and the solid flow patterns in the top section of the bed, it can be found that the vertical dispersion coefficients in patterns A and B (Figures 6.7-1a and 6.7-2a) are large where strong descending solid streams present and are small where significantly large bubbles can be observed. These phenomena, as discussed previously, are due to the fact that bubbles coalescing into larger sizes and burst at the bed surface that result in a greatly reduced solid concentration in this area. According to the aforementioned solid mixing mechanisms, bubble bursting induces large solid horizontal displacement over the bed surface, and solids will no longer rise after bubble bursting occurs at the bed surface; this may indicate that solid vertical mixing will mainly occur in the solid descending stream and solid horizontal mixing will increase with bubble bursting near the bed surface. In patterns A and B, particles are near the bed surface at a layer 150-200 mm above the air distributor. In patterns C and D, a uniform vertical dispersion profile can be seen over the whole layer (Figures 6.7-3a and 6.7-4a); this reveals a higher bed expansion, a uniform bubble development and a large gas-solid contact efficiency for patterns C and D. Considering the uniformity and magnitude of solid dispersion (Table 6.1 and Figure 6.8), the hierarchy of solid mixing behaviour among the four patterns in the top section of the bed can be identified as D > C > B > A in the vertical direction and C and D > A and B in the horizontal direction.

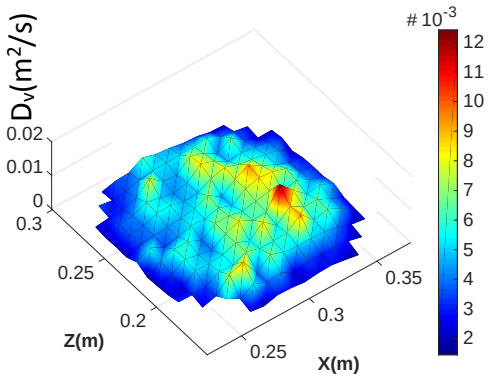

(1-a)

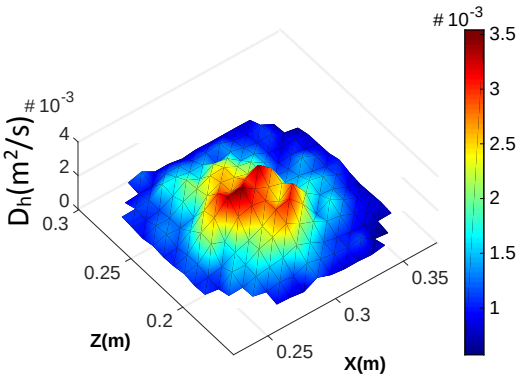

(1-b)

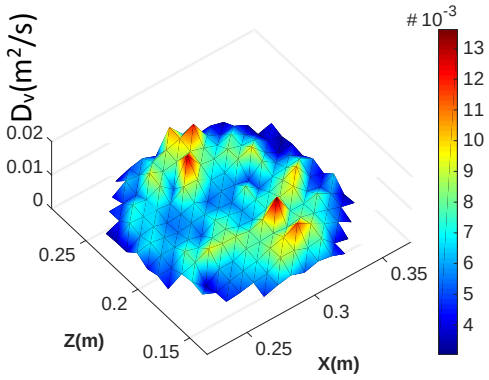

(2-a)

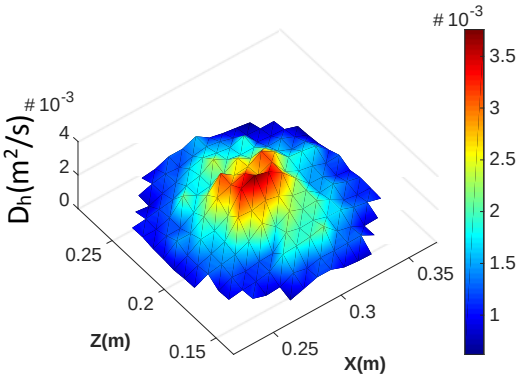

(2-b)

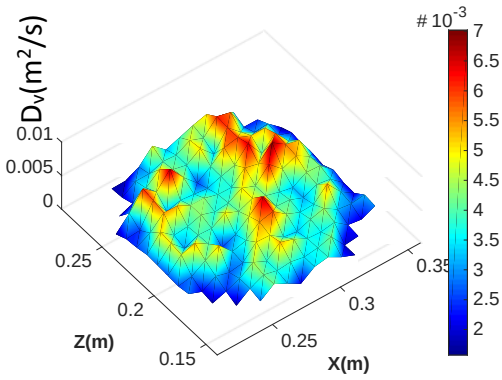

(3-a)

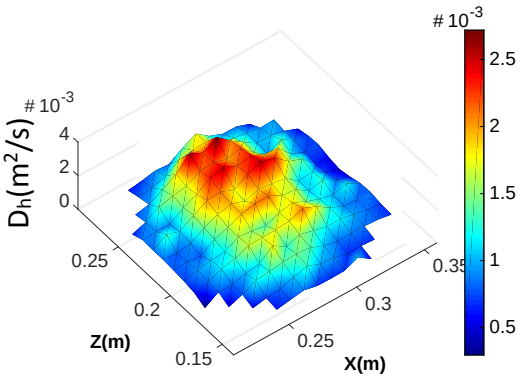

(3-b)

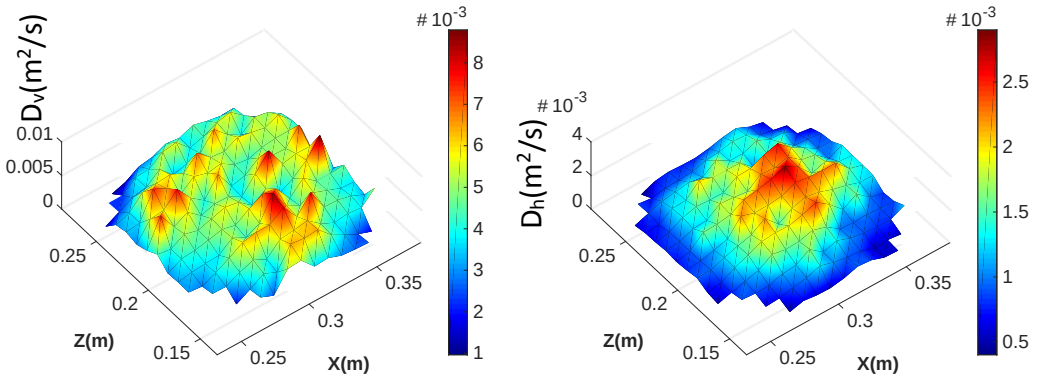

(4-a) (4-b)

Figure 6.7 Dispersion coefficient map for the upper section of the bed (150-200 mm): (1) pattern A; (2) pattern B; (3) pattern C; (4) pattern D; (a) vertical direction; (b) horizontal direction.

Table 6.1 Uniformity of solid dispersion coefficient distribution.

Section	**Bottom**				**Intermediate**				**Top**			
Pattern	**A**	**B**	**C**	**D**	**A**	**B**	**C**	**D**	**A**	**B**	**C**	**D**
Vertical	○	●	●	●	○	●	●	●	~	~	●	●
Horizontal	~	~	●	●	○	○	~	●	○	○	~	~

● **– Good**: When the dispersion coefficients in different areas have similar values and relevantly large/small dispersion coefficients are not observed as being concentrated in the same regions, the uniformity of the dispersion coefficient distribution is considered “good”.

○ **– Poor**: When almost all of the relevantly large/small dispersion coefficients are observed as being concentrated in limited areas, the uniformity of the distribution is considered “poor”.

~ – **Middling**: When the dispersion coefficients in different areas do not have very similar values but no significant areas containing almost all of the relevantly large/small dispersion coefficients are observed, the distribution is "middling" that between good and poor uniformity.

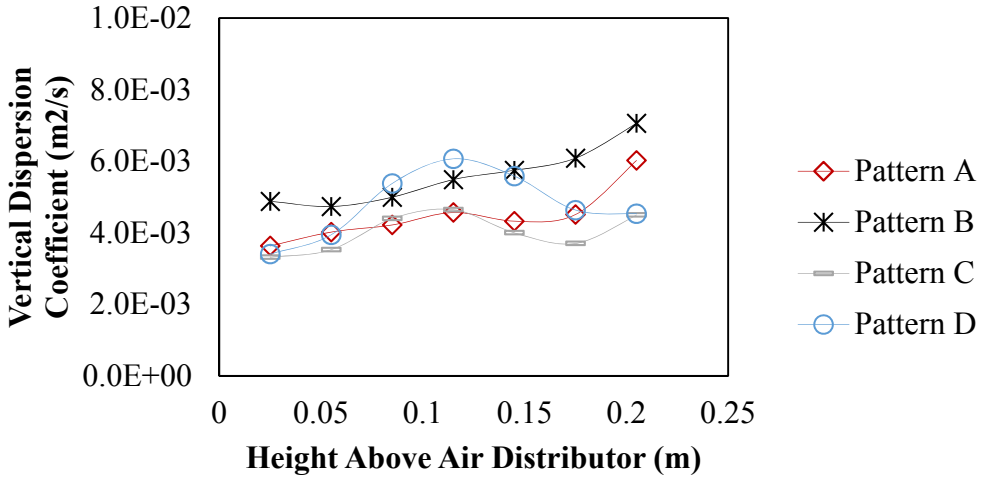

(a)

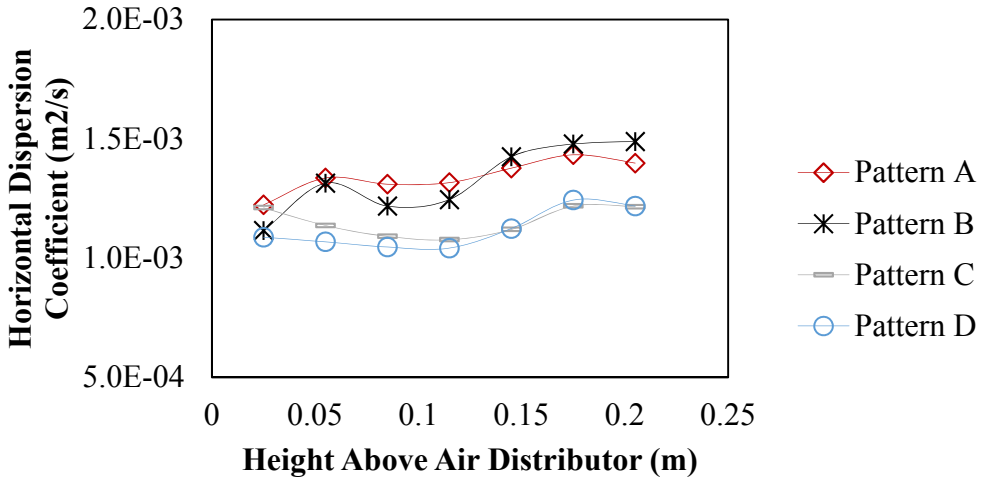

(b)

Figure 6.8 Dispersion coefficients of solids against bed heights: (a) vertical direction; (b) horizontal direction.

In order to assist quantitatively evaluate the uniformity of solid dispersion coefficient, the variance (σ^2), of both solid vertical and horizontal dispersion coefficients in the bottom, intermediate, and top sections of the bed for different flow patterns, has been calculated. The results are shown in Figures 6.9-6.10. The variance indicates the difference between coefficients, and it should be as small as possible to represent that the solid dispersion coefficients at different locations have similar values. It can be seen that patterns C and D have smaller variances than patterns A and B except the intermediate section in Figure 6.10, where, pattern C has a larger variance of the solid horizontal dispersion coefficient than pattern B. This means that the value uniformity of solid dispersion coefficient is relevantly better in patterns C and D than in patterns A and B.

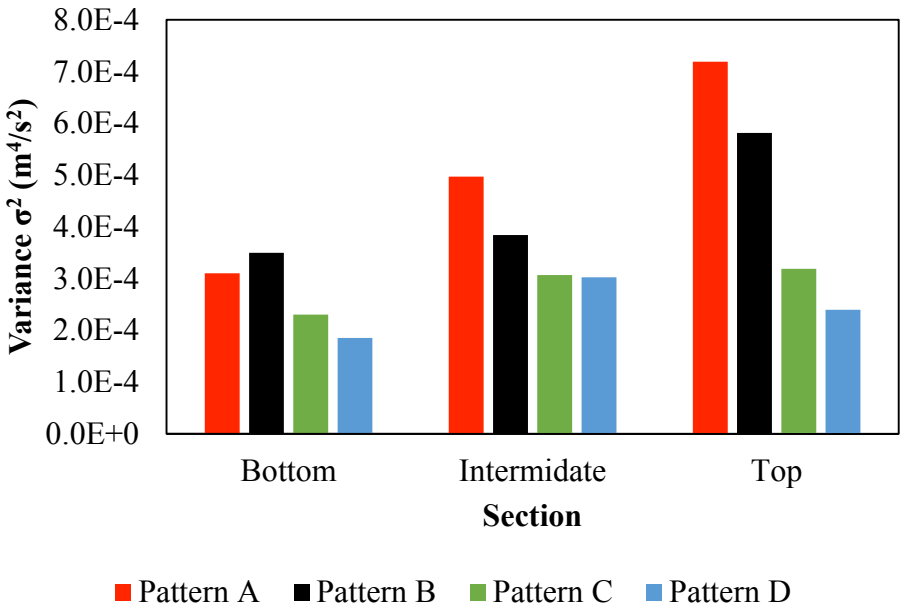

Figure 6.9 Variance (σ^2) of solid vertical dispersion coefficient.

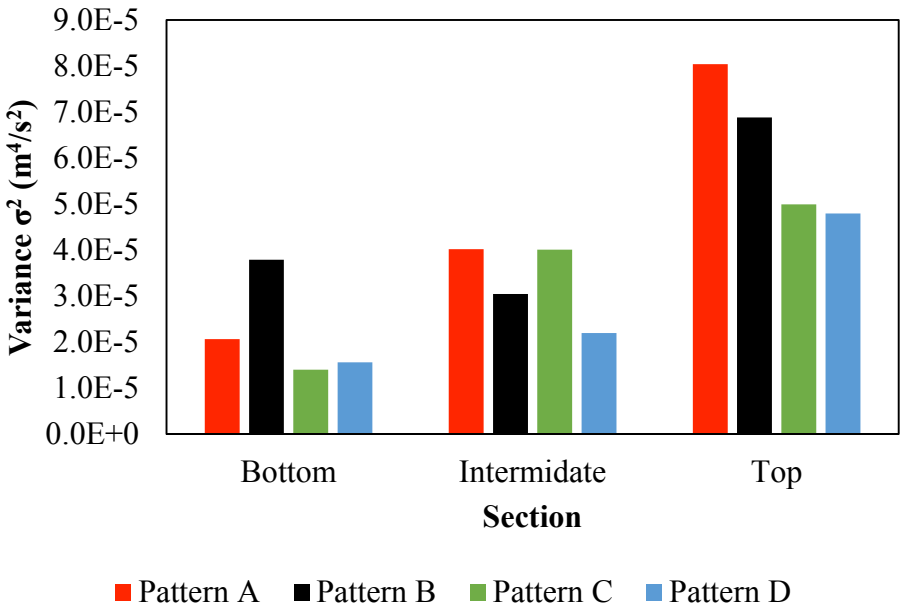

Figure 6.10 Variance (σ^2) of solid horizontal dispersion coefficient.

In consideration of both value uniformity and distribution uniformity of solid dispersion coefficient, it can be said that overall, pattern D has the best solid mixing profile among all flow patterns based on the coefficient obtained from the reconstructed solid dispersion. The vertical dispersion coefficient is always 3-5 times higher than the horizontal dispersion coefficient and dominates the solid mixing. Since particles used to calculate the dispersion efficiency are randomly selected from all particles that have passed through the starting point, it is therefore meaningful to assess the deviation between different runs to ensure the reliability of the method. Hence, for each compartment, the calculation of the dispersion efficiency is repeated for 5 runs to investigate the deviation among the dispersion coefficients obtained from these runs. The results indicate that the difference in dispersion coefficients among the 5 runs ranges between 0 and 2.5%, representing very small deviation. This confirms that the

proposed method is reliable and can be applied to estimate solid dispersion. However, using the dispersion coefficient to qualify solid mixing does have its limitations. A large dispersion coefficient does not always represent good solid mixing over the entire bed. In some cases, the high dispersion efficiency is only due to a significant but non-uniform bubble motion at a particular point in time that results in strong solid motion and dispersion in a limited area. The behaviour of solid mixing should be evaluated based on both the uniformity and magnitude of the dispersion coefficient throughout the whole bed. In order to further investigate the solid mixing within fluidized beds using the PEPT technique, an AI has been proposed and will be discussed in the subsequent section of this thesis.

6.3 Active Index of Particles

In a fluidized bed, particles are moving around due to bubbling. When a bed is uniformly fluidized, small bubbles should be uniformly distributed throughout and particles should move to different places with uniform velocities. As a key property of fluidized beds, solid mixing should likewise be uniform throughout to maximize efficiency of the processes that takes place in a fluidized bed. In other words, at any location within the bed, every particle should be motivated to move around throughout the entire bed, and no dead zone should exist. In every region of the bed, the particles should be similarly active. The probability for particles to enter or leave any particular region should be similar. Based on this concept, an AI is proposed in this study to further evaluate the solid mixing behaviour within fluidized beds. It is defined based on the number of times of particles pass through a unit of volume within a unit of time, as shown in Equation 6.10. To count the number of times particles pass through a

particular volume, each time the tracer particle falls into a measured volume, its previous location is recorded, and it is considered as an inflow point to the volume. The particle can stay for some time and move to different locations within this volume before it flows out of the volume. Among all the close following positions of the particle from this inflow point, the first position where it is out of this volume will be considered as the successive outflow point from the inflow point for the measured volume, as illustrated in Figure 6.11. It is understood that if the particle in a region is active, it should flow in and flow out of the region many times. It is also understood that, if the solid mixing is good and particles are fluidized uniformly in a bed, the tracer particle should go everywhere within the bed and has a very similar probability to flow in and flow out of a volume selected from anywhere of the bed. The AI therefore represents the activity of particles in different areas and describes the frequency and probability of particles moving to different locations. For uniform solid mixing, the AI obtained in a different region throughout the entire fluidized bed should have a uniform profile.

$$Activ\ Index = \frac{The\ number\ of\ passes}{Measured\ Volume \times Total\ tracking\ time}\ (/cm^3 \cdot s) \qquad (6.10)$$

In order to determine the AI profile throughout the entire bed, the bed has been divided into small compartments with the dimension of 10 mm and height of 35 mm. For each compartment, only an inflow with a subsequent outflow of the tracer particle is considered as one pair of entrance, as mentioned previously (Figure 6.11). An inflow without a subsequent outflow or an outflow missing an inflow of the tracer particle is regarded as an erroneous count and is then discarded from the original data to make

the new trajectory data smooth. Once all pairs of entrance have been taken into account from the entire time-position data of the tracer particle, the number of pairs is divided by the compartment volume and the total tracking time of the new smooth data in order to determine the AI value. This procedure is performed repeatedly for all of the compartments throughout the bed with the calculation step of 5 mm, and the cross-sectional AI map is then obtained as a function of bed heights, as shown in Figure 6.12.

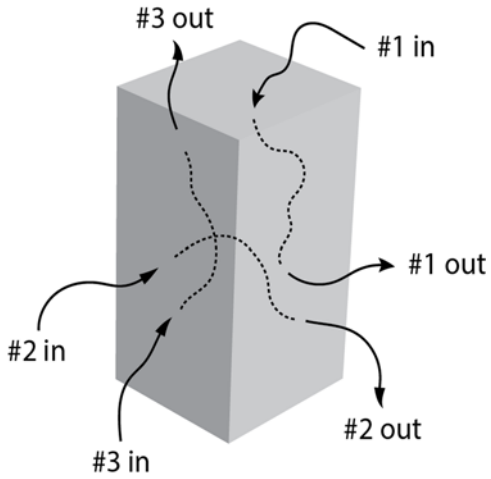

Figure 6.11 Definition of the pairs of entrance.

Figure 6.12 shows the AI map at different heights of the bed for patterns A, B, C and D. It can be seen that the AI map is quite uniform overall for flow patterns B, C and D in different layers, whereas pattern A is not uniform in the 10-45 mm and 160-195 mm layers. The two small areas at the corner of the bed in the 10-45 mm layer of pattern A have very small to no AI value, as seen in Figure 6.12A1. This indicates a dead zone, where the tracer particle rarely visits during the experiment. The AI map of pattern A at the bed height of 160-195 mm is also uneven, as seen in Figure 6.12A4, with the AI being much smaller along half of the bed wall than near the centre. This is because

that 160-195 mm layer in pattern A is close to the bed surface, and the solid concentration is low.

In order to investigate the effect of solid flow patterns on AI and solid mixing, the AIs are averaged for each layer and a mean value is obtained as a function of bed heights. The results for different flow patterns are presented in Figure 6.13. In pattern D, the AI starts at 0.012 /(cm^3s) near the air distributor and increases to 0.025 /(cm^3s) at an intermediate height of 0.15 m. The subsequent decrease is due to the bed height reaching the bed surface. In pattern C, the AI is 0.006 /(cm^3s) near the air distributor and increases to 0.015 /(cm^3s) at an intermediate height, followed by a progressive decrease to the bed surface. In pattern B, the AI is 0.005 /(cm^3s) near the air distributor and increases to 0.01 /(cm^3s) at an intermediate height, followed by a slow decrease towards the bed surface. In pattern A, the AI is 0.005 /(cm^3s) near the air distributor and increases to 0.013 /(cm^3s) at an intermediate height, followed by a dramatic decrease to the bed surface. The overall AI for the 4 patterns decreases as D > C > A and B. This indicates that particles in pattern D are more active and have a similar probability to visit every compartment in the bed. The small AIs obtained in different regions of the bed in pattern A and B show that particles may stay in specific locations rather than moving frequently to different regions. For all flow patterns, the AI reaches its maximum around an intermediate height. This is because increased bubble activities (i.e., splitting and coalescence) occur around an intermediate height of the bed, which enhances solid mixing.

	1	2	3	4
A	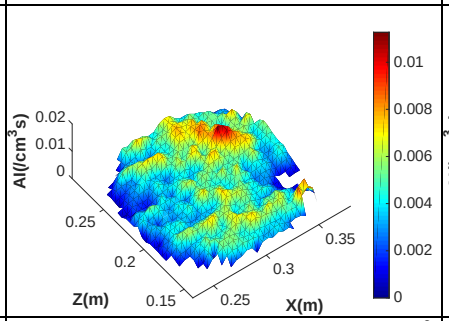	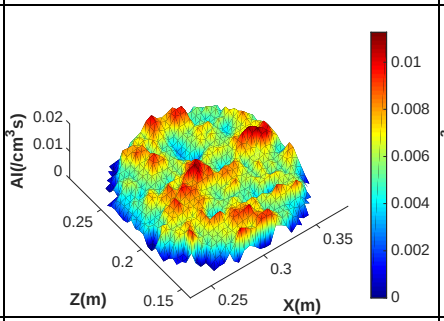	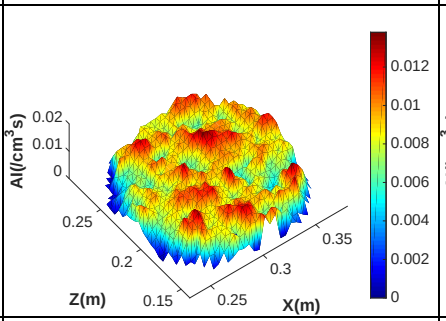	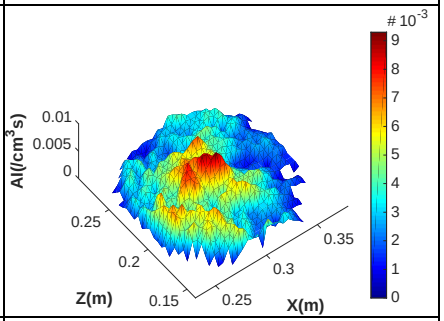
B	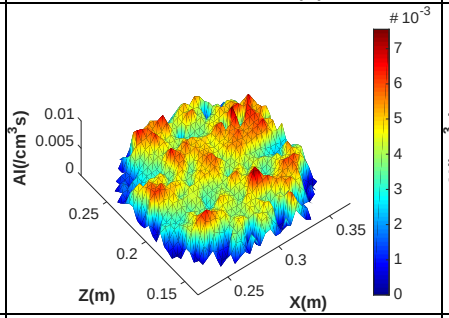	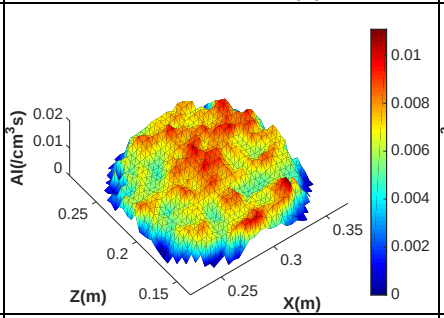	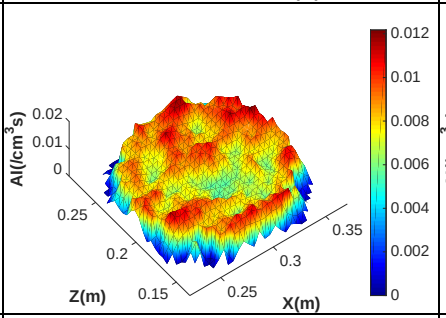	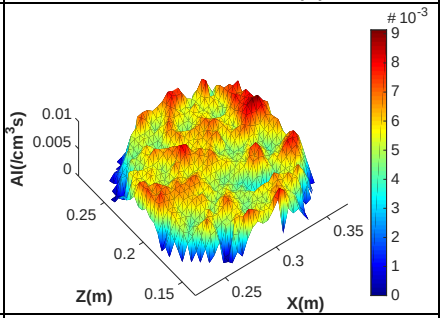
C	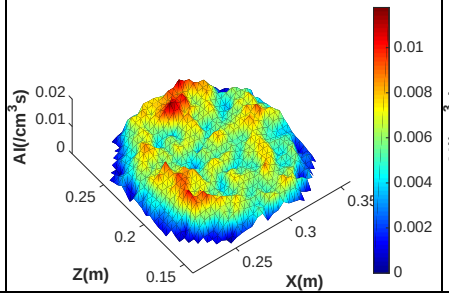	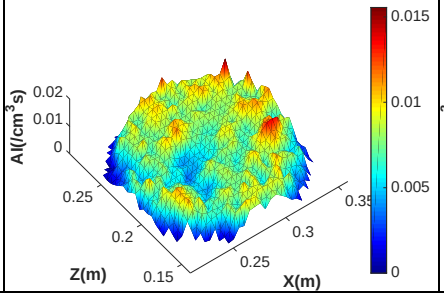	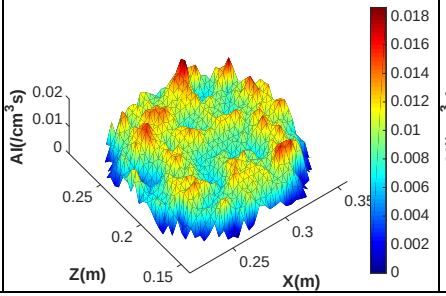	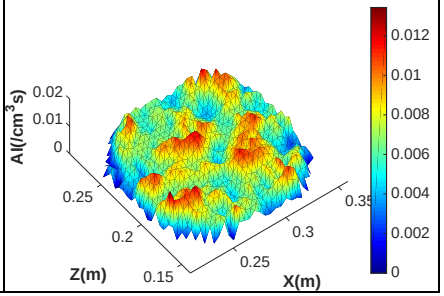

(Continued from the previous chart)

	1	2	3	4
D	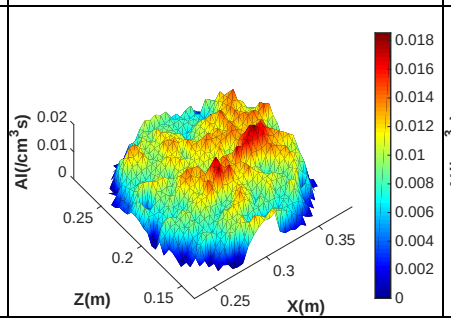	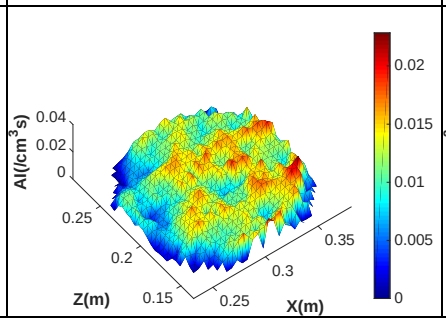	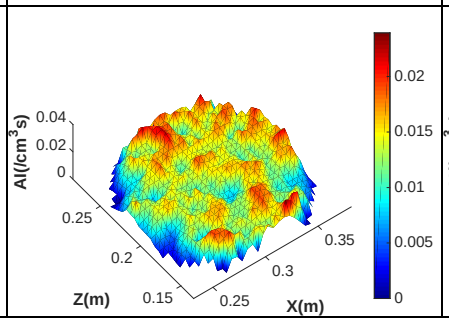	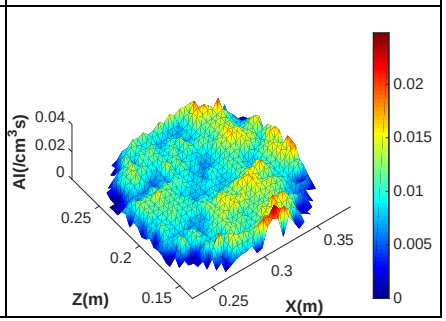

Figure 6.12 Active Index (AI) map: (A) pattern A; (B) pattern B; (C) pattern C; (D) pattern D; (1) layer 10-45 mm; (2) layer 60-95 mm; (3) layer 110-145 mm; (4) layer 160-195 mm.

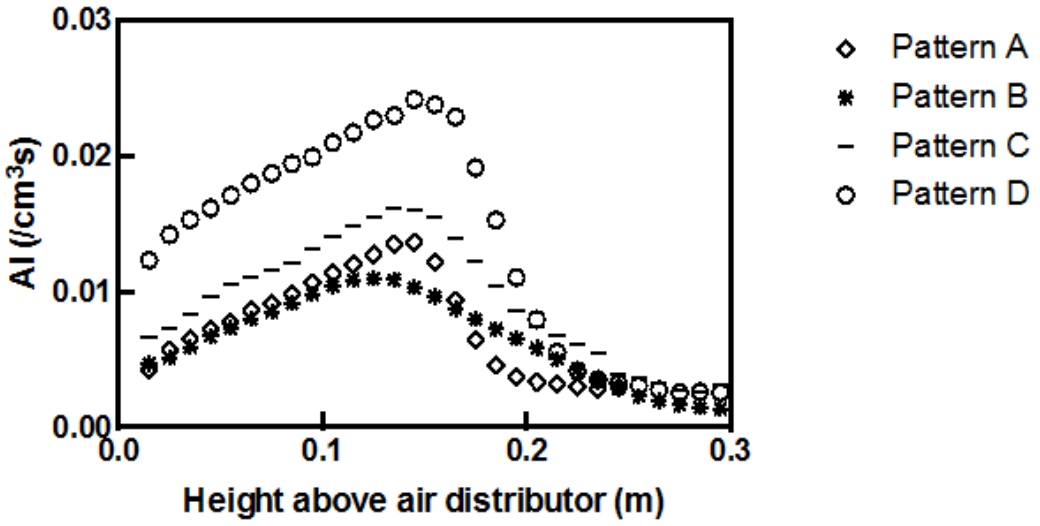

Figure 6.13 Averaged AI against bed heights.

6.4 Residence Time Distribution of Particles within the Bed

The AI gives the distribution of the opportunity and frequency of solid particles moving to particular positions within a fluidized bed. In addition to the AI, it is worthwhile knowing the residence time of the particles in a specific area within the bed. The residence time of solids in a particular area is an important factor in fluidized beds, and the residence time must be uniform to attain a high efficiency and productivity during continuous processes [2]. In addition, as suggested by Stein [1], it is critical to determine information about the time spent in certain parts of the bed using the PEPT technique in order to understand solid motion, especially at the air distributor or near the bed wall. This determination of residence time is attempted in this section. Both the AI and the residence time distribution will help garner an

understanding of solid mixing within fluidized beds and in the investigation of the stagnant zones where particles are less active due to non-uniform bubble development.

To determine the distribution of the particle residence time throughout the entire bed, the bed is partitioned into many compartments using the same manner described previously for determining the AI. For each compartment, once a pair of entrance has been detected, the time interval between the inflow and outflow is calculated and recorded. After all pairs of passes have been determined for a compartment, the average residence time for every entrance of the tracer particle in this compartment is calculated using the total time spent in the compartment divided by the entrance number. The obtained average residence time of tracer particle is then divided by the compartment volume to calculate the average residence time per unit volume (s/m^3) of the tracer particle at this position. The average residence time of particles at different locations throughout the entire bed has been calculated. The distribution of the residence time (RTD) map at different bed heights shows that the particle residence time is significantly larger in the areas close to the bed wall than in the bed centre for all flow patterns. This indicates that particles move slow by and stay longer at the bed wall than in the bed centre because of particle to wall friction. The significantly longer residence time near the bed wall confirms that the wall effect is considerable and cannot be neglected. In order to investigate the effects of solid flow patterns on the RTD, the residence times at different layers have been averaged, and the average residence time, as a function of bed height, is obtained and presented in Figure 6.14. The average residence time per unit volume of particles in the entire bed of patterns C and D is below 5 s/m^3 and does not change significantly along the bed height. However,

the average residence time per unit volume of particles throughout the entire bed for patterns A and B is greater than 10 s/m^3, which is much larger than in patterns C and D, and it increases and decreases significantly along the bed heights. These results show that the residence time of particles is short and uniform throughout the entire bed for patterns C and D, whereas it is longer and varies significantly along the bed height for patterns A and B. These results also indicate that particles in patterns C and D are much more active than those in patterns A and B. Particles do not stay in a particular location for a long time in patterns C and D. Instead, particles rapidly leave one position and travel to different areas in the bed, enhancing the solid mixing. Particles in patterns A and B stay in particular regions for a long time and do not frequently move out from those regions, which may initialize dead zones.

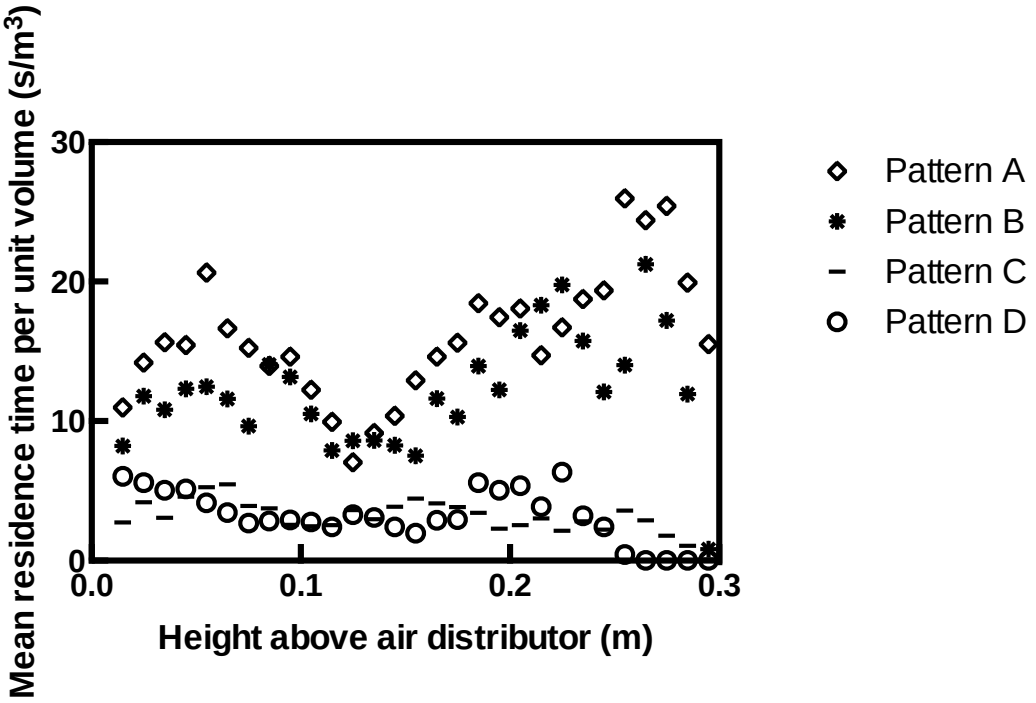

Figure 6.14 Mean residence time per entrance per unit volume.

6.5 Conclusion

The solid mixing in bubbling fluidized beds has been evaluated based on dispersion coefficients, AI and particle residence time distributions in this chapter. The dispersion coefficients of particles, which are defined by analogy with diffusion coefficients, imply the dispersion/displacement of particles through a unit surface in a unit time (m^2/s) and is usually used to qualify the solid mixing behaviour. The solid dispersion coefficient in both vertical and horizontal directions are calculated based on tracer particle trajectories/solid motions in this chapter. The results are on the order of 10^{-3} and are within the same range of results in the published literature. Typically, the solid vertical dispersion coefficient is 3-5 times larger than the horizontal dispersion coefficient and dominates the solid mixing. The solid mixing behaviour is significantly affected by bubble spatial distribution and solid flow patterns. The mixing of solids is favourable where bubbles are uniformly distributed and solids undergo many circulations with uniform traveling velocities. Similar to the results presented in Chapters 4 and 5, pattern D provides better solid mixing due to its uniform bubble spatial distribution profile and solid circulation pattern.

The AI is defined as the amount of tracer pass through per unit volume within a unit time. It describes the activity, frequency and opportunity of particles moving to different locations within the bed. The AI is obtained at different positions within the bed. The non-uniform AI map at different bed heights in pattern A reveals a dead zone at the corner of the bed near the air distributor. It also reveals that the expanded bed height of pattern A is lower than other flow patterns. The average AI for pattern D is

close to 0.02 /(cm^3s), which is greater than 0.01 /(cm^3s) for pattern C. The average AI for patterns A and B is less than 0.01 /cm^3s. These results indicate that particles are more active in pattern D and move around in the entire bed with higher and more uniform opportunities and frequencies than those in other flow patterns.

The mean residence time distribution of particles is also investigated in this chapter. It is defined as the average residence time per entrance per unit volume (m^3) of the tracer particle. The mean residence time distribution of particles within the entire bed can assist in the understanding of solid mixing and solid motion and can reveal the stagnant zones (i.e., dead zones) in fluidized beds. The results show that particle residence time is much longer near the bed wall than in the bed centre for all flow patterns. This confirms the significant influence of bed walls on flow structures. The average particle residence time throughout the entire bed for patterns C and D is less than 5 s/m^3, and the residence time has a uniform value along the bed heights. Conversely, the average particle residence time throughout the entire bed for patterns A and B is greater than 10 s/m^3 and varies significantly along the bed heights. Hence, particles in patterns C and D are more active. Particles stay in the same locations with a very short residence time in patterns C and D and rapidly leave one position and travel to different areas in the bed, thereby enhancing the solid mixing. Meanwhile, particles in patterns A and B stay in particular regions for a longer time.

Overall, solid mixing is greatly affected by solid flow patterns and bubble spatial distributions. Solid mixing is efficient with uniform bubble spatial distribution. In pattern D, particles disperse uniformly throughout the bed and move around frequently

to different positions with short residence times. In pattern A, a considerable dead zone presents, which lowers the gas-solid mixing and contact. Patterns B and C represent intermediate patterns positioned between A and D in terms of the fluidized bed behaviour. The solid mixing behaviour of the four flow patterns determined in the present study is in robust agreement with the results presented in previous chapters (i.e., solid flow patterns and bubble spatial distributions). The gas-solid contact and mixing efficiency should be greatly improved in pattern D compared with those in patterns C, B, and A.

Chapter 7: Conclusions and Future Work

Bubbling fluidized beds have been applied in various industrial processes as an effective means of solid and gas contact and mixing, as well as excellent heat transfer. Industrial applications include coal combustion for electricity generation and gasification for producing syngas. Although research has been carried out to better understand the dynamic behaviour within a fluidized bed for many years, uncertainties still remain due to a lack of reliable measurement techniques. This thesis offers insights into solid and gas flow structures within 3-D bubbling fluidized beds of Geldart B particles using the non-invasive PEPT technique that has been discussed at length in Chapter 3. Solid motion, bubble behaviour and solid mixing have been assessed during the experiments, and the results have been discussed in Chapters 4-6. In this chapter, a summary of conclusions from the present study, as well as the main contributions of this thesis, is provided, and future work is recommended.

7.1 Conclusions

The solid flow structure, bubble properties, bubble spatial distribution and solid mixing behaviour within a bubbling fluidized bed has been investigated under different operational conditions and bed configurations in this study. The solid microscopic motion and vector map was measured using the PEPT technique, and the average velocity of solids as a function of spatial positions was obtained using a MATLAB programme.

A method has been developed to reconstruct bubble spatial distributions based on solid motions measured by the PEPT technique. The reconstructed bubble spatial distribution is in agreement with the results published recently by means of X-ray tomographic scanner [271]. The bubble rise velocity, bubble size and specific surface area of bubbles calculated based on the PEPT data are likewise in agreement with the predictions from well-known empirical correlations. The correlations proposed by Kunii and Levenspiel, Yasui and Johanson and Mori and Wen demonstrate better agreement with the measured results of the present study than those suggested by Davidson and Harrison and Darton.

Solid mixing within the fluidized bed was estimated based on the solid dispersion coefficient, the active index (AI) and the average residence time distribution of solids in the bed. The solid dispersion coefficient was estimated based on a reconstructed dispersion process of solids, and the results were within the same order of that reported in the literature. A parameter (i.e., AI) has been proposed to calculate the frequency and opportunity of solids to move into various positions within the bed, and the average residence time of solids has been determined as a function of spatial positions based on AI.

The solid motion, bubble properties and solid mixing within fluidized beds vary significantly with operational conditions and bed designs, and the flow structure in fluidized beds has been classified into four patterns based on their different characteristics. They are named as pattern A, B, C and D, among which pattern C was newly discovered in this thesis.

In pattern A, bubbles are developed in a narrow area along a restricted side of the bed wall at the air distributor and travel up with significantly increasing sizes and velocities. Particles in pattern A undergo a large circulation vortex over the bed, ascending along one side of bed wall and descending on the other side. Solids only disperse well within a limited area in the bed, and solids stay in same locations for quite a long time, traveling to various other positions with a low frequency. Pattern A should be avoided in industrial processes due to the presence of its considerably large dead zone and low gas-solid contact and mixing efficiency.

In pattern B, bubbles are uniformly developed near the air distributor and coalesce inwards to the centre as they rise, generating large bubbles above an intermediate height. Solids travel with uniform velocities near the air distributor and travel up following the bubbles towards the centre, generating toroidal solid circulation vortexes that ascend along the central axis and descend along the bed wall. Solids disperse more uniformly than in pattern A in the vertical direction, while in the horizontal direction, solids only disperse well around the centre. Solids also spend quite a long time at same locations and only travel to various other positions with a low frequency.

In pattern C, the bubble development is relatively uniform near the air distributor. As bubbles rise to higher bed levels, bubble coalescence and splitting occurs frequently, generating various sizes of bubbles along the bed height. Solids in pattern C move upwards along one side of the bed wall and downwards along the other side in the bed bottom section, generating a small circulation vortex just above the air distributor. In

the bed top section, solids move upwards along the central axis and downwards along the bed wall, generating similar toroidal vortexes to those in pattern B. In the intermediate bed section, solid flow is quite complex. Solid dispersion is relatively uniform in both vertical and horizontal directions, and solids only fall in the same locations for a short time before subsequently traveling to various other positions with a higher frequency compared with patterns A and B.

In pattern D, bubbles develop in the annular region close to the bed wall at the air distributor and progressively coalesce inwards to the bed centre as the bed height increases. Bubble size increases slowly with bed height when near the air distributor and decreases significantly due to frequent bubble splitting around an intermediate height of the bed. Bubbles remain relatively small in size with slowly increasing velocities in pattern D, generating a large specific surface area for contact with solids. Solids ascend along the bed wall and descend in centre in the bottom section, whereas bubbles travel up along the central axis and down near the bed wall in the top section, generating the top and bottom toroidal vortexes in pattern D. In the intermediate section, solids are mixed and redirected into the top and bottom circulations. Solid dispersion is very uniform over the whole fluidized bed in both the vertical and horizontal directions. Solids will not stay in same locations for a considerable length of time in pattern D; instead, they move rapidly and travel into various other positions with the highest frequency among all of the flow patterns investigated. Pattern D is the most desirable flow structure in that solids are fluidized uniformly, and high gas-solid contact and mixing efficiency can be expected.

The general conditions of the four different flow patterns generated has been investigated, and both the independent and collective effects of solid properties, pore sizes of the air distributor, bed aspect ratio (H/D) and superficial gas velocities on the flow patterns have been determined. A condition map has been proposed to illustrate the relationships between flow patterns and various factors. Moreover, a FPP has been proposed to further identify and predict different flow patterns based on solid kinetic energy and various other factors. Flow patterns can be clearly distinguished into different regions based on the FPP, and the results are useful for both academic and industrial research to optimize operational conditions and enhance fluidized bed designs. Experimental results derived from the FPP are also useful for numerical simulations to verify and develop more accurate models.

7.2 Future Work

The immediate and obvious extension of the present research is to expand the experimental conditions. As discussed in Chapter 4, a more accurate FPP range for different flow patterns can be expected if more experiments are conducted using materials with different densities and a larger size range. The extension of experimental conditions is also meaningful to generate a dimensionless FPP that employs only easily measurable parameters without the use of the particle kinetic energy.

The lab-scale experiments conducted in the current research use a 15-cm I.D. fluidized bed, whereas the diameters of fluidized beds in commercial practice are much larger. Therefore, it is worth considering additional factors (i.e., bed diameter) and

investigating the flow structure within bubbling fluidized beds at an increased scale for industrial purposes. Using this approach, the correlating knowledge between systems of different scales can be bridged, which is essential for improving the understanding of scale-up effects on fluidized bed behaviours.

The PEPT technique is a powerful tool for following particle trajectories within opaque 3-D systems with reasonable spatial and temporal resolutions, even when particles travel with high velocities. However, only a single tracer particle is tracked during the experiments of the present study, which limits the measurement capabilities of simultaneously following multiple tracer particles. This limitation could be resolved by applying an algorithm to locate the positions of multiple tracer particles from the LOR defined via coincidence detection of pairs of γ-rays. Several such attempts have been made by Yang et al. [26], Yang et al. [24], Bickell et al. [285] and Langford et al. [286]. With the possibility of simultaneously tracking multiple particles within a fluidized bed, an enhanced and more accurate estimation of solid mixing can be achieved; this is crucial for generalizing criteria to qualify solid mixing, since the results of experiments qualifying solid mixing in fluidized beds still vary significantly in the published literature due to the unreliable measurement techniques used.

The bubble spatial distribution presented in the present study represents reconstructed results obtained using the method developed herein. Although the reconstruction method provides reliable results in agreement with the observations reported in the literature, the experimental measurement can be further improved by applying another advanced, non-invasive measurement technique to simultaneously observe the bubble

behaviour in a 3-D fluidized bed with multiple particles being followed by the PEPT technique, such as the X-ray tomography [192, 271, 287-289]. The simultaneous measurement of both particle motions and bubble behaviours will lead to a better understanding of the relationship and interaction between gas voids and solids in fluidized beds.

References

[1] M. G. Stein, "Particle motion in fluidised beds," Doctor of Philosophy, University of Birmingham, 1999.

[2] D. Kunii and O. Levenspiel, *Fluidization engineering*, 2nd ed. Boston: Butterworth-Heinemann, 1991.

[3] X. Fan, Z. Yang, X. Fan, and Z. Yang, "Re-Interpretation of Fluidization," in *Catalytic Combustion*, S. A. Cottilard, Ed., ed Hauppauge, N.Y.: Nova Science Publishers Inc, 2011.

[4] J. Xu, "Hydrodynamics studies on macro- and micro-flow structure with effects of particle properties in a circulating fluidized bed," Doctor of Philosophy, Department of Chemical and Biochemical Engineering, The University of Western Ontario, 2010.

[5] Y. S. Wong. (2003). *Experimental and numerical investigations of fluidisation behaviour with & without the presence of immersed tubes*.

[6] M. Kashyap, "Measurements and computation of dispersion and mass transfer coefficients in fluidized beds," Ph.D. DISSERTATION, Illinois Institute of Technology, Illinois Institute of Technology, United States, 2010.

[7] M. J. V. Goldschmidt, J. M. Link, S. Mellema, and J. A. M. Kuipers, "Digital image analysis measurements of bed expansion and segregation dynamics in dense gas-fluidised beds," *Powder Technology,* vol. 138, pp. 135-159, Dec 10 2003.

[8] J. G. Yates and S. J. R. Simons, "Experimental Methods in Fluidization Research," *International Journal of Multiphase Flow,* vol. 20, pp. 297-330, Aug 1994.

[9] F. Hernandez-Jimenez, J. Sanchez-Prieto, A. Soria-Verdugo, and A. Acosta-Iborra, "Experimental quantification of the particle-wall frictional forces in pseudo-2D gas fluidised beds," *Chemical Engineering Science,* vol. 102, pp. 257-267, Oct 11 2013.

[10] N. P. Cheremisinoff, "Review of experimental methods for studying the hydrodynamics of gas-solid fluidized beds," *Industrial & Engineering Chemistry Process Design and Development,* vol. 25, pp. 329-351, 1986/04/01 1986.

[11] J. Werther, "Measurement techniques in fluidized beds," *Powder Technology,* vol. 102, pp. 15-36, Apr 1999.

[12] G. Yasui and L. N. Johanson, "Characteristics of gas pockets in fluidized beds," *AIChE Journal,* vol. 4, pp. 445-452, 1958.

[13] M. Liu, Y. Zhang, H. Bi, J. R. Grace, and Y. Zhu, "Non-intrusive determination of bubble size in a gas–solid fluidized bed: An evaluation," *Chemical Engineering Science,* vol. 65, pp. 3485-3493, 6/1/ 2010.

[14] L. R. Glicksman, W. K. Lord, and M. Sakagami, "Bubble properties in large-particle fluidized-beds," *Chemical Engineering Science,* vol. 42, pp. 479-491, 1987.

[15] M. Rüdisüli, T. J. Schildhauer, S. M. A. Biollaz, and J. R. Van Ommen, "Measurement, monitoring and control of fluidized bed combustion and gasification," in *Fluidized Bed Technologies for Near-Zero Emission Combustion and Gasification*, F. Scala, Ed., ed: Woodhead Publishing, 2013, pp. 813-864.

[16] J. Drake, "Hydrodynamic Characterization of 3D Fluidized Beds Using Noninvasive Techniques," Doctor of Philosophy Dissertation, Mechanical Engineering, Iowa State University, 2011.

[17] H. Zhang, P. M. Johnston, J. X. Zhu, H. I. de Lasa, and M. A. Bergougnou, "A novel calibration procedure for a fiber optic solids concentration probe," *Powder Technology,* vol. 100, pp. 260-272, 12/1/ 1998.

[18] R. D. Morse and C. O. Ballou, "The Uniformity of Fluidization - Its Measurement and Use," *Chemical Engineering Progress,* vol. 47, pp. 199-204, 1951.

[19] P. N. Rowe and H. Masson, "Interaction of Bubbles with Probes in Gas-Fluidized Beds," *Transactions of the Institution of Chemical Engineers,* vol. 59, pp. 177-185, 1981.

[20] N. K. G. Keller, "Mixing and segregation in 3D multi-component, two-phase fluidized beds," Doctor of Philosophy Dissertation, Mechanical Engineering, Iowa State University, 2012.

[21] V. a. Zivkovic, D. H. Glass, and M. Biggs, "Study of granular temperature in dense fluidized beds by diffusing wave spectroscopy," Doctor of Philosophy Thesis (Ph.D.), University of Edinburgh, 2009.

[22] D. J. Parker, D. A. Allen, D. M. Benton, P. Fowles, P. A. McNeil, M. Tan *et al.*, "Developments in particle tracking using the Birmingham Positron Camera," *Nuclear Instruments & Methods in Physics Research Section a-Accelerators Spectrometers Detectors and Associated Equipment,* vol. 392, pp. 421-426, Jun 21 1997.

[23] X. Fan, D. J. Parker, and M. D. Smith, "Enhancing F-18 uptake in a single particle for positron emission particle tracking through modification of solid surface chemistry," *Nuclear Instruments & Methods in Physics Research Section a-Accelerators Spectrometers Detectors and Associated Equipment,* vol. 558, pp. 542-546, Mar 15 2006.

[24] Z. Yang, P. J. Fryer, S. Bakalis, X. Fan, D. J. Parker, and J. P. K. Seville, "An improved algorithm for tracking multiple, freely moving particles in a Positron Emission Particle Tracking system," *Nuclear Instruments & Methods in Physics Research Section a-Accelerators Spectrometers Detectors and Associated Equipment,* vol. 577, pp. 585-594, Jul 11 2007.

[25] X. Fan, D. J. Parker, and M. D. Smith, "Labelling a single particle for positron emission particle tracking using direct activation and ion-exchange techniques," *Nuclear Instruments & Methods in Physics Research Section a-Accelerators Spectrometers Detectors and Associated Equipment,* vol. 562, pp. 345-350, Jun 15 2006.

[26] Z. Yang, D. J. Parker, P. J. Fryer, S. Bakalis, and X. Fan, "Multiple-particle tracking—an improvement for positron particle tracking," *Nuclear Instruments and Methods in Physics Research Section A: Accelerators, Spectrometers, Detectors and Associated Equipment,* vol. 564, pp. 332-338, 8/1/ 2006.

[27] M. Barigou, "Particle Tracking in Opaque Mixing Systems: An Overview of the Capabilities of PET and PEPT," *Chemical Engineering Research and Design,* vol. 82, pp. 1258-1267, 9// 2004.

[28] D. J. Parker and X. F. Fan, "Positron emission particle tracking - Application and labelling techniques," *Particuology,* vol. 6, pp. 16-23, Feb 2008.

[29] W. Polashenski Jr and J. C. Chen, "Normal solid stress in fluidized beds," *Powder Technology,* vol. 90, pp. 13-23, 1// 1997.

[30] N. Menon and D. J. Durian, "Particle Motions in a Gas-Fluidized Bed of Sand," *Physical Review Letters,* vol. 79, pp. 3407-3410, 11/03/ 1997.

[31] W.-c. Yang, *Handbook of fluidization and fluid-particle systems*. New York: Marcel Dekker, 2003.

[32] L.-S. Fan and C. Zhu, *Principles of gas-solid flows*. Cambridge: Cambridge University Press, 1998.

[33] P. S. B. Stewart, "Fluidization: Some Hydrodynamic Studies," Doctor of Philosophy Ph.D. Dissertation Cambridge University, 1965.

[34] P. S. B. Stewart and J. F. Davidson, "Slug flow in fluidised beds," *Powder Technology,* vol. 1, pp. 61-80, 6// 1967.

[35] D. Gidaspow, *Multiphase flow and fluidization : continuum and kinetic theory descriptions*. Boston ; London: Academic Press, 1994.

[36] R. Jackson, *The dynamics of fluidized particles*. Cambridge: Cambridge University Press, 2000.

[37] M. Kwauk, J. H. Li, and D. J. Liu, "Particulate and aggregative fluidization - 50 years in retrospect," *Powder Technology,* vol. 111, pp. 3-18, Aug 21 2000.

[38] D. Geldart, "Types of Gas Fluidization," *Powder Technology,* vol. 7, pp. 285-292, 1973.

[39] J. Valverde Millán, "Introduction. The Classical Geldart's Diagram and the New Type of Gas-Fluidization Behavior," in *Fluidization of Fine Powders*. vol. 18, ed: Springer Netherlands, 2013, pp. 1-6.

[40] D. Geldart and A. R. Abrahamsen, "Homogeneous Fluidization of Fine Powders Using Various Gases and Pressures," *Powder Technology,* vol. 19, pp. 133-136, 1978.

[41] A. a. Harms, "Fast pyrolysis and nitrogenolysis of biomass and biogenic residues : production of a sustainable slow release fertiliser," Doctor of Philosophy Thesis (Ph.D.), Aston University, 2013.

[42] P. den Hoed, "Spotlight-Ifsa 2011: Industrial Fluidization South Africa," *Journal of the Southern African Institute of Mining and Metallurgy,* vol. 112, pp. Viii-Viii, Jun 2012.

[43] S. Kaewluan and S. Pipatmanomai, "Potential of synthesis gas production from rubber wood chip gasification in a bubbling fluidised bed gasifier," *Energy Conversion and Management,* vol. 52, pp. 75-84, Jan 2011.

[44] B. Leckner, "Atmospheric (non-circulating) fluidized bed (FB) combustion," in *Fluidized Bed Technologies for Near-Zero Emission Combustion and Gasification*, F. Scala, Ed., ed: Woodhead Publishing, 2013, pp. 641-668.

[45] N. P. Perez, E. B. Machin, D. T. Pedroso, J. S. Antunes, and J. L. Silveira, "Fluid-dynamic assessment of sugarcane bagasse to use as feedstock in bubbling fluidized bed gasifiers," *Applied Thermal Engineering,* vol. 73, pp. 238-244, Dec 5 2014.

[46] J. S. Dennis, "Properties of stationary (bubbling) fluidised beds relevant to combustion and gasification systems," in *Fluidized Bed Technologies for Near-Zero Emission Combustion and Gasification*, F. Scala, Ed., ed: Woodhead Publishing, 2013, pp. 77-148e.

[47] A. Lyngfelt, "Chemical looping combustion (CLC)," in *Fluidized Bed Technologies for Near-Zero Emission Combustion and Gasification*, F. Scala, Ed., ed: Woodhead Publishing, 2013, pp. 895-930.

[48] D. Meier, B. van de Beld, A. V. Bridgwater, D. C. Elliott, A. Oasmaa, and F. Preto, "State-of-the-art of fast pyrolysis in IEA bioenergy member countries," *Renewable & Sustainable Energy Reviews,* vol. 20, pp. 619-641, Apr 2013.

[49] T. Dyakowski and A. J. Jaworski, "Application of non-invasive techniques for imaging fluidized beds — A review," in *Handbook of Powder Technology*. vol. Volume 10, A. Levy and H. Kalman, Eds., ed: Elsevier Science B.V., 2001, pp. 807-823.

[50] C. N. Lim. (2004). *The dynamics and control of bubbling fluidised beds*.

[51] J. R. van Ommen and R. F. Mudde, "Measuring the Gas-Solids Distribution in Fluidized Beds-A Review," *International Journal of Chemical Reactor Engineering,* vol. 6, 2008.

[52] D. L. Keairns, *Fluidization technology*. Washington: Hemisphere, in association with McGraw-Hill, 1976.

[53] P. M. Herbert, T. A. Gauthier, C. L. Briens, and M. A. Bergougnou, "Application of fiber optic reflection probes to the measurement of local particle velocity and concentration in gas—solid flow," *Powder Technology,* vol. 80, pp. 243-252, 1994/09/01 1994.

[54] H. Johnsson and F. Johnsson, "Measurements of local solids volume-fraction in fluidized bed boilers," *Powder Technology,* vol. 115, pp. 13-26, Mar 7 2001.

[55] J. Liu, J. R. Grace, and X. Bi, "Novel multifunctional optical-fiber probe: I. Development and validation," *AIChE Journal,* vol. 49, pp. 1405-1420, 2003.

[56] M. E. Mainland and J. R. Welty, "Use of Optical Probes to Characterize Bubble Behavior in Gas-Solid Fluidized-Beds," *Aiche Journal,* vol. 41, pp. 223-228, Feb 1995.

[57] H. Kage, N. Iwasaki, H. Yamaguchi, and Y. Matsuno, "Frequency-Analysis of Pressure Fluctuation in Fluidized-Bed Plenum," *Journal of Chemical Engineering of Japan,* vol. 24, pp. 76-81, Feb 1991.

[58] S. W. Kim, J. Y. Ahn, S. D. Kim, and D. Hyun Lee, "Heat transfer and bubble characteristics in a fluidized bed with immersed horizontal tube bundle," *International Journal of Heat and Mass Transfer,* vol. 46, pp. 399-409, 1// 2003.

[59] D. Rensner and J. Werther, "Estimation of the Effective Measuring Volume of Single-Fibre Reflection Probes for solid volume concentration measurements," *Particle & Particle Systems Characterization,* vol. 10, pp. 48-55, 1993.

[60] R. Rundqvist, A. Magnusson, B. G. M. van Wachem, and A. E. Almstedt, "Dual optical fibre measurements of the particle concentration in gas/solid flows," *Experiments in Fluids,* vol. 35, pp. 572-579, Dec 2003.

[61] M. Rüdisüli, T. J. Schildhauer, S. M. A. Biollaz, and J. R. van Ommen, "Monte Carlo simulation of the bubble size distribution in a fluidized bed with intrusive probes," *International Journal of Multiphase Flow,* vol. 44, pp. 1-14, 9// 2012.

[62] K. P. Lanneau, "Gas-solids contacting in fluidized beds," *Transactions of the Institution of Chemical Engineers,* vol. 38, pp. 125-143, 1960.

[63] D. Geldart and J. R. Kelsey, "The use of capacitance probes in gas fluidised beds," *Powder Technology,* vol. 6, pp. 45-50, 7// 1972.

[64] J. Werther and O. Molerus, "The local structure of gas fluidized beds —I. A statistically based measuring system," *International Journal of Multiphase Flow,* vol. 1, pp. 103-122, 10/10/ 1973.

[65] A.-E. Almstedt and E. Olsson, "Measurements of bubble behaviour in a pressurized fluidized bed burning coal, using capacitance probes." vol. 1, s. 89-98, ed: DOE, Proc. 7th Int. Conf. on Fluidized Bed Combustion, Philadelphia, 1982.

[66] C. H. Soong, T. K., and C. J.C., "Identification of Particle Clusters in Circulating Fluidized Bed," in *Circulating Fluidized Bed Technology IV: Proceedings of the Fourth International Conference on Circulating Fluidized Beds*, A. A. Avidan, Ed., ed U.S.A.: Mobil Research and Development Corporation, Paulsboro Research Laboratory, 1993, pp. 615-620.

[67] C. A. Riley and M. Louge, "Quantitative capacitive measurements of voidage in gas-solid flows," *Particulate Science and Technology,* vol. 7, pp. 51-59, 1989/01/01 1989.

[68] C. Sobrino, J. A. Almendros-Ibáñez, D. Santana, C. Vázquez, and M. de Vega, "Maximum entropy estimation of the bubble size distribution in fluidized beds," *Chemical Engineering Science,* vol. 64, pp. 2307-2319, 5/15/ 2009.

[69] Y. Yeh and H. Z. Cummins, "LOCALIZED FLUID FLOW MEASUREMENTS WITH AN He–Ne LASER SPECTROMETER," *Applied Physics Letters,* vol. 4, pp. 176-178, 1964.

[70] V. Mathiesen, T. Solberg, H. Arastoopour, and B. H. Hjertager, "Experimental and computational study of multiphase gas/particle flow in a CFB riser," *AIChE Journal,* vol. 45, pp. 2503-2518, 1999.

[71] H. Arastoopour and S. Shao, "Laser doppler anemometry: Applications in multiphase flow systems," in *Non-Invasive Monitoring of Multiphase Flows*, J. C. L. P. Duduković, Ed., ed Amsterdam: Elsevier Science B.V., 1997, pp. 455-494.

[72] Y. Levy and F. C. Lockwood, "Laser doppler measurements of flow in freeboard of a fluidized bed," *AIChE Journal,* vol. 29, pp. 889-895, 1983.

[73] A. Samuelsberg and B. H. Hjertager, "An experimental and numerical study of flow patterns in a circulating fluidized bed reactor," *International Journal of Multiphase Flow,* vol. 22, pp. 575-591, 6// 1996.

[74] S. B. Kumar, M. P. Duduković, and B. A. Toseland, "Measurement techniques for local and global fluid dynamic quantities in two and three phase systems," in *Non-Invasive Monitoring of Multiphase Flows*, J. C. L. P. Duduković, Ed., ed Amsterdam: Elsevier Science B.V., 1997, pp. 1-45.

[75] W. D. Bachalo, "Experimental methods in multiphase flows," *International Journal of Multiphase Flow,* vol. 20, pp. 261-295, 1994/08/01 1994.

[76] J. Chaouki, F. Larachi, and M. P. Duduković, "Noninvasive Tomographic and Velocimetric Monitoring of Multiphase Flows," *Industrial & Engineering Chemistry Research,* vol. 36, pp. 4476-4503, 1997/11/01 1997.

[77] J. W. Czarske, "Laser Doppler velocimetry using powerful solid-state light sources," *Measurement Science and Technology,* vol. 17, p. R71, 2006.

[78] H. G. Barth and R. B. Flippen, "Particle Size Analysis," *Analytical Chemistry,* vol. 67, pp. 257-272, 1995/06/01 1995.

[79] J. R. Reese and L. S. Fan, "Particle image velocimetry: Application for the characterization of the flow structure in three phase fluidized beds," in *Non-Invasive Monitoring of Multiphase Flows*, J. C. L. P. Duduković, Ed., ed Amsterdam: Elsevier Science B.V., 1997, pp. 495-518.

[80] M. Campbell, J. A. Cosgrove, C. A. Greated, S. Jack, and D. Rockliff, "Review of LDA and PIV applied to the measurement of sound and acoustic streaming," *Optics & Laser Technology,* vol. 32, pp. 629-639, 10// 2000.

[81] R. J. Adrian, "Particle-Imaging Techniques for Experimental Fluid Mechanics," *Annual Review of Fluid Mechanics,* vol. 23, pp. 261-304, 1991.

[82] J. S. Halow, "Electrical capacitance imaging of fluidized beds," in *Non-Invasive Monitoring of Multiphase Flows*, J. C. L. P. Duduković, Ed., ed Amsterdam: Elsevier Science B.V., 1997, pp. 263-307.

[83] J. A. Laverman, I. Roghair, M. v. S. Annaland, and H. Kuipers, "Investigation into the hydrodynamics of gas–solid fluidized beds using particle image

velocimetry coupled with digital image analysis," *The Canadian Journal of Chemical Engineering,* vol. 86, pp. 523-535, 2008.

[84] J. S. Halow and P. Nicoletti, "Observations of fluidized-bed coalescence using capacitance imaging," *Powder Technology,* vol. 69, pp. 255-277, Mar 1992.

[85] S. Liu, W. Q. Yang, H. Wang, F. Jiang, and Y. Su, "Investigation of square fluidized beds using capacitance tomography: preliminary results," *Measurement Science & Technology,* vol. 12, pp. 1120-1125, Aug 2001.

[86] Y. T. Makkawi and P. C. Wright, "Fluidization regimes in a conventional fluidized bed characterized by means of electrical capacitance tomography," *Chemical Engineering Science,* vol. 57, pp. 2411-2437, Jul 2002.

[87] H. G. Wang, W. Q. Yang, T. Dyakowski, and S. Liu, "Study of bubbling and slugging fluidized beds by simulation and ECT," *Aiche Journal,* vol. 52, pp. 3078-3087, Sep 2006.

[88] T. Pugsley, H. Tanfara, S. Malcus, H. Cui, J. Chaouki, and C. Winters, "Verification of fluidized bed electrical capacitance tomography measurements with a fibre optic probe," *Chemical Engineering Science,* vol. 58, pp. 3923-3934, Sep 2003.

[89] Y. T. Makkawi and P. C. Wright, "Electrical capacitance tomography for conventional fluidized bed measurements-remarks on the measuring technique," *Powder Technology,* vol. 148, pp. 142-157, Nov 2004.

[90] B. Du, W. Warsito, and L. S. Fan, "ECT studies of gas-solid fluidized beds of different diameters," *Industrial & Engineering Chemistry Research,* vol. 44, pp. 5020-5030, Jul 6 2005.

[91] Q. Marashdeh, L. S. Fan, B. Du, and W. Warsito, "Electrical Capacitance Tomography − A Perspective," *Industrial & Engineering Chemistry Research,* vol. 47, pp. 3708-3719, 2008/05/01 2008.

[92] J. S. Halow, G. E. Fasching, P. Nicoletti, and J. L. Spenik, "Observations of a fluidized bed using capacitance imaging," *Chemical Engineering Science,* vol. 48, pp. 643-659, 2// 1993.

[93] S. M. Huang, A. B. Plaskowski, C. G. Xie, and M. S. Beck, "Tomographic imaging of two-component flow using capacitance sensors," *Journal of Physics E: Scientific Instruments,* vol. 22, p. 173, 1989.

[94] S. M. Huang, C. G. Xie, R. Thorn, D. Snowden, and M. S. Beck, "Design of sensor electronics for electrical capacitance tomography," *Circuits, Devices and Systems, IEE Proceedings G,* vol. 139, pp. 83-88, 1992.

[95] C. G. Xie, S. M. Huang, B. S. Hoyle, R. Thorn, C. Lenn, D. Snowden *et al.*, "Electrical capacitance tomography for flow imaging: system model for development of image reconstruction algorithms and design of primary sensors," *Circuits, Devices and Systems, IEE Proceedings G,* vol. 139, pp. 89-98, 1992.

[96] C. A. M. da Silva, J. J. Butzge, M. Nitz, and O. P. Taranto, "Monitoring and control of coating and granulation processes in fluidized beds – A review," *Advanced Powder Technology,* vol. 25, pp. 195-210, 1// 2014.

[97] T. Dyakowski, L. F. C. Jeanmeure, and A. J. Jaworski, "Applications of electrical tomography for gas–solids and liquid–solids flows — a review," *Powder Technology,* vol. 112, pp. 174-192, 10/31/ 2000.

[98] H. S. Tapp, A. J. Peyton, E. K. Kemsley, and R. H. Wilson, "Chemical engineering applications of electrical process tomography," *Sensors and Actuators B: Chemical,* vol. 92, pp. 17-24, 7/1/ 2003.

[99] W. A. Al-Masry, E. M. Ali, S. A. Alshebeili, and F. M. Mousa, "Non-invasive imaging of shallow bubble columns using electrical capacitance tomography," *Journal of Saudi Chemical Society,* vol. 14, pp. 269-280, 7// 2010.

[100] F. T. Kühn and P. A. v. Halderen, "Design of an active-differentiator-based capacitance transducer for electrical capacitance tomography," *Measurement Science & Technology,* vol. 8, pp. 947-950, Aug 1997.

[101] W. Warsito and L. S. Fan, "ECT imaging of three-phase fluidized bed based on three-phase capacitance model," *Chemical Engineering Science,* vol. 58, pp. 823-832, 2// 2003.

[102] W. Warsito, Q. Marashdeh, and L. S. Fan, "Electrical capacitance volume tomography," *Ieee Sensors Journal,* vol. 7, pp. 525-535, Mar-Apr 2007.

[103] T. Grassler and K. E. Wirth, "X-ray computer tomography - potential and limitation for the measurement of local solids distribution in circulating fluidized beds," *Chemical Engineering Journal,* vol. 77, pp. 65-72, Apr 15 2000.

[104] T. J. Heindel, "A Review of X-Ray Flow Visualization With Applications to Multiphase Flows," *Journal of Fluids Engineering,* vol. 133, pp. 074001-074001, 2011.

[105] S. Liu, Q. Chen, H. G. Wang, F. Jiang, I. Ismail, and W. Q. Yang, "Electrical capacitance tomography for gas-solids flow measurement for circulating fluidized beds," *Flow Measurement and Instrumentation,* vol. 16, pp. 135-144, Apr-Jun 2005.

[106] I. Øyvind, "A review of reconstruction techniques for capacitance tomography," *Measurement Science and Technology,* vol. 7, p. 325, 1996.

[107] T. Loser, R. Wajman, and D. Mewes, "Electrical capacitance tomography: image reconstruction along electrical field lines," *Measurement Science & Technology,* vol. 12, pp. 1083-1091, Aug 2001.

[108] Q. M. Marashdeh, "Advances in electrical capacitance tomography," The Ohio State University, 2006.

[109] A. Kantzas, "Computation of holdups in fluidized and trickle beds by computer-assisted tomography," *AIChE Journal,* vol. 40, pp. 1254-1261, 1994.

[110] R. F. Mudde, "Time-resolved X-ray tomography of a fluidized bed," *Powder Technology,* vol. 199, pp. 55-59, Apr 10 2010.

[111] W. F. Banholzer, C. L. Spiro, P. G. Kosky, and D. H. Maylotte, "Direct imaging of time-averaged flow patterns in a fluidized reactor using x-ray computed tomography," *Industrial & Engineering Chemistry Research,* vol. 26, pp. 763-767, 1987/04/01 1987.

[112] T. J. Heindel, J. N. Gray, and T. C. Jensen, "An X-ray system for visualizing fluid flows," *Flow Measurement and Instrumentation,* vol. 19, pp. 67-78, Apr 2008.

[113] C. Rautenbach, R. F. Mudde, X. Yang, M. C. Melaaen, and B. M. Halvorsen, "A comparative study between electrical capacitance tomography and time-resolved X-ray tomography," *Flow Measurement and Instrumentation,* vol. 30, pp. 34-44, 4// 2013.

[114] B. Wu, G. Yu, C. Bellehumeur, and A. Kantzas, "Dynamic flow behavior measurements in gas–solid fluidized beds using different non-intrusive

techniques and polyethylene powder," *Flow Measurement and Instrumentation,* vol. 18, pp. 197-203, 10// 2007.

[115] A. Kantzas and N. Kalogerakis, "Monitoring the fluidization characteristics of polyolefin resins using X-ray Computer Assisted Tomography scanning," *Chemical Engineering Science,* vol. 51, pp. 1979-1990, 5// 1996.

[116] A. Kantzas, I. Wright, and N. Kalogerakis, "Quantification of channelling in polyethylene resin fluid beds using X-ray computer assisted tomography (CAT)," *Chemical Engineering Science,* vol. 52, pp. 2023-2035, 7// 1997.

[117] G. C. Brouwer, E. C. Wagner, J. R. van Ommen, and R. F. Mudde, "Effects of pressure and fines content on bubble diameter in a fluidized bed studied using fast X-ray tomography," *Chemical Engineering Journal,* vol. 207, pp. 711-717, Oct 2012.

[118] D. Escudero and T. J. Heindel, "Bed height and material density effects on fluidized bed hydrodynamics," *Chemical Engineering Science,* vol. 66, pp. 3648-3655, Aug 15 2011.

[119] T. Kai, M. Misawa, T. Takahashi, I. Tiseanu, N. Ichikawa, and N. Takada, "Application of fast X-ray CT scanner to visualization of bubbles in fluidized bed," *Journal of Chemical Engineering of Japan,* vol. 33, pp. 906-909, Dec 2000.

[120] R. F. Mudde, "Bubbles in a Fluidized Bed: A Fast X-Ray Scanner," *Aiche Journal,* vol. 57, pp. 2684-2690, Oct 2011.

[121] J. L. Hubers, A. C. Striegel, T. J. Heindel, J. N. Gray, and T. C. Jensen, "X-ray computed tomography in large bubble columns," *Chemical Engineering Science,* vol. 60, pp. 6124-6133, 11// 2005.

[122] N. P. Franka, T. J. Heindel, and F. Battaglia, "Visualizing cold-flow fluidized beds with X-rays," *Proceedings of the Asme International Mechanical Engineering Congress and Exposition 2007, Vol 8, Pts a and B,* pp. 99-105, 2008.

[123] J. Grant, M. Morgan, J. Davis, and P. Wells, "X-ray diffraction tomography: Application to imaging heterogeneous systems," in *Non-Invasive Monitoring of Multiphase Flows*, J. C. L. P. Duduković, Ed., ed Amsterdam: Elsevier Science B.V., 1997, pp. 213-245.

[124] I. Costello, P. Wells, J. R. Davis, N. Benci, D. Skerrett, and D. R. Davies, "X-ray and gamma-ray computed tomography for industrial nondestructive testing and evaluation," 1994, pp. 460-469.

[125] S. B. Kumar and M. P. Duduković, "Computer assisted gamma and X-ray tomography: Applications to multiphase flow systems," in *Non-Invasive Monitoring of Multiphase Flows*, J. C. L. P. Duduković, Ed., ed Amsterdam: Elsevier Science B.V., 1997, pp. 47-103.

[126] H. Y. Wei and M. Soleimani, "Electromagnetic Tomography for Medical and Industrial Applications: Challenges and Opportunities," *Proceedings of the Ieee,* vol. 101, pp. 559-565, Mar 2013.

[127] E. Kadic and T. J. Heindel, "Experimental Measurement Techniques," in *An Introduction to Bioreactor Hydrodynamics and Gas-Liquid Mass Transfer*, ed: John Wiley & Sons, Inc., 2014, pp. 17-57.

[128] G. D. Harvel, K. Hori, K. Kawanishi, and J. S. Chang, "Cross-sectional void fraction distribution measurements in a vertical annulus two-phase flow by high speed X-ray computed tomography and real-time neutron radiography techniques," *Flow Measurement and Instrumentation,* vol. 10, pp. 259-266, 12// 1999.

[129] T. Kai, M. Misawa, T. Takahashi, I. Tiseanu, and N. Ichikawa, "Observation of 3-D Structure of Bubbles in a Fluidized Catalyst Bed," *The Canadian Journal of Chemical Engineering,* vol. 83, pp. 113-118, 2005.

[130] C. Wu, Y. Cheng, Y. Ding, F. Wei, and Y. Jin, "A novel X-ray computed tomography method for fast measurement of multiphase flow," *Chemical Engineering Science,* vol. 62, pp. 4325-4335, 8// 2007.

[131] M. Bieberle and U. Hampel, "Evaluation of a limited angle scanned electron beam x-ray CT approach for two-phase pipe flows," *Measurement Science and Technology,* vol. 17, p. 2057, 2006.

[132] M. Bieberle, F. Fischer, E. Schleicher, H. J. Menz, H. G. Mayer, and U. Hampel, "Ultrafast cross-sectional imaging of gas-particle flow in a fluidized bed," *AIChE Journal,* vol. 56, pp. 2221-2225, 2010.

[133] M. Bieberle, E. Schleicher, F. Fischer, D. Koch, H. J. Menz, H. G. Mayer *et al.*, "Dual-plane ultrafast limited-angle electron beam x-ray tomography," *Flow Measurement and Instrumentation,* vol. 21, pp. 233-239, 9// 2010.

[134] R. F. Mudde, "Double X-ray Tomography of a Bubbling Fluidized Bed," *Industrial & Engineering Chemistry Research,* vol. 49, pp. 5061-5065, Jun 2 2010.

[135] H. M. Prasser, M. Misawa, and I. Tiseanu, "Comparison between wire-mesh sensor and ultra-fast X-ray tomograph for an air–water flow in a vertical pipe," *Flow Measurement and Instrumentation,* vol. 16, pp. 73-83, 4// 2005.

[136] Y. T. Shah, B. G. Kelkar, S. P. Godbole, and W. D. Deckwer, "Design parameters estimations for bubble column reactors," *AIChE Journal,* vol. 28, pp. 353-379, 1982.

[137] M. Stein, T. W. Martin, J. P. K. Seville, P. A. McNeil, and D. J. Parker, "Positron emission particle tracking: Particle velocities in gas fluidised beds, mixers and other applications," in *Non-Invasive Monitoring of Multiphase Flows*, J. C. L. P. Duduković, Ed., ed Amsterdam: Elsevier Science B.V., 1997, pp. 309-333.

[138] C. Champion and C. Le Loirec, "Positron follow-up in liquid water: II. Spatial and energetic study for the most important radioisotopes used in PET," *Physics in Medicine and Biology,* vol. 52, pp. 6605-6625, Nov 2007.

[139] D. J. Parker, C. J. Broadbent, P. Fowles, M. R. Hawkesworth, and P. McNeil, "Positron emission particle tracking - a technique for studying flow within engineering equipment," *Nuclear Instruments and Methods in Physics Research Section A: Accelerators, Spectrometers, Detectors and Associated Equipment,* vol. 326, pp. 592-607, 3/10/ 1993.

[140] Z. Yang, X. Fan, P. J. Fryer, D. J. Parker, and S. Bakalis, "Improved multiple-particle tracking for studying flows in multiphase systems," *Aiche Journal,* vol. 53, pp. 1941-1951, Aug 2007.

[141] Z. Yang, X. Fan, S. Bakalis, D. J. Parker, and P. J. Fryer, "A method for characterising solids translational and rotational motions using Multiple-Positron Emission Particle Tracking (Multiple-PEPT)," *International Journal of Multiphase Flow,* vol. 34, pp. 1152-1160, 12// 2008.

[142] M. Stein, Y. L. Ding, J. P. K. Seville, and D. J. Parker, "Solids motion in bubbling gas fluidised beds," *Chemical Engineering Science,* vol. 55, pp. 5291-5300, Nov 2000.

[143] M. Aghbashlo, R. Sotudeh-Gharebagh, R. Zarghami, A. S. Mujumdar, and N. Mostoufi, "Measurement Techniques to Monitor and Control Fluidization Quality in Fluidized Bed Dryers: A Review," *Drying Technology,* vol. 32, pp. 1005-1051, 2014.

[144] F. Depypere, J. G. Pieters, and K. Dewettinck, "PEPT visualisation of particle motion in a tapered fluidised bed coater," *Journal of Food Engineering,* vol. 93, pp. 324-336, Aug 2009.

[145] S. Bakalis, P. W. Cox, A. B. Russell, D. J. Parker, and P. J. Fryer, "Development and use of positron emitting particle tracking (PEPT) for velocity measurements in viscous fluids in pilot scale equipment," *Chemical Engineering Science,* vol. 61, pp. 1864-1877, Mar 2006.

[146] J. Conway-Baker, R. W. Barley, R. A. Williams, X. Jia, J. Kostuch, B. McLoughlin *et al.*, "Measurement of the motion of grinding media in a vertically stirred mill using positron emission particle tracking (PEPT)," *Minerals Engineering,* vol. 15, pp. 53-59, Jan 2002.

[147] P. W. Cox, S. Bakalis, H. Ismail, R. Forster, D. J. Parker, and P. J. Fryer, "Visualisation of three-dimensional flows in rotating cans using positron emission particle tracking (PEPT)," *Journal of Food Engineering,* vol. 60, pp. 229-240, Dec 2003.

[148] Y. L. Ding, J. P. K. Seville, R. Forster, and D. J. Parker, "Solids motion in rolling mode rotating drums operated at low to medium rotational speeds," *Chemical Engineering Science,* vol. 56, pp. 1769-1780, Mar 2001.

[149] P. G. Fairhurst, M. Barigou, P. J. Fryer, J. P. Pain, and D. J. Parker, "Using positron emission particle tracking (PEPT) to study nearly neutrally buoyant particles in high solid fraction pipe flow," *International Journal of Multiphase Flow,* vol. 27, pp. 1881-1901, 11// 2001.

[150] H. P. Kuo, P. C. Knight, D. J. Parker, and J. P. K. Seville, "Solids circulation and axial dispersion of cohesionless particles in a V-mixer," *Powder Technology,* vol. 152, pp. 133-140, 4/29/ 2005.

[151] T. W. Martin, J. P. K. Seville, and D. J. Parker, "A general method for quantifying dispersion in multiscale systems using trajectory analysis," *Chemical Engineering Science,* vol. 62, pp. 3419-3428, Jul 2007.

[152] M. Stein, J. P. K. Seville, and D. J. Parker, "Attrition of porous glass particles in a fluidised bed," *Powder Technology,* vol. 100, pp. 242-250, Dec 1998.

[153] R. D. Wildman, J. M. Huntley, J. P. Hansen, D. J. Parker, and D. A. Allen, "Single-particle motion in three-dimensional vibrofluidized granular beds," *Physical Review E,* vol. 62, pp. 3826-3835, Sep 2000.

[154] R. D. Wildman, J. M. Huntley, and D. J. Parker, "Convection in highly fluidized three-dimensional granular beds," *Physical Review Letters,* vol. 86, pp. 3304-3307, Apr 2001.

[155] R. D. Wildman, J. M. Huntley, and D. J. Parker, "Granular temperature profiles in three-dimensional vibrofluidized granular beds," *Physical Review E,* vol. 63, p. 10, Jun 2001.

[156] Y. S. Wong and J. P. K. Seville, "Single-particle motion and heat transfer in fluidized beds," *Aiche Journal,* vol. 52, pp. 4099-4109, Dec 2006.

[157] X. F. Fan, D. J. Parker, Z. F. Yang, J. P. K. Seville, and J. Baeyens, "The effect of bed materials on the solid/bubble motion in a fluidised bed," *Chemical Engineering Science,* vol. 63, pp. 943-950, Feb 2008.

[158] D. J. Parker, A. E. Dijkstra, T. W. Martin, and J. P. K. Seville, "Positron emission particle tracking studies of spherical particle motion in rotating drums," *Chemical Engineering Science,* vol. 52, pp. 2011-2022, 7// 1997.

[159] J. A. Laverman, X. Fan, A. Ingram, M. V. Annaland, D. J. Parker, J. P. K. Seville *et al.*, "Experimental study on the influence of bed material on the scaling of solids circulation patterns in 3D bubbling gas-solid fluidized beds of glass and polyethylene using positron emission particle tracking," *Powder Technology,* vol. 224, pp. 297-305, Jul 2012.

[160] C. J. Broadbent, J. Bridgwater, D. J. Parker, S. T. Keningley, and P. Knight, "A phenomenological study of a batch mixer using a positron camera," *Powder Technology,* vol. 76, pp. 317-329, 9// 1993.

[161] B. F. C. Laurent, J. Bridgwater, and D. J. Parker, "Motion in a particle bed agitated by a single blade," *AIChE Journal,* vol. 46, pp. 1723-1734, 2000.

[162] R. L. Stewart, J. Bridgwater, and D. J. Parker, "Granular flow over a flat-bladed stirrer," *Chemical Engineering Science,* vol. 56, pp. 4257-4271, 7// 2001.

[163] A. Ingram, J. P. K. Seville, D. J. Parker, X. Fan, and R. G. Forster, "Axial and radial dispersion in rolling mode rotating drums," *Powder Technology,* vol. 158, pp. 76-91, 10/27/ 2005.

[164] M. P. Dudukovic, "Opaque multiphase reactors: Experimentation, modeling and troubleshooting," *Oil & Gas Science and Technology-Revue D Ifp Energies Nouvelles,* vol. 55, pp. 135-158, Mar-Apr 2000.

[165] J. Chaouki, M. P. Dudukovi*c, and F. Larachi. (1997). *Non-invasive monitoring of multiphase flows* [text].

[166] M. Askarishahi, M.-S. Salehi, H. R. Godini, and G. Wozny, "CFD study on solids flow pattern and solids mixing characteristics in bubbling fluidized bed: Effect of fluidization velocity and bed aspect ratio," *Powder Technology,* vol. 274, pp. 379-392, 4// 2015.

[167] X. F. Fan, Z. F. Yang, and D. J. Parker, "Impact of solid sizes on flow structure and particle motions in bubbling fluidization," *Powder Technology,* vol. 206, pp. 132-138, Jan 18 2011.

[168] S. L. Yang, K. Luo, M. M. Fang, and J. R. Fan, "LES-DEM investigation of the solid transportation mechanism in a 3-D bubbling fluidized bed. Part II: Solid dispersion and circulation properties," *Powder Technology,* vol. 256, pp. 395-403, Apr 2014.

[169] W. C. Yang, B. Ettehadieh, and G. B. Haldipur, "Solids Circulation Pattern and Particles Mixing in a Large Jetting Fluidized-Bed," *Aiche Journal,* vol. 32, pp. 1994-2001, Dec 1986.

[170] M. Rudisuli, T. J. Schildhauer, S. M. A. Biollaz, and J. R. van Ommen, "Scale-up of bubbling fluidized bed reactors - A review," *Powder Technology,* vol. 217, pp. 21-38, Feb 2012.

[171] O. A. Jaiboon, B. Chalermsinsuwan, L. Mekasut, and P. Piumsomboon, "Effect of flow patterns/regimes on CO2 capture using K2CO3 solid sorbent in fluidized bed/circulating fluidized bed," *Chemical Engineering Journal,* vol. 219, pp. 262-272, Mar 1 2013.

[172] J. P. K. Seville, H. Silomon-Pflug, and P. C. Knight, "Modelling of sintering in high temperature gas fluidisation," *Powder Technology,* vol. 97, pp. 160-169, Jun 15 1998.

[173] E. N. Ziegler and W. T. Brazelton, "Mechanism of Heat Transfer to a Fixed Surface in a Fluidized Bed," *Industrial & Engineering Chemistry Fundamentals,* vol. 3, pp. 94-98, 1964/05/01 1964.

[174] P. N. Rowe and B. A. Partridge, *Particle movement caused by bubbles in a fluidised bed*: European Federation of Chemical Engineering. Congress, Institution of Chemical Engineers, 1962.

[175] J. S. Lin, M. M. Chen, and B. T. Chao, "A Novel Radioactive Particle Tracking Facility for Measurement of Solids Motion in Gas-Fluidized Beds," *Aiche Journal,* vol. 31, pp. 465-473, 1985.

[176] D. Geldart, *Gas fluidization technology*. Chichester: Wiley, 1986.

[177] A. B. Whitehead, G. Gartside, and D. C. Dent, "Flow and pressure maldistribution at the distributor level of a gas-solid fluidised bed," *The Chemical Engineering Journal,* vol. 1, pp. 175-185, // 1970.

[178] J. Werther and O. Molerus, "The local structure of gas fluidized beds —II. The spatial distribution of bubbles," *International Journal of Multiphase Flow,* vol. 1, pp. 123-138, 10/10/ 1973.

[179] A. B. Whitehead, "Prediction of bubble-size in a gas-fluidized bed," *Chemical Engineering Science,* vol. 34, pp. 751-751, 1979.

[180] D. Geldart, "The effect of particle size and size distribution on the behaviour of gas-fluidised beds," *Powder Technology,* vol. 6, pp. 201-215, 10/4/ 1972.

[181] H. V. Nguyen, A. B. Whitehead, and O. E. Potter, "Gas backmixing, solids movement, and bubble activities in large scale fluidized beds," *AIChE Journal,* vol. 23, pp. 913-922, 1977.

[182] A. B. Whitehead, D. C. Dent, and J. C. H. McAdam, "Fluidization studies in large gas—solid systems Part V. Long and short term pressure instabilities," *Powder Technology,* vol. 18, pp. 231-237, 11// 1977.

[183] D. Pallares and H. Johnsson, "A novel technique for particle tracking in cold 2-dimensional fluidized beds - simulating fuel dispersion," *Chemical Engineering Science,* vol. 61, pp. 2710-2720, Apr 2006.

[184] X. F. Fan, Z. F. Yang, D. J. Parker, and B. Armstrong, "Prediction of bubble behaviour in fluidised beds based on solid motion and flow structure," *Chemical Engineering Journal,* vol. 140, pp. 358-369, Jul 1 2008.

[185] A. B. Whitehead and A. A. Auff, "Fluidization studies in large gas—solid systems. Part IV. Similarity criteria for different size systems," *Powder Technology,* vol. 15, pp. 77-87, 9// 1976.

[186] A. B. Whitehead, G. Gartside, and D. C. Dent, "Fluidization studies in large gas—solid systems. Part III. The effect of bed depth and fluidizing velocity on solids circulation patterns," *Powder Technology,* vol. 14, pp. 61-70, 5// 1976.

[187] N. Mostoufi and J. Chaouki, "Local solid mixing in gas-solid fluidized beds," *Powder Technology,* vol. 114, pp. 23-31, Jan 15 2001.

[188] H. T. Bi, N. Ellis, I. A. Abba, and J. R. Grace, "A state-of-the-art review of gas–solid turbulent fluidization," *Chemical Engineering Science,* vol. 55, pp. 4789-4825, 11// 2000.

[189] E. Sette, D. Pallarès, and F. Johnsson, "Experimental evaluation of lateral mixing of bulk solids in a fluid-dynamically down-scaled bubbling fluidized bed," *Powder Technology,* vol. 263, pp. 74-80, 9// 2014.

[190] I. N. M. Woollard and O. E. Potter, "Solids mixing in fluidized beds," *AIChE Journal,* vol. 14, pp. 388-391, 1968.

[191] P. N. Rowe, B. A. Partridge, A. G. Cheney, G. A. Henwood, and E. Lyall, "The mechanisms of solids mixing in fluidized beds," *Transactions of the Institution of Chemical Engineers,* vol. 43, pp. T271-T286, 1965.

[192] P. N. Rowe and B. A. Partridge, "An X-Ray Study of Bubbles in Fluidised Beds," *Transactions of the Institution of Chemical Engineers and the Chemical Engineer,* vol. 43, pp. T157-&, 1965.

[193] S. Sánchez-Delgado, C. Marugán-Cruz, A. Acosta-Iborra, and D. Santana, "Dense-phase velocity fluctuation in a 2-D fluidized bed," *Powder Technology,* vol. 200, pp. 37-45, 6/15/ 2010.

[194] D. Santana, S. Nauri, A. Acosta, N. García, and A. Macías-Machín, "Initial particle velocity spatial distribution from 2-D erupting bubbles in fluidized beds," *Powder Technology,* vol. 150, pp. 1-8, 1/31/ 2005.

[195] J. A. Almendros-Ibáñez, C. Sobrino, M. de Vega, and D. Santana, "A new model for ejected particle velocity from erupting bubbles in 2-D fluidized beds," *Chemical Engineering Science,* vol. 61, pp. 5981-5990, 9// 2006.

[196] J. A. Valenzuela and L. R. Glicksman, "An experimental study of solids mixing in a freely bubbling two-dimensional fluidized bed," *Powder Technology,* vol. 38, pp. 63-72, 3// 1984.

[197] K. S. Lim, J. X. Zhu, and J. R. Grace, "Hydrodynamics of gas-solid fluidization," *International Journal of Multiphase Flow,* vol. 21, pp. 141-193, Dec 1995.

[198] Y. V. Lam Cheun U, "Solids motion in fluidised beds of fine particles," Doctor of Philosophy, University of Birmingham, 2010.

[199] K. S. Lim, V. S. Gururajan, and P. K. Agarwal, "Mixing of homogeneous solids in bubbling fluidized beds: Theoretical modelling and experimental investigation using digital image analysis," *Chemical Engineering Science,* vol. 48, pp. 2251-2265, // 1993.

[200] G. A. Bokkers, M. van Sint Annaland, and J. A. M. Kuipers, "Mixing and segregation in a bidisperse gas–solid fluidised bed: a numerical and experimental study," *Powder Technology,* vol. 140, pp. 176-186, 2/25/ 2004.

[201] Y. F. Shi and L. T. Fan, "Lateral mixing of solids in batch gas-solids fluidized beds," *Industrial & Engineering Chemistry Process Design and Development,* vol. 23, pp. 337-341, 1984/04/01 1984.

[202] B. Du, L.-S. Fan, F. Wei, and W. Warsito, "Gas and solids mixing in a turbulent fluidized bed," *AIChE Journal,* vol. 48, pp. 1896-1909, 2002.

[203] E. R. Gilliland and E. A. Mason, "Gas and Solid Mixing in Fluidized Beds," *Industrial & Engineering Chemistry,* vol. 41, pp. 1191-1196, 1949/06/01 1949.

[204] W. G. May, "Fluidized-bed reactor studies," *Chem Eng Progress,* vol. 55, pp. 49-56, 1959.

[205] W. Brötz, "Untersuchungen über Transportvorgänge in durchströmtem, gekörntem Gut," *Chemie Ingenieur Technik,* vol. 28, pp. 165-174, 1956.

[206] P. Xiao, G. Yan, and D. Wang, "Investigation on horizontal mixing of particles in dense bed in Circulating Fluidized Bed (CFB)," *Journal of Thermal Science,* vol. 7, pp. 78-84, 1998/06/01 1998.

[207] A. Avidan and J. Yerushalmi. (1985, 01). Solids mixing in an expanded top fluid bed. *AIChE Journal 31(5),* 835-841. Available: http://onlinelibrary.wiley.com/doi/10.1002/aic.690310520/abstract

[208] D. Bellgardt and J. Werther, "A Novel Method for the Investigation of Particle Mixing in Gas Solid Systems," *Powder Technology,* vol. 48, pp. 173-180, Oct 1986.

[209] R. Chirone, F. Miccio, and F. Scala, "On the Relevance of Axial and Transversal Fuel Segregation during the FB Combustion of a Biomass," *Energy & Fuels,* vol. 18, pp. 1108-1117, 2004/07/01 2004.

[210] G. Grasa and J. C. Abanades, "The use of two different models to describe the axial mixing of solids in fluidised beds," *Chemical Engineering Science,* vol. 57, pp. 2791-2798, 7// 2002.

[211] J. J. van Deemter, "Mixing and contacting in gas-solid fluidized beds," *Chemical Engineering Science,* vol. 13, pp. 143-154, 2// 1961.

[212] J. J. van Deemter, "Mixing," in *Fluidization*, J. F. Davidson, R. Clift, and D. Harrison, Eds., 2nd ed London, England: Academic Press, Inc., 1985, pp. 331-355.

[213] L. Shen and M. Zhang, "Effect of particle size on solids mixing in bubbling fluidized beds," *Powder Technology,* vol. 97, pp. 170-177, 6/15/ 1998.

[214] C. N. Lim, M. A. Gilbertson, and A. J. L. Harrison, "Bubble distribution and behaviour in bubbling fluidised beds," *Chemical Engineering Science,* vol. 62, pp. 56-69, Jan 2007.

[215] P. K. Baumgarten and R. L. Pigford, "Density fluctuations in fluidized beds," *AIChE Journal,* vol. 6, pp. 115-123, 1960.

[216] W. H. Park, W. K. Kang, C. E. Capes, and G. L. Osberg, "The properties of bubbles in fluidized beds of conducting particles as measured by an electroresistivity probe," *Chemical Engineering Science,* vol. 24, pp. 851-865, 5// 1969.

[217] J. R. Grace and D. Harrison, "The Distribution of Bubbles Within a Gas-Fluidized Bed," *Inst. Chem. Eng. Sym. Ser.,* vol. 30, pp. 105-113, 1968.

[218] J. R. Grace and D. Harrison, "Behaviour of Freely Bubbling Fluidised Beds," *Chemical Engineering Science,* vol. 24, pp. 497-&, 1969.

[219] J. M. Weber and J. S. Mei, "Bubbling fluidized bed characterization using Electrical Capacitance Volume Tomography (ECVT)," *Powder Technology,* vol. 242, pp. 40-50, Jul 2013.

[220] V. Verma, J. T. Padding, N. G. Deen, J. A. M. Kuipers, F. Barthel, M. Bieberle *et al.*, "Bubble dynamics in a 3-D gas-solid fluidized bed using ultrafast electron beam X-ray tomography and two-fluid model," *Aiche Journal,* vol. 60, pp. 1632-1644, May 2014.

[221] J. Saayman, W. Nicol, J. R. Van Ommen, and R. F. Mudde, "Fast X-ray tomography for the quantification of the bubbling-, turbulent-and fast fluidization-flow regimes and void structures," *Chemical Engineering Journal,* vol. 234, pp. 437-447, Dec 2013.

[222] P. A. Olowson and A. E. Almstedt, "Influence of pressure and fluidization velocity on the bubble behaviour and gas flow distribution in a fluidized bed," *Chemical Engineering Science,* vol. 45, pp. 1733-1741, // 1990.

[223] G. R. Caicedo, J. J. P. Marques, M. G. Ruiz, and J. G. Soler, "A study on the behaviour of bubbles of a 2D gas-solid fluidized bed using digital image analysis," *Chemical Engineering and Processing,* vol. 42, pp. 9-14, Jan 2003.

[224] R. F. Mudde, H. B. M. Schulte, and H. E. A. Vandenakker, "Analysis of a Bubbling 2-D Gas-Fluidized Bed Using Image-Processing," *Powder Technology,* vol. 81, pp. 149-159, Nov 1994.

[225] S. Mori and C. Y. Wen, "Estimation of Bubble Diameter in Gaseous Fluidized-Beds," *Aiche Journal,* vol. 21, pp. 109-115, 1975.

[226] J. S. Sung and J. M. Burgess, "A laser-based method for bubble parameter measurement in two-dimensional fluidised beds," *Powder Technology,* vol. 49, pp. 165-175, 1// 1987.

[227] S. Karimipour and T. Pugsley, "A critical evaluation of literature correlations for predicting bubble size and velocity in gas-solid fluidized beds," *Powder Technology,* vol. 205, pp. 1-14, Jan 10 2011.

[228] D. Geldart, "The size and frequency of bubbles in two- and three-dimensional gas-fluidised beds," *Powder Technology,* vol. 4, pp. 41-55, 11// 1970.

[229] D. Geldart, "The expansion of bubbling fluidised beds," *Powder Technology,* vol. 1, pp. 355-368, 4// 1968.

[230] A. Whitehead and A. Young, "Fluidization performance in large scale equipment," *Proc. Intern. Symp. on Fluidization,* pp. 284-293, 1967.

[231] P. N. Rowe and D. J. Everett, "Fluidized-bed bubbles viewed by X-rays. 3. Bubble size and number when unrestrained 3-dimensional growth occurs," *Transactions of the Institution of Chemical Engineers and the Chemical Engineer,* vol. 50, pp. 55-&, 1972.

[232] R. C. Darton, R. D. Lanauze, J. F. Davidson, and D. Harrison, "Bubble-Growth Due to Coalescence in Fluidized-Beds," *Transactions of the Institution of Chemical Engineers,* vol. 55, pp. 274-280, 1977.

[233] C. Fryer and O. E. Potter, "Experimental investigation of models for fluidized bed catalytic reactors," *AIChE Journal,* vol. 22, pp. 38-47, 1976.

[234] J. Werther, "Influence of bed diameter in scale enlargement of gas-solid fluidized-beds," *Chemie Ingenieur Technik,* vol. 46, pp. 41-42, 1974.

[235] J. Werther, "Effect of gas distributor on the hydrodynamics of gas fluidized beds," *Ger Chem Eng,* vol. 1, pp. 166-174, 1978.

[236] W. Bauer, J. Werther, and G. Emig, "Influence of gas distributor design on the performance of fluidized bed reactor," *German Chemical Engineering,* vol. 4, pp. 291-298, 1981.

[237] R. M. Davies and G. Taylor, "The Mechanics of Large Bubbles Rising through Extended Liquids and through Liquids in Tubes," *Proceedings of the Royal Society of London Series a-Mathematical and Physical Sciences,* vol. 200, pp. 375-390, 1950.

[238] J. F. Davidson and D. Harrison, *Fluidised particles*. Cambridge: CUP, 1963.

[239] K. Hilligardt and J. Werther, "Local bubble gas hold-up and expansion of gas/solid fluidized beds," *German chemical engineering,* vol. 9, pp. 215-221, 1986.

[240] J. Chaouki, F. Larachi, and M. P. Dudukovic, *Non-invasive monitoring of multiphase flows*. Amsterdam ; Oxford: Elsevier, 1997.

[241] D. M. Benton and D. J. Parker, "Non-medical applications of positron emission tomography," in *Non-Invasive Monitoring of Multiphase Flows*, J. C. L. P. Duduković, Ed., ed Amsterdam: Elsevier Science B.V., 1997, pp. 161-184.

[242] P. Hautojarvi, *Positrons in Solids*. Berlin: Springer-Verlag, 1979.

[243] D. J. Parker, R. N. Forster, P. Fowles, and P. S. Takhar, "Positron emission particle tracking using the new Birmingham positron camera," *Nuclear Instruments & Methods in Physics Research Section a-Accelerators Spectrometers Detectors and Associated Equipment,* vol. 477, pp. 540-545, Jan 21 2002.

[244] T. W. Leadbeater, "The development of positron imaging systems for applications in industrial process tomography," Doctor of Philosophy, University of Birmingham, 2009.

[245] S. A. Cottilard, *Catalytic combustion*. Hauppauge, N.Y.: Nova Science, 2011.

[246] A. W. Nienow and D. J. Cheesman, "The Effect of Shape on the Mixing and Segregation of Large Particles in a Gas-Fluidised Bed of Small Ones," in *Fluidization*, J. R. Grace and J. M. Matsen, Eds., ed Boston, MA: Springer US, 1980, pp. 373-380.

[247] L. ChungLim and S. M. Arun, "Fluidized Bed Dryers," in *Handbook of Industrial Drying, Fourth Edition*, ed: CRC Press, 2014, pp. 161-189.

[248] Y. Li, H. Fan, and X. Fan, "Identify of flow patterns in bubbling fluidization," *Chemical Engineering Science,* vol. 117, pp. 455-464, 9/27/ 2014.

[249] J. Li and M. Kwauk, *Particle-fluid two-phase flow: the energy-minimization multi-scale method*. Beijing: Metallurgical Industry Press, 1994.

[250] Z. S. Shi, W. Wang, and J. H. Li, "A bubble-based EMMS model for gas-solid bubbling fluidization," *Chemical Engineering Science,* vol. 66, pp. 5541-5555, Nov 15 2011.

[251] Q. G. Xiong, L. J. Deng, W. Wang, and W. Ge, "SPH method for two-fluid modeling of particle-fluid fluidization," *Chemical Engineering Science,* vol. 66, pp. 1859-1865, May 1 2011.

[252] N. Herzog, M. Schreiber, C. Egbers, and H. J. Krautz, "A comparative study of different CFD-codes for numerical simulation of gas-solid fluidized bed hydrodynamics," *Computers & Chemical Engineering,* vol. 39, pp. 41-46, Apr 6 2012.

[253] X. K. Ku, T. Li, and T. Lovas, "Influence of drag force correlations on periodic fluidization behavior in Eulerian-Lagrangian simulation of a bubbling

fluidized bed," *Chemical Engineering Science,* vol. 95, pp. 94-106, May 24 2013.

[254] Y. Wang, Z. Zou, H. Li, and Q. Zhu, "A new drag model for TFM simulation of gas–solid bubbling fluidized beds with Geldart-B particles," *Particuology,* 2013.

[255] B. Trisakti, J. Oshitani, and Z. Tanaka, "Circulating particle flow and air bubble behavior at various superficial air velocities in two-dimensional gas-solid fluidized beds," *Advanced Powder Technology,* vol. 12, pp. 507-519, 2001.

[256] T. Kai, T. Kanda, T. Takahashi, and M. Kawaji, "Application of photochromic dye to the measurement of particle movement in a fluidized bed," *Powder Technology,* vol. 129, pp. 22-29, Jan 8 2003.

[257] A. Soria-Verdugo, L. M. Garcia-Gutierrez, S. Sanchez-Delgado, and U. Ruiz-Rivas, "Circulation of an object immersed in a bubbling fluidized bed," *Chemical Engineering Science,* vol. 66, pp. 78-87, Jan 1 2011.

[258] L. M. Garcia-Gutierrez, A. Soria-Verdugo, N. Garcia-Hernando, and U. Ruiz-Rivas, "Simulation of object motion in a bubbling fluidized bed using a Monte Carlo method," *Chemical Engineering Science,* vol. 96, pp. 26-32, Jun 7 2013.

[259] Y.-C. Lin and C.-S. Chyang, "Radial gas mixing in a fluidized bed using response surface methodology," *Powder Technology,* vol. 131, pp. 48-55, 3/3/ 2003.

[260] K. Smolders and J. Baeyens, "Gas fluidized beds operating at high velocities: a critical review of occurring regimes," *Powder Technology,* vol. 119, pp. 269-291, Sep 24 2001.

[261] Y. L. Ding, Z. L. Wang, D. S. Wen, M. Ghadiri, X. F. Fan, and D. Parker, "Solids behaviour in a dilute gas-solid two-phase mixture flowing through monolith channels," *Chemical Engineering Science,* vol. 61, pp. 1561-1570, Mar 2006.

[262] J. W. Wang, M. A. van der Hoef, and J. A. M. Kuipers, "The role of scale resolution versus inter-particle cohesive forces in two-fluid modeling of bubbling fluidization of Geldart A particles," *Chemical Engineering Science,* vol. 66, pp. 4229-4240, Sep 15 2011.

[263] C. R. Müller, J. F. Davidson, J. S. Dennis, P. S. Fennell, L. F. Gladden, A. N. Hayhurst *et al.*, "Oscillations in gas-fluidized beds: Ultra-fast magnetic resonance imaging and pressure sensor measurements," *Powder Technology,* vol. 177, pp. 87-98, 8/15/ 2007.

[264] H. Sedighikamal and R. Zarghami, "Dynamic characteristics of bubbling fluidization through recurrence rate analysis of pressure fluctuations," *Particuology,* vol. 11, pp. 282-287, Jun 2013.

[265] A. G. Mychkovsky and S. L. Ceccio, "LDV measurements and analysis of gas and particulate phase velocity profiles in a vertical jet plume in a 2D bubbling fluidized bed Part III: The effect of fluidization," *Powder Technology,* vol. 220, pp. 37-46, Apr 2012.

[266] D. Mewes, "Visualization Techniques in Process Engineering," in *Ullmann's Encyclopedia of Industrial Chemistry*, ed: Wiley-VCH Verlag GmbH & Co. KGaA, 2000.

[267] J. F. Davidson, D. Harrison, and J. R. F. G. D. Carvalho, "On the Liquidlike Behavior of Fluidized Beds," *Annual Review of Fluid Mechanics,* vol. 9, pp. 55-86, 1977.

[268] P. G. Smith, *Applications of fluidization to food processing*. Oxford ; Ames, Iowa: Blackwell Science, 2007.

[269] E. K. Levy, H. S. Caram, J. C. Dille, and S. Edelstein. (1983, 01). Mechanisms for solids ejection from gas-fluidized beds. *AIChE Journal 29(3),* 383-388. Available: http://onlinelibrary.wiley.com/doi/10.1002/aic.690290306/abstract

[270] J. Szekely, J. W. Evans, and H. Y. Sohn, *Gas-solid reactions*. New York: Academic Press, 1976.

[271] S. Maurer, E. C. Wagner, T. J. Schildhauer, J. R. van Ommen, S. M. A. Biollaz, and R. F. Mudde, "X-ray measurements of bubble hold-up in fluidized beds with and without vertical internals," *International Journal of Multiphase Flow,* vol. 74, pp. 118-124, 9// 2015.

[272] L. T. Fan, J. C. Song, and N. Yutani, "Radial particle mixing in gas-solids fluidized beds," *Chemical Engineering Science,* vol. 41, pp. 117-122, // 1986.

[273] Y. Zhang, C. Lu, and M. Shi, "Evaluating solids dispersion in fluidized beds of fine particles by gas backmixing experiments," *Chemical Engineering Research and Design,* vol. 87, pp. 1400-1408, 10// 2009.

[274] D. Liu and X. Chen, "Lateral solids dispersion coefficient in large-scale fluidized beds," *Combustion and Flame,* vol. 157, pp. 2116-2124, 11// 2010.

[275] A. Einstein, "Über die von der molekularkinetischen Theorie der Wärme geforderte Bewegung von in ruhenden Flüssigkeiten suspendierten Teilchen," *Annalen der Physik,* vol. 322, pp. 549-560, 1905.

[276] K. Pearson, "The problem of the random walk," *Nature,* vol. 72, pp. 294-294, May-Oct 1905.

[277] F. Niklasson, H. Thunman, F. Johnsson, and B. Leckner, "Estimation of Solids Mixing in a Fluidized-Bed Combustor," *Industrial & Engineering Chemistry Research,* vol. 41, pp. 4663-4673, 2002/09/01 2002.

[278] A. Esin and M. Altun, "Correlation of axial mixing of solids in fluidized beds by a dispersion coefficient," *Powder Technology,* vol. 39, pp. 241-244, 9// 1984.

[279] Y.-F. Shi and L. T. Fan, "Lateral mixing of solids in gas—solid fluidized beds with continuous flow of solids," *Powder Technology,* vol. 41, pp. 23-28, 1// 1985.

[280] S. Chandrasekhar, "Stochastic Problems in Physics and Astronomy," *Reviews of Modern Physics,* vol. 15, pp. 1-89, 01/01/ 1943.

[281] E. C. Eckstein, D. G. Bailey, and A. H. Shapiro, "Self-Diffusion of Particles in Shear-Flow of a Suspension," *Journal of Fluid Mechanics,* vol. 79, pp. 191-208, 1977.

[282] O. Oke, P. Lettieri, P. Salatino, R. Solimene, and L. Mazzei, "Numerical simulations of lateral solid mixing in gas-fluidized beds," *Chemical Engineering Science,* vol. 120, pp. 117-129, 12/16/ 2014.

[283] V. A. Borodulya, Y. G. Epanov, and Y. S. Teplitskii, "Horizontal particle mixing in a free fluidized bed," *Journal of engineering physics,* vol. 42, pp. 528-533, 1982/05/01 1982.

[284] T. Hirama, M. Ishida, and T. Shirai, "The Lateral Dispersion of Solid Particles in Fluidized Beds," *KAGAKU KOGAKU RONBUNSHU,* vol. 1, pp. 272-276, 1975.

[285] M. Bickell, A. Buffler, I. Govender, and D. J. Parker, "A new line density tracking algorithm for PEPT and its application to multiple tracers," *Nuclear Instruments and Methods in Physics Research Section A: Accelerators, Spectrometers, Detectors and Associated Equipment,* vol. 682, pp. 36-41, 8/1/ 2012.

[286] S. Langford, C. Wiggins, D. Tenpenny, and A. Ruggles, "Positron Emission Particle Tracking (PEPT) for Fluid Flow Measurements," *Nuclear Engineering and Design*.

[287] P. N. Rowe and R. Matsuno, "Single Bubbles Injected into a Gas Fluidised Bed and Observed by X-Rays," *Chemical Engineering Science,* vol. 26, pp. 923-&, 1971.

[288] I. Wright, K. Hamilton, S. Kruychkov, J. W. Chen, F. Li, and A. Kantzas, "On the measurement of hydrodynamic properties of an air-polyethylene fluidized bed system," *Chemical Engineering Science,* vol. 56, pp. 4085-4097, Jul 2001.

[289] S. Maurer, E. C. Wagner, J. R. van Ommen, T. J. Schildhauer, S. L. Teske, S. M. A. Biollaz *et al.*, "Influence of vertical internals on a bubbling fluidized bed characterized by X-ray tomography," *International Journal of Multiphase Flow,* vol. 75, pp. 237-249, 10// 2015.